Dynamic homogenization of linear waves in periodic media and origami-inspired structures

A DISSERTATION
SUBMITTED TO THE FACULTY OF THE GRADUATE SCHOOL
OF THE UNIVERSITY OF MINNESOTA
BY

Othman Oudghiri-Idrissi

IN PARTIAL FULFILLMENT OF THE REQUIREMENTS
FOR THE DEGREE OF
DOCTOR OF PHILOSOPHY

Adviser: Bojan B. Guzina

March, 2022

Acknowledgements

The achievement of my dissertation work was possible thanks to the support of several people to whom I am deeply grateful.

I would like to express first my sincere thanks to my Adviser Professor Bojan B. Guzina for his constant guidance and support during my PhD studies. I would like to thank equally my dissertation committee, Professor Vaughan R. Voller, Professor Stefano Gonella and Professor Ryan S. Elliott for their time and commitment.

My profound gratitude goes as well to my Teachers and Professors in Morocco, France and USA for their fundamental contribution in building my scholarship. I will eternally be thankful to them.

My studies at the University of Minnesota have been colorful thanks to the unique friendships that I developed and benefited from. I would like to thank specifically my friend and fellow Danial Panahandeh-Shahraki for all the good discussions and precious time that we had within and outside the University.

My pursuit of knowledge journey wouldn't have been fruitful without the continuous support and prayers of my parents and family who will always owe my immense gratitude.

Dedication

To my parents, Ms. Souad Benjelloun and Mr. Abdelaziz Oudghiri-Idrissi. To my uncle and aunt, Mr. Mohamed Benjelloun and Ms. Anissa Benjelloun.

Abstract

This dissertation aims to establish a comprehensive analytical framework for dynamic homogenization of wave motion at arbitrary frequency in (i) "perforated" periodic continua, and (ii) periodic origami-inspired structures described via "bar-and-hinge" computational paradigm. For a given spectral (i.e. frequency-wavenumber) content the body force acting on the structure, the "activated" Bloch eigenstates of the lattice are identified and classified depending on the multiplicity of participating energy levels. In the vicinity of an isolated dispersion surface (single energy level), an effective field equation with homogenized source term is formulated (via projection onto the dominant Bloch eigenstate) to obtain the leading- and second-order approximations of both macroscopic, i.e. "mean", and microscopic wave motion. When the activated spectral neighborhood features more than one dispersion surface, the zeroth- and first-order systems of effective field equations with homogenized source terms are formulated, covering a variety of topological configurations such as Dirac points, avoided crossings, and near-Dirac points. On setting the source term to zero, the featured system of equations degenerates to a low-order algebraic eigenvalue problem that accurately captures the local geometry of (a cluster of) dispersion surfaces. The proposed homogenization framework is verified by comparing the asymptotic approximation of the dispersion relationship with its numerically-evaluated counterpart and deployed to approximate the total and effective motion in: (i) two-dimensional (2D) Kagome lattice featuring nearly-hexagonal Neumann exclusions, (ii) 2D square lattice of circular Dirichlet obstacles, (iii) 2D Miura-ori origami structure, and (iv) 1D Miura tube. Specifically, the asymptotic model is shown to approximate the dispersion relationship in the neighborhood of isolated dispersion surfaces and tight clusters thereof with equal fidelity. It is also found that the homogenized model is capable of accurately capturing the body-force induced waveforms in a lattice, both in terms of macroscopic i.e. effective motion and microstructural motion when higher-order models are considered.

Contents

List of Tables

List of Figures

Chapter 1

Introduction

1.1 Dynamic Homogenization

Dynamic homogenization of periodic media such as composites, phononic crystals, and metamaterials serves to (i) deepen insight into the underpinning physical phenomena such as wave directivity, stop bands, and negative refraction [8, 21, 47], (ii) reduce the burden of multi-scale numerical simulations, and (iii) aid the "microstructural" design catering for applications such us cloaking [15], vibration control [11], logic circuits [28], or seismic shielding [1]. To survey the lay of the land in terms of homogenization strategies, it is generally convenient to distinguish between competing frequency and wavelength regimes.

In the low-wavenumber, low-frequency (LW-LF) regime, one assumes the separation in scale between some finite wavelength and the vanishing lengthscale of medium periodicity, which then provides a perturbation parameter for the two-scale homogenization method [5, 17, 12, 43] and the Bloch-wave expansion (BWE) approach [3, 39, 44] towards establishing a macroscopic i.e. effective description of the medium. In this regime, a non-asymptotic effective medium model introduced by Willis [45, 35, 46], that links in coupled form the momentum and stress to particle velocity and strain, has also gained notable traction in the literature [72, 47].

In principle, the two- (or more generally multiple-) scale homogenization framework applies equally to the low-wavenumber, high-frequency (LW-HF) regime where the lengthscale "ℓ" of medium periodicity vanishes in the limit, while the dominant wavelength is kept at $O(1)$ irrespective of the vibration frequency. In this case, eigenfrequencies of the unit cell problem grow as $O(\ell^{-1})$, which justifies the customary "high frequency" designation. In this vein, Allaire and Conca [4] introduced the Bloch wave

homogenization method, which is essentially a combination of BWE and two-scale convergence analysis [2]. The subject of LW-HF homogenization via multiple-scale expansion has since been pursued in a number of studies, with applications to e.g. Maxwell equations [42] and Navier equations [10].

In the finite-wavenumber, finite-frequency (FW-FF) regime, the wavelength and the unit cell size may be of the same order. For this class of problems, the "high frequency homogenization" (HFH) treatment introduced by Craster and co-workers [53] loosely exploits the small size of the unit cell relative to dimensions of the periodic domain to establish a two-scale analysis of the homogeneous wave equation in periodic media. The method yields zeroth- i.e. leading-order effective description of the medium, in the vicinity of simple and multiple eigenfrequencies, that is shown to capture dynamic phenomena such as anisotropic wave motion [8, 16] and all-angle negative refraction [19]. In more recent studies, the HFH has extended to deal with zero-frequency stop-band media, i.e. those with Dirichlet inclusions [7, 30], and to periodic media with Neumann inclusions [6]. From the mathematical viewpoint, the existence of FW-FF effective differential operators was formally established by Birman and Suslina [13, 14], who considered the behavior of periodic systems near the edge of an internal band gap. On the engineering side, an effort was also made to extend the Willis' homogenization approach to finite frequencies and wavelengths [36] by introducing additional kinematic degrees of freedom; however the uniqueness of such effective model remains an open question. Recently, a systematic framework for homogenization of the scalar wave equation in the FW-FF regime was proposed in [23]. This study, catering for rectangular lattices, makes use of PWE to secure a "tight handle" on the wavenumber, and defines the perturbation parameter as a distance in the frequency-wavenumber space in order to obtain effective medium description in the vicinity of simple, repeated, and and nearby eigenfrequencies. As a means to deal with finite (non-zero) wavenumbers, the authors in [23] make use of the so-called multicell technique [20, 22], which essentially restricts the applicability of their model to the apexes of the first Brillouin zone and its quadrants in $\mathbb{R}^2$ (resp. octants in $\mathbb{R}^3$). In essence, such restriction on the wavenumber ensures that the germane Bloch eigenfunctions have constant phase over the unit cell, which lends itself to an immediate proof that the effective medium properties are real-valued there. Unlike the HFH approach, this study also includes a homogenization treatment of the source term, which (as it turns out) is also subject to asymptotic corrections; see also [3, 72] in the context of LW-LF homogenization.

In a broader context, a closely related problem is that of multiple scattering of low-frequency waves by periodic or aperiodic arrays of obstacles. For instance, the dispersive behavior of two-dimensional lattices of sub-wavelength Dirichlet scatterers in acoustic media was studied in [41] via the method of matched asymptotic expansions and Fourier

series. Concerning the multiple scattering of scalar waves, an effective wavefield and transmission condition across a distribution of inertial inclusions along a smooth contour was obtained in [32] using the method of meso-scale approximation. Similar results were obtained in [49] for a cluster of inhomogeneities and Neumann exclusions, and in [48] for inclusions with impedance boundary conditions. Analogous mathematical models were obtained for scatterers in thin plates by way of the Kirchhoff-Love model [38, 31], and within the linear elasticity framework [25].

1.2 Origami Structures

Origami, the ancient Japanese art of paper folding (see examples in Fig. 1.1), has become a source of artistic and technologic inspiration and a keen subject of studies for architects, engineers, mathematicians and scientists for its unique scalability, programability, deployability and configurability properties. This class of structures have rapidly found applications ranging from nano to large scales in science, engineering and architecture with examples including medical stents [62], artificial muscles [70], sandwich panels fold cores [54], energy absorbing structures [80], vibration control [89], emergency shelters [73], sound barriers [83], inflatable structures [82], and large spacecraft structures [50]. Origami-like engineered structures have also been found to exhibit the so-called metaproperties that are not observed in conventional structures and natural materials [63], for instance auxeticity (negative Poisson's ratio), infinite shear stiffness or negative bending stiffness [85], unidirectional flexibility in the deployment direction [57], Poisson's ratio sign switch [79], strain reversal in origami tubes [86, 59], superflexibility [61] or supratransmission [88].

In general, the full-resolution deformation of origami structures can be assessed numerically via nonlinear dynamic finite element (FE) simulations where origami panels are discretized using shell elements [76]. However the essential deformation of origami structures can be captured, at a fraction of computational cost, by using a discrete model [55, 52], where: (i) the folding and bending elastic potentials are assigned respectively to the fold lines and panels' diagonal lines, and (ii) an isometric deformation is assumed for the elemental triangulated panels. In a departure from such multi-rigid-body model toward more flexible origami description, a "pin-jointed" framework was proposed by Schenk and Guest [81] to study the folding mechanisms and global stiffness of folded sheets, where the in-plane stiffness of origami quadrilateral panels is modeled with five elastic bars that link four pin-joints on the panels' vertices. The folding mechanism of the origami sheet and internal bending of the panels were taken into account via rotational linear springs placed respectively on the fold and diagonal lines of the panels. This model enabled the identification of folding modes using a stiffness matrix approach (vs. the

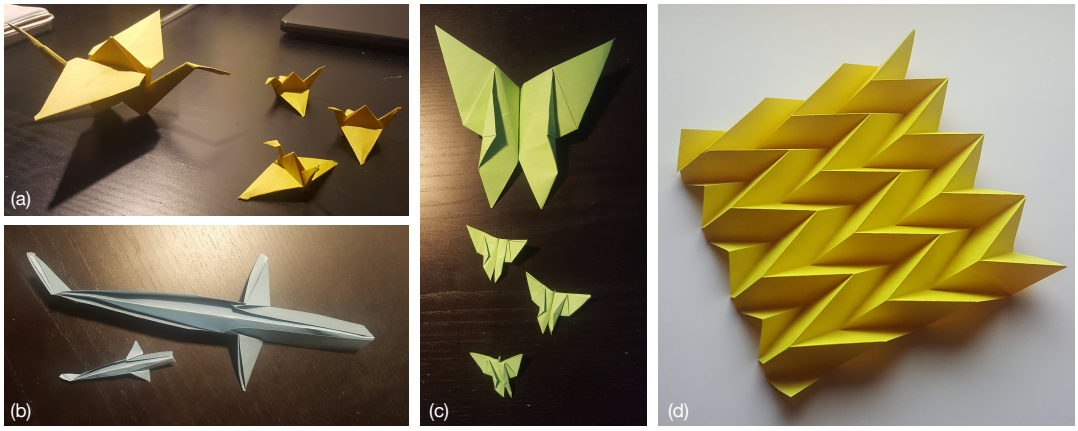

Figure 1.1: Origami paper creations: (a) cranes; (b) whales; (c) butterflies; (d) Miura-ori pattern (folded by OOI).

earlier kinematic approach); yet, it suffered from a non-symmetry and non-isotropy of the in-plane deformation of origami panels [58]. A similar approach was considered by Wei et al. [85] to derive analytically (resp. evaluate numerically) the in-plane stretching and out-of-plane bending of a periodic Miura-ori structure based on the analysis of the unit cell (resp. full structure). A bar-and-hinge element with an additional diagonal bar was proposed in [56] to symmetrize the in-plane response of individual panels; however, a key limitation on their bending approximation was identified. Building upon the earlier works, Filipov et al. [58] developed and studied numerically a simple yet effective bar-and-hinge approximation framework where the isotropic in-plane stretching and sheering of the origami panels are captured with eight bars that link the panels' vertices to each other and to a central node, while the folding of the origami creases and bending of its panels are modeled with elastic hinges distributed along the peripheral and diagonal bars. The later model was found to be scalable and to allow for the description of large panel deformation. For instance, Liu et al. [65] studied the finite deformation of non-rigid origami structures using bar-and-hinge model within a nonlinear mechanics framework. The model was shown to be numerically efficient in describing the global folding kinematics, bending curvatures and multi-stability of origami structures when compared to a shell-element based FE model. On the downside, the bar-and-hinge model discretizes the origami structure by following the intrinsic geometry of its panels, which limits its approximation of local stresses [58]. However, the local deformation and stress approximations can always be improved by refining the origami (polygonal) panels triangulation [65]. In such model, material properties of the origami structure (the bar and hinge stiffnesses) can be either informed analytically from the plate theory,

calibrated numerically [58], or assessed experimentally [69, 77] by examining the statics of folding and in-plane deformation of thin sheets.

Unlike the statics and slow-rate kinematics of origami structures, the dynamic behavior of origami structures remains an open research question [84]. In this regime, Yasuda [86] unveiled a rich linear and nonlinear wave dynamics of origami-based structures by studying Tachi-Miura-polyhedron and triangulated-cylindrical origami structures. More recently, Liu et al. [64] proposed a five-step approach to fabricate a Miura tube whose fundamental frequency and displacement amplitude can be extremized by by optimizing its geometrical properties (folding angle, unit cell dimensions, and number of unit cells). On the computational side of the problem, Wu et al. [84] considered a multi-degree-of-freedom dynamic model of origami tubes to describe their transient free-deployment by assuming rigid folding of the origami panels, assigning an elastic potential energy to the folds and investigating the effect of physical and geometrical properties. In the dynamic regime, a simplified bar-and-hinge paradigm can be generally adopted to reduce computational cost of full FE simulations of an origami structure toward evaluating e.g. its natural frequencies, band gaps, or global forced motion. Yet, even if the later model is deployed, the problem size (in terms of the number degrees of freedom) scales up quickly with the number of unit cells used to construct large origami structures and diminishing wavelength. Therefore, a more efficient framework is needed to capture the essential dynamics of origami structures while reducing the cost of numerical simulations. One viable approach to achieve both goals is that of dynamic homogenization.

The existing literature on the homogenization of periodic origami-like structures can be classified chiefly by (i) the dynamic regime of study (namely static, low-frequency, or high-frequency regime), and (ii) the mechanistic framework adopted to model the origami panels. In the static regime, Lebe and Sab [66] derived analytically the upper and lower bounds of the effective transverse shear moduli of a chevron folded paper using the Reissner-Mindlin plate theory for the panels. They equally pursued a homogenization analysis of periodic thick plates [68] using the bending-gradient plate theory [67]. On the other hand, when an origami structure is modeled using the bar-and-hinge paradigm, the existing literature on trusses can be deployed to study its dynamic properties. Concerning the latter subject, Craster et al. [53] extended the homogenization theory of discrete periodic lattices to high frequency and propagating wavelengths that are commensurate with the size of the unit cell. Targeting the same dynamic regime, Nolde et al. [74] formulated the effective equations that govern two-dimensional nets, while Makwana and Craster [71] derived continuum-based homogenized equations that capture the dispersion of waves in discrete hexagonal lattices and honeycomb structures. A finite wavelength-finite frequency (FW-FF) homogenization framework was proposed by Guzina et al. [23] to describe the effective wave motion in periodic media

with orthogonal Bravais lattices in the spectral neighborhood of simple, repeated, and nearby eigenfrequencies located at the origin or vertices of the first Brillouin zone. More recently, Oudghiri-Idrissi et al. [75] extended the FW-FF homogenization framework to "perforated" periodic continua supported on general Bravais lattices by considering the spectral neighborhoods of an arbitrary wavenumber within the first Brillouin zone and eigenfrequency clusters of arbitrary size. On the application side, Pratappa et al. [78] made use of the Bloch-wave framework and bar-and-hinge model to design tunable periodic origami acoustic metamaterials by optimizing the geometry and folding state of the unit cell [56, 58].

By building upon the FW-FF homogenization approach [23, 75], we aim to better understand the wave motion in origami structures by providing an origami-specific, dynamic homogenization framework that leverages the bar-and-hinge paradigm [58] (see Fig. 1.2). Such formulation specifically aims to: (i) capture the essential dynamics of the problem, (ii) analytically illuminate the origami behavior near spectral singularities (e.g. Dirac points), (iii) reduce the computational cost, and (iv) aid the design of programable and tunable (periodic) origami structures.

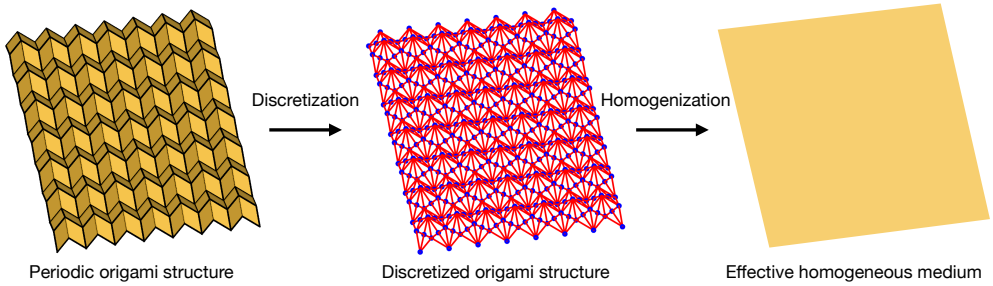

Figure 1.2: Homogenization of periodic origami structures via the bar-and-hinge model.

1.3 Outline

In Chapter 2, we consider homogenization of the scalar wave equation in periodic media at finite wavenumbers and frequencies, with the focus on continua that are (a) supported on an arbitrary Bravais lattice in $\mathbb{R}^d$, $d \geqslant 2$, and (b) endowed with "perforations" subject to homogeneous (Neumann or Dirichlet) boundary conditions. Making use of the Bloch wave expansion, we pursue this goal via an asymptotic ansatz featuring the "spectral distance" from a given wavenumber-eigenfrequency pair (situated *anywhere* within the first Brillouin zone) as the perturbation parameter. We then introduce the effective wave motion via projection(s) of the scalar wavefield onto the Bloch eigenfunction(s) for the unit cell of periodicity, evaluated at the origin of a spectral

neighborhood. For generality, we account for the presence of the source term in the wave equation and we consider – at a given wavenumber – generic cases of isolated, repeated, and nearby eigenvalues. In this way we obtain a palette of effective models, featuring both wave- and Dirac-type behaviors, whose applicability is controlled by the local band structure and eigenfunction basis. In all spectral regimes, we pursue the homogenized description up to at least first order of expansion, featuring asymptotic corrections of the homogenized Bloch-wave operator and the homogenized source term. Inherently, such framework provides a convenient platform for the synthesis of a wide range of intriguing wave phenomena, including negative refraction and topologically protected states in metamaterials and phononic crystals. The proposed homogenization framework is illustrated by approximating asymptotically the dispersion relationships for (i) Kagome lattice featuring hexagonal Neumann exclusions, and (ii) square lattice of circular Dirichlet exclusions. We complete the numerical portrayal of analytical developments by studying the response of a Kagome lattice due to a dipole-like source term acting near the edge of a band gap.

In Chapter 3, we establish a dynamic homogenization framework catering for linear elastic wave motion in periodic origami structures. The latter are modeled using a "bar-and-hinge" paradigm where: (i) the folding of the structure and bending of the origami panels are modeled via elastic hinges, and (ii) the in-plane deformation of each panel is modeled with elastic bars. Using so formulated discrete model of a periodic origami structure, we pursue finite wavenumber-finite frequency (FW-FF) homogenization of the wave motion over a spectral neighborhood of simple, repeated, and nearby eigenfrequencies at an arbitrary wavenumber within the first Brillouin zone. For completeness, a source term acting on the nodes of the discrete structure is considered, expanded in Bloch waves and included in the analysis, and periodic (internal) homogeneous Dirichlet boundary conditions are systematically considered. We express the leading-order (system of) effective equation(s) in the considered spectral neighborhoods and we approximate asymptotically the corresponding Bloch dispersion relationship. We illustrate the developed framework by comparing numerically the Bloch dispersion relationship to its asymptotic approximation for (i) a 2D-periodic Miura-ori structure and (ii) a 1D-periodic Miura tube. We conclude the numerical illustration by presenting the effective motion of the 2D-periodic Miura-ori structure near the edge of a band gap and within a band pass. The dissertation is concluded in Chapter 4 via summary and outlook.

Chapter 2

Spectral asymptotics of waves in periodic continua

In the present chapter, we generalize the FW-FF homogenization framework in [23] to enable treatment of periodic media in $\mathbb{R}^d$, $d \geqslant 2$ that are supported by generic Bravais lattice and may contain "voids" that are subject to homogeneous Neumann and/or Dirichlet boundary conditions. The scalar wave equation under consideration bears relevance, for instance, to the description of anti-plane shear waves in two-dimensional composites, transverse electric (TE) or transverse magnetic (TM) fields in photonic crystals, and acoustic waves in three-dimensional phononic crystals. In a departure from the preceding work, our analysis further (a) permits expansion about an *arbitrary* wavenumber-eigenfrequency pair within the first Brillouin zone; (b) allows for spatially-varying (as opposed to constant) Bloch-wave representation of the source term, and (c) pursue the homogenized description near simple, repeated, and nearby eigenvalues up to at least the first order of asymptotic correction. We illustrate the proposed homogenization framework through the study of (i) Kagome lattice featuring hexagonal Neumann exclusions, and (ii) square lattice of circular Dirichlet obstacles. We complete the numerical portrayal by studying the response of a Kagome lattice due to a dipole-like source term acting near the edge of an internal band gap.

2.1 Preliminaries

2.1.1 Geometry

Consider an infinite periodic medium in $\mathbb{R}^d$ ($d \geqslant 2$) affiliated with a Bravais lattice

$$\boldsymbol{R} \;=\; \Big\{ \sum_{j=1}^{d} n^j \boldsymbol{e}_j \colon\; n^j \in \mathbb{Z} \Big\}, \tag{2.1}$$

featuring the basis $\boldsymbol{e}_j \in \mathbb{R}^d$, $j = \overline{1,d}$. Letting hereon $j \in \overline{1,d}$ implicitly unless stated otherwise, we denote by x^j the contravariant components of the position vector $\boldsymbol{x} \in \mathbb{R}^d$ with reference to the lattice basis $\boldsymbol{e}_j$, and by $r^j \in \mathbb{Z}$ the contravariant coordinates of the lattice point $\boldsymbol{r} \in \boldsymbol{R}$. Next, let

$$Y_0 \;=\; \{\boldsymbol{x} \colon 0 < x^j < 1\}$$

denote the "elemental parallelepiped" of the lattice attached to the origin, and let $Y^{\mathrm{N}}, Y^{\mathrm{D}} \subset Y_0$ denote a pair of disjointed open sets, each representing a union of 1-connected sets as illustrated in Fig. 2.1. With such definitions, one may define the support of the periodic medium as

$$S \;=\; \mathbb{R}^d \setminus \bigcup_{\boldsymbol{r} \in \boldsymbol{R}} \big(\boldsymbol{r} + \overline{Y^{\mathrm{N}} \cup Y^{\mathrm{D}}}\big), \tag{2.2}$$

whose unit cell of periodicity is given by

$$Y \;=\; Y_0 \cap S. \tag{2.3}$$

Here it is useful to observe that Y is connected set thanks to the foregoing restrictions on Y^{N} and Y^{D}. We further define the domain boundaries $\partial Y^{(\mathrm{N})}$, $\partial Y^{(\mathrm{D})}$, $\partial Y'$, ∂S^{N} and ∂S^{D} respectively as

$$\begin{gathered} \partial Y^{(\mathrm{N})} = \partial Y \cap \partial Y^{\mathrm{N}}, \quad \partial Y^{(\mathrm{D})} = \partial Y \cap \partial Y^{\mathrm{D}}, \quad \partial Y' = \partial Y \setminus (\partial Y^{(\mathrm{N})} \cup \partial Y^{(\mathrm{D})}), \\ \partial S^{\mathrm{N}} = \textstyle\bigcup_{\boldsymbol{r} \in \boldsymbol{R}} (\boldsymbol{r} + \partial Y^{(\mathrm{N})}), \quad \partial S^{\mathrm{D}} = \textstyle\bigcup_{\boldsymbol{r} \in \boldsymbol{R}} (\boldsymbol{r} + \partial Y^{(\mathrm{D})}), \end{gathered} \tag{2.4}$$

such that $\partial Y = \partial Y' \cup \partial Y^{(\mathrm{N})} \cup \partial Y^{(\mathrm{D})}$ and $\partial S = \partial S^{\mathrm{N}} \cup \partial S^{\mathrm{D}}$. In physical terms, subtraction of $\overline{Y^{\mathrm{N}} \cup Y^{\mathrm{D}}}$ from Y in (2.2) accounts for the "holes" featured by the periodic medium. Accordingly, the boundary conditions defined on ∂S^{N} and $\partial Y^{(\mathrm{N})}$ (resp. ∂S^{D} and $\partial Y^{(\mathrm{D})}$) are considered only if Y^{N} (resp. Y^{D}) is a nonempty set. Examples of 2D and 3D unit cells geometries as defined above are illustrated in Fig. 2.1. To facilitate the analysis,

we will also make use of the short-hand notation

$$\partial Y'_{jm} = \{\boldsymbol{x} \in \partial Y' \colon\ x^j = m\}, \quad m = \overline{0,1}. \tag{2.5}$$

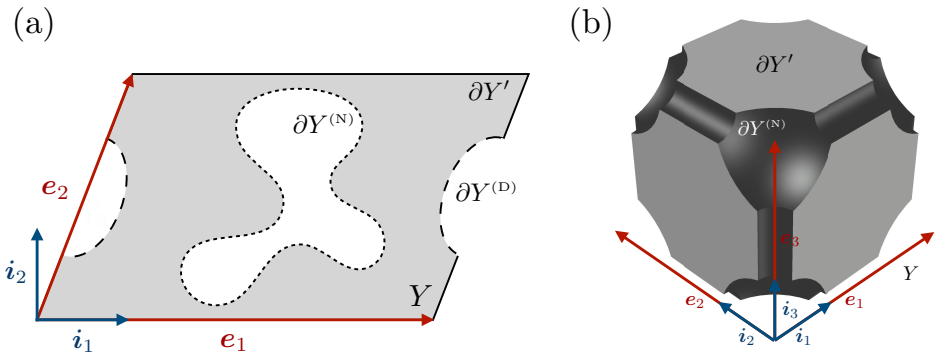

Figure 2.1: Examples of the unit cell indicating the lattice basis vectors $\boldsymbol{e}_j$ as well as boundaries $\partial Y'$, $\partial Y^{(\mathrm{N})}$ and $\partial Y^{(\mathrm{D})}$ in: (a) $\mathbb{R}^2$, and (b) $\mathbb{R}^3$.

For further reference, we denote by $\boldsymbol{e}^j \in \mathbb{R}^d$ the covariant lattice basis that spans the reciprocal space $\mathbb{R}^d$ and satisfies $\boldsymbol{e}^j \cdot \boldsymbol{e}_i = 2\pi\delta_{ij}$ $(i,j = \overline{1,d})$ where δ_{ij} is the Kronecker delta; by

$$\boldsymbol{R}^* \ = \ \Big\{ \sum_{j=1}^{d} n_j \boldsymbol{e}^j \ :\ n_j \in \mathbb{Z} \Big\} \tag{2.6}$$

the reciprocal Bravais lattice; by k_j the covariant components of wave vector $\boldsymbol{k} \in \mathbb{R}^d$ tied to the basis $\boldsymbol{e}^j$; by $r_j^* \in \mathbb{Z}$ the covariant coordinates of the lattice point $\boldsymbol{r}^* \in \boldsymbol{R}^*$; by Y_0^* the reciprocal of Y_0 defined by

$$Y_0^* \ = \ \{\boldsymbol{k} \colon 0 < k_j < 1\},$$

and by

$$\mathcal{B} = \big\{ \boldsymbol{k} \in \mathbb{R}^d \colon\ \boldsymbol{k} \cdot \boldsymbol{\kappa} \leqslant \tfrac{1}{2}\|\boldsymbol{\kappa}\|^2,\ \boldsymbol{\kappa} = \sum_{j=1}^{d} n_j \boldsymbol{e}^j,\ n_j \in \{-1,0,1\} \big\} \tag{2.7}$$

the first Brillouin zone of the lattice. We also denote by $|\mathcal{D}|$ the volume of a finite domain $\mathcal{D} \subset \mathbb{R}^d$ and by $v = (1 - |Y||Y_0|^{-1})$ the *porosity* of the periodic medium S. With such definitions, one may note that $|\mathcal{B}| = |Y_0^*| = (2\pi)^d |Y_0|^{-1}$.

2.1.2 Function spaces

In what follows, we will deal with mappings of type $g : D \mapsto \mathbb{C}$ for some $D \subseteq \mathbb{R}^d$, and their tensorial generalizations. To help set up the table for discussion, we first define the space

$$L^2(D) \;=\; \big\{g\colon \int_D g\,\overline{g}\,\mathrm{d}\boldsymbol{x} < \infty\big\}, \tag{2.8}$$

and we introduce a generalized inner product over Y, namely

$$(\boldsymbol{g},\boldsymbol{h}) \;=\; |Y|^{-1}\int_Y \boldsymbol{g}\colon\overline{\boldsymbol{h}}\,\mathrm{d}\boldsymbol{x}, \qquad \boldsymbol{g}\in (L^2(Y))^{d^m},\ \boldsymbol{h}\in (L^2(Y))^{d^n}, \quad m,n\geqslant 0, \tag{2.9}$$

where

$$(L^2(Y))^{d^m} \;=\; (L^2(Y))^{d\times d\times\ldots\times d} \quad (m \text{ times}),$$

and ":" stands for the usual product, the inner product, and the $\min(m,n)$-tuple tensor contraction when $m=n=0$, $m=n=1$, and $\max(m,n)>1$, respectively. In situations when $g : S \mapsto \mathbb{C}$ is Y-periodic, we will also make use of the periodic function spaces

$$\begin{aligned} L^2_p(Y) &= \{g : g|_Y \in L^2(Y),\ g(\boldsymbol{x}+\boldsymbol{r}) = g(\boldsymbol{x})\ \ \forall \boldsymbol{x}\in S,\, \boldsymbol{r}\in\boldsymbol{R}\},\\ L^2_{p0}(Y) &= \{g\in L^2_p(Y) :\ g|_{\partial Y^{(\mathrm{D})}} = 0\},\\ H^1_{p0}(Y) &= \{g \in L^2_{p0}(Y) : \nabla g \in (L^2(Y))^d\}. \end{aligned} \tag{2.10}$$

2.1.3 Wave equation, boundary conditions and Bloch wave expansion

Consider the time-harmonic wave equation in S at frequency ω, namely

$$-\omega^2\rho(\boldsymbol{x})u - \nabla\cdot\big(G(\boldsymbol{x})\nabla u\big) \;=\; f(\boldsymbol{x}) \qquad \text{in } S, \tag{2.11}$$

where $f\in L^2(S)$. In what follows, we assume the coefficients $0<G<\infty$ and $0<\rho<\infty$ to be Y-periodic, piecewise-continuous, and bounded away from zero. In this case, we note that $L^2_{p0}(Y)$ equivalently defines the class of "kinematically-compatible" periodic functions satisfying $(\rho g, g) < \infty$. To complete the formulation of the problem, we assume that u satisfies homogeneous Neumann and Dirichlet boundary conditions on ∂S^{N} and ∂S^{D}, respectively. In other words, we let

$$\boldsymbol{\nu}\cdot G\nabla u \;=\; 0 \qquad \text{on } \partial S^{\mathrm{N}}, \tag{2.12}$$

$$u \;=\; 0 \qquad \text{on } \partial S^{\mathrm{D}}, \tag{2.13}$$

where $\boldsymbol{\nu}$ is the unit outward normal on ∂S^{N}. For generality, we note that (2.11) pertains to a wide class of physical processes including: (i) anti-plane shear waves (when $d = 2$) in an elastic solid with mass density ρ and shear modulus G, (ii) transverse electric (TE) or transverse magnetic (TM) waves (when $d = 2$) in a dielectric medium endowed with permittivity $\varepsilon = G^{-1}$ and permeability $\mu = \rho^{-1}$, and (iii) acoustic i.e. pressure waves (when $d = 2, 3$) in a fluid characterized by the mass density $\varrho = G^{-1}$ and bulk modulus $\kappa = \rho^{-1}$.

At this point, we can deploy the results in [37, 12] to demonstrate (see A.1 for details) that any $g \in L^2(S)$ permits the Bloch wave expansion (BWE) as

$$g(\boldsymbol{x}) = |\mathcal{B}|^{-1} \int_{\boldsymbol{k}_s+\mathcal{B}} \tilde{g}_{\boldsymbol{k}}(\boldsymbol{x}) e^{i\boldsymbol{k}\cdot\boldsymbol{x}} \, \mathrm{d}\boldsymbol{k}, \tag{2.14}$$

where $\boldsymbol{k}_s \in \mathbb{R}^d$ is an arbitrary shift vector, and

$$\tilde{g}_{\boldsymbol{k}}(\boldsymbol{x}) = \sum_{\boldsymbol{r}\in\boldsymbol{R}} g(\boldsymbol{x}+\boldsymbol{r}) e^{-i\boldsymbol{k}\cdot(\boldsymbol{x}+\boldsymbol{r})} \tag{2.15}$$

belongs to $L^2_p(Y)$. This motivates us to consider a relatively broad class of source terms given by

$$f(\boldsymbol{x}) = |\mathcal{C}|^{-1} \int_{\boldsymbol{k}_s+\mathcal{C}} \tilde{f}_{\boldsymbol{k}}(\boldsymbol{x}) e^{i\boldsymbol{k}\cdot\boldsymbol{x}} \, \mathrm{d}\boldsymbol{k}, \quad \boldsymbol{k}_s \in \overline{\mathcal{B}}, \tag{2.16}$$

where $\mathcal{C} \subset \mathcal{B}$ and $\tilde{f}_{\boldsymbol{k}} \in L^2_p(Y)$ for $\boldsymbol{k} \in \boldsymbol{k}_s + \mathcal{C}$. Since $\mathcal{C} \subset \mathcal{B}$, it is clear that (2.16) is nothing but a restriction of (2.14) which implicitly defines a subset of $L^2(\mathbb{R}^d)$. The main motivation behind (2.16) is to *spectrally localize* f, and thus u, to a neighborhood of some $\boldsymbol{k}_s \in \overline{\mathcal{B}}$, which then greatly facilitates the asymptotic treatment. For future reference, we note that (2.16) covers the special cases where: (i) $\tilde{f}_{\boldsymbol{k}}(\boldsymbol{x}) = \rho(\boldsymbol{x})\hat{f}(\boldsymbol{k}, \boldsymbol{x})$ with $\hat{f}(\boldsymbol{k}, \cdot) \in L^2_p(Y)$, and (ii) $\tilde{f}_{\boldsymbol{k}}(\boldsymbol{x}) = 1$ (with $Y^{\mathrm{N}} = Y^{\mathrm{D}} = \emptyset$) as in the related asymptotic treatments [23, 72] that rely on the plane wave expansion.

Claim 1 *Assuming $f \in L^2(S)$, the Fourier integral representation*

$$f(\boldsymbol{x}) = \int_{\mathbb{R}^d} \mathfrak{F}(\boldsymbol{k}) e^{i\boldsymbol{k}\cdot\boldsymbol{x}} \, d\boldsymbol{k}, \tag{2.17}$$

is referred to as the plane wave expansion (PWE) of f. The relationship between BWE (2.14) *and PWE* (2.17) *is given by*

$$|\mathcal{B}|^{-1} \tilde{f}_{\boldsymbol{k}}(\boldsymbol{x}) \;=\; \sum_{\boldsymbol{r}^*\in\boldsymbol{R}^*} \mathfrak{F}(\boldsymbol{r}^* + \boldsymbol{k}) e^{i\boldsymbol{r}^*\cdot\boldsymbol{x}}. \tag{2.18}$$

Further, when $\mathfrak{F}(\boldsymbol{k})$ is compactly supported within $\boldsymbol{k}_s + \mathcal{B}$, relationship (2.18) *simplifies to*

$$|\mathcal{B}|^{-1} \tilde{f}_{\boldsymbol{k}}(\boldsymbol{x}) = \mathfrak{F}(\boldsymbol{k}), \tag{2.19}$$

see A.2 for proof.

Remark 1 *For $\phi \in L^2_p(Y)$ and $f \in L^2(S)$, function $g(\boldsymbol{x}) = \phi(\boldsymbol{x}) f(\boldsymbol{x}) \in L^2(S)$ and its BWE is given by* (2.14)*, where $\tilde{g}_{\boldsymbol{k}}(\boldsymbol{x}) = \phi(\boldsymbol{x}) \tilde{f}_{\boldsymbol{k}}(\boldsymbol{x})$ and $\tilde{f}_{\boldsymbol{k}}$ is given by* (2.15)*.*

By the linearity of (2.11), we can account for (2.16) by focusing our analysis on the reduced field equation

$$-\omega^2 \rho(\boldsymbol{x}) u - \nabla \cdot \big(G(\boldsymbol{x}) \nabla u\big) \;=\; \tilde{f}_{\boldsymbol{k}}(\boldsymbol{x})\; e^{i\boldsymbol{k}\cdot\boldsymbol{x}} \quad \text{in} \;\; S. \tag{2.20}$$

Thanks to the periodicity of ρ and G and the fact that $\tilde{f}_{\boldsymbol{k}} \in L^2_p(Y)$, (2.20) admits a Bloch wave solution $\tilde{u}(\boldsymbol{x}) e^{i\boldsymbol{k}\cdot\boldsymbol{x}}$, where $\tilde{u} := \tilde{u}_{\boldsymbol{k}}$ is Y-periodic and solves

$$-\omega^2 \rho(\boldsymbol{x}) \tilde{u} - \nabla_{\boldsymbol{k}} \cdot \big(G(\boldsymbol{x}) \nabla_{\boldsymbol{k}} \tilde{u}\big) \;=\; \tilde{f}_{\boldsymbol{k}}(\boldsymbol{x}) \quad \text{in} \;\; Y, \tag{2.21}$$

subject to boundary conditions

$$\begin{aligned} \tilde{u}|_{\partial Y'_{j0}} &= \tilde{u}|_{\partial Y'_{j1}}, \\ \boldsymbol{\nu} \cdot G \nabla_{\boldsymbol{k}} \tilde{u}|_{\partial Y'_{j0}} &= -\boldsymbol{\nu} \cdot G \nabla_{\boldsymbol{k}} \tilde{u}|_{\partial Y'_{j1}}, \\ \boldsymbol{\nu} \cdot G \nabla_{\boldsymbol{k}} \tilde{u}|_{\partial Y^{(\mathrm{N})}} &= 0, \\ \tilde{u}|_{\partial Y^{(\mathrm{D})}} &= 0, \end{aligned} \tag{2.22}$$

where $\partial Y'_{jm}$ ($m = \overline{0,1}$) are given by (2.5), $\nabla_{\boldsymbol{k}} = \nabla + i\boldsymbol{k}$, and $\boldsymbol{\nu}$ is the unit outward normal on ∂Y. For brevity of notation, the dependence of $\tilde{u}$ on $\boldsymbol{k}$ and ω in (2.21) and thereon is assumed implicitly.

2.1.4 Eigenvalue problem

For $\boldsymbol{k} \in \mathbb{R}^d$ and $u, v \in H^1_{p0}(Y)$, we have

$$\begin{aligned} \big(\nabla_{\boldsymbol{k}} \cdot (G(\boldsymbol{x}) \nabla_{\boldsymbol{k}} u), v\big) &= |Y|^{-1} \int_Y \nabla_{\boldsymbol{k}} \cdot (G(\boldsymbol{x}) \nabla_{\boldsymbol{k}} u(\boldsymbol{x}))\, \overline{v(\boldsymbol{x})}\, \mathrm{d}\boldsymbol{x} \\ &= -|Y|^{-1} \int_Y G(\boldsymbol{x}) \nabla_{\boldsymbol{k}} u(\boldsymbol{x}) \cdot \overline{\nabla_{\boldsymbol{k}} v(\boldsymbol{x})}\, \mathrm{d}\boldsymbol{x} \\ &\quad + |Y|^{-1} \int_{\partial Y} \boldsymbol{\nu} \cdot (G(\boldsymbol{x}) \nabla_{\boldsymbol{k}} u(\boldsymbol{x})) \overline{v(\boldsymbol{x})}\, \mathrm{d}\boldsymbol{x} \\ &= -(G(\boldsymbol{x}) \nabla_{\boldsymbol{k}} u, \nabla_{\boldsymbol{k}} v) \end{aligned} \tag{2.23}$$

thanks to the divergence theorem and boundary conditions (2.22). As a result, we find from the variational formulation that the operator $(-\rho^{-1}\nabla_{\boldsymbol{k}}\cdot(G\nabla_{\boldsymbol{k}}))^{-1}$ from $L^2_{p0}(Y)$ to $L^2_{p0}(Y)$, subject to the germane boundary conditions, is self-adjoint and compact. Accordingly, (2.21)–(2.22) are affiliated with the eigensystem $\{\tilde{\lambda}_n(\boldsymbol{k})\in\mathbb{R},\ \tilde{\phi}_n(\boldsymbol{k})\in H^1_{p0}(Y)\}$, that satisfies

$$-\tilde{\lambda}_n\rho(\boldsymbol{x})\tilde{\phi}_n - \nabla_{\boldsymbol{k}}\cdot\big(G(\boldsymbol{x})\nabla_{\boldsymbol{k}}\ \tilde{\phi}_n\big) \ = \ 0 \quad \text{in} \ \ Y, \tag{2.24}$$

subject to the boundary conditions

$$\begin{aligned}
\tilde{\phi}_n|_{\partial Y'_{j0}} &= \tilde{\phi}_n|_{\partial Y'_{j1}},\\
\boldsymbol{\nu}\cdot G\nabla_{\boldsymbol{k}}\tilde{\phi}_n|_{\partial Y'_{j0}} &= -\boldsymbol{\nu}\cdot G\nabla_{\boldsymbol{k}}\tilde{\phi}_n|_{\partial Y'_{j1}},\\
\boldsymbol{\nu}\cdot G\nabla_{\boldsymbol{k}}\tilde{\phi}_n|_{\partial Y^{(\mathrm{N})}} &= 0,\\
\tilde{\phi}_n|_{\partial Y^{(\mathrm{D})}} &= 0.
\end{aligned} \tag{2.25}$$

Note that the sequence $\{\tilde{\phi}_n\}$ is complete in $H^1_{p0}(Y)$ and ρ-orthogonal. We normalize the eigenfunctions so that $\|\tilde{\phi}_n\| = 1$, whereby

$$(\rho\tilde{\phi}_n, \tilde{\phi}_m) \ = \ (\rho\tilde{\phi}_n, \tilde{\phi}_n)\ \delta_{nm}. \tag{2.26}$$

For given $\boldsymbol{k}\in\mathbb{R}^d$, periodic medium S thus permits the propagation of "free" Bloch waves $\tilde{\phi}_n(\boldsymbol{k})e^{i(\boldsymbol{k}\cdot\boldsymbol{x}-\omega_n t)}$ at eigenfrequency $\omega_n(\boldsymbol{k}) = (\tilde{\lambda}_n)^{\frac{1}{2}}$. The set of all wavenumber-eigenfrequency pairs $(\boldsymbol{k},\omega_n)$ defines the *Bloch dispersion relationship* of the medium. The latter is periodic in the reciprocal space, and is described completely by the first Brillouin zone $\mathcal{B}$ of the lattice. By the completeness of $\tilde{\phi}_n$ in $H^1_{p0}(Y)$, the solution $\tilde{u}$ of (2.21)–(2.22) can be expanded as

$$\tilde{u}(\boldsymbol{x}) = \sum_{n=1}^{\infty}\alpha_n\tilde{\phi}_n(\boldsymbol{x}). \tag{2.27}$$

Provided that $\omega^2\neq\tilde{\lambda}_n\ \forall n\in\mathbb{Z}^+$, (2.27) yields

$$\tilde{u}(\boldsymbol{x}) = -\sum_{n=1}^{\infty}\frac{(\tilde{f}_{\boldsymbol{k}},\tilde{\phi}_n)\ \tilde{\phi}_n(\boldsymbol{x})}{(\rho\tilde{\phi}_n,\tilde{\phi}_n)(\omega^2-\tilde{\lambda}_n)}, \tag{2.28}$$

thanks to (2.21) and (2.23). Then, by the linearity of (2.11), the total solution is expressed as

$$u(\boldsymbol{x}) = \frac{1}{|\mathcal{C}|}\int_{\boldsymbol{k}_s+\mathcal{C}}\Big(-\sum_{n=1}^{\infty}\frac{(\tilde{f}_{\boldsymbol{k}},\tilde{\phi}_n)\ \tilde{\phi}_n(\boldsymbol{x})e^{i\boldsymbol{k}\cdot\boldsymbol{x}}}{(\rho\tilde{\phi}_n,\tilde{\phi}_n)(\omega^2-\tilde{\lambda}_n)}\Big)\,\mathrm{d}\boldsymbol{k}. \tag{2.29}$$

For future reference, we note that the weight of the *nth* Bloch eigenmode in (2.29) is inversely proportional to the spectral distance $|\omega^2 - \tilde{\lambda}_n|$.

2.1.5 Scaling

In what follows, we seek a homogenized description of (2.21)–(2.22) in a spectral neighborhood of the wavenumber-frequency pair

$$\big(\boldsymbol{k}_s, \omega_n(\boldsymbol{k}_s) = (\tilde{\lambda}_n(\boldsymbol{k}_s))^{1/2}\big) \in \overline{\mathcal{B}} \times \mathbb{R}, \qquad n \in \mathbb{Z}^+,$$

and we assume all quantities to be *a priori* normalized by some reference "mass density" ρ_0, "shear modulus" G_0 and lengthscale ℓ_0. On making use of the short-hand notation $\tilde{\lambda}_n = \tilde{\lambda}_n(\boldsymbol{k}_s)$ and $\omega_n = \omega_n(\boldsymbol{k}_s)$ hereon, we next introduce the perturbation parameter $\epsilon = o(1)$ defining the spectral neighborhood as

$$\begin{aligned} &\boldsymbol{k} = \boldsymbol{k}_s + \epsilon\hat{\boldsymbol{k}}, \qquad \omega^2 = \tilde{\lambda}_n + \epsilon\check{\sigma}\check{\omega}^2 + \epsilon^2\hat{\sigma}\hat{\omega}^2, \\ &\check{\sigma}, \hat{\sigma} \in \{-1, 0, 1\}, \quad \check{\sigma}\,\hat{\sigma} = 0, \quad |\check{\sigma} + \hat{\sigma}| = 1. \end{aligned} \tag{2.30}$$

Remark 2 *Through the design of $\check{\sigma}$ and $\hat{\sigma}$, frequency separation parameters $\check{\omega}$ and $\hat{\omega}$ are meant to be used in the "either or" sense, depending on the driving frequency (when $\tilde{f}_{\boldsymbol{k}} \neq 0$) and the local geometry of germane dispersion surface (when $\tilde{f}_{\boldsymbol{k}} = 0$). Specifically when $\tilde{f}_{\boldsymbol{k}} \neq 0$ whereby ω is given, we have*

$$\omega^2 - \tilde{\lambda}_n \;=\; \begin{cases} O(\epsilon) & \Rightarrow \quad |\check{\sigma}| = 1, \quad \hat{\sigma} \;= 0 \\ O(\epsilon^2) & \Rightarrow \quad \check{\sigma} \;= 0, \quad |\hat{\sigma}| = 1 \end{cases} . \tag{2.31}$$

When $\tilde{f}_{\boldsymbol{k}} = 0$, on the other hand, it will be for instance shown that for dispersion surfaces with locally parabolic (resp. conical) sections, the frequency in those $\boldsymbol{k}$-directions scales as $\omega_n^2(\boldsymbol{k}) - \tilde{\lambda}_n = \epsilon^2\hat{\omega}^2$ (resp. $\omega_n^2(\boldsymbol{k}) - \tilde{\lambda}_n = \epsilon\check{\omega}^2$). Since such information is not available beforehand, the idea is to substitute (2.30) *"as is" into the field equation* (2.21)*, and then to identify the appropriate frequency scaling (by letting either $\check{\sigma} = 0$ or $\hat{\sigma} = 0$) depending on the local eigenfunction structure. In order to bring the analyses of both forced ($\tilde{f}_{\boldsymbol{k}} \neq 0$) and free ($\tilde{f}_{\boldsymbol{k}} = 0$) wave motion under a common umbrella, we will uniformly start from the agnostic scaling law* (2.30) *throughout the remainder of this work.*

In the context of (2.30), we are now in position to pursue the ansatz

$$\tilde{u}(\boldsymbol{x}) \;=\; \epsilon^{-2} \sum_{m=0}^{\infty} \epsilon^m \tilde{u}_m(\boldsymbol{x}), \tag{2.32}$$

via the asymptotic expansion of (2.21)–(2.22), see also [72, 23]. For completeness, we note that the presence of the factor ϵ^{-2} in front of the series is motivated by (2.28) and the smallness of $|\omega^2 - \tilde{\lambda}_n(\boldsymbol{k})|$ suggested by (2.30). On inserting (2.30)–(2.32) into (2.21)–(2.22) and letting $\tilde{f}_{\boldsymbol{k}} = O(1)$, we obtain a cascade of field equations over Y, namely

$$
\begin{aligned}
O(\epsilon^{-2}): &\quad -\tilde{\lambda}_n\rho\tilde{u}_0 - \nabla_{\boldsymbol{k}_s}\cdot\big(G\nabla_{\boldsymbol{k}_s}\tilde{u}_0\big) = 0, && (2.33)\\
O(\epsilon^{-1}): &\quad -\tilde{\lambda}_n\rho\tilde{u}_1 - \nabla_{\boldsymbol{k}_s}\cdot\big(G(\nabla_{\boldsymbol{k}_s}\tilde{u}_1 + \tilde{u}_0 i\hat{\boldsymbol{k}})\big) - G(\nabla_{\boldsymbol{k}_s}\tilde{u}_0)\cdot i\hat{\boldsymbol{k}} - \check{\sigma}\check{\omega}^2\rho\tilde{u}_0 = 0, && (2.34)\\
O(1): &\quad -\tilde{\lambda}_n\rho\tilde{u}_2 - \nabla_{\boldsymbol{k}_s}\cdot\big(G(\nabla_{\boldsymbol{k}_s}\tilde{u}_2 + \tilde{u}_1 i\hat{\boldsymbol{k}})\big) - G(\nabla_{\boldsymbol{k}_s}\tilde{u}_1 + \tilde{u}_0 i\hat{\boldsymbol{k}})\cdot i\hat{\boldsymbol{k}}\\
&\qquad -\check{\sigma}\check{\omega}^2\rho\tilde{u}_1 - \hat{\sigma}\hat{\omega}^2\rho\tilde{u}_0 = \tilde{f}_{\boldsymbol{k}}, && (2.35)\\
O(\epsilon^{m\geqslant 1}): &-\tilde{\lambda}_n\rho\tilde{u}_{m+2} - \nabla_{\boldsymbol{k}_s}\cdot\big(G(\nabla_{\boldsymbol{k}_s}\tilde{u}_{m+2} + \tilde{u}_{m+1} i\hat{\boldsymbol{k}})\big) - G(\nabla_{\boldsymbol{k}_s}\tilde{u}_{m+1} + \tilde{u}_m i\hat{\boldsymbol{k}})\cdot i\hat{\boldsymbol{k}}\\
&\qquad -\check{\sigma}\check{\omega}^2\rho\tilde{u}_{m+1} - \hat{\sigma}\hat{\omega}^2\rho\tilde{u}_m = 0, && (2.36)
\end{aligned}
$$

along with the sequence of boundary conditions

$$
\begin{aligned}
\tilde{u}_m|_{\partial Y'_{j0}} &= \tilde{u}_m|_{\partial Y'_{j1}},\\
\boldsymbol{\nu}\cdot G(\nabla_{\boldsymbol{k}_s}\tilde{u}_m + \tilde{u}_{m-1} i\hat{\boldsymbol{k}})|_{\partial Y'_{j0}} &= -\boldsymbol{\nu}\cdot G(\nabla_{\boldsymbol{k}_s}\tilde{u}_m + \tilde{u}_{m-1} i\hat{\boldsymbol{k}})|_{\partial Y'_{j1}}\\
\boldsymbol{\nu}\cdot G(\nabla_{\boldsymbol{k}_s}\tilde{u}_m + \tilde{u}_{m-1} i\hat{\boldsymbol{k}})|_{\partial Y^{(\mathrm{N})}} &= 0,\\
\tilde{u}_m|_{\partial Y^{(\mathrm{D})}} &= 0, \quad m \geqslant 0, && (2.37)
\end{aligned}
$$

where $\tilde{u}_{-1} \equiv 0$. In the sequel, we say that tensor $\boldsymbol{g} \in (H^1_{p0}(Y))^{d^q}$, $q \geqslant 1$ satisfies the *"flux boundary conditions"* if

$$
\begin{aligned}
\boldsymbol{\nu}\cdot\boldsymbol{g}|_{\partial Y'_{j0}} &= -\boldsymbol{\nu}\cdot\boldsymbol{g}|_{\partial Y'_{j1}},\\
\boldsymbol{\nu}\cdot\boldsymbol{g}|_{\partial Y^{(\mathrm{N})}} &= \boldsymbol{0}. && (2.38)
\end{aligned}
$$

2.1.6 Averaging operators and effective solution

Let $n_q \in \mathbb{Z}^+$ ($q = \overline{1,Q}$) collect the "nearby" dispersion branches $\omega_{n_q}(\boldsymbol{k})$ traversing the vicinity of $(\boldsymbol{k}_s, \tilde{\lambda}_n^{1/2})$, where we aim to pursue ansatz (2.32). With such setup in mind, we introduce the *averaging* operators $\langle\cdot\rangle^{n_q}$ and $\langle\cdot\rangle^{n_q}_\rho$ and the "zero mean" Sobolev space $\bar{H}^1_{p0}(Y)$ as

$$
\begin{aligned}
\langle\tilde{g}\rangle^{n_q} &= (\tilde{g}, \tilde{\phi}_{n_q}), && (2.39)\\
\langle\tilde{g}\rangle^{n_q}_\rho &= (\rho\tilde{\phi}_{n_q}, \tilde{\phi}_{n_q})^{-1}(\rho\tilde{g}, \tilde{\phi}_{n_q}), && (2.40)\\
\bar{H}^1_{p0}(Y) &= \{\tilde{g} \in H^1_{p0}(Y) : \langle\tilde{g}\rangle^{n_q}_\rho = 0,\ q = \overline{1,Q}\}. && (2.41)
\end{aligned}
$$

For completeness, we note that our definition (2.41) of the "zero mean" Sobolev space $\bar{H}^1_{p0}(Y)$ is different from that in [23] which postulates $\langle\tilde{g}\rangle^{n_q}=0$ in lieu of $\langle\tilde{g}\rangle^{n_q}_\rho=0$, and from that in [53] where the functions $\{\tilde{g},\tilde{\varphi}_q(q=\overline{1,Q})\}$ are assumed to be linearly independent. For $\tilde{g}=\tilde{u}$, we will use the short-hand notation

$$u_{mq}(\epsilon\hat{\boldsymbol{k}}) \;:=\; \langle\tilde{u}_m\rangle^{n_q}_\rho, \qquad q=\overline{1,Q}. \tag{2.42}$$

On the basis of (2.32) and (2.42), we can adapt the definition of *effective solution* [23] at wavenumber $\boldsymbol{k}_s+\epsilon\hat{\boldsymbol{k}}$ as

$$\langle\tilde{u}\rangle^{n_q}_\rho(\epsilon\hat{\boldsymbol{k}}) \;=\; \sum_{m=0}^{\infty}\epsilon^{m-2}u_{mq}, \qquad q=\overline{1,Q} \tag{2.43}$$

which then provides the basis for computing the (set of) effective solution(s) near $\boldsymbol{k}_s$ in the physical space as

$$\langle u\rangle^{n_q}_\rho(\boldsymbol{x}) \;=\; |\mathcal{C}|^{-1}\int_{\mathcal{C}}\langle\tilde{u}\rangle^{n_q}_\rho(\epsilon\hat{\boldsymbol{k}})\,e^{i(\boldsymbol{k}_s+\epsilon\hat{\boldsymbol{k}})\cdot\boldsymbol{x}}\,\mathrm{d}(\epsilon\hat{\boldsymbol{k}}), \quad \boldsymbol{x}\in\mathbb{R}^d. \tag{2.44}$$

Remark 3 *In situations where $Q=1$ and $n_1=n$ which corresponds to the case of an isolated branch, $\langle\cdot\rangle^n$, $\langle\cdot\rangle^n_\rho$, and u_{m1} will be conveniently denoted as $\langle\cdot\rangle$, $\langle\cdot\rangle_\rho$ and u_m, respectively. In this case,* (2.43) *and* (2.44) *reduce to*

$$\langle\tilde{u}\rangle_\rho(\epsilon\hat{\boldsymbol{k}}) \;=\; \sum_{m=0}^{\infty}\epsilon^{m-2}u_m, \qquad \langle u\rangle_\rho(\boldsymbol{x}) \;=\; |\mathcal{C}|^{-1}\int_{\mathcal{C}}\langle\tilde{u}\rangle_\rho(\epsilon\hat{\boldsymbol{k}})\,e^{i(\boldsymbol{k}_s+\epsilon\hat{\boldsymbol{k}})\cdot\boldsymbol{x}}\,d(\epsilon\hat{\boldsymbol{k}}). \tag{2.45}$$

For future reference, we also define the symmetrization operators $\{\cdot\}$ and $\{\cdot\}'$ on tensors $\boldsymbol{\tau}\in\mathbb{C}^{d^n}$, $n\geqslant 2$ as

$$\{\boldsymbol{\tau}\}_{p_1,p_2,\ldots,p_n} \;=\; \frac{1}{n!}\sum_{(q_1,q_2,\ldots,q_n)\in\Pi_n}\boldsymbol{\tau}_{q_1,q_2,\ldots,q_n}, \tag{2.46}$$

$$\{\boldsymbol{\tau}\}'_{p_1,p_2,\ldots,p_n} \;=\; \frac{1}{(n-1)!}\sum_{(q_2,\ldots,q_n)\in\Pi_{n-1}}\boldsymbol{\tau}_{p_1,q_2,\ldots,q_n}, \quad p_1,p_2,\ldots,p_n\in\overline{1,d}, \tag{2.47}$$

respectively, where Π_n is the set of all permutations of set $\overline{1,n}$.

Remark 4 *In the context of* (2.30)*, we first recall the multicell homogenization i.e. "folding" technique [7, 20, 23, 22] which enables evaluation of the effective properties of a periodic medium at rational wavenumbers $\boldsymbol{k}_s=\sum_j q_j\boldsymbol{e}^j\in\overline{\mathcal{B}}$, $q_j\in\mathbb{Q}$. A leading-order expansion about an arbitrary (rational or irrational) wavenumber $\boldsymbol{k}_s\in\overline{\mathcal{B}}$ was implicitly*

considered in [30], via multiple scales approach, near simple and repeated eigenfrequencies. With reference to (2.42)*, we specifically pursue explicit (first- or second-order) effective descriptions governing* u_{mq} *(*$m = \overline{0,2}$*,* $q = \overline{1,Q}$*) at an arbitrary wavenumber* $\boldsymbol{k}_s \in \overline{\mathcal{B}}$ *near simple, multiple, and nearby eigenfrequencies.*

Remark 5 *When* $f_{\boldsymbol{k}} = 0$ *identically, the applicability of any effective model for given perturbation vector* $\hat{\boldsymbol{k}}$ *also implies its validity for* $\alpha\hat{\boldsymbol{k}}$*,* $\alpha \leqslant O(1)$ *thanks to the arbitrariness of* $\epsilon = o(1)$ *in* (2.33)–(2.36)*. When* $f_{\boldsymbol{k}} \neq 0$*, on the other hand, this implication holds as long as the point* $(\boldsymbol{k}_s + \alpha\epsilon\hat{\boldsymbol{k}}, \omega)$ *does not lie on the germane dispersion branch, i.e. as long as* $\omega_{n_q}(\boldsymbol{k}_s + \alpha\epsilon\hat{\boldsymbol{k}}) \neq \omega$*. To provide a focus for the analysis, we hereon (i) identify the wavenumber perturbations by their direction* $\hat{\boldsymbol{k}}/\|\hat{\boldsymbol{k}}\|$*, and (ii) for* $f_{\boldsymbol{k}} \neq 0$ *we restrict our consideration to* $\hat{\boldsymbol{k}} \in \mathcal{K}_\epsilon$*, where*

$$\mathcal{K}_\epsilon = \{\hat{\boldsymbol{k}} \in \mathbb{R}^d : \epsilon\hat{\boldsymbol{k}} \in \mathcal{C},\ \omega_{n_q}^{(m)}(\boldsymbol{k}_s + \epsilon\hat{\boldsymbol{k}}) \neq \omega\}, \qquad q = \overline{1,Q}, \tag{2.48}$$

where $\omega_{n_q}^{(m)}(\boldsymbol{k})$ *denotes the* m*th order approximation of* $\omega_{n_q}(\boldsymbol{k})$ *affiliated with* u_{mq} *in* (2.42)*.*

2.2 Simple eigenvalue

2.2.1 Leading-order approximation

With reference to the eigenvalue problem (2.24)-(2.25), the solution of (2.33) in the vicinity of a simple eigenfrequency ω_n is expressed as

$$\tilde{u}_0(\boldsymbol{x}) \ = \ u_0\tilde{\phi}_n(\boldsymbol{x}), \quad u_0 \in \mathbb{C}, \tag{2.49}$$

where $u_0 = \langle \tilde{u}_0 \rangle_\rho$ as stated before. Then, by inserting (2.49) into (2.34) and integrating $((2.34), \tilde{\phi}_n)$ by parts via the boundary conditions (2.37) with $m = 1$, we obtain the averaged $O(\epsilon^{-1})$ statement as

$$-(\boldsymbol{\theta}^{(0)} \cdot (i\hat{\boldsymbol{k}}) + \check{\sigma}\check{\omega}^2\rho^{(0)})u_0 \ = 0, \tag{2.50}$$

where

$$\boldsymbol{\theta}^{(0)} = \langle G\nabla_{\boldsymbol{k}_s}\tilde{\phi}_n \rangle - \overline{\langle G\nabla_{\boldsymbol{k}_s}\tilde{\phi}_n \rangle} \in i\mathbb{R}^d, \qquad \rho^{(0)} = \langle \rho\tilde{\phi}_n \rangle \in \mathbb{R}^+. \tag{2.51}$$

On substituting (2.49) in (2.34), one finds by the linearity of the problem that

$$\tilde{u}_1(\boldsymbol{x}) = u_0\ \boldsymbol{\chi}^{(1)}(\boldsymbol{x}) \cdot (i\hat{\boldsymbol{k}}) + u_1\tilde{\phi}_n(\boldsymbol{x}), \quad u_1 \in \mathbb{C}, \tag{2.52}$$

where $u_1 = \langle \tilde{u}_1 \rangle_\rho$ and $\boldsymbol{\chi}^{(1)} \in (\bar{H}^1_{p0}(Y))^d$ uniquely solves the unit cell problem

$$\tilde{\lambda}_n \rho \boldsymbol{\chi}^{(1)} + \nabla_{\boldsymbol{k}_s} \cdot \big(G(\nabla_{\boldsymbol{k}_s} \boldsymbol{\chi}^{(1)} + \tilde{\phi}_n \boldsymbol{I}) \big) + G \nabla_{\boldsymbol{k}_s} \tilde{\phi}_n - \frac{\rho}{\rho^{(0)}} \tilde{\phi}_n \boldsymbol{\theta}^{(0)} \ = \ \boldsymbol{0}, \tag{2.53}$$

subject to the boundary conditions (2.38) with $\boldsymbol{g} = G(\nabla_{\boldsymbol{k}_s} \boldsymbol{\chi}^{(1)} + \tilde{\phi}_n \boldsymbol{I})$ and $\boldsymbol{I}$ denoting the second-order identity tensor.

We next consider the $O(1)$ field equation (2.35). On recalling (2.49) and (2.52), we can integrate $((2.35), \tilde{\phi}_n)$ by parts aided by the boundary conditions (2.37) with $m = 2$ to obtain the averaged $O(1)$ statement

$$- \big(\boldsymbol{\mu}^{(0)} : (i\hat{\boldsymbol{k}})^2 + \hat{\sigma}\hat{\omega}^2 \rho^{(0)} \big) u_0 - (\boldsymbol{\theta}^{(0)} \cdot (i\hat{\boldsymbol{k}}) + \check{\sigma}\check{\omega}^2 \rho^{(0)}) u_1 \ = \ \langle \tilde{f}_{\boldsymbol{k}} \rangle, \tag{2.54}$$

where

$$(i\hat{\boldsymbol{k}})^m \ = \ (i\hat{\boldsymbol{k}}) \otimes (i\hat{\boldsymbol{k}}) \ldots \otimes (i\hat{\boldsymbol{k}}) \quad (m \text{ times}),$$

and

$$\boldsymbol{\mu}^{(0)} = \langle G\{\nabla_{\boldsymbol{k}_s} \ \boldsymbol{\chi}^{(1)} + \tilde{\phi}_n \boldsymbol{I}\} \rangle - \big\{ \big(G\boldsymbol{\chi}^{(1)} \otimes \overline{\nabla_{\boldsymbol{k}_s} \tilde{\phi}_n}, 1 \big) \big\}. \tag{2.55}$$

Claim 2 *For any $\boldsymbol{k}_s \in \overline{\mathcal{B}}$, effective tensor $\boldsymbol{\mu}^{(0)}$ is real-valued, i.e. $\boldsymbol{\mu}^{(0)} \in \mathbb{R}^{d \times d}$. See A.4 for proof.*

Claim 3 *For wavenumbers $\boldsymbol{k}_s = \frac{1}{2}(\sum_j n_j \boldsymbol{e}^j)$, $n_j \in \{-1, 0, 1\}$, which include the origin and apexes of the first Brillouin zone $\mathcal{B}$, Bloch eigenfunction $\tilde{\phi}_n(\boldsymbol{x}) e^{i\boldsymbol{k}_s \cdot \boldsymbol{x}}$ is real-valued up to a constant multiplier $e^{i\varphi_0}$. As a result, in such cases we find that $\boldsymbol{\theta}^{(0)} = \boldsymbol{0}$. See A.4.2 for proof.*

Claim 3 motivates us to consider separately the situations when $\boldsymbol{\theta}^{(0)} \neq \boldsymbol{0}$ and $\boldsymbol{\theta}^{(0)} = \boldsymbol{0}$, which we address next.

Effective model for non-trivial $\boldsymbol{\theta}^{(0)}$

As can be seen from the foregoing analysis, presence of the source term in the $O(1)$ statement (2.54) requires that its $O(\epsilon^{-1})$ predecessor (2.50) be satisfied *identically*. When $\tilde{f}_{\boldsymbol{k}} \neq 0$ and $\omega^2 - \omega_n^2 = O(\epsilon)$ whereby $|\check{\sigma}| = 1$ due to (2.31), we must have $u_0 = 0$ in (2.50) thanks to Remark 23 which guarantees that the multiplier $(\boldsymbol{\theta}^{(0)} \cdot (i\hat{\boldsymbol{k}}) + \check{\sigma}\rho^{(0)}\check{\omega}^2)$ is non-trivial. As a result, (2.54) yields the leading-order effective equation

$$- (\boldsymbol{\theta}^{(0)} \cdot (i\hat{\boldsymbol{k}}) + \check{\sigma}\check{\omega}^2 \rho^{(0)}) u_1 \ = \ \langle \tilde{f}_{\boldsymbol{k}} \rangle. \tag{2.56}$$

A similar treatment can be pursued for the situation when $\omega^2 - \omega_n^2 = O(\epsilon^2)$, in which case $|\hat{\sigma}| = 1$. This case is not addressed for the reasons of brevity.

In the absence of the source term $\tilde{f}_{\boldsymbol{k}}$, on the other hand, the existence of a non-trivial wavefield solving (2.50) and (2.54) independently requires that $|\check{\sigma}| = 1$. In this case, (2.56) with $\langle \tilde{f}_{\boldsymbol{k}} \rangle = 0$ furnishes the leading-order asymptotic approximation of the dispersion relationship and group velocity near $(\boldsymbol{k}_s, \omega_n > 0)$ as

$$\omega_n^2(\boldsymbol{k}) \;=\; \omega_n^2 - \frac{1}{\rho^{(0)}} i\boldsymbol{\theta}^{(0)} \cdot (\epsilon \hat{\boldsymbol{k}}), \qquad \boldsymbol{c}_g = \frac{\mathrm{d}\omega_n(\boldsymbol{k})}{\mathrm{d}\boldsymbol{k}} \;=\; \frac{-1}{2\omega_n \rho^{(0)}} i\boldsymbol{\theta}^{(0)} \tag{2.57}$$

respectively, where ω_n (without an argument) refers to $\omega_n(\boldsymbol{k}_s)$ as stated earlier. Geometrically, (2.57) describes the nth dispersion (hyper-) surface locally as a (hyper-) plane, where $\boldsymbol{c}_g$ signifies its "steepest slope".

Effective model for trivial $\boldsymbol{\theta}^{(0)}$

When $\tilde{f}_{\boldsymbol{k}} \neq 0$ and $\omega^2 - \omega_n^2 = O(\epsilon^2)$, we have that $|\hat{\sigma}| = 1$ thanks to (2.31). In this case the $O(\epsilon^{-1})$ statement (2.50) is satisfied identically, while its $O(1)$ companion (2.54) produces the effective equation

$$-\left(\boldsymbol{\mu}^{(0)} : (i\hat{\boldsymbol{k}})^2 + \hat{\sigma}\rho^{(0)}\hat{\omega}^2\right) u_0 \;=\; \langle \tilde{f}_{\boldsymbol{k}} \rangle, \tag{2.58}$$

With reference to Claim 3, (2.58) in particular describes the response of a periodic medium near the *origin* and *apexes* of the first Brillouin zone. The nature of such response depends on (i) the sign definiteness of $\boldsymbol{\mu}^{(0)}$, and (ii) the sign of $\omega^2 - \omega_n^2$. For example, when $\boldsymbol{\mu}^{(0)}$ is sign-definite oppositely to the sign of $\omega^2 - \omega_n^2$, the effective medium is "dissipative" in that ω resides inside a band gap [23] terminating at ω_n.

When $\tilde{f}_{\boldsymbol{k}} = 0$, on the other hand, from (2.50) and (2.54) we find that a non-trivial solution is possible only if $\check{\sigma} = 0$, i.e. $|\hat{\sigma}| = 1$. In this case (2.50) is again satisfied identically, while (2.54) provides the leading-order approximation of dispersion relationship and group velocity near $(\boldsymbol{k}_s, \omega_n > 0)$ as

$$\omega_n^2(\boldsymbol{k}) \;=\; \omega_n^2 + \frac{1}{\rho^{(0)}}\, \boldsymbol{\mu}^{(0)} : (\epsilon\hat{\boldsymbol{k}})^2, \qquad \boldsymbol{c}_g(\boldsymbol{k}) \;=\; \frac{1}{\omega_n \rho^{(0)}}\, \boldsymbol{\mu}^{(0)} \cdot (\epsilon\hat{\boldsymbol{k}}). \tag{2.59}$$

2.2.2 Second-order correctors

With (2.49) and (2.52) in place, one can make use of the averaged statements (2.50) and (2.54) to solve the $O(1)$ field equation (2.35) in terms of $\tilde{u}_2$ as

$$\tilde{u}_2(\boldsymbol{x}) = u_0 \boldsymbol{\chi}^{(2)}(\boldsymbol{x}) : (i\hat{\boldsymbol{k}})^2 + u_1 \boldsymbol{\chi}^{(1)}(\boldsymbol{x}) \cdot (i\hat{\boldsymbol{k}}) + u_2 \tilde{\phi}_n(\boldsymbol{x}) + \eta^{(0)}(\boldsymbol{x}), \quad u_2 \in \mathbb{C}, \tag{2.60}$$

where $\boldsymbol{\chi}^{(2)} \in \big(\bar{H}^1_{p0}(Y)\big)^{d\times d}$ is a source-independent cell function, while $\eta^{(0)} \in \bar{H}^1_{p0}(Y)$ solves the unit cell problem entailing $\tilde{f}_{\boldsymbol{k}}$ as detailed in A.3.

Remark 6 *Cell function $\eta^{(0)}$ depends implicitly on $\epsilon\hat{\boldsymbol{k}}$ via $\tilde{f}_{\boldsymbol{k}} = \tilde{f}_{\boldsymbol{k}}(\boldsymbol{x})$. In situations when $\tilde{f}_{\boldsymbol{k}}(\boldsymbol{x}) = F(\epsilon\hat{\boldsymbol{k}})\phi(\boldsymbol{x})$, the solution of* (A.7) *is given by $\eta^{(0)}(\boldsymbol{x}) = F(\epsilon\hat{\boldsymbol{k}})\zeta^{(0)}(\boldsymbol{x})$, where $\zeta^{(0)}$ uniquely solves*

$$-\tilde{\lambda}_n\rho\zeta^{(0)} - \nabla_{\boldsymbol{k}_s}\cdot\big(G\nabla_{\boldsymbol{k}_s}\zeta^{(0)}\big) \;=\; \phi - \frac{\rho}{\rho^{(0)}}\langle\phi\rangle\,\tilde{\phi}_n, \tag{2.61}$$

with $G\nabla_{\boldsymbol{k}_s}\zeta^{(0)}$ satisfying the flux boundary conditions (2.38).

Claim 4 *The following identity holds:*

$$(G\eta^{(0)}, \nabla_{\boldsymbol{k}_s}\tilde{\phi}_n) - \langle G\nabla_{\boldsymbol{k}_s}\eta^{(0)}\rangle \;=\; (\tilde{f}_{\boldsymbol{k}}, \boldsymbol{\chi}^{(1)}). \tag{2.62}$$

See A.4.1 for proof.

We next consider the $O(\epsilon)$ field equation (2.36) with $m = 1$. On substituting (2.49), (2.52) and (2.60) into (2.36), integrating $((2.36), \tilde{\phi}_n)$ by parts via the boundary conditions (2.37) with $m = 3$, and exploiting Claim 4, we obtain the averaged $O(\epsilon)$ statement

$$-\boldsymbol{\theta}^{(1)} : (i\hat{\boldsymbol{k}})^3 u_0 - \big(\boldsymbol{\mu}^{(0)} : (i\hat{\boldsymbol{k}})^2 + \hat{\sigma}\rho^{(0)}\hat{\omega}^2\big)\; u_1 - (\boldsymbol{\theta}^{(0)}\cdot(i\hat{\boldsymbol{k}}) + \check{\sigma}\check{\omega}^2\rho^{(0)})\; u_2 \;=\; M_1(\hat{\boldsymbol{k}}) \tag{2.63}$$

where

$$\begin{aligned} \boldsymbol{\theta}^{(1)} &= \langle G\{\nabla_{\boldsymbol{k}_s}\boldsymbol{\chi}^{(2)} + \boldsymbol{I}\otimes\boldsymbol{\chi}^{(1)}\}\rangle - \big\{\big(G\boldsymbol{\chi}^{(2)}\otimes\overline{\nabla_{\boldsymbol{k}_s}\tilde{\phi}_n}, 1\big)\big\}, \\ M_1(\hat{\boldsymbol{k}}) &= -(\tilde{f}_{\boldsymbol{k}}, \boldsymbol{\chi}^{(1)})\cdot(i\hat{\boldsymbol{k}}). \end{aligned} \tag{2.64}$$

Claim 5 *For any $\boldsymbol{k}_s \in \overline{\mathcal{B}}$, effective tensor $\boldsymbol{\theta}^{(1)}$ is imaginary-valued, namely $\boldsymbol{\theta}^{(1)} \in i\mathbb{R}^{d\times d\times d}$. See A.4 for proof.*

Proceeding with the analysis, we make use of the solutions (2.49), (2.52) and (2.60) in conjunction with the averaged statements (2.50), (2.54) and (2.63) to solve the $O(\epsilon)$ field equation (2.36) with $m = 1$ in terms of $\tilde{u}_3$ as

$$\begin{aligned} \tilde{u}_3(\boldsymbol{x}) \;=\;& u_0\boldsymbol{\chi}^{(3)}(\boldsymbol{x}) : (i\hat{\boldsymbol{k}})^3 + u_1\boldsymbol{\chi}^{(2)}(\boldsymbol{x}) : (i\hat{\boldsymbol{k}})^2 + u_2\boldsymbol{\chi}^{(1)}(\boldsymbol{x})\cdot(i\hat{\boldsymbol{k}}) + u_3\tilde{\phi}_n(\boldsymbol{x}) \\ &+\boldsymbol{\eta}^{(1)}(\boldsymbol{x})\cdot(i\hat{\boldsymbol{k}}) + \check{\sigma}\check{\omega}^2\eta^{(2)}(\boldsymbol{x}), \end{aligned} \tag{2.65}$$

where $u_3 \in \mathbb{C}$; $\boldsymbol{\chi}^{(3)} \in \big(\bar{H}^1_{p0}(Y)\big)^{d\times d\times d}$ is a source-independent cell function, while $\boldsymbol{\eta}^{(1)} \in \big(\bar{H}^1_{p0}(Y)\big)^d$ and $\eta^{(2)} \in \bar{H}^1_{p0}(Y)$ solve the respective unit cell problems involving $\tilde{f}_{\boldsymbol{k}}$ as described in A.3.

Next, in order to "average" the $O(\epsilon^2)$ field equation (2.36) with $m = 2$, we insert the solutions (2.49), (2.52), (2.60) and (2.65) into (2.36) and integrate $((2.36), \tilde{\phi}_n)$ by parts using boundary conditions (2.37) with $m = 4$. In this way, we obtain

$$\begin{aligned} -\boldsymbol{\mu}^{(2)} : (i\hat{\boldsymbol{k}})^4 u_0 - \boldsymbol{\theta}^{(1)} : (i\hat{\boldsymbol{k}})^3 u_1 - \left(\boldsymbol{\mu}^{(0)} : (i\hat{\boldsymbol{k}})^2 + \hat{\sigma}\rho^{(0)}\hat{\omega}^2\right) u_2 \\ -(\boldsymbol{\theta}^{(0)} \cdot (i\hat{\boldsymbol{k}}) + \check{\sigma}\check{\omega}^2\rho^{(0)})\, u_3 \;=\; M_2(\hat{\boldsymbol{k}}, \hat{\sigma}\check{\omega}^2) \end{aligned} \tag{2.66}$$

where

$$\begin{aligned} M_2(\hat{\boldsymbol{k}}, \hat{\sigma}\check{\omega}^2) &= \hat{\sigma}\check{\omega}^2\big(\langle G\nabla_{\boldsymbol{k}_s}\eta^{(2)}\rangle - (G\eta^{(2)}, \nabla_{\boldsymbol{k}_s}\tilde{\phi}_n)\big) \cdot (i\hat{\boldsymbol{k}}) \\ &\quad + \big(\langle G\{\nabla_{\boldsymbol{k}_s}\boldsymbol{\eta}^{(1)} + \eta^{(0)}\boldsymbol{I}\}\rangle - (G\{\boldsymbol{\eta}^{(1)} \otimes \overline{\nabla_{\boldsymbol{k}_s}\tilde{\phi}_n}\}, 1)\big) : (i\hat{\boldsymbol{k}})^2, \quad (2.67) \\ \boldsymbol{\mu}^{(2)} &= \langle G\{\nabla_{\boldsymbol{k}_s}\boldsymbol{\chi}^{(3)} + \boldsymbol{I} \otimes \boldsymbol{\chi}^{(2)}\}\rangle - \big\{\big(G\boldsymbol{\chi}^{(3)} \otimes \overline{\nabla_{\boldsymbol{k}_s}\tilde{\phi}_n}, 1\big)\big\}. \quad (2.68) \end{aligned}$$

Claim 6 *For any $\boldsymbol{k}_s \in \overline{\mathcal{B}}$, effective tensor $\boldsymbol{\mu}^{(2)}$ is real-valued, i.e. $\boldsymbol{\mu}^{(2)} \in \mathbb{R}^{d\times d\times d\times d}$. See A.4 for proof.*

Claim 7 *We have the following identities*

$$(G\eta^{(2)}, \nabla_{\boldsymbol{k}_s}\tilde{\phi}_n) - \langle G\nabla_{\boldsymbol{k}_s}\eta^{(2)}\rangle \;=\; (\rho\eta^{(0)}, \boldsymbol{\chi}^{(1)}), \tag{2.69}$$

$$\begin{aligned} &\langle\{G\nabla_{\boldsymbol{k}_s}\boldsymbol{\eta}^{(1)} + \eta^{(0)}\boldsymbol{I}\}\rangle - (G\{\boldsymbol{\eta}^{(1)} \otimes \overline{\nabla_{\boldsymbol{k}_s}\tilde{\phi}_n}\}, 1) = (\tilde{f}_{\boldsymbol{k}}, \boldsymbol{\chi}^{(2)}) \\ &\quad + \tfrac{\langle\tilde{f}_{\boldsymbol{k}}\rangle}{\rho^{(0)}}\{(\rho\boldsymbol{\chi}^{(1)} \otimes \overline{\boldsymbol{\chi}^{(1)}}, 1)\} + \tfrac{1}{\rho^{(0)}}\{\boldsymbol{\theta}^{(0)} \otimes (\rho\eta^{(0)}, \boldsymbol{\chi}^{(1)})\}, \end{aligned} \tag{2.70}$$

see A.4.1 for proof.

With the effective equations (2.63) and (2.66) featuring u_2 and u_3 in place, we next evaluate the second-order counterparts of (2.56) and (2.58) depending on the triviality of $\boldsymbol{\theta}^{(0)}$.

Effective model for non-trivial $\boldsymbol{\theta}^{(0)}$

When the source term $\tilde{f}_{\boldsymbol{k}} \neq 0$ and $\omega^2 - \omega_n^2 = O(\epsilon)$, we have $|\check{\sigma}| = 1$ due to Remark 2. In this case, we evaluate the weighted sum (2.56) + ϵ(2.63) + ϵ^2(2.66) to obtain

$$\begin{aligned} -\epsilon^2\boldsymbol{\theta}^{(1)} : (i\hat{\boldsymbol{k}})^3 u_1 - \epsilon^2\boldsymbol{\mu}^{(0)} : (i\hat{\boldsymbol{k}})^2\, u_2 - \epsilon^2(\boldsymbol{\theta}^{(0)} \cdot (i\hat{\boldsymbol{k}}) + \check{\sigma}\check{\omega}^2\rho^{(0)})\, u_3 - \epsilon\, \boldsymbol{\mu}^{(0)} : (i\hat{\boldsymbol{k}})^2\, u_1 \\ -\epsilon(\boldsymbol{\theta}^{(0)} \cdot (i\hat{\boldsymbol{k}}) + \check{\sigma}\check{\omega}^2\rho^{(0)})\, u_2 - (\boldsymbol{\theta}^{(0)} \cdot (i\hat{\boldsymbol{k}}) + \check{\sigma}\check{\omega}^2\rho^{(0)}) u_1 \;=\; M_2'(\epsilon\hat{\boldsymbol{k}}, \epsilon\check{\sigma}\check{\omega}^2) \end{aligned} \tag{2.71}$$

where the effective source term is given by

$$M_2'(\epsilon\hat{\boldsymbol{k}},\epsilon\check{\sigma}\check{\omega}^2) \;=\; \langle\tilde{f}_{\boldsymbol{k}}\rangle(\epsilon\hat{\boldsymbol{k}}) - (\tilde{f}_{\boldsymbol{k}},\boldsymbol{\chi}^{(1)})\cdot(i\epsilon\hat{\boldsymbol{k}}) + \epsilon\check{\sigma}\check{\omega}^2\big(\langle G\nabla_{\boldsymbol{k}_s}\eta^{(2)}\rangle - (G\eta^{(2)},\nabla_{\boldsymbol{k}_s}\tilde{\phi}_n)\big)\cdot(i\epsilon\hat{\boldsymbol{k}}) + \big(\langle G\{\nabla_{\boldsymbol{k}_s}\boldsymbol{\eta}^{(1)}+\eta^{(0)}\boldsymbol{I}\}\rangle - (G\{\boldsymbol{\eta}^{(1)}\otimes\overline{\nabla_{\boldsymbol{k}_s}\tilde{\phi}_n}\},1)\big) : (i\epsilon\hat{\boldsymbol{k}})^2.$$

This yields the second-order effective equation

$$-\big(\boldsymbol{\theta}^{(1)}\vdots(i\epsilon\hat{\boldsymbol{k}})^3 + \boldsymbol{\mu}^{(0)}\vdots(i\epsilon\hat{\boldsymbol{k}})^2 + \boldsymbol{\theta}^{(0)}\cdot(i\epsilon\hat{\boldsymbol{k}}) + \epsilon\check{\sigma}\check{\omega}^2\rho^{(0)}\big)\langle\tilde{u}\rangle_\rho \;\overset{\epsilon^3}{=}\; M_2'(\epsilon\hat{\boldsymbol{k}},\epsilon\check{\sigma}\check{\omega}^2), \quad (2.72)$$

where "$\overset{\epsilon^3}{=}$" denotes equality with an $O(\epsilon^3)$ residual.

In the absence of the source term, we find from (2.56), (2.58), (2.63) and (2.66) that a non-trivial effective solution in terms of $u_m = \langle\tilde{u}_m\rangle_\rho$ ($m=\overline{0,3}$) is possible only if $|\check{\sigma}|=1$. In this case, (2.72) with $\tilde{f}_{\boldsymbol{k}}=0$ i.e. $M_2'=0$ can be shown to describe a cubic approximation of the dispersion relationship near $(\boldsymbol{k}_s,\omega_n>0)$ as

$$\omega_n^2(\boldsymbol{k}) \;=\; \omega_n^2 - \frac{1}{\rho^{(0)}}i\boldsymbol{\theta}^{(0)}\cdot(\epsilon\hat{\boldsymbol{k}}) + \frac{1}{\rho^{(0)}}\,\boldsymbol{\mu}^{(0)}:(\epsilon\hat{\boldsymbol{k}})^2 + \frac{1}{\rho^{(0)}}i\boldsymbol{\theta}^{(1)}:(\epsilon\hat{\boldsymbol{k}})^3. \quad (2.73)$$

Effective model for trivial $\boldsymbol{\theta}^{(0)}$

Assuming that the source term $\tilde{f}_{\boldsymbol{k}}\neq 0$ and $\omega^2-\omega_n^2=O(\epsilon^2)$ whereby $|\hat{\sigma}|=1$, we obtain the second-order effective equation by evaluating the weighted sum (2.58) + ϵ(2.63) + ϵ^2(2.66), namely

$$-\epsilon^2\boldsymbol{\mu}^{(2)}\vdots(i\hat{\boldsymbol{k}})^4u_0 - \epsilon^2\boldsymbol{\theta}^{(1)}:(i\hat{\boldsymbol{k}})^3u_1 - \epsilon^2\big(\boldsymbol{\mu}^{(0)}:(i\hat{\boldsymbol{k}})^2+\hat{\sigma}\rho^{(0)}\hat{\omega}^2\big)\,u_2 - \epsilon\,\boldsymbol{\theta}^{(1)}:(i\hat{\boldsymbol{k}})^3u_0 - \epsilon\big(\boldsymbol{\mu}^{(0)}:(i\hat{\boldsymbol{k}})^2+\hat{\sigma}\rho^{(0)}\hat{\omega}^2\big)\,u_1 - \big(\boldsymbol{\mu}^{(0)}\vdots(i\hat{\boldsymbol{k}})^2+\hat{\sigma}\rho^{(0)}\hat{\omega}^2\big)u_0 \;=\; M_2''(\epsilon\hat{\boldsymbol{k}}), \quad (2.74)$$

where the effective source term is given by

$$M_2''(\epsilon\hat{\boldsymbol{k}}) \;=\; \langle\tilde{f}_{\boldsymbol{k}}\rangle(\epsilon\hat{\boldsymbol{k}}) - (\tilde{f}_{\boldsymbol{k}},\boldsymbol{\chi}^{(1)})\cdot(i\epsilon\hat{\boldsymbol{k}}) + \big(\langle G\{\nabla_{\boldsymbol{k}_s}\boldsymbol{\eta}^{(1)}+\eta^{(0)}\boldsymbol{I}\}\rangle - (G\{\boldsymbol{\eta}^{(1)}\otimes\overline{\nabla_{\boldsymbol{k}_s}\tilde{\phi}_n}\},1)\big) : (i\epsilon\hat{\boldsymbol{k}})^2. \quad (2.75)$$

This yields

$$-\big(\boldsymbol{\mu}^{(2)}\vdots(i\epsilon\hat{\boldsymbol{k}})^4 + \boldsymbol{\theta}^{(1)}\vdots(i\epsilon\hat{\boldsymbol{k}})^3 + \boldsymbol{\mu}^{(0)}\vdots(i\epsilon\hat{\boldsymbol{k}})^2 + \epsilon^2\hat{\sigma}\hat{\omega}^2\rho^{(0)}\big)\langle\tilde{u}\rangle_\rho \;\overset{\epsilon^3}{=}\; M_2''(\epsilon\hat{\boldsymbol{k}}). \quad (2.76)$$

Claim 8 *For $\boldsymbol{k}_s=\frac{1}{2}(\sum_j n_j\boldsymbol{e}^j)$, $n_j\in\{-1,0,1\}$, which includes the origin and apexes*

of $\overline{\mathcal{B}}$, Bloch functions $\tilde{\phi}_n(\boldsymbol{x})e^{i\boldsymbol{k}_s\cdot\boldsymbol{x}}$, $\boldsymbol{\chi}^{(1)}(\boldsymbol{x})e^{i\boldsymbol{k}_s\cdot\boldsymbol{x}}$, $\boldsymbol{\chi}^{(2)}(\boldsymbol{x})e^{i\boldsymbol{k}_s\cdot\boldsymbol{x}}$ and $\boldsymbol{\chi}^{(3)}(\boldsymbol{x})e^{i\boldsymbol{k}_s\cdot\boldsymbol{x}}$ are real-valued up to a constant phase factor $e^{i\varphi_0}$. Consequently, $\boldsymbol{\theta}^{(1)}=\boldsymbol{0}$ which in particular motivates our pursuit of the second-order approximation. See A.4.2 for proof.

When $\tilde{f}_{\boldsymbol{k}}=0$, on the other hand, we deduce from (2.56), (2.58), (2.63) and (2.66) that $|\hat{\sigma}|=1$ in order to have a non-trivial solution. As a result, one finds that (2.76) with $M_2''=0$ furnishes a quadratic approximation of the dispersion relationship near $(\boldsymbol{k}_s,\omega_n>0)$ as

$$\omega_n^2(\boldsymbol{k}) \;=\; \omega_n^2+\frac{1}{\rho^{(0)}}\,\boldsymbol{\mu}^{(0)}:(\epsilon\hat{\boldsymbol{k}})^2+\frac{1}{\rho^{(0)}}\,i\boldsymbol{\theta}^{(1)}:(\epsilon\hat{\boldsymbol{k}})^3-\frac{1}{\rho^{(0)}}\,\boldsymbol{\mu}^{(2)}:(\epsilon\hat{\boldsymbol{k}})^4. \tag{2.77}$$

Remark 7 *In the special case where $\tilde{f}_{\boldsymbol{k}}(\boldsymbol{k},\boldsymbol{x})=1$ and $\boldsymbol{k}_s=\frac{1}{2}(\sum_j n_j\boldsymbol{e}^j)$, $n_j\in\{-1,0,1\}$, effective equation (2.76) reduces, thanks to Claim 3, Claim 7 and Claim 8, to*

$$-\big(\boldsymbol{\mu}^{(2)}\colon(i\epsilon\hat{\boldsymbol{k}})^4+\boldsymbol{\mu}^{(0)}\colon(i\epsilon\hat{\boldsymbol{k}})^2+\epsilon^2\hat{\sigma}\hat{\omega}^2\rho^{(0)}\big)\langle\tilde{u}\rangle_\rho \;\overset{\epsilon^3}{=}\; M_2'''(\epsilon\hat{\boldsymbol{k}}), \tag{2.78}$$

where

$$\begin{aligned} M_2'''(\epsilon\hat{\boldsymbol{k}}) \;=\;& \langle 1\rangle-\overline{(\boldsymbol{\chi}^{(1)},1)}\cdot(i\epsilon\hat{\boldsymbol{k}})\\ &+\big(\langle G\{\nabla_{\boldsymbol{k}_s}\boldsymbol{\eta}^{(1)}+\eta^{(0)}\boldsymbol{I}\}\rangle-(G\{\boldsymbol{\eta}^{(1)}\otimes\overline{\nabla_{\boldsymbol{k}_s}\tilde{\phi}_n}\},1)\big):(i\epsilon\hat{\boldsymbol{k}})^2. \end{aligned} \tag{2.79}$$

We note that (2.78)–(2.79) can be reduced to the FF-FW effective model [23] upon: (i) accounting for the "unfolding" of Y according to the multicell homogenization approach [7, 20] and (ii) using $\langle\tilde{u}\rangle$ instead of $\langle\tilde{u}\rangle_\rho$ to define the "mean" motion.

2.3 Repeated eigenvalue

Let ω_n be an eigenfrequency of multiplicity $Q>1$, and let n_q ($q=\overline{1,Q}$) be the indexes of associated eigenfunctions.

Remark 8 *In what follows, we assume $p,q,s\in\overline{1,Q}$, unless stated otherwise. Further, we will use the short-hand notation $\sum_q$ for $\sum_{q=1}^{Q}$.*

2.3.1 Leading-order approximation

With reference to the eigenvalue problem (2.24)-(2.25), the solution of (2.33) in the vicinity of a repeated eigenfrequency ω_n can be decomposed as

$$\tilde{u}_0(\boldsymbol{x})=\sum_q u_{0q}\;\tilde{\phi}_{n_q}(\boldsymbol{x}),\quad u_{0q}\in\mathbb{C}, \tag{2.80}$$

consistent with the definition (2.42) of u_{0q}. Then, by inserting (2.80) in (2.34) and integrating $((2.34), \tilde{\phi}_{n_p})$ by parts via the boundary conditions (2.37) with $m = 1$, we obtain the averaged $O(\epsilon^{-1})$ statement

$$\sum_q \big(\boldsymbol{\theta}^{(0)}_{pq} \cdot i\hat{\boldsymbol{k}} + \check{\sigma}\check{\omega}^2 \rho^{(0)}_p \delta_{pq}\big) u_{0q} \;=\; 0, \qquad p \in \overline{1, Q}, \tag{2.81}$$

where

$$\boldsymbol{\theta}^{(0)}_{pq} = \langle G \nabla_{\boldsymbol{k}_s} \tilde{\phi}_{n_q} \rangle^{n_p} - \overline{\langle G \nabla_{\boldsymbol{k}_s} \tilde{\phi}_{n_p} \rangle^{n_q}} \quad \text{and} \quad \rho^{(0)}_p = \langle \rho \tilde{\phi}_{n_p} \rangle^{n_p}. \tag{2.82}$$

For convenience, system of equations (2.81) can be expressed in the matrix form as

$$(\boldsymbol{A}^{(0)}(\hat{\boldsymbol{k}}) + \check{\sigma}\check{\omega}^2 \boldsymbol{D}) \boldsymbol{u}_0 \;=\; \boldsymbol{0} \quad \text{where} \quad A^{(0)}_{pq}(\hat{\boldsymbol{k}}) = \boldsymbol{\theta}^{(0)}_{pq} \cdot i\hat{\boldsymbol{k}} \;\text{ and }\; D_{pq} = \rho^{(0)}_p \delta_{pq}. \tag{2.83}$$

Remark 9 *Effective vectors $\boldsymbol{\theta}^{(0)}_{qq}$ are imaginary-valued, i.e. $\boldsymbol{\theta}^{(0)}_{qq} \in i\mathbb{R}^d$. Coefficient matrix $\boldsymbol{D} \in \mathbb{R}^{Q\times Q}$ is diagonal, and $\boldsymbol{A}^{(0)} \in \mathbb{C}^{Q\times Q}$ is Hermitian.*

On the basis of (2.80)–(2.81), we can solve the $O(\epsilon^{-1})$ field equation (2.34) in terms of $\tilde{u}_1$ as

$$\tilde{u}_1(\boldsymbol{x}) = \sum_q \big(u_{0q}\; \boldsymbol{\chi}^{(1)}_q(\boldsymbol{x}) \cdot (i\hat{\boldsymbol{k}}) + u_{1q}\; \tilde{\phi}_{n_q}(\boldsymbol{x})\big), \quad u_{1q} \in \mathbb{C}, \tag{2.84}$$

where $\boldsymbol{\chi}^{(1)}_q \in \big(\bar{H}^1_{p0}(Y)\big)^d$ solves uniquely the unit cell problem

$$\tilde{\lambda}_n \rho \boldsymbol{\chi}^{(1)}_q + \nabla_{\boldsymbol{k}_s} \cdot \big(G(\nabla_{\boldsymbol{k}_s} \boldsymbol{\chi}^{(1)}_q + \tilde{\phi}_{n_q} \boldsymbol{I})\big) + G \nabla_{\boldsymbol{k}_s} \tilde{\phi}_{n_q} - \sum_s \frac{\rho}{\rho^{(0)}_s} \tilde{\phi}_{n_s} \boldsymbol{\theta}^{(0)}_{sq} \;=\; \boldsymbol{0}, \tag{2.85}$$

subject to the flux boundary conditions (2.38) in terms of $G(\nabla_{\boldsymbol{k}_s} \boldsymbol{\chi}^{(1)}_q + \tilde{\phi}_{n_q} \boldsymbol{I})$.

We next consider the $O(1)$ field equation (2.35). On recalling (2.80) and (2.84) and integrating $((2.35), \tilde{\phi}_{n_p})$ by parts via the boundary conditions (2.37) with $m = 2$, we obtain the averaged $O(1)$ statement

$$-\sum_q \Big(\big(\boldsymbol{\mu}^{(0)}_{pq} : (i\hat{\boldsymbol{k}})^2 + \hat{\sigma}\hat{\omega}^2 \rho^{(0)}_p \delta_{pq}\big) u_{0q} + (\boldsymbol{\theta}^{(0)}_{pq} \cdot (i\hat{\boldsymbol{k}}) + \check{\sigma}\check{\omega}^2 \rho^{(0)}_p \delta_{pq}) u_{1q}\Big) \;=\; \langle \tilde{f}_{\boldsymbol{k}} \rangle^{n_p}, \tag{2.86}$$

where

$$\boldsymbol{\mu}^{(0)}_{pq} = \langle G\{\nabla_{\boldsymbol{k}_s} \boldsymbol{\chi}^{(1)}_q + \tilde{\phi}_{n_q} \boldsymbol{I}\}\rangle^{n_p} - \big\{\big(G \boldsymbol{\chi}^{(1)}_q \otimes \overline{\nabla_{\boldsymbol{k}_s} \tilde{\phi}_{n_p}}, 1\big)\big\}. \tag{2.87}$$

We rewrite (2.86) in the matrix form as

$$-(\boldsymbol{B}^{(0)}(\hat{\boldsymbol{k}}) + \hat{\sigma}\hat{\omega}^2 \boldsymbol{D}) \boldsymbol{u}_0 - (\boldsymbol{A}^{(0)}(\hat{\boldsymbol{k}}) + \check{\sigma}\check{\omega}^2 \boldsymbol{D}) \boldsymbol{u}_1 \;=\; \mathbf{f}_0 \quad \text{where} \quad B^{(0)}_{pq}(\hat{\boldsymbol{k}}) = \boldsymbol{\mu}^{(0)}_{pq} : (i\hat{\boldsymbol{k}})^2 \;\text{ and }\; \mathrm{f}_{0p} = \langle \tilde{f}_{\boldsymbol{k}} \rangle^{n_p}. \tag{2.88}$$

Claim 9 *Matrix $\boldsymbol{B}^{(0)} \in \mathbb{C}^{Q\times Q}$ is Hermitian. See A.4 for proof.*

Eigenfunction basis

For a fixed direction $\hat{\boldsymbol{k}}/\|\hat{\boldsymbol{k}}\|$, let $\boldsymbol{P} \in \mathbb{C}^{Q\times Q}$ denote the matrix of eigenvectors associated with the generalized eigenvalue problem

$$\boldsymbol{A}^{(0)}\boldsymbol{v} \;=\; \tau \boldsymbol{D}\boldsymbol{v}. \tag{2.89}$$

In this setting, we conveniently introduce the "recombined" eigenfunctions $\tilde{\psi}_q$ as

$$\tilde{\psi}_q = \sum_s P_{sq}\, \tilde{\phi}_{n_s}, \quad q \in \overline{1, Q}. \tag{2.90}$$

Then, by taking the eigenfunctions $\{\tilde{\psi}_q\}$ as the projection basis in (2.80) and (2.82) instead of $\{\tilde{\phi}_{n_q}\}$, we find that

$$\boldsymbol{A}^{(0)}(\hat{\boldsymbol{k}}) = \mathrm{diag}(0, \ldots, 0, \tau_{N_0+1}, \tau_{N_0+2}, \ldots, \tau_Q) \tag{2.91}$$

where $\tau_q = \boldsymbol{\theta}^{(0)}_{qq} \cdot i\hat{\boldsymbol{k}}$ and $0 \leqslant N_0 \leqslant Q$ is the number of trivial diagonal entries of $\boldsymbol{A}^{(0)}$.

Claim 10 *For $\boldsymbol{k}_s = \frac{1}{2}(\sum_j n_j \boldsymbol{e}^j)$, $n_j \in \{-1, 0, 1\}$ which include the origin and apexes of the first Brillouin zone, Bloch eigenfunctions $\tilde{\phi}_{n_p} e^{i\boldsymbol{k}_s\cdot\boldsymbol{x}}$ have constant phase and can be taken as real-valued. In this case, vector $\boldsymbol{\theta}^{(0)}_{pq} \in \mathbb{R}^d$ and $\boldsymbol{\theta}^{(0)}_{pp} = \boldsymbol{0}$, whereby $\boldsymbol{A}^{(0)}$ is imaginary-valued and skew-symmetric. Consequently, the nonzero eigenvalues of $\boldsymbol{A}^{(0)}$ consist of pairs $\{\tau, -\tau\}$ whose respective eigenvectors are complex conjugates of each other. See A.4.2 for proof.*

In this setting, we also define the sub-matrices $\bar{\boldsymbol{B}}^{(0)}(\hat{\boldsymbol{k}}) \in \mathbb{C}^{N_0\times N_0}$ and $\bar{\boldsymbol{D}} \in \mathbb{R}^{N_0\times N_0}$ such that

$$\bar{B}^{(0)}_{pq} \;=\; B^{(0)}_{pq} \quad \text{and} \quad \bar{D}_{pq} \;=\; D_{pq}, \qquad p, q \in \overline{1, N_0}.$$

When $N_0 > 0$, we denote by $\bar{\boldsymbol{P}}$ the matrix of eigenvectors of the generalized eigenvalue problem

$$\bar{\boldsymbol{B}}^{(0)}\boldsymbol{v} \;=\; \tau \bar{\boldsymbol{D}}\boldsymbol{v}, \tag{2.92}$$

and we define the eigenfunction basis $\tilde{\psi}'_q$ as

$$\tilde{\psi}'_q \;=\; \begin{cases} \sum_{s=1}^{N_0} \bar{P}_{sq}\, \tilde{\psi}_s, & q \leqslant N_0 \\ \tilde{\psi}_q, & q > N_0 \end{cases}. \tag{2.93}$$

Remark 10 *Eigenfunctions $\tilde{\psi}'_q$ ($q = \overline{1,Q}$) are ρ-orthogonal in the sense of* (2.26)*, see A.4 for proof. For simplicity of discussion, we hereon relabel $\tilde{\psi}'_q$ as $\tilde{\phi}_{n_q}$. In this setting, we have*

$$\bar{\boldsymbol{B}}^{(0)} \;=\; diag(\boldsymbol{\mu}_{11}^{(0)}:(i\hat{\boldsymbol{k}})^2,\ldots,\boldsymbol{\mu}_{N_0N_0}^{(0)}:(i\hat{\boldsymbol{k}})^2). \tag{2.94}$$

Additional scaling

Depending on the perturbation direction, certain non-zero diagonal entries of $\boldsymbol{A}^{(0)}(\hat{\boldsymbol{k}})$ in (2.91) can become vanishingly small, namely $\tau_q = o(1)$ for some q. In the context of Section 2.2.1, for instance, this situation would correspond to directions $\hat{\boldsymbol{k}}/\|\hat{\boldsymbol{k}}\|$ for which $\boldsymbol{\theta}^{(0)}\cdot(i\hat{\boldsymbol{k}}) = o(1)$. To account for such situations, we decompose $\boldsymbol{A}^{(0)}$ as

$$\boldsymbol{A}^{(0)}(\hat{\boldsymbol{k}}) \;=\; \mathrm{diag}(0,\ldots,0,\underbrace{\tau_{N_0+1},\ldots,\tau_N}_{O(\epsilon)},\underbrace{\tau_{N+1},\ldots\tau_Q}_{O(1)}) \;=\; \dot{\boldsymbol{A}}^{(0)}(\hat{\boldsymbol{k}}) + \epsilon\ddot{\boldsymbol{A}}^{(0)}(\hat{\boldsymbol{k}}) \tag{2.95}$$

$$\dot{\boldsymbol{A}}^{(0)}(\hat{\boldsymbol{k}}) \;=\; \mathrm{diag}(0,\ldots,0,\underbrace{\tau_{N+1},\ldots\tau_Q}_{O(1)}) \;\in\; \mathbb{R}^{Q\times Q}, \tag{2.96}$$

$$\ddot{\boldsymbol{A}}^{(0)}(\hat{\boldsymbol{k}}) \;=\; \mathrm{diag}(0,\ldots,0,\underbrace{\epsilon^{-1}\tau_{N_0+1},\ldots,\epsilon^{-1}\tau_N}_{O(1)},0,\ldots,0), \;\in\; \mathbb{R}^{Q\times Q} \tag{2.97}$$

and we *carry over* thus incurred $O(\epsilon)$ residual in (2.83) to (2.88) as

$$(\dot{\boldsymbol{A}}^{(0)}(\hat{\boldsymbol{k}}) + \breve{\sigma}\breve{\omega}^2\boldsymbol{D})\boldsymbol{u}_0 \;=\; \boldsymbol{0}, \tag{2.98}$$

$$-(\boldsymbol{B}^{(0)}(\hat{\boldsymbol{k}}) + \ddot{\boldsymbol{A}}^{(0)}(\hat{\boldsymbol{k}}) + \hat{\sigma}\hat{\omega}^2\boldsymbol{D})\boldsymbol{u}_0 - (\dot{\boldsymbol{A}}^{(0)}(\hat{\boldsymbol{k}}) + \breve{\sigma}\breve{\omega}^2\boldsymbol{D})\boldsymbol{u}_1 \;=\; \mathbf{f}_0. \tag{2.99}$$

On the basis of (2.98)–(2.99), we next pursue a family of first-order effective field equations (in prescribed direction $\hat{\boldsymbol{k}}/\|\hat{\boldsymbol{k}}\|$) as controlled by: (i) proximity of the driving frequency ω^2 to $\tilde{\lambda}_n$ (see Remark 2), and (ii) the nature of $\boldsymbol{A}^{(0)}(\hat{\boldsymbol{k}})$ according to (2.95)–(2.97).

Effective solution for full-rank $\boldsymbol{A}^{(0)}$ when $\ddot{\boldsymbol{A}}^{(0)}=\boldsymbol{0}$

We first consider the case where $\mathrm{rank}(\boldsymbol{A}^{(0)}(\hat{\boldsymbol{k}})) = Q$ and $\ddot{\boldsymbol{A}}^{(0)} = \boldsymbol{0}$. With reference to (2.91), this specifically implies that $\tau_q = \boldsymbol{\theta}_{qq}^{(0)}\cdot i\hat{\boldsymbol{k}} = O(1)$, $q = \overline{1,Q}$. Letting further $\tilde{f}_{\boldsymbol{k}} \neq \boldsymbol{0}$ and $\omega^2 - \omega_n^2 = O(\epsilon)$ so that $|\breve{\sigma}| = 1$ by Remark 2, we find from the $O(\epsilon^{-1})$ statement (2.98) that $\boldsymbol{u}_0 = \boldsymbol{0}$ thanks to Remark 23. From (2.99), we then obtain the leading-order model

$$-(\boldsymbol{A}^{(0)}(\hat{\boldsymbol{k}}) + \breve{\sigma}\breve{\omega}^2\boldsymbol{D})\boldsymbol{u}_1 \;=\; \mathbf{f}_0. \tag{2.100}$$

In the absence of the driving source $\tilde{f}_{\boldsymbol{k}}$, the existence of a non-trivial solution

to (2.98)–(2.99) also requires that $|\check{\sigma}| = 1$. As a result, (2.98) constitutes a generalized eigenvalue problem (GEP) whose eigenvalues

$$\omega_{n_q}^2(\boldsymbol{k}) \;=\; \omega_n^2 - \frac{1}{\rho_q^{(0)}} i\boldsymbol{\theta}_{qq}^{(0)} \cdot (\epsilon\hat{\boldsymbol{k}}), \tag{2.101}$$

describe the leading-order, *linear* dispersion relationship in direction $\hat{\boldsymbol{k}}$.

Effective solution for near-trivial $\boldsymbol{A}^{(0)}$

When $\boldsymbol{A}^{(0)}(\hat{\boldsymbol{k}}) = \epsilon\ddot{\boldsymbol{A}}^{(0)}$ i.e. $\dot{\boldsymbol{A}}^{(0)} = \boldsymbol{0}$, we consider the situation where $\tilde{f}_{\boldsymbol{k}} \neq 0$ and $\omega^2 - \omega_n^2 = O(\epsilon^2)$ so that $|\hat{\sigma}| = 1$. In this case (2.98) is satisfied identically, and we find from (2.99) that the leading-order solution $\boldsymbol{u}_0$ solves

$$-(\boldsymbol{B}^{(0)}(\hat{\boldsymbol{k}}) + \ddot{\boldsymbol{A}}^{(0)}(\hat{\boldsymbol{k}}) + \hat{\sigma}\hat{\omega}^2\boldsymbol{D})\boldsymbol{u}_0 \;=\; \mathbf{f}_0. \tag{2.102}$$

In the degenerate case when $\boldsymbol{A}^{(0)} = \epsilon\ddot{\boldsymbol{A}}^{(0)} = \boldsymbol{0}$, (2.102) becomes

$$-(\boldsymbol{B}^{(0)}(\hat{\boldsymbol{k}}) + \hat{\sigma}\hat{\omega}^2\boldsymbol{D})\boldsymbol{u}_0 \;=\; \mathbf{f}_0. \tag{2.103}$$

In this case we conveniently let $P_{sq} = \delta_{sq}$ in (2.90), and we have $N_0 = Q$ whereby $\boldsymbol{B}^{(0)} = \bar{\boldsymbol{B}}^{(0)}$ becomes diagonal according to (2.94).

When $\tilde{f}_{\boldsymbol{k}} = 0$, the existence of a non-trivial solution requires that $\check{\sigma} = 0$ i.e. $|\hat{\sigma}| = 1$. In this case, the leading-order approximation of the dispersion relationships $\omega_{n_q}(\boldsymbol{k})$, $q = \overline{1,Q}$ is obtained by solving the eigenvalue problem $(\boldsymbol{B}^{(0)} + \ddot{\boldsymbol{A}}^{(0)})\boldsymbol{v} = \tau\boldsymbol{D}\boldsymbol{v}$. When $\ddot{\boldsymbol{A}}^{(0)}$ vanishes, the solution is given explicitly by

$$\omega_{n_q}^2(\boldsymbol{k}) \;=\; \omega_n^2 + \frac{1}{\rho_q^{(0)}}\, \boldsymbol{\mu}_{qq}^{(0)} : (\epsilon\hat{\boldsymbol{k}})^2, \tag{2.104}$$

thanks to the fact that $\boldsymbol{B}^{(0)}$ is diagonal in this case.

Effective solution for partial rank $\boldsymbol{A}^{(0)}$

We next assume that $\boldsymbol{A}^{(0)}$ has a partial rank, i.e. $0 < N_0 < Q$. Letting $\tilde{f}_{\boldsymbol{k}} \neq 0$ and $\omega^2 - \omega_n^2 = O(\epsilon^2)$, we have $|\hat{\sigma}| = 1$. Thanks to the fact that $\boldsymbol{A}^{(0)}$ is diagonal due to (2.91), the last $Q - N$ components of $\boldsymbol{u}_0$ must vanish by enforcing (2.98) to the

leading order. By virtue of this result and (2.99), we find that

$$-\sum_{q=1}^{N}(B_{pq}^{(0)}(\hat{\boldsymbol{k}})+\ddot{A}_{pq}^{(0)}(\hat{\boldsymbol{k}})+\hat{\sigma}\hat{\omega}^2 D_{pq})\,u_{0q} \;=\; \mathrm{f}_{0p}, \quad p\in\overline{1,N}, \tag{2.105}$$

$$u_{0p} \;=\; 0, \quad p\in\overline{N+1,Q}. \tag{2.106}$$

When $\tilde{f}_{\boldsymbol{k}}=0$, we enable a non-trivial solution to (2.98)– (2.99) in terms of $\boldsymbol{u}_0$ by taking $|\hat{\sigma}|=1$. In this case, (2.105) with $\mathrm{f}_{0p}=0$ constitute a GEP yielding the leading-order approximation the first N dispersion branches $\omega_{n_q}(\boldsymbol{k})$, $q=\overline{1,N}$.

Letting $\tilde{f}_{\boldsymbol{k}}\neq 0$ and $\omega^2-\omega_n^2=O(\epsilon)$, on the other hand, we have $|\check{\sigma}|=1$ whereby $\boldsymbol{u}_0=\boldsymbol{0}$ thanks to (2.98). From (2.99), we accordingly find that $\boldsymbol{u}_1$ solves

$$-(\dot{\boldsymbol{A}}^{(0)}(\hat{\boldsymbol{k}})+\check{\sigma}\check{\omega}^2\boldsymbol{D})\boldsymbol{u}_1 \;=\; \mathbf{f}_0, \tag{2.107}$$

to the leading order (specifically, we discard the $O(\epsilon)$ residual in (2.99) by superseding $\boldsymbol{A}^{(0)}$ with $\dot{\boldsymbol{A}}^{(0)}$). Assuming $\tilde{f}_{\boldsymbol{k}}=0$, we are now left with exposing the leading-order behavior the last $Q-N$ dispersion branches $\omega_{n_q}(\boldsymbol{k})$, $q=\overline{N+1,Q}$. In this case we must set $|\check{\sigma}|=1$ because all dispersion branches permitting the $\hat{\sigma}$-description are already given by (2.105) with $\mathrm{f}_{0p}=0$. This yields the sought approximation via (2.107) with $\mathbf{f}_0=\boldsymbol{0}$ as

$$\omega_{n_q}^2(\boldsymbol{k}) \;=\; \omega_n^2-\frac{1}{\rho_q^{(0)}}i\boldsymbol{\theta}_{qq}^{(0)}\cdot(\epsilon\hat{\boldsymbol{k}}), \qquad q=\overline{N+1,Q}. \tag{2.108}$$

2.3.2 First-order correctors

With the aid of the averaged $O(\epsilon^{-1})$ statement (2.86), one may solve the $O(1)$ field equation (2.35) as

$$\tilde{u}_2(\boldsymbol{x})=\sum_q(u_{0q}\;\boldsymbol{\chi}_q^{(2)}(\boldsymbol{x}):(i\hat{\boldsymbol{k}})^2+u_{1q}\;\boldsymbol{\chi}_q^{(1)}(\boldsymbol{x})\cdot(i\hat{\boldsymbol{k}})+u_{2q}\;\tilde{\phi}_{n_q}(\boldsymbol{x}))+\eta^{(0)}(\boldsymbol{x}), \qquad u_{2q}\in\mathbb{C}, \tag{2.109}$$

where $\boldsymbol{\chi}_q^{(2)}\in\big(\bar{H}^1_{p0}(Y)\big)^{d\times d}$ and $\eta^{(0)}\in\bar{H}^1_{p0}(Y)$ are the cell functions specified in A.3.

Claim 11 *We have the following identity*

$$(G\eta^{(0)},\nabla_{\boldsymbol{k}_s}\tilde{\phi}_{n_q})-\langle G\nabla_{\boldsymbol{k}_s}\eta^{(0)}\rangle^{n_q} \;=\; (\tilde{f}_{\boldsymbol{k}},\boldsymbol{\chi}_q^{(1)}), \tag{2.110}$$

See Appendix section A.4.1 for proof.

On substituting (2.80) and (2.84) into (2.36) with $m=1$, integrating $((2.36),\tilde{\phi}_n)$ by parts via boundary conditions (2.37) with $m=3$, and exploiting the result of Claim 11,

we obtain the averaged $O(\epsilon)$ statement

$$-\sum_q \Big(\boldsymbol{\theta}_{pq}^{(1)} : (i\hat{\boldsymbol{k}})^3 u_{0q} + \big(\boldsymbol{\mu}_{pq}^{(0)} : (i\hat{\boldsymbol{k}})^2 + \hat{\sigma}\hat{\omega}^2 \rho_p^{(0)} \delta_{pq} \big)\, u_{1q} + (\boldsymbol{\theta}_{pq}^{(0)} \cdot (i\hat{\boldsymbol{k}}) + \check{\sigma}\check{\omega}^2 \rho_p^{(0)} \delta_{pq})\, u_{2q} \Big) = \mathrm{f}_{1p}, \tag{2.111}$$

where

$$\begin{aligned} \boldsymbol{\theta}_{pq}^{(1)} &= \langle G\{\nabla_{\boldsymbol{k}_s} \boldsymbol{\chi}_q^{(2)} + \boldsymbol{I} \otimes \boldsymbol{\chi}_q^{(1)}\}\rangle^{n_p} - \big\{ \big(G \boldsymbol{\chi}_q^{(2)} \otimes \overline{\nabla_{\boldsymbol{k}_s} \tilde{\phi}_{n_p}}, 1 \big) \big\}, \\ \mathrm{f}_{1p} &= -(\tilde{f}_{\boldsymbol{k}}, \boldsymbol{\chi}_p^{(1)}) \cdot (i\hat{\boldsymbol{k}}). \end{aligned} \tag{2.112}$$

We can conveniently rewrite (2.111) in the matrix form as

$$-\boldsymbol{A}^{(1)}(\hat{\boldsymbol{k}})\, \boldsymbol{u}_0 - (\boldsymbol{B}^{(0)}(\hat{\boldsymbol{k}}) + \hat{\sigma}\hat{\omega}^2 \boldsymbol{D}) \boldsymbol{u}_1 - (\boldsymbol{A}^{(0)}(\hat{\boldsymbol{k}}) + \check{\sigma}\check{\omega}^2 \boldsymbol{D}) \boldsymbol{u}_2 \;=\; \mathbf{f}_1, \qquad A_{pq}^{(1)} = \boldsymbol{\theta}_{pq}^{(1)} : (i\hat{\boldsymbol{k}})^3. \tag{2.113}$$

Remark 11 *At this point, we recall the decomposition of* $\boldsymbol{A}^{(0)}$ *according to* (2.95)–(2.97)*, and the fact that* (2.99) *accordingly incurs an* $O(\epsilon)$ *residual, manifest in the term* $-\epsilon \ddot{\boldsymbol{A}}^{(0)} \boldsymbol{u}_1$*, that carries over to the next order of asymptotic approximation.*

On accounting in (2.113) for the $O(\epsilon)$ residual stemming from (2.99), we obtain the averaged statement

$$-\boldsymbol{A}^{(1)}(\hat{\boldsymbol{k}})\, \boldsymbol{u}_0 - (\boldsymbol{B}^{(0)}(\hat{\boldsymbol{k}}) + \ddot{\boldsymbol{A}}^{(0)}(\hat{\boldsymbol{k}}) + \hat{\sigma}\hat{\omega}^2 \boldsymbol{D}) \boldsymbol{u}_1 - (\dot{\boldsymbol{A}}^{(0)}(\hat{\boldsymbol{k}}) + \check{\sigma}\check{\omega}^2 \boldsymbol{D}) \boldsymbol{u}_2 \;=\; \mathbf{f}_1. \tag{2.114}$$

which allows us to compute the first-order correction $\boldsymbol{u}_1$ (resp. $\boldsymbol{u}_2$) of the leading-order model $\boldsymbol{u}_0$ (resp. $\boldsymbol{u}_1$). With reference to section §2.3.1, we pursue such task for three canonical situations driven by the nature of $\boldsymbol{A}^{(0)}$. Before proceeding, we conveniently denote by $\langle \tilde{\boldsymbol{u}} \rangle_\rho$ the effective solution vector collecting the left-hand sides in (2.43), which gives

$$\langle \tilde{\boldsymbol{u}} \rangle_\rho(\epsilon \boldsymbol{k}) = \sum_{m=0}^{\infty} \epsilon^{m-2} \boldsymbol{u}_m. \tag{2.115}$$

For brevity, we focus our attention on the effective equations only, noting that the respective approximations of the dispersion relationship can be uniformly obtained by: (i) setting the source term in the effective equation to zero, and (ii) solving the resulting GEP.

Effective solution for full-rank $\boldsymbol{A^{(0)}}$ when $\boldsymbol{\ddot{A}^{(0)}= 0}$

Assuming $\text{rank}(\boldsymbol{A}^{(0)}) = Q$ and $\boldsymbol{A}^{(0)} = \dot{\boldsymbol{A}}^{(0)}$, we let $\tilde{f}_{\boldsymbol{k}} \neq 0$ and $\omega^2 - \omega_n^2 = O(\epsilon)$. In this case $|\breve{\sigma}| = 1$, $\boldsymbol{u}_0 = \boldsymbol{0}$, and by (2.114) the first-order order corrector $\boldsymbol{u}_2$ solves

$$-\boldsymbol{B}^{(0)}(\hat{\boldsymbol{k}})\boldsymbol{u}_1 - (\boldsymbol{A}^{(0)}(\hat{\boldsymbol{k}}) + \breve{\sigma}\breve{\omega}^2\boldsymbol{D})\boldsymbol{u}_2 \;=\; \mathbf{f}_1, \tag{2.116}$$

where $\boldsymbol{u}_1$ is given by (2.100). Thanks to (2.115), we can now evaluate the weighted sum (2.100) + ϵ(2.116) in order to obtain the first-order effective model, namely

$$-\epsilon\, \boldsymbol{B}^{(0)}(\hat{\boldsymbol{k}})\boldsymbol{u}_1 - \epsilon(\boldsymbol{A}^{(0)}(\hat{\boldsymbol{k}}) + \breve{\sigma}\breve{\omega}^2\boldsymbol{D})\boldsymbol{u}_2 - (\boldsymbol{A}^{(0)}(\hat{\boldsymbol{k}}) + \breve{\sigma}\breve{\omega}^2\boldsymbol{D})\boldsymbol{u}_1 \;=\; \mathbf{f}_0 + \epsilon\mathbf{f}_1, \tag{2.117}$$

which yields

$$-(\boldsymbol{B}^{(0)}(\epsilon\hat{\boldsymbol{k}}) + \boldsymbol{A}^{(0)}(\epsilon\hat{\boldsymbol{k}}) + \epsilon\breve{\sigma}\breve{\omega}^2\boldsymbol{D})\langle\tilde{\boldsymbol{u}}\rangle_\rho \;\overset{\epsilon^2}{=}\; \mathbf{f}_0 + \epsilon\mathbf{f}_1, \tag{2.118}$$

where the components of $\mathbf{f}_0$ and $\mathbf{f}_1$ are given respectively by (2.88) and (2.112). For completeness, one may note that (2.118) carries the same structure as its simple-eigenvalue counterpart (2.72) when truncated to the first order.

Effective solution for near-trivial $\boldsymbol{A^{(0)}}$

When $\boldsymbol{A}^{(0)} = \epsilon\ddot{\boldsymbol{A}}^{(0)}$, $\tilde{f}_{\boldsymbol{k}} \neq 0$ and $\omega^2 - \omega_n^2 = O(\epsilon^2)$ i.e. $|\hat{\sigma}| = 1$, the leading-order model is given by $\boldsymbol{u}_0$ solving (2.102). In this case we discard the second-order correction $\boldsymbol{u}_2$ in (2.114), which then yields

$$-\boldsymbol{A}^{(1)}(\hat{\boldsymbol{k}})\boldsymbol{u}_0 - (\boldsymbol{B}^{(0)}(\hat{\boldsymbol{k}}) + \ddot{\boldsymbol{A}}^{(0)}(\hat{\boldsymbol{k}}) + \hat{\sigma}\hat{\omega}^2\boldsymbol{D})\boldsymbol{u}_1 \;=\; \mathbf{f}_1. \tag{2.119}$$

From the weighted sum (2.102) + ϵ(2.119), i.e.

$$-\epsilon\, \boldsymbol{A}^{(1)}(\hat{\boldsymbol{k}})\boldsymbol{u}_0 - \epsilon(\boldsymbol{B}^{(0)}(\hat{\boldsymbol{k}}) + \ddot{\boldsymbol{A}}^{(0)}(\hat{\boldsymbol{k}}) + \hat{\sigma}\hat{\omega}^2\boldsymbol{D})\boldsymbol{u}_1 - (\boldsymbol{B}^{(0)}(\hat{\boldsymbol{k}}) + \ddot{\boldsymbol{A}}^{(0)}(\hat{\boldsymbol{k}}) + \hat{\sigma}\hat{\omega}^2\boldsymbol{D})\boldsymbol{u}_0 \;=\; \mathbf{f}_0 + \epsilon\mathbf{f}_1, \tag{2.120}$$

we obtain the first-order effective model

$$-(\boldsymbol{A}^{(1)}(\epsilon\hat{\boldsymbol{k}}) + \boldsymbol{B}^{(0)}(\epsilon\hat{\boldsymbol{k}}) + \ddot{\boldsymbol{A}}^{(0)}(\epsilon\hat{\boldsymbol{k}}) + \epsilon^2\hat{\sigma}\hat{\omega}^2\boldsymbol{D})\langle\tilde{\boldsymbol{u}}\rangle_\rho \;\overset{\epsilon^2}{=}\; \mathbf{f}_0 + \epsilon\mathbf{f}_1. \tag{2.121}$$

When $\ddot{\boldsymbol{A}}^{(0)} = \boldsymbol{0}$, (2.121) carries the same structure as its simple-eigenvalue counterpart (2.76) after truncation to the first order.

Effective solution for partial rank $\boldsymbol{A}^{(0)}$

When $\text{rank}(\boldsymbol{A}^{(0)}) < Q$, $\tilde{f}_{\boldsymbol{k}} \neq 0$ and $\omega^2 - \omega_n^2 = O(\epsilon)$, the leading-order solution $\boldsymbol{u}_1$ satisfies (2.107), while the first-order corrector $\boldsymbol{u}_2$ solves (2.116). On the other hand, when $\omega^2 - \lambda_n = O(\epsilon^2)$, the leading-order model $\boldsymbol{u}_0$ is given by (2.105)–(2.106), while its corrector $\boldsymbol{u}_1$ satisfies

$$-\sum_{q=1}^{N}(B_{pq}^{(0)}(\hat{\boldsymbol{k}}) + \ddot{A}_{pq}^{(0)}(\hat{\boldsymbol{k}}) + \hat{\sigma}\hat{\omega}^2 D_{pq})u_{1q} = \mathrm{f}_{1p} + \textstyle\sum_{q=1}^{N} A_{pq}^{(1)}(\hat{\boldsymbol{k}})u_{0q}, \quad p \in \overline{1,N}, \tag{2.122}$$

$$-\dot{A}_{pp}^{(0)}(\hat{\boldsymbol{k}})u_{1p} = \mathrm{f}_{0p} + \textstyle\sum_{q=1}^{N} B_{pq}^{(0)}(\hat{\boldsymbol{k}})u_{0q}, \quad p \in \overline{N+1,Q}. \tag{2.123}$$

In this case, we obtain the first-order model as $\langle \tilde{\boldsymbol{u}} \rangle_\rho \overset{\epsilon^0}{=} \epsilon^{-2}\boldsymbol{u}_0 + \epsilon^{-1}\boldsymbol{u}_1$, where the scaled summands are directly computable from (2.105)–(2.106) and (2.122)–(2.123) upon replacing $\hat{\boldsymbol{k}}$ and $\hat{\sigma}\hat{\omega}$ respectively by $\epsilon\hat{\boldsymbol{k}}$ and $\epsilon^2\hat{\sigma}\hat{\omega}$.

2.4 Cluster of nearby eigenvalues

We conclude the general analysis by letting the driving frequency be near a cluster of nearby eigenfrequencies $\{\omega_{n_q}\}$, $q = \overline{1,Q}$ depicted in Fig. 2.2. This situation was originally considered in [23] in an effort to handle the "short asymptotic range" exhibited by single- and repeated-eigenfrequency models within $(\boldsymbol{k},\omega)$ regions characterized by closely spaced dispersion curves. Our goal is to extend the analysis in [23] by: (i) permitting expansion about an arbitrary point $(\boldsymbol{k}_s,\omega)$, $\boldsymbol{k}_s \in \overline{\mathcal{B}}$ and (ii) exposing the first-order correction of the leading-order model.

We let $\bar{Q}$ be the number of distinct eigenvalues within set $\{\omega_{n_q}\}$, and we denote by $(\boldsymbol{k}_s,\omega_{n_0})$ for some $n_0 \in \{n_q\}$ the origin of asymptotic expansion in (2.30). In this setting, we conveniently redeploy the scaling parameter $\epsilon = o(1)$ to quantify the "smallness" of distances between the neighboring eigenvalues by letting

$$\lambda_{n_q} = \lambda_{n_0} - \epsilon\gamma_q, \qquad q = \overline{1,\bar{Q}}. \tag{2.124}$$

Remark 12 *Note that the logic behind such use of ϵ is consistent with previous developments. Specifically, in sections §2.2 and §2.3, we defined the size of the "asymptotic box" surrounding $(\boldsymbol{k}_s,\omega)$ as either $O(\epsilon)^d \times O(\epsilon)$ or $O(\epsilon)^d \times O(\epsilon^2)$ depending on (a) the driving frequency when $\tilde{f}_{\boldsymbol{k}} \neq 0$, and (b) the flatness of the n dispersion branch for $\tilde{f}_{\boldsymbol{k}} = 0$. In the present case, by* (2.124) *we ensure that such "asymptotic box" captures all (relevant)*

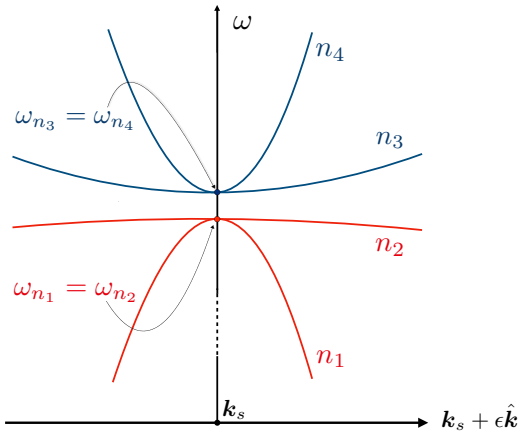

Figure 2.2: Example of a cluster of nearby dispersion branches.

dispersion surfaces in the cluster.

With (2.124) in place, we consider the local eigenfunction basis $\{\tilde{\phi}_{n_q}(\boldsymbol{k}) \in H^1_{p0}(Y)\}$ that satisfies

$$-(\tilde{\lambda}_{n0} - \epsilon\gamma_q)\rho(\boldsymbol{x})\tilde{\phi}_{n_q} - \nabla_{\boldsymbol{k}}\cdot\big(G(\boldsymbol{x})\nabla_{\boldsymbol{k}}\,\tilde{\phi}_{n_q}\big) \;=\; 0 \quad \text{in} \;\; Y, \qquad q = \overline{1,Q} \tag{2.125}$$

together with boundary conditions (2.25). As can be seen from (2.125), the current problem can be described as an "almost repeated" eigenvalue case, which allows us to take advantage of the foregoing developments.

With the insight into $\tilde{u}$ solving (2.21) gained in Section 2.2 and Section 2.3, we skip intermediate steps and proceed by specifying ansatz (2.32) up to $m = 2$ as

$$\begin{aligned}\tilde{u}(\boldsymbol{x}) \;\overset{\epsilon}{=}\; \sum_q \Big(&\epsilon^{-2}u_{0q}\,\tilde{\phi}_{n_q}(\boldsymbol{x}) + \epsilon^{-1}u_{1q}\,\tilde{\phi}_{n_q}(\boldsymbol{x}) + \epsilon^{-1}u_{0q}\,\boldsymbol{\chi}^{(1)}_q(\boldsymbol{x})\cdot(i\hat{\boldsymbol{k}}) + u_{0q}\,\boldsymbol{\chi}^{(2)}_q(\boldsymbol{x}) : (i\hat{\boldsymbol{k}})^2 \\ &+\; u_{1q}\,\boldsymbol{\chi}^{(1)}_q(\boldsymbol{x})\cdot(i\hat{\boldsymbol{k}}) + u_{2q}\,\tilde{\phi}_{n_q}(\boldsymbol{x})\Big) \;+\; \sum_{q=1}^{\bar{Q}}\eta^{(0)}_q(\boldsymbol{x}),\end{aligned} \tag{2.126}$$

where $u_{0q}, u_{1q}, u_{2q} \in \mathbb{C}$, $\eta^{(0)}_q \in \bar{H}^1_{p0}(Y)$, $\boldsymbol{\chi}^{(1)}_q \in \big(\bar{H}^1_{p0}(Y)\big)^d$ and $\boldsymbol{\chi}^{(2)}_q \in \big(\bar{H}^1_{p0}(Y)\big)^{d\times d}$ uniquely solve the respective equations

$$\tilde{\lambda}_{n_q}\rho\boldsymbol{\chi}_q^{(1)} + \nabla_{\boldsymbol{k}_s}\cdot\big(G(\nabla_{\boldsymbol{k}_s}\boldsymbol{\chi}_q^{(1)} + \tilde{\phi}_{n_q}\boldsymbol{I})\big) + G\nabla_{\boldsymbol{k}_s}\tilde{\phi}_{n_q} \;=\; \sum_s \frac{\rho}{\rho_s^{(0)}}\tilde{\phi}_{n_s}\boldsymbol{\theta}_{sq}^{(0)}, \tag{2.127}$$

$$\begin{aligned}\tilde{\lambda}_{n_q}\rho\boldsymbol{\chi}_q^{(2)} + \nabla_{\boldsymbol{k}_s}\cdot\big(G(\nabla_{\boldsymbol{k}_s}\boldsymbol{\chi}_q^{(2)} + \tilde{\phi}_{n_q}\ \{\boldsymbol{I}\otimes\boldsymbol{\chi}_q^{(1)}\}')\big)&\\ +\{G(\nabla_{\boldsymbol{k}_s}\boldsymbol{\chi}_q^{(1)} + \tilde{\phi}_{n_q}\boldsymbol{I})\} \;=\; \sum_s \Big(\frac{\rho}{\rho_s^{(0)}}\{\boldsymbol{\theta}_{sq}^{(0)}\otimes\boldsymbol{\chi}_s^{(1)}\} + \frac{\rho}{\rho_s^{(0)}}\tilde{\phi}_{n_s}\boldsymbol{\mu}_{sq}^{(0)}\Big),&\end{aligned} \tag{2.128}$$

$$-\tilde{\lambda}_{n_q}\rho\eta_q^{(0)} - \nabla_{\boldsymbol{k}_s}\cdot\big(G\nabla_{\boldsymbol{k}_s}\eta_q^{(0)}\big) \;=\; \tilde{f}_{\boldsymbol{k}} - \sum_s \frac{\rho}{\rho_s^{(0)}}\langle\tilde{f}_{\boldsymbol{k}}\rangle^{n_s}\tilde{\phi}_{n_s}, \tag{2.129}$$

with $G(\nabla_{\boldsymbol{k}_s}\boldsymbol{\chi}_q^{(1)} + \tilde{\phi}_{n_q}\boldsymbol{I})$, $G(\nabla_{\boldsymbol{k}_s}\boldsymbol{\chi}_q^{(2)} + \{\boldsymbol{I}\otimes\boldsymbol{\chi}_q^{(1)}\}')$ and $G\nabla_{\boldsymbol{k}_s}\eta_q^{(0)}$ each being subject to the flux boundary conditions (2.38). Note also that Remark 31 still applies in this case. Our goal is then to find the coupled effective equations satisfied by u_{0q}, u_{1q} and u_{2q}. To this end, we (i) insert (2.126) in (2.21); (ii) integrate $\langle(2.21)\rangle_\rho^{n_p}$ by parts using the boundary conditions (2.22), and (iii) expand the result in powers of ϵ as

$$O(\epsilon^{-1}): \qquad (\boldsymbol{A}^\gamma(\hat{\boldsymbol{k}}) + \breve{\sigma}\breve{\omega}^2\boldsymbol{D})\boldsymbol{u}_0 \;=\; \boldsymbol{0}, \tag{2.130}$$

$$O(1): \qquad -(\boldsymbol{B}^{(0)}(\hat{\boldsymbol{k}}) + \hat{\sigma}\hat{\omega}^2\boldsymbol{D})\boldsymbol{u}_0 - (\boldsymbol{A}^\gamma(\hat{\boldsymbol{k}}) + \breve{\sigma}\breve{\omega}^2\boldsymbol{D})\boldsymbol{u}_1 \;=\; \mathbf{f}_0, \tag{2.131}$$

$$O(\epsilon): \qquad -\boldsymbol{A}^{(1)}(\hat{\boldsymbol{k}})\boldsymbol{u}_0 - (\boldsymbol{B}^{(0)}(\hat{\boldsymbol{k}}) + \hat{\sigma}\hat{\omega}^2\boldsymbol{D})\boldsymbol{u}_1 - (\boldsymbol{A}^\gamma(\hat{\boldsymbol{k}}) + \breve{\sigma}\breve{\omega}^2\boldsymbol{D})\boldsymbol{u}_2 \;=\; \mathbf{f}_1, \tag{2.132}$$

where

$$\boldsymbol{A}^\gamma(\hat{\boldsymbol{k}}) \;=\; \boldsymbol{A}^{(0)}(\hat{\boldsymbol{k}}) + \boldsymbol{\Gamma}\boldsymbol{D}, \qquad \boldsymbol{\Gamma}_{pq} = \delta_{pq}\gamma_q \tag{2.133}$$

accounts for the eigenvalue separations in (2.125), while $\boldsymbol{A}^{(0)}$, $\boldsymbol{B}^{(0)}$, $\boldsymbol{A}^{(1)}$, $\boldsymbol{D}$, $\mathbf{f}_0$ and $\mathbf{f}_1$ are given by (2.83), (2.88), (2.112) and (2.113) as before.

Remark 13 *We observe a clear similarity between* (2.130), (2.131), (2.132) *and their repeated-eigenvalue predecessors* (2.83), (2.88) *and* (2.113) *respectively. In fact, the differences are in this case confined to the diagonal matrix* $\boldsymbol{\Gamma}\boldsymbol{D} = \boldsymbol{A}^\gamma - \boldsymbol{A}^{(0)}$ *that accounts for separations between the neighboring eigenvalues according to* (2.124)*. Further, since* $\boldsymbol{A}^{(0)}$ *is Hermitian, so is* $\boldsymbol{A}^\gamma$*.*

2.4.1 Eigenfunction basis

Let $\boldsymbol{P}$ denote the matrix of eigenvectors associated with the generalized eigenvalue problem

$$\boldsymbol{A}^\gamma(\hat{\boldsymbol{k}})\boldsymbol{v} \;=\; \tau\boldsymbol{D}\boldsymbol{v}.$$

In order to diagonalize $\boldsymbol{A}^\gamma$, we express $\boldsymbol{u}_0, \boldsymbol{u}_1, \boldsymbol{u}_2, \mathbf{f}_0$ and $\mathbf{f}_1$ in terms of $\boldsymbol{P}$ as

$$\boldsymbol{u}_0 = \boldsymbol{P}\boldsymbol{u}_0', \quad \boldsymbol{u}_1 = \boldsymbol{P}\boldsymbol{u}_1', \quad \boldsymbol{u}_2 = \boldsymbol{P}\boldsymbol{u}_2', \quad \mathbf{f}_0 = \boldsymbol{P}\mathbf{f}_0',, \quad \mathbf{f}_1 = \boldsymbol{P}\mathbf{f}_1' \tag{2.134}$$

and we premultiply (2.130)–(2.132) by $\overline{\boldsymbol{P}}^T$. For simplicity, we then drop the prime symbol from the "rotated" vectors $\boldsymbol{u}_0', \boldsymbol{u}_1', \boldsymbol{u}_2', \mathbf{f}_0'$ and $\mathbf{f}_1'$, and we keep the original notation of the transformed matrices in (2.130)–(2.132). In this setting, we have

$$\boldsymbol{A}^\gamma(\hat{\boldsymbol{k}}) \;=\; \mathrm{diag}(\tau_1, \tau_2, \ldots, \tau_Q), \tag{2.135}$$

noting for future reference that $\tau_q = 0$ ($q = \overline{1, N_0}$) when $\mathrm{rank}(\boldsymbol{A}^\gamma) = Q - N_0$.

2.4.2 Leading-order approximation

Thanks to the presence of the "penalty" term $\boldsymbol{\Gamma}\boldsymbol{D}$ in (2.133), $\boldsymbol{A}^\gamma$ is of at least partial rank when $\boldsymbol{A}^{(0)} = \mathbf{0}$. As a result, in the sequel we present the effective models for full- and partial-rank $\boldsymbol{A}^\gamma$ only.

Effective solution for full-rank $\boldsymbol{A}^\gamma$

When $\mathrm{rank}(\boldsymbol{A}^\gamma) = Q$, $\tilde{f}_{\boldsymbol{k}} \neq 0$, and $\omega^2 - \omega_n^2 = O(\epsilon)$ i.e. $|\hat{\sigma}| = 1$, we must have $\boldsymbol{u}_0 = \mathbf{0}$ due to (2.130). As a result, (2.131) yields the leading-order effective equation

$$-(\boldsymbol{A}^\gamma + \check{\sigma}\check{\omega}^2\boldsymbol{D})\boldsymbol{u}_1 \;=\; \mathbf{f}_0. \tag{2.136}$$

When $\tilde{f}_{\boldsymbol{k}} = 0$, eigenvalues of the GEP stemming from (2.130) (or equivalently (2.136)) define the leading-order asymptotic approximation of the dispersion relationships in direction $\hat{\boldsymbol{k}}/\|\hat{\boldsymbol{k}}\|$ as

$$\omega_{n_q}^2 \;=\; \omega_{n_0}^2 - \epsilon\frac{\tau_q}{\rho_q^{(0)}}, \tag{2.137}$$

where τ_q denotes the qth eigenvalue of $\boldsymbol{A}^\gamma(\hat{\boldsymbol{k}})$.

Remark 14 *When $\boldsymbol{A}^\gamma$ is of full rank,* (2.136) *and* (2.137) *provide a general framework to handle the clusters of nearby dispersion branches, regardless of the fact whether they intersect or "almost touch" for example at $\boldsymbol{k} = \boldsymbol{k}_s$.*

Effective solution for partial-rank $\boldsymbol{A}^\gamma$

When $\mathrm{rank}(\boldsymbol{A}^\gamma) = Q - N_0$ for some $N_0 > 0$ and $\tilde{f}_{\boldsymbol{k}} \neq 0$, we first consider the situation where $\omega^2 - \lambda_{n_0} = O(\epsilon)$ i.e. $|\check{\sigma}| = 1$. In this case the leading-order effective equation

is again given by (2.136), while the last $Q - N_0$ dispersion branches are approximated by (2.137) for $q \in \overline{N_0+1, Q}$.

On the other hand, when $\omega^2 - \omega_{n_0}^2 = O(\epsilon^2)$ i.e. $|\hat{\sigma}| = 1$, the leading-order effective model $\boldsymbol{u}_0$ is given by

$$-\sum_{q=1}^{N_0}(B_{pq}^{(0)}(\hat{\boldsymbol{k}}) + \hat{\sigma}\hat{\omega}^2 D_{pq})u_{0q} \;=\; \mathrm{f}_{0p}, \quad p \in \overline{1, N_0}, \tag{2.138}$$

$$u_{0p} \;=\; 0, \quad p \in \overline{N_0 + 1, Q}. \tag{2.139}$$

When $\tilde{f}_{\boldsymbol{k}} = 0$, the leading-order approximation of the first N_0 dispersion branches is obtained by solving the GEP affiliated with (2.138).

2.4.3 First-order correctors

Effective solution for full-rank $\boldsymbol{A}^\gamma$

When $\boldsymbol{A}^\gamma$ is of full rank, $\tilde{f}_{\boldsymbol{k}} \neq 0$, and $\omega^2 - \omega_n^2 = O(\epsilon)$ i.e. $|\check{\sigma}| = 1$, one can show that the first-order corrector $\boldsymbol{u}_2$ solves

$$-\boldsymbol{B}^{(0)}(\hat{\boldsymbol{k}})\boldsymbol{u}_1 - (\boldsymbol{A}^\gamma(\hat{\boldsymbol{k}}) + \check{\sigma}\check{\omega}^2\boldsymbol{D})\boldsymbol{u}_2 \;=\; \mathbf{f}_1, \tag{2.140}$$

with $\boldsymbol{u}_1$ being given by (2.136). Thanks to (2.115), the weighted sum (2.136)$+\epsilon$(2.140), namely

$$-\epsilon\, \boldsymbol{B}^{(0)}(\hat{\boldsymbol{k}})\boldsymbol{u}_1 - \epsilon(\boldsymbol{A}^\gamma(\hat{\boldsymbol{k}}) + \check{\sigma}\check{\omega}^2\boldsymbol{D})\boldsymbol{u}_2 - (\boldsymbol{A}^\gamma(\hat{\boldsymbol{k}}) + \check{\sigma}\check{\omega}^2\boldsymbol{D})\boldsymbol{u}_1 \;=\; \mathbf{f}_0 + \epsilon\mathbf{f}_1, \tag{2.141}$$

yields the first-order effective model

$$-(\boldsymbol{B}^{(0)}(\epsilon\hat{\boldsymbol{k}}) + \boldsymbol{A}^\gamma(\epsilon\hat{\boldsymbol{k}}) + \epsilon\check{\sigma}\check{\omega}^2\boldsymbol{D})\langle\tilde{\boldsymbol{u}}\rangle_\rho \;\overset{\epsilon^2}{=}\; \mathbf{f}_0 + \epsilon\mathbf{f}_1. \tag{2.142}$$

Effective solution for partial rank $\boldsymbol{A}^\gamma$

When $\mathrm{rank}(\boldsymbol{A}^\gamma) < Q$, $\tilde{f}_{\boldsymbol{k}} \neq 0$ and $\omega^2 - \lambda_{n_0} = O(\epsilon)$, the first-order corrector $\boldsymbol{u}_2$ is given by (2.140). In contrast, when $\omega^2 - \lambda_{n_0} = O(\epsilon^2)$, the first-order corrector is given by $\boldsymbol{u}_1$ whose components can be shown to satisfy

$$-\sum_{q=1}^{N}(B_{pq}^{(0)}(\hat{\boldsymbol{k}}) + \hat{\sigma}\hat{\omega}^2 D_{pq})u_{1q} \;=\; \mathrm{f}_{1p} + \textstyle\sum_{q=1}^{N_0} A_{pq}^{(1)}(\hat{\boldsymbol{k}})u_{0q}, \quad p \in \overline{1, N_0}, \tag{2.143}$$

$$-A_{pp}^\gamma(\hat{\boldsymbol{k}})u_{1p} \;=\; \mathrm{f}_{0p} + \textstyle\sum_{q=1}^{N_0} B_{pq}^{(0)}(\hat{\boldsymbol{k}})u_{0q}, \quad p \in \overline{N_0+1, Q}, \tag{2.144}$$

with u_{0q} ($q = \overline{N_0+1, Q}$) being subject to (3.104). For this configuration, we obtain the first-order model as

$$\langle \tilde{\boldsymbol{u}} \rangle_\rho \overset{\epsilon^0}{=} \epsilon^{-2}\boldsymbol{u}_0 + \epsilon^{-1}\boldsymbol{u}_1,$$

with the scaled summands being directly computable from (2.138)–(3.105) and (2.143)–(2.144) on replacing $\hat{\boldsymbol{k}}$ and $\hat{\sigma}\hat{\omega}$ respectively by $\epsilon\hat{\boldsymbol{k}}$ and $\epsilon^2\hat{\sigma}\hat{\omega}$.

2.5 Discussion

In this section, we share new insights stemming from the general analysis, and we discuss several special cases in support of the numerical simulations (Section 2.6).

Remark 15 *A common thread of our developments is that we approximate the Bloch wave in terms of its projection to the nearest Q branches, $Q \geqslant 1$. In this vein, term $\tilde{u}(\boldsymbol{x})$ on the left-hand side of ansatz* (2.32) *and its descendants such as* (2.126) *should be interpreted in the sense of restriction of* (2.28) *to the nearest Q dispersion branches, namely*

$$-\sum_{n=1}^{\infty} \frac{(\tilde{f}_{\boldsymbol{k}}, \tilde{\phi}_n)\ \tilde{\phi}_n(\boldsymbol{x})}{(\rho\tilde{\phi}_n, \tilde{\phi}_n)(\omega^2 - \tilde{\lambda}_n)} \quad \Longrightarrow \quad -\sum_{q=1}^{Q} \frac{(\tilde{f}_{\boldsymbol{k}}, \tilde{\phi}_{n_q})\ \tilde{\phi}_{n_q}(\boldsymbol{x})}{(\rho\tilde{\phi}_{n_q}, \tilde{\phi}_{n_q})(\omega^2 - \tilde{\lambda}_{n_q})}. \tag{2.145}$$

This leaves an open question regarding the contribution of "remote" branches ($n \neq n_q, q = \overline{1, Q}$) that is beyond the scope of this study, see for instance the recent discussion in [34].

2.5.1 Energy considerations

On the basis of the results in Section 2.4 which covers the instances of simple and repeated eigenvalues as degenerate cases, we find from (2.126) that the instantaneous

power density $(\tilde{f}_{\boldsymbol{k}}, i\omega\tilde{u}) = -i\omega(\tilde{f}_{\boldsymbol{k}}, \tilde{u})$ generated by the source term $\tilde{f}_{\boldsymbol{k}}$ can be approximated as

$$\begin{aligned}
\text{Leading order:}\quad -i\omega(\tilde{f}_{\boldsymbol{k}}, \tilde{u}) &\overset{\epsilon^{-1}}{=} -i\omega \sum_q \langle \tilde{f}_{\boldsymbol{k}} \rangle^{n_q} \overline{\langle \tilde{u} \rangle_\rho^{n_q}}, \\
\text{First order:}\quad -i\omega(\tilde{f}_{\boldsymbol{k}}, \tilde{u}) &\overset{1}{=} -i\omega \sum_q \big(\langle \tilde{f}_{\boldsymbol{k}} \rangle^{n_q} - (\tilde{f}_{\boldsymbol{k}}, \boldsymbol{\chi}_q^{(1)}) \cdot (i\epsilon\hat{\boldsymbol{k}}) \big) \overline{\langle \tilde{u} \rangle_\rho^{n_q}}, \\
\text{Second order:}\quad -i\omega(\tilde{f}_{\boldsymbol{k}}, \tilde{u}) &\overset{\epsilon}{=} -i\omega \sum_q \big(\langle \tilde{f}_{\boldsymbol{k}} \rangle^{n_q} - (\tilde{f}_{\boldsymbol{k}}, \boldsymbol{\chi}_q^{(1)}) \cdot (i\epsilon\hat{\boldsymbol{k}}) \big) \overline{\langle \tilde{u} \rangle_\rho^{n_q}} \\
&\quad - i\omega \sum_q \big((\tilde{f}_{\boldsymbol{k}}, \boldsymbol{\chi}_q^{(2)}) : (i\epsilon\hat{\boldsymbol{k}})^2 \big) \overline{\langle \tilde{u} \rangle_\rho^{n_q}} - i\omega \sum_{q=1}^{\bar{Q}} (\tilde{f}_{\boldsymbol{k}}, \eta_q^{(0)}).
\end{aligned}$$

The above result in particular demonstrates that the instantaneous power density and therefore the work, averaged in space over Y, equal – up to the first order – that exerted by the effective source term on the averaged displacement. This result is in line with the well known Hill-Mandel condition [24], requiring that the volume average of the increment of work performed on the representative volume element be equal to the increment of local work performed by the macroscopic i.e. averaged quantities.

2.5.2 Asymptotic solution in physical space near the edge of a band gap

With reference to the class (2.16) of source distributions, one immediate application of the foregoing analysis is the case where: (i) $\boldsymbol{k}_s = \frac{1}{2}(\sum_j n_j \boldsymbol{e}^j)$, $n_j \in \{-1, 0, 1\}$; (ii) the driving frequency is within a band gap near simple eigenfrequency $\omega_n(\boldsymbol{k}_s)$, and (iii) the source function $\tilde{f}_{\boldsymbol{k}}$ is given by

$$\tilde{f}_{\boldsymbol{k}}(\boldsymbol{x}) \,=\, F(\boldsymbol{k})\phi(\boldsymbol{x}), \qquad \phi \in L_p^2(Y), \quad \operatorname{supp}(F) = \mathcal{C} \subset \mathcal{B}. \tag{2.146}$$

On recalling BWE (2.14) and ansatz (2.32), we conveniently introduce the pth-order asymptotic solution in the physical space as

$$\begin{aligned}
u^{[\mathrm{p}]}(\boldsymbol{x}) \;&:=\; \sum_{m=0}^{p} \epsilon^{m-2} \hat{u}_m(\boldsymbol{x}), \quad \boldsymbol{x} \in S, \\
\text{where}\quad \hat{u}_m(\boldsymbol{x}) \;&:=\; |\mathcal{C}|^{-1} \int_{\mathcal{C}} \tilde{u}_m(\boldsymbol{x})\, e^{i(\boldsymbol{k}_s + \epsilon\hat{\boldsymbol{k}})\cdot\boldsymbol{x}}\, \mathrm{d}(\epsilon\hat{\boldsymbol{k}}).
\end{aligned} \tag{2.147}$$

From (2.49), (2.52), (2.54), (2.60), (2.63), (2.66), Claim 3, Claim 7, Claim 8 and Remark 6, we specifically find that

$$\tilde{u}_0(\boldsymbol{x}) \;=\; -\epsilon^2\,\frac{\tilde{\phi}_n(\boldsymbol{x})\,\langle\tilde{f}_{\boldsymbol{k}}\rangle}{\rho^{(0)}(\omega^2-\omega_n^2)+\boldsymbol{\mu}^{(0)}:(i\epsilon\hat{\boldsymbol{k}})^2}, \tag{2.148}$$

$$\tilde{u}_1(\boldsymbol{x}) \;=\; \epsilon\,\frac{\big[\tilde{\phi}_n(\boldsymbol{x})(\tilde{f}_{\boldsymbol{k}},\boldsymbol{\chi}^{(1)})-\langle\tilde{f}_{\boldsymbol{k}}\rangle\;\boldsymbol{\chi}^{(1)}(\boldsymbol{x})\big]\cdot(i\epsilon\hat{\boldsymbol{k}})}{\rho^{(0)}(\omega^2-\omega_n^2)+\boldsymbol{\mu}^{(0)}:(i\epsilon\hat{\boldsymbol{k}})^2}, \tag{2.149}$$

$$\begin{aligned}\tilde{u}_2(\boldsymbol{x}) \;=\; &-\frac{\tilde{\phi}_n(\boldsymbol{x})\big((\tilde{f}_{\boldsymbol{k}},\boldsymbol{\chi}^{(2)})+\frac{\langle\tilde{f}_{\boldsymbol{k}}\rangle}{\rho^{(0)}}\{(\rho\boldsymbol{\chi}^{(1)}\otimes\overline{\boldsymbol{\chi}^{(1)}},1)\}\big):(i\epsilon\hat{\boldsymbol{k}})^2}{\rho^{(0)}(\omega^2-\omega_n^2)+\boldsymbol{\mu}^{(0)}:(i\epsilon\hat{\boldsymbol{k}})^2}\\ &+\frac{\big(\{(\tilde{f}_{\boldsymbol{k}},\boldsymbol{\chi}^{(1)})\otimes\boldsymbol{\chi}^{(1)}(\boldsymbol{x})\}+\langle\tilde{f}_{\boldsymbol{k}}\rangle\boldsymbol{\chi}^{(2)}(\boldsymbol{x})\big):(i\epsilon\hat{\boldsymbol{k}})^2}{\rho^{(0)}(\omega^2-\omega_n^2)+\boldsymbol{\mu}^{(0)}:(i\epsilon\hat{\boldsymbol{k}})^2}\\ &-\frac{\epsilon^{-2}\tilde{u}_0(\boldsymbol{x})\;\boldsymbol{\mu}^{(2)}:(i\epsilon\hat{\boldsymbol{k}})^4}{\rho^{(0)}(\omega^2-\omega_n^2)+\boldsymbol{\mu}^{(0)}:(i\epsilon\hat{\boldsymbol{k}})^2}\;+\;\zeta^{(0)}(\boldsymbol{x})\,F(\boldsymbol{k}_s+\epsilon\hat{\boldsymbol{k}}).\end{aligned} \tag{2.150}$$

In terms of the *effective solution*, by (3.50) we can similarly introduce the pth-order mean motion in the physical space as

$$\langle u\rangle_\rho^{[\mathrm{p}]}(\boldsymbol{x}) \;:=\; \sum_{m=0}^{p}\epsilon^{m-2}|\mathcal{C}|^{-1}\int_{\mathcal{C}}u_m(\epsilon\hat{\boldsymbol{k}})\,e^{i(\boldsymbol{k}_s+\epsilon\hat{\boldsymbol{k}})\cdot\boldsymbol{x}}\,\mathrm{d}(\epsilon\hat{\boldsymbol{k}}),\quad \boldsymbol{x}\in\mathbb{R}^d, \tag{2.151}$$

via superposition of the averaged Bloch-wave solutions, $u_m(\epsilon\hat{\boldsymbol{k}})=\langle\tilde{u}_m\rangle_\rho$. From (2.148)–(2.150), we clearly have

$$u_0(\epsilon\hat{\boldsymbol{k}}) \;=\; -\epsilon^2\,\frac{\langle\tilde{f}_{\boldsymbol{k}}\rangle}{\rho^{(0)}(\omega^2-\omega_n^2)+\boldsymbol{\mu}^{(0)}:(i\epsilon\hat{\boldsymbol{k}})^2}, \tag{2.152}$$

$$u_1(\epsilon\hat{\boldsymbol{k}}) \;=\; \epsilon\,\frac{(\tilde{f}_{\boldsymbol{k}},\boldsymbol{\chi}^{(1)})\cdot(i\epsilon\hat{\boldsymbol{k}})}{\rho^{(0)}(\omega^2-\omega_n^2)+\boldsymbol{\mu}^{(0)}:(i\epsilon\hat{\boldsymbol{k}})^2}, \tag{2.153}$$

$$u_2(\epsilon\hat{\boldsymbol{k}}) \;=\; -\frac{\big((\tilde{f}_{\boldsymbol{k}},\boldsymbol{\chi}^{(2)})+\frac{\langle\tilde{f}_{\boldsymbol{k}}\rangle}{\rho^{(0)}}\{(\rho\boldsymbol{\chi}^{(1)}\otimes\overline{\boldsymbol{\chi}^{(1)}},1)\}\big):(i\epsilon\hat{\boldsymbol{k}})^2+\epsilon^{-2}u_0(\epsilon\hat{\boldsymbol{k}})\;\boldsymbol{\mu}^{(2)}:(i\epsilon\hat{\boldsymbol{k}})^4}{\rho^{(0)}(\omega^2-\omega_n^2)+\boldsymbol{\mu}^{(0)}:(i\epsilon\hat{\boldsymbol{k}})^2}. \tag{2.154}$$

In Section 2.6, we shall make use of the above results toward approximating the "full" and mean wave motion near the edge of a band gap.

2.5.3 Dirac behavior in $\mathbb{R}^2$ for $Q = 2$

Consider a two-dimensional periodic medium, $S \subset \mathbb{R}^2$, whose spectral neighborhood (2.30) features two nearby eigenfrequencies $\omega_{n_1} = \omega_{n_1}(\boldsymbol{k}_s)$ and $\omega_{n_2} = \omega_{n_2}(\boldsymbol{k}_s)$ ($Q = 2$). In this case, matrix $\boldsymbol{A}^\gamma$ reads

$$\boldsymbol{A}^\gamma = \begin{pmatrix} \boldsymbol{\theta}_{11}^{(0)} \cdot i\hat{\boldsymbol{k}} & \boldsymbol{\theta}_{12}^{(0)} \cdot i\hat{\boldsymbol{k}} \\ -\overline{\boldsymbol{\theta}_{12}^{(0)}} \cdot i\hat{\boldsymbol{k}} & \boldsymbol{\theta}_{22}^{(0)} \cdot i\hat{\boldsymbol{k}} + \gamma\rho_2^{(0)} \end{pmatrix}, \qquad \gamma = \epsilon^{-1}(\omega_{n1}^2 - \omega_{n2}^2). \tag{2.155}$$

By way of (2.130), the two dispersion relationships are accordingly given by

$$\begin{aligned} \omega_{n_{1/2}}^2(\boldsymbol{k}) \;\; &= \;\; \omega_{n_1}^2 - \frac{\epsilon}{2}\Big(\gamma + \frac{\boldsymbol{\theta}_{11}^{(0)} \cdot i\hat{\boldsymbol{k}}}{\rho_1^{(0)}} + \frac{\boldsymbol{\theta}_{22}^{(0)} \cdot i\hat{\boldsymbol{k}}}{\rho_2^{(0)}}\Big) \\ &\quad \mp \frac{\epsilon}{2}\sqrt{\Big(\gamma - \frac{\boldsymbol{\theta}_{11}^{(0)} \cdot i\hat{\boldsymbol{k}}}{\rho_1^{(0)}} + \frac{\boldsymbol{\theta}_{22}^{(0)} \cdot i\hat{\boldsymbol{k}}}{\rho_2^{(0)}}\Big)^2 + \frac{4\{\boldsymbol{\theta}_{12}^{(0)} \otimes \overline{\boldsymbol{\theta}_{12}^{(0)}}\} : (\hat{\boldsymbol{k}})^2}{\rho_1^{(0)}\rho_2^{(0)}}}, \end{aligned} \tag{2.156}$$

where the matrix $\{\boldsymbol{\theta}_{12}^{(0)} \otimes \overline{\boldsymbol{\theta}_{12}^{(0)}}\} \in \mathbb{R}^{2\times 2}$ is in general positive semi-definite, and specifically positive definite when

$$\boldsymbol{\theta}_{12}^{(0)} \cdot \boldsymbol{i}_1 \neq 0, \quad \boldsymbol{\theta}_{12}^{(0)} \cdot \boldsymbol{i}_2 \neq 0, \quad \text{and} \quad \arg(\boldsymbol{\theta}_{12}^{(0)} \cdot \boldsymbol{i}_1) - \arg(\boldsymbol{\theta}_{12}^{(0)} \cdot \boldsymbol{i}_2) \neq n\pi, \quad n \in \mathbb{Z}. \tag{2.157}$$

Equations (2.156) describe "almost touching" (resp. crossing) branches when $\gamma \neq 0$ (resp. $\gamma = 0$) featuring the middle plane

$$(\mathcal{P}): \quad \omega_{\mathcal{P}}^2(\boldsymbol{k}) \;=\; \omega_{n_1}^2 - \frac{\epsilon}{2}\Big(\gamma + \frac{\boldsymbol{\theta}_{11}^{(0)} \cdot i\hat{\boldsymbol{k}}}{\rho_1^{(0)}} + \frac{\boldsymbol{\theta}_{22}^{(0)} \cdot i\hat{\boldsymbol{k}}}{\rho_2^{(0)}}\Big). \tag{2.158}$$

When $(\mathcal{P})$ is horizontal, we further have

$$\frac{1}{\rho_1^{(0)}}\boldsymbol{\theta}_{11}^{(0)} + \frac{1}{\rho_2^{(0)}}\boldsymbol{\theta}_{22}^{(0)} \;=\; \boldsymbol{0}, \tag{2.159}$$

which holds true for any ρ-orthogonal eigenfunction basis, by the conservation of the trace of $\boldsymbol{A}^\gamma$. In this case, dispersion relationship (2.156) simplifies to

$$\omega_{n_{1/2}}^2(\boldsymbol{k}) = \omega_{n_1}^2 - \frac{\epsilon}{2}\Big(\gamma \pm \sqrt{\Big(\gamma - \frac{2\boldsymbol{\theta}_{11}^{(0)} \cdot i\hat{\boldsymbol{k}}}{\rho_1^{(0)}}\Big)^2 + \frac{4\{\boldsymbol{\theta}_{12}^{(0)} \otimes \overline{\boldsymbol{\theta}_{12}^{(0)}}\} : (\hat{\boldsymbol{k}})^2}{\rho_1^{(0)}\rho_2^{(0)}}}\Big). \tag{2.160}$$

Dirac cones

When $\gamma = 0$ i.e. $\omega_{n_1} = \omega_{n_2}$, from (2.160) we find that

$$\omega^2_{n_{1/2}}(\boldsymbol{k}) = \omega^2_{n_1} \mp \sqrt{\left(\frac{\boldsymbol{\theta}^{(0)}_{11} \cdot (i\epsilon\hat{\boldsymbol{k}})}{\rho^{(0)}_1}\right)^2 + \frac{\{\boldsymbol{\theta}^{(0)}_{12} \otimes \overline{\boldsymbol{\theta}^{(0)}_{12}}\} : (\epsilon\hat{\boldsymbol{k}})^2}{\rho^{(0)}_1 \rho^{(0)}_2}}. \tag{2.161}$$

In such instances, the eigenfunction basis can be conveniently recombined so that $\boldsymbol{A}^\gamma = \boldsymbol{A}^{(0)}$ is diagonal in a given direction $\hat{\boldsymbol{k}}_0/\|\hat{\boldsymbol{k}}_0\|$. Using this specific eigenfunction basis, we find that $\boldsymbol{\theta}^{(0)}_{pq}$ are imaginary-valued up to a complex multiplier, since $\boldsymbol{\theta}^{(0)}_{11}, \boldsymbol{\theta}^{(0)}_{22} \in i\mathbb{R}^2$ by (2.82) and $\boldsymbol{\theta}^{(0)}_{12} \cdot i\hat{\boldsymbol{k}}_0 = \boldsymbol{0}$. As a result, the dispersion relationships (2.161) are characterized by (i) elliptical isocontours when the vectors $(\rho^{(0)}_1)^{-1}\boldsymbol{\theta}^{(0)}_{11}$ and $(\rho^{(0)}_1\rho^{(0)}_2)^{-1/2}\boldsymbol{\theta}^{(0)}_{12}$ are linearly independent, and (ii) circular isocontours when they are orthogonal with equal norms. In the latter case, (2.161) reduces to

$$\omega^2_{n_{1/2}}(\boldsymbol{k}) = \omega^2_{n_1} \mp \frac{\|\boldsymbol{\theta}^{(0)}_{12}\|}{(\rho^{(0)}_1\rho^{(0)}_2)^{1/2}}\|\epsilon\hat{\boldsymbol{k}}\|, \tag{2.162}$$

which describe axisymmetric Dirac cones as depicted in Fig. 2.3(a).

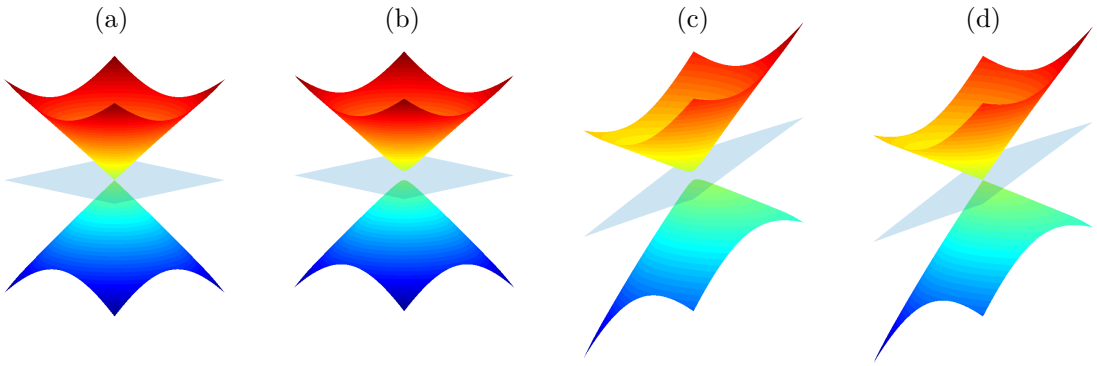

Figure 2.3: Examples of: (a) Dirac cones, (c) Blunted Dirac cones, (c) tilted-blunted Dirac cones, and (d) tilted Dirac cones. All panels include the "middle plane" ($\mathcal{P}$) according to (2.158).

Blunted Dirac cones

When $\gamma \neq 0$ in (2.160), assuming $\mathrm{d}\omega_{n_{1/2}}/\mathrm{d}\boldsymbol{k}|_{\boldsymbol{k}=\boldsymbol{k}_s} = \boldsymbol{0}$ implies that $\boldsymbol{\theta}_{11}^{(0)} = \boldsymbol{0}$ and thus $\boldsymbol{\theta}_{22}^{(0)} = \boldsymbol{0}$ by (2.159). This reduces (2.160) to

$$\omega_{n_{1/2}}^2(\boldsymbol{k}) = \omega_{n_1}^2 - \frac{\epsilon}{2}\Big(\gamma \pm \sqrt{\gamma^2 + \frac{4\{\boldsymbol{\theta}_{12}^{(0)} \otimes \overline{\boldsymbol{\theta}_{12}^{(0)}}\} : (\hat{\boldsymbol{k}})^2}{\rho_1^{(0)}\rho_2^{(0)}}}\Big). \tag{2.163}$$

Further, if the matrix $\{\boldsymbol{\theta}_{12}^{(0)} \otimes \overline{\boldsymbol{\theta}_{12}^{(0)}}\}$ is positive-definite due to (2.157), the dispersion relationships in (2.163) are characterized by elliptic isocontours and thus exhibit cone-like geometry. As a special case, the isotropy of $\{\boldsymbol{\theta}_{12}^{(0)} \otimes \overline{\boldsymbol{\theta}_{12}^{(0)}}\}$ is attained when $\boldsymbol{\theta}_{12}^{(0)} \parallel \boldsymbol{i}_1 \pm i\boldsymbol{i}_2$, in which situation (2.163) becomes

$$\omega_{n_{1/2}}^2(\boldsymbol{k}) = \omega_{n_1}^2 - \frac{\epsilon}{2}\Big(\gamma \pm \sqrt{\gamma^2 + \frac{4\|\boldsymbol{\theta}_{12}^{(0)}\|^2}{\rho_1^{(0)}\rho_2^{(0)}}\|\hat{\boldsymbol{k}}\|^2}\Big). \tag{2.164}$$

Geometrically, (3.119) describe an axisymmetric variant of the *blunted* Dirac cones shown in Fig. 2.3(b).

Remark 16 *At "apexes" of the first Brillouin zone $\boldsymbol{k}_s = \frac{1}{2}(\sum_j n_j \boldsymbol{e}^j)$, $n_j \in \{-1, 0, 1\}$, we have $\boldsymbol{\theta}_{11}^{(0)} = \boldsymbol{0}$ and $\boldsymbol{\theta}_{12}^{(0)} \in \mathbb{R}^d$ by Claim 10. As a result, we cannot have axisymmetric Dirac cones* (2.162) *nor axisymmetric blunted Dirac cones* (3.119) *there. This claim also applies to situations without axial symmetry.*

Tilted- and tilted-blunted Dirac cones

Let us next forgo condition (2.159) which ensures that $(\mathcal{P})$ is horizontal. When $\gamma \neq 0$, (2.156) describes a pair of *tilted-blunted* Dirac cones only if: (i) the first term under the square-root sign reduces to γ^2, namely

$$\frac{1}{\rho_1^{(0)}}\boldsymbol{\theta}_{11}^{(0)} = \frac{1}{\rho_2^{(0)}}\boldsymbol{\theta}_{22}^{(0)} \neq \boldsymbol{0}, \tag{2.165}$$

and (ii) $\{\boldsymbol{\theta}_{12}^{(0)} \otimes \overline{\boldsymbol{\theta}_{12}^{(0)}}\}$ is positive-definite according to (2.157). If further $\boldsymbol{\theta}_{12}^{(0)} \parallel \boldsymbol{i}_1 \pm i\boldsymbol{i}_2$, the two cones become "symmetric" in that $\omega_{1/2}^2(\boldsymbol{k}) - \omega_{\mathcal{P}}^2(\boldsymbol{k})$ is axisymmetric in terms of $\hat{\boldsymbol{k}}$ as depicted in Fig. 2.3(c).

When $\gamma = 0$, and (2.159) is violated, on the other hand, (2.156) describe *tilted* Dirac cones (see Fig. 2.3(d)) provided that the vectors $(\rho_1^{(0)})^{-1}\boldsymbol{\theta}_{11}^{(0)} - (\rho_2^{(0)})^{-1}\boldsymbol{\theta}_{22}^{(0)}$ and $(\rho_1^{(0)}\rho_2^{(0)})^{-1/2}\boldsymbol{\theta}_{12}^{(0)}$ are linearly independent. In this case, the "cone symmetry" is relaxed and applies as long as the two vectors are mutually orthogonal with the same norm.

2.5.4 Dirac behavior in $\mathbb{R}^2$ for $Q = 3$

Consider a cluster of three eigenfrequencies, $\omega_{n_1} = \omega_{n_2}$ and ω_{n_3}, at $\boldsymbol{k}_s = \frac{1}{2}(\sum_j n_j \boldsymbol{e}^j)$, $n_j \in \{-1, 0, 1\}$. Thanks to Claim 10, we find that

$$\boldsymbol{A}^\gamma = \begin{pmatrix} 0 & \boldsymbol{\theta}_{12}^{(0)} \cdot i\hat{\boldsymbol{k}} & \boldsymbol{\theta}_{13}^{(0)} \cdot i\hat{\boldsymbol{k}} \\ -\boldsymbol{\theta}_{12}^{(0)} \cdot i\hat{\boldsymbol{k}} & 0 & \boldsymbol{\theta}_{23}^{(0)} \cdot i\hat{\boldsymbol{k}} \\ -\boldsymbol{\theta}_{13}^{(0)} \cdot i\hat{\boldsymbol{k}} & -\boldsymbol{\theta}_{23}^{(0)} \cdot i\hat{\boldsymbol{k}} & \gamma\rho_3^{(0)} \end{pmatrix}, \qquad \gamma = \epsilon^{-1}(\omega_{n_1}^2 - \omega_{n_3}^2), \quad \boldsymbol{\theta}_{pq}^{(0)} \in \mathbb{R}^2. \tag{2.166}$$

When $\gamma \neq 0$ and $\boldsymbol{A}^\gamma$ has partial rank in all directions $\hat{\boldsymbol{k}}/\|\hat{\boldsymbol{k}}\|$, condition $\det \boldsymbol{A}^\gamma = 0$, implies that $\boldsymbol{\theta}_{12}^{(0)} = \boldsymbol{0}$. In this case, we have $\omega_{n1}^2(\hat{\boldsymbol{k}}) = \omega_{n1}^2$ (a horizontal plane), and

$$\omega_{n_{2/3}}^2(\boldsymbol{k}) \;=\; \omega_{n_1}^2 - \frac{\epsilon}{2}\Big(\gamma \pm \sqrt{\gamma^2 + \frac{4(\boldsymbol{\theta}_{13}^{(0)})^2 : (\hat{\boldsymbol{k}})^2}{\rho_1^{(0)}\rho_3^{(0)}} + \frac{4(\boldsymbol{\theta}_{23}^{(0)})^2 : (\hat{\boldsymbol{k}})^2}{\rho_2^{(0)}\rho_3^{(0)}}}\Big), \tag{2.167}$$

which describe a pair of Dirac cones (with elliptic isocontours) as long as the vectors $(\rho_1^{(0)}\rho_3^{(0)})^{-\frac{1}{2}}\boldsymbol{\theta}_{13}^{(0)}$ and $(\rho_2^{(0)}\rho_3^{(0)})^{-\frac{1}{2}}\boldsymbol{\theta}_{23}^{(0)}$ are linearly independent. As before, the axial symmetry of (2.167) is attained when the two vectors are orthogonal and have equal norms.

Assuming $\gamma = 0$, on the other hand, $\boldsymbol{A}^\gamma$ becomes anti-symmetric and thus necessarily rank deficient. In this case, the counterpart of (2.167) reads

$$\omega_{n_{2/3}}^2(\boldsymbol{k}) = \omega_{n_1}^2 \mp \epsilon \sqrt{\frac{(\boldsymbol{\theta}_{12}^{(0)})^2 : (\hat{\boldsymbol{k}})^2}{\rho_1^{(0)}\rho_2^{(0)}} + \frac{(\boldsymbol{\theta}_{13}^{(0)})^2 : (\hat{\boldsymbol{k}})^2}{\rho_1^{(0)}\rho_3^{(0)}} + \frac{(\boldsymbol{\theta}_{23}^{(0)})^2 : (\hat{\boldsymbol{k}})^2}{\rho_2^{(0)}\rho_3^{(0)}}}, \tag{2.168}$$

which describe a pair of Dirac cones provided that the sum inside the square root is axially-symmetric in terms of $\hat{\boldsymbol{k}}$. We illustrate this case by letting $\boldsymbol{\theta}_{12}^{(0)} = \boldsymbol{0}$ and assuming that $(\rho_1^{(0)}\rho_3^{(0)})^{-\frac{1}{2}}\boldsymbol{\theta}_{13}^{(0)}$ and $(\rho_2^{(0)}\rho_3^{(0)})^{-\frac{1}{2}}\boldsymbol{\theta}_{23}^{(0)}$ are orthogonal with equal norms. In such instance, (2.168) reduces to

$$\omega_{n_{2/3}}^2(\boldsymbol{k}) = \omega_{n_1}^2 \mp \epsilon \frac{\|\boldsymbol{\theta}_{13}^{(0)}\|}{(\rho_1^{(0)}\rho_3^{(0)})^{1/2}}\|\hat{\boldsymbol{k}}\|, \tag{2.169}$$

which yield the respective group velocities as

$$\boldsymbol{c}_{g_{2/3}}(\boldsymbol{k}) = \mp \frac{\|\boldsymbol{\theta}_{13}^{(0)}\|}{2\omega_{n_1}(\rho_1^{(0)}\rho_3^{(0)})^{1/2}} \frac{\hat{\boldsymbol{k}}}{\|\hat{\boldsymbol{k}}\|}. \tag{2.170}$$

Remark 17 *Equations* (2.169) *and* (2.170) *describe the behavior of the so-called Zero Index Metamaterials (ZIM) [9, 27, 26] where Dirac-like dispersion relationship occurs*

(for some $\omega_{n_1}=\omega_{n_2}=\omega_{n_3}$) at the origin of the Brillouin zone $\boldsymbol{k}_s=\boldsymbol{0}$. In this neighborhood, the phase velocity of branches n_2 and n_3 approaches infinity, while the affiliated group velocities are non-trivial – and in fact constant in any given direction $\hat{\boldsymbol{k}}/\|\hat{\boldsymbol{k}}\|$. This allows for the propagation of energy with near-zero phase delay across finite distances which has applications to e.g. cloaking, wave tunneling, and directive emission [9].

2.5.5 Dirac behavior in $\mathbb{R}^3$ for $Q = 2$

Consider a periodic medium $S \subset \mathbb{R}^3$ that presents two nearby (or repeated) eigenfrequencies, ω_{n_1} and ω_{n_2}. The two dispersion relationships are in this case also given by (2.156), where the matrix $\{\boldsymbol{\theta}_{12}^{(0)}\otimes\overline{\boldsymbol{\theta}_{12}^{(0)}}\} \in \mathbb{R}^{3\times 3}$ is positive semi-definite and necessarily rank deficient. When $\gamma \neq 0$ and $\mathrm{d}\omega_{n_{1/2}}/\mathrm{d}\boldsymbol{k}|_{\boldsymbol{k}=\boldsymbol{k}_s} = \boldsymbol{0}$, we find that $\boldsymbol{\theta}_{11}^{(0)} = \boldsymbol{\theta}_{22}^{(0)} = \boldsymbol{0}$ which reduces (2.156) to

$$\omega^2_{n_{1/2}}(\boldsymbol{k}) = \omega^2_{n_1} - \frac{\epsilon}{2}\Big(\gamma \pm \sqrt{\gamma^2 + \frac{4\{\boldsymbol{\theta}_{12}^{(0)}\otimes\overline{\boldsymbol{\theta}_{12}^{(0)}}\} : (\hat{\boldsymbol{k}})^2}{\rho_1^{(0)}\rho_2^{(0)}}}\Big). \tag{2.171}$$

Expressions (2.171) describe anisotropic dispersion relationships that are: (a) invariant in the direction $\mathrm{Re}(\boldsymbol{\theta}_{12}^{(0)})\times\mathrm{Im}(\boldsymbol{\theta}_{12}^{(0)})$ of $\hat{\boldsymbol{k}}$ when $\mathrm{Re}(\boldsymbol{\theta}_{12}^{(0)})$ and $\mathrm{Im}(\boldsymbol{\theta}_{12}^{(0)})$ are linearly independent (see Fig. 2.4(a)), and (b) invariant within the planes orthogonal to $\mathrm{Re}(\boldsymbol{\theta}_{12}^{(0)})$ when the latter two vectors are parallel (se Fig. 2.4(b)).

On the other hand, when $\gamma = 0$, equations (2.156) describe *hyper-cones* provided that (i) condition (2.159) holds, and (ii) the vectors $(\rho_1^{(0)})^{-1}\boldsymbol{\theta}_{11}^{(0)}$, $(\rho_1^{(0)}\rho_2^{(0)})^{-\frac{1}{2}}\mathrm{Re}(\boldsymbol{\theta}_{12}^{(0)})$ and $(\rho_1^{(0)}\rho_2^{(0)})^{-\frac{1}{2}}\mathrm{Im}(\boldsymbol{\theta}_{12}^{(0)})$ are mutually orthogonal with equal norms. In such case, the dispersion relationships are given by (2.162), a scenario that is illustrated in Fig. 2.4(c).

Remark 18 *With reference to Claim 10, the real-valuedness of $\boldsymbol{\theta}_{pq}^{(0)}$ prevents the existence of hyper-conical dispersion relationships at "apexes" $\boldsymbol{k}_s = \frac{1}{2}(\sum_j n_j\boldsymbol{e}^j)$, $n_j \in \{-1, 0, 1\}$ of the first Brillouin zone.*

2.6 Numerical examples

In this section, we seek to illustrate the utility of the proposed homogenization framework by considering both free ($\tilde{f}_{\boldsymbol{k}} = 0$) and forced ($\tilde{f}_{\boldsymbol{k}} \neq 0$) wave motion problems.

2.6.1 Dispersion relationships

Let us first examine the performance of the asymptotic solution in terms of local approximation of the dispersion relationships. To this end, we consider a non-orthogonal

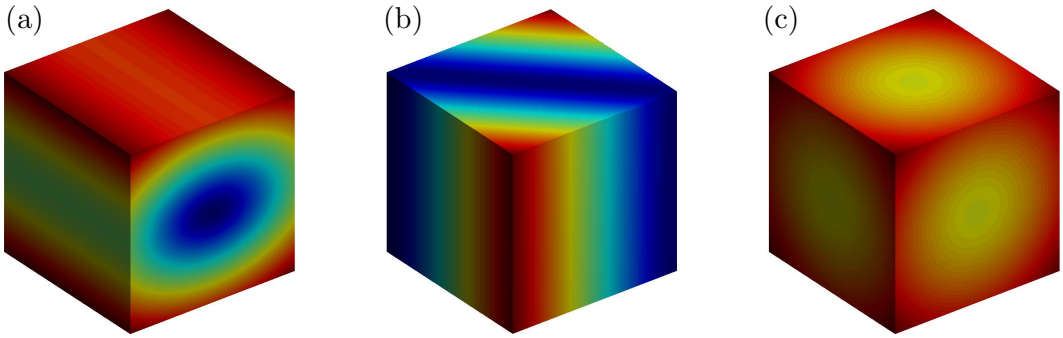

Figure 2.4: Cross-sections of the dispersion relationship $\omega_{n_2}(\boldsymbol{k})$ for $d = 3$ according to: (a) equation (2.171) where $\mathrm{Re}(\boldsymbol{\theta}_{12}^{(0)})$ and $\mathrm{Im}(\boldsymbol{\theta}_{12}^{(0)})$ are linearly independent; (b) equation (2.171) where $\mathrm{Re}(\boldsymbol{\theta}_{12}^{(0)})$ and $\mathrm{Im}(\boldsymbol{\theta}_{12}^{(0)})$ are parallel, and (c) equation (2.162) depicting a single hyper-cone.

lattice with Neumann exclusions, and an orthogonal lattice with Dirichlet exclusions.

Kagome lattice

As a first example, we consider the anti-plane shear wave motion in a Kagome lattice $S \subset \mathbb{R}^2$. This configuration is motivated by a recent experimental study [29] of the wave transport in symmetric and asymmetric Kagome lattices, that revealed frequency-dependent directive behavior in the bulk and the existence of (evanescent) edge modes. With reference to Fig. 2.5(a), our lattice is characterized by a trihexagonal tiling geometry where the equilateral triangles of side $a = 1$ are linked by hinges of thickness $h = 0.04a$, yielding the porosity of $v = 0.75$. For completeness, Fig. 2.5(b) shows the unit cell of periodicity including the lattice basis vectors $\boldsymbol{e}_1$ and $\boldsymbol{e}_2$, while Fig. 2.5(c) displays the first Brillouin zone including the reciprocal basis vectors $\boldsymbol{e}^1$ and $\boldsymbol{e}^2$. The motion in the medium is governed by the wave equation (2.11) with $\rho(\boldsymbol{x}) = 1$ and $G(\boldsymbol{x}) = 1$, subject to the traction-free boundary condition along the perimeter of hexagonal voids. In this case, the lattice basis vectors and the reciprocal basis vectors are given by

$$\boldsymbol{e}_1 = a\big(\boldsymbol{i}_1 + \sqrt{3}\boldsymbol{i}_2\big), \quad \boldsymbol{e}_2 = a\big(-\boldsymbol{i}_1 + \sqrt{3}\boldsymbol{i}_2\big), \quad \boldsymbol{e}^1 = \tfrac{\pi}{a}\big(\boldsymbol{i}_1 + \tfrac{1}{\sqrt{3}}\boldsymbol{i}_2\big), \quad \boldsymbol{e}^2 = \tfrac{\pi}{a}\big(-\boldsymbol{i}_1 + \tfrac{1}{\sqrt{3}}\boldsymbol{i}_2\big).$$

In the absence of the source term ($\tilde{f}_{\boldsymbol{k}} = 0$), the foregoing homogenization framework enables local approximation of the dispersion relationship in the vicinity of an *arbitrary pair* $(\boldsymbol{k}_s, \omega_n(\boldsymbol{k}_s))$, $\boldsymbol{k}_s \in \overline{\mathcal{B}}$, which is a way to access the effective properties of the medium. With reference to Fig. 2.5(c), we illustrate this by taking $\boldsymbol{k}_s$ as the origin of the Brillouin zone (point A), apex points B and C, and internal points M and N given respectively

by

$$\overrightarrow{\mathrm{AB}} = \tfrac{1}{2}\boldsymbol{e}^1, \qquad \overrightarrow{\mathrm{AC}} = \tfrac{\pi}{a}\big(\tfrac{1}{3}\boldsymbol{i}_1 + \tfrac{1}{\sqrt{3}}\boldsymbol{i}_2\big), \qquad \overrightarrow{\mathrm{AM}} = 0.4125\,\overrightarrow{\mathrm{AC}}, \qquad \overrightarrow{\mathrm{AN}} = 0.4761\,\overrightarrow{\mathrm{AB}}.$$

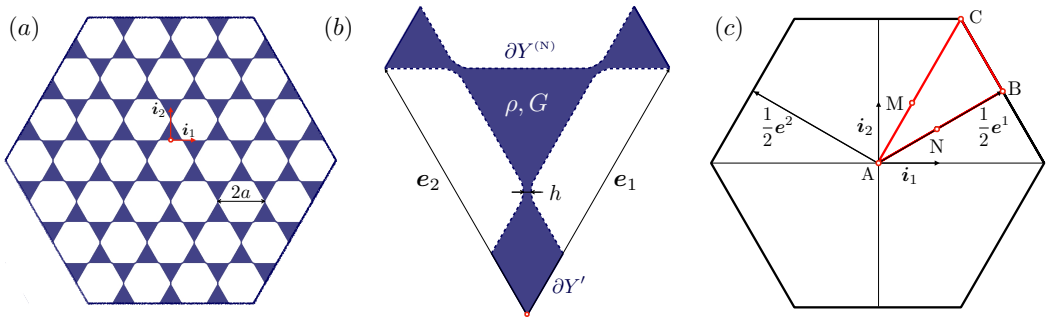

Figure 2.5: Schematics of (a) Kagome lattice $S \subset \mathbb{R}^2$ including the origin of the canonical basis; (b) unit cell of periodicity Y, with $\delta Y'$ (solid lines) and $\delta Y^{(\mathrm{N})}$ (dashed lines) indicating respectively the support of periodic and homogeneous Neumann boundary conditions; and (c) the first Brillouin zone featuring "test" points A, B, C, M and N.

The reference dispersion relationship along path BACB, as well as the cell functions at each wavenumber-eigenfrequency pair $(\boldsymbol{k}_s, \omega_n(\boldsymbol{k}_s))$ required to evaluate the asymptotic approximation, are computed numerically via the finite element platform NGSolve [40] by discretizing the unit cell with triangular elements of order 5 and maximum size $h_{max} = 0.02a$. Fig. 2.6 compares the first 12 dispersion branches with their respective approximations in the neighborhood of points A, B and C, while Fig. 2.7 focuses on branches 13–20 and the neighborhood of points A, B, C, M and N. In each case, we specify the extent of repeated- or cluster-eigenvalue asymptotic approximation (as applicable) by the set

$$\mathcal{N}_\ell^\star = \{n_1, n_2, \ldots n_Q\}, \qquad \star \in \{A, B, C, M, N\}$$

where, for given index $\star$, ℓ locates the cluster in the order of increasing frequency.

In Figs. 2.6 and 2.7, clusters $\mathcal{N}_1^A$ through $\mathcal{N}_5^A$ and $\mathcal{N}_7^A$ each feature a repeated eigenfrequency of multiplicity $Q = 2$, where $\boldsymbol{A}(\hat{\boldsymbol{k}}) = \boldsymbol{0}$ in all perturbation directions; hence the dispersion relationship in those neighborhoods is uniformly described by (2.104). In the cluster $\mathcal{N}_6^A$ with $Q = 3$, matrix $\boldsymbol{A}^\gamma(\hat{\boldsymbol{k}})$ obtained after expanding about the 15th branch ($n_0 = 15$) is found to be of full rank in all perturbation directions; as a result, the local description of the dispersion relationship is in this case provided by (2.137). Alternatively, if the same cluster were expanded about the 16th branch ($n_0 = 16$) instead,

one would find the local asymptotic description to be given by $\omega_{n1}^2(\boldsymbol{k}) = \omega_{n1}^2$ and (2.167) with $(n_1, n_2, n_3) = (16, 17, 15)$.

Clusters $\mathcal{N}_4^A$ in Fig. 2.6 and $\mathcal{N}_7^A$, $\mathcal{N}_6^B$ and $\mathcal{N}_6^C$ in Fig. 2.7, on the other hand, each feature two distinct eigenvalues ($Q=2, \gamma \neq 0$) and trivial effective matrices, $\boldsymbol{A}^{(0)}(\hat{\boldsymbol{k}})=\boldsymbol{0}$ and $\boldsymbol{B}^{(0)}(\hat{\boldsymbol{k}})=\boldsymbol{0}$, in all perturbation directions. As a result, matrix $\boldsymbol{A}^{\gamma}(\hat{\boldsymbol{k}})$ has partial rank, whereby the local dispersion relationships are described by (2.137) with $q = 2$ and (2.138) with $N_0 = 1$. Concerning the cluster $\mathcal{N}_1^B$ in Fig. 2.6 where similarly $Q = 2$, $\gamma \neq 0$, it is worth noting that the effective matrix $\boldsymbol{B}^{(0)}$ is in this case *sign-indefinite* as seen from the "inverted" curvatures in the directions BA and BC.

In Fig. 2.6 and Fig. 2.7, clusters $\mathcal{N}_1^C$, $\mathcal{N}_2^C$, $\mathcal{N}_3^C$, $\mathcal{N}_5^C$ and $\mathcal{N}_7^C$ feature pure Dirac behavior ($Q = 2$) in directions CB and CA, as described by (2.160) with $\gamma = 0$ and $\boldsymbol{\theta}_{11}^{(0)} \nparallel \boldsymbol{\theta}_{12}^{(0)}$. From Fig. 2.7, we also note that the local approximation of wave dispersion at *internal points* M and N describes with high fidelity the respective numerical results. This holds true for both isolated frequencies and clusters $\mathcal{N}_1^M$ and $\mathcal{N}_1^N$ of size $Q = 3$. Concerning the clusters $\mathcal{N}_2^B$, $\mathcal{N}_3^B$, $\mathcal{N}_4^B$, $\mathcal{N}_5^B$ and $\mathcal{N}_7^B$, of sizes $Q \in \{2, 3, 4\}$, the affiliated GEPs stemming from the asymptotic models (2.136) and (2.138) are deployed to approximate the featured dispersion relationships as shown in the figures. For brevity of presentation, we omit the discussion of these approximations.

Dirichlet colonnade

As a second example, we take $S \subset \mathbb{R}^2$ as a homogeneous medium ($G=1$, $\rho=1$) endowed with a square lattice of circular Dirichlet obstacles, where $u(\boldsymbol{x}) = 0$. Referring to Fig. 2.8(a), the array of pins is characterized by the spacing $a = 1$ and diameter $0.25a$, resulting in the lattice porosity of $v = 0.05$. In this case, the lattice basis vectors and the reciprocal basis vectors are given by

$$\boldsymbol{e}_1 = a\boldsymbol{i}_1, \quad \boldsymbol{e}_2 = a\boldsymbol{i}_2, \quad \boldsymbol{e}^1 = \tfrac{2\pi}{a}\boldsymbol{i}_1, \quad \boldsymbol{e}^2 = \tfrac{2\pi}{a}\boldsymbol{i}_2.$$

For completeness, Fig. 2.8(b) details the unit cell of periodicity Y, and Fig. 2.8(c) illustrates the first Brillouin zone including the "test" points A, B, C, M_1, M_2, N_1, and N_2 given by

$$\begin{aligned} &\overrightarrow{\mathrm{AB}} = \tfrac{1}{2}\boldsymbol{e}^1, \quad \overrightarrow{\mathrm{AC}} = \tfrac{1}{2}(\boldsymbol{e}_1 + \boldsymbol{e}_2), \quad \overrightarrow{\mathrm{AM}_1} = 0.4250\overrightarrow{\mathrm{AC}} \quad \overrightarrow{\mathrm{AM}_2} = 0.5250\,\overrightarrow{\mathrm{AC}}, \\ &\overrightarrow{\mathrm{AN}_1} = 0.5125\,\overrightarrow{\mathrm{AB}} \quad \overrightarrow{\mathrm{AN}_2} = 0.7125\,\overrightarrow{\mathrm{AB}}. \end{aligned} \tag{2.172}$$

Fig. 2.9 examines the performance of the asymptotic models in terms of the first eleven branches of the dispersion relationship. The reference numerical values along path BACB, as well as the cell functions at each wavenumber-eigenfrequency pair

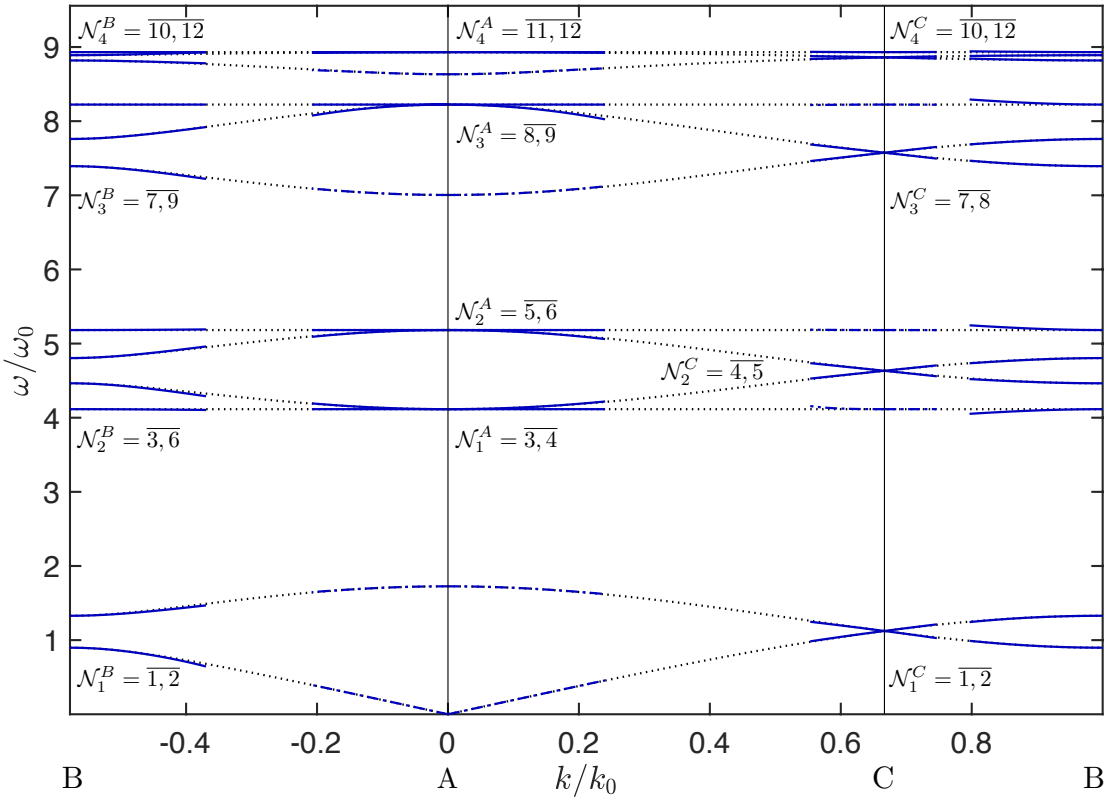

Figure 2.6: Approximation of the first twelve dispersion branches for the Kagome lattice near points A, B and C in Fig 2.5(c). In the display, dotted lines track the reference numerical results; solid lines signify the leading-order approximation of the clusters of nearby branches ($Q > 1$), and dash-dotted lines plot the second-order approximation of isolated dispersion branches ($Q = 1$). The normalization parameters are defined as $k_0 = \pi/a$ and $\omega_0 = \sqrt{G/(\rho a^2)}$.

$(\boldsymbol{k}_s, \omega_n(\boldsymbol{k}_s))$ required to evaluate the asymptotic approximation, are computed via NG-Solve by discretizing the unit cell with triangular elements of order 5 and maximum size $h_{max} = 0.0175a$. As indicated earlier, the comparison is made in a neighborhood of the origin A, apex points B and C, and internal points M_1, M_2, N_1 and N_2, of the first Brillouin zone.

From Fig. 2.9, one first observes that the introduction of "pins" (where $u=0$) in an otherwise homogeneous medium results in both zero-frequency band gap, and another complete band gap just above the first dispersion branch. In terms of the asymptotic

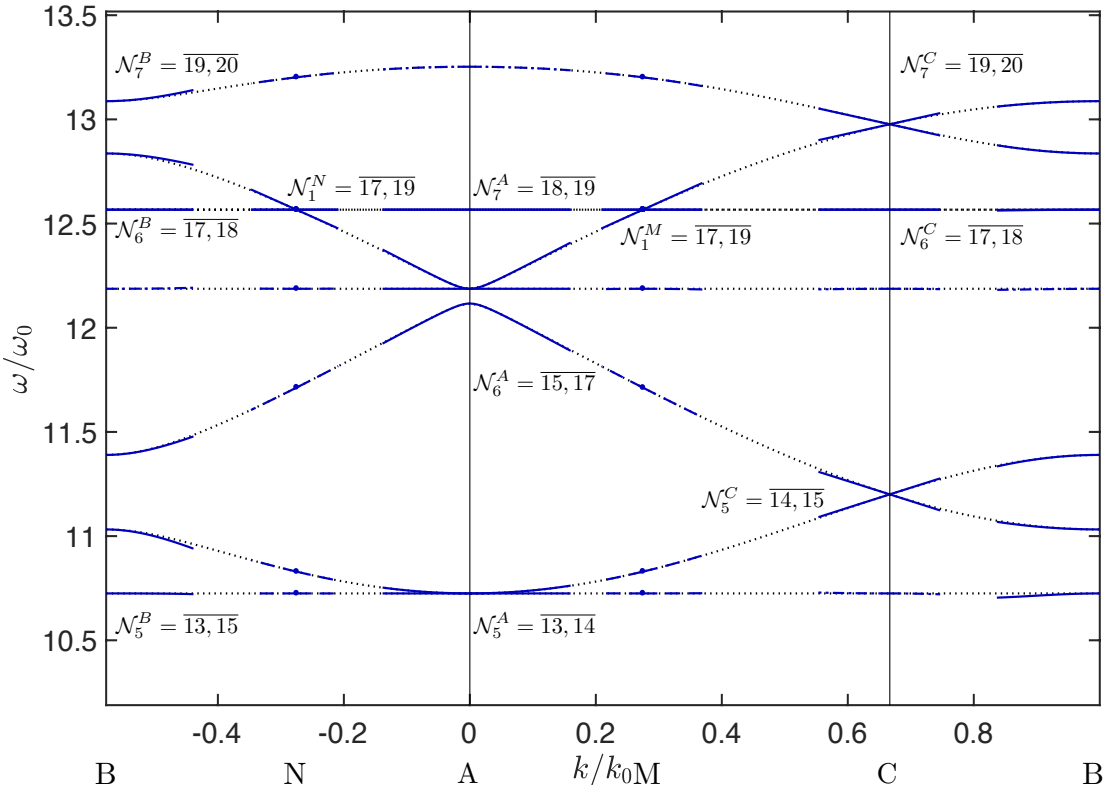

Figure 2.7: Approximation of the dispersion branches 13–20 for the Kagome lattice near points A, B, C, M and N in Fig 2.5(c). In the display, dotted lines track the reference numerical results; solid lines signify the leading-order approximation of the clusters of nearby branches ($Q>1$); dashed lines indicate first-order approximation of isolated dispersion branches ($Q=1$) at M and N, and dash-dotted lines plot the second-order approximation of isolated dispersion branches. The normalization parameters are defined as $k_0 = \pi/a$ and $\omega_0 = \sqrt{G/(\rho a^2)}$.

approximation, we note that clusters $\mathcal{N}_1^B$ and $\mathcal{N}_2^B$ of size $Q = 2$ exhibit *direction-dependent* behavior. Concerning $\mathcal{N}_1^B$ for example, we specifically find that the cluster's behavior in direction BC (where $\boldsymbol{A}^\gamma(\hat{\boldsymbol{k}})$ is of full rank) is approximated by (2.137), whereas in direction BA (where $\mathrm{rank}(\boldsymbol{A}^\gamma(\hat{\boldsymbol{k}}) = 1)$ (2.138) applies. Analogous comment applies to $\mathcal{N}_2^B$, with the roles of directions BC and BA reversed.

Further, cluster $\mathcal{N}_3^C$ in Fig. 2.9 describes a repeated eigenvalue of multiplicity $Q = 2$; in this case $\boldsymbol{A}^{(0)}(\hat{\boldsymbol{k}}) = \boldsymbol{0}$, and the dispersion relationships are approximated by (2.104). In contrast, clusters $\mathcal{N}_1^{N_1}$, $\mathcal{N}_1^{N_2}$, $\mathcal{N}_1^{M_1}$, and $\mathcal{N}_1^{M_2}$, which carry the same size, are commonly

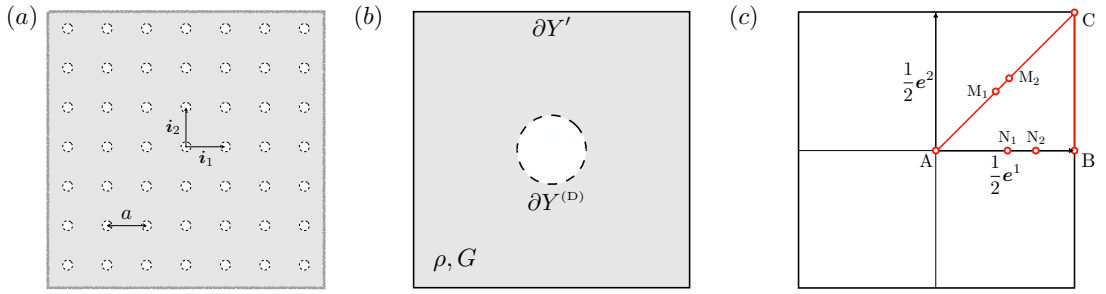

Figure 2.8: Schematics of (a) Dirichlet colonnade $S \subset \mathbb{R}^2$; (b) unit cell of periodicity Y, with $\partial Y'$ (solid lines) and $\partial Y^{(\mathrm{D})}$ (dashed lines) indicating respectively the support of periodic and homogeneous Dirichlet boundary conditions; and (c) first Brillouin zone featuring "test" points A, B, C, M_1, M_2, N_1, and N_2.

characterized by the full-rank $\boldsymbol{A}^{(0)}(\hat{\boldsymbol{k}})$ in the respective directions of the band diagram. Accordingly, these clusters are described (to the leading order) by (2.101).

Moving our attention to larger clusters, we note that $\mathcal{N}_2^A$ and $\mathcal{N}_1^C$ (with $Q=3$) each describe the case where $\gamma \neq 0$ and $\mathrm{rank}(\boldsymbol{A}^\gamma)=2$, examined in sections §2.4.3 and §2.5.4. With reference to Section 2.5.4, we specifically let $(n_1, n_2, n_3)_{\mathcal{N}_2^A} = (6, 7, 5)$ with $n_0 = 6$, and $(n_1, n_2, n_3)_{\mathcal{N}_1^C} = (2, 3, 1)$ with $n_0 = 2$. Finally, we note that the "superclusters" $\mathcal{N}_1^A$ (with $Q = 4$) and $\mathcal{N}_2^C$ (with $Q = 5$) are approximated very well by the leading-order model (2.138), with $\boldsymbol{A}^\gamma(\hat{\boldsymbol{k}})$ being of full rank in each relevant direction of the band diagram.

2.6.2 Forced medium motion

To illustrate the asymptotic approximation of the forced motion problem, we next examine the response of a two-dimensional Kagome lattice detailed in Section 2.6.1, at frequency $\omega^2 = \omega_2^2(\boldsymbol{0}) + \epsilon^2$ within the first band gap (see Fig. 2.6). On recalling Claim 1 and Remark 1, for the source term $f(\boldsymbol{x})$ according to (2.16) we assume Gaussian source distribution with $\boldsymbol{k}_s = \boldsymbol{0}$ (i.e. $\boldsymbol{k} = \epsilon\hat{\boldsymbol{k}}$) given by

$$\tilde{f}_{\boldsymbol{k}}(\boldsymbol{x}) \;=\; F(\boldsymbol{k})\phi(\boldsymbol{x}), \qquad F(\boldsymbol{k}) \;=\; |\mathcal{C}|\,\frac{a^2}{\pi} e^{-a^2\|\hat{\boldsymbol{k}}\|^2} e^{-i\epsilon\hat{\boldsymbol{k}}\cdot\boldsymbol{x}_\circ}, \qquad \phi \in L_p^2(Y), \tag{2.173}$$

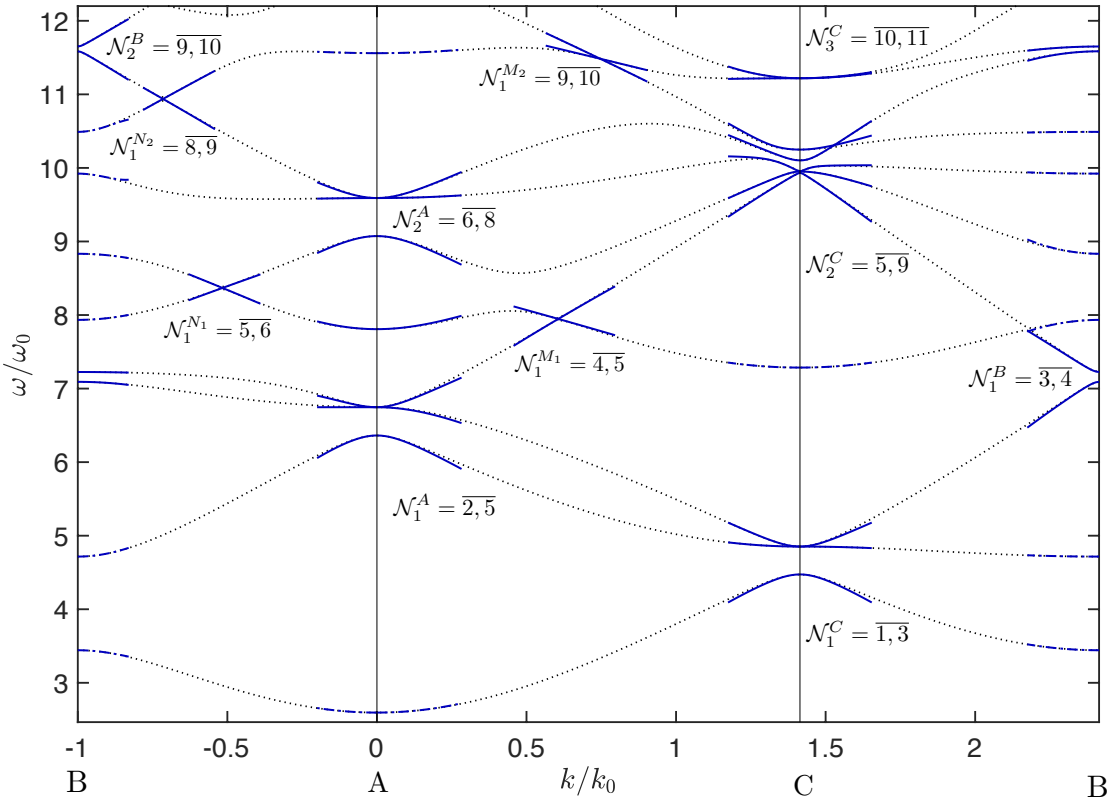

Figure 2.9: Approximation of the dispersion branches 1–11 for the Dirichlet colonnade near points A, B, C, M_1, M_2, N_1 and N_2 in Fig 2.8(c). In the diagram, dotted lines track the reference numerical results; solid lines signify the leading-order approximation of the clusters of nearby branches ($Q>1$), and dash-dotted lines plot the second-order approximation of isolated dispersion branches ($Q=1$). The normalization parameters are defined as $k_0 = \pi/a$ and $\omega_0 = \sqrt{G/(\rho a^2)}$.

and

$$\phi(\boldsymbol{x}) \;=\; \sum_{k=0}^{M} \frac{4}{3\pi(2k+1)} \big[\sin\big(2\pi(2k+1)(\tfrac{1}{4} - x^1)\big) + \sin\big(2\pi(2k+1)(\tfrac{1}{4} - x^2)\big) + \sin\big(2\pi(2k+1)(x^1 + x^2)\big)\big], \tag{2.174}$$

with $\boldsymbol{x}_\circ = -0.25(\boldsymbol{e}_1 + \boldsymbol{e}_2)$. Note that (2.174) approximates a dipole on Y as $M \to \infty$.

We consider the response of the Kagome lattice for $\epsilon \in \{0.25, 0.5\}$ in terms of the full field $u^{[\mathrm{p}]}$ and the mean field $\langle u \rangle_\rho^{[\mathrm{p}]}$ $(p = 0, 1, 2)$ according to (2.147) and (2.151).

Thanks to the exponential decay with $\boldsymbol{k}$ of $\tilde{f}_{\boldsymbol{k}}$ in (2.148)–(2.150) and (2.152)–(2.154), in computations we conveniently supersede the domain of integration $\mathcal{C}$ by $[-\pi/a, \pi/a] \times [-\pi/a, \pi/a]$. To compute the featured eigenfunction, the cell functions, and the effective coefficients in (2.148)–(2.150) and (2.152)–(2.154), we solve the the respective unit cell problems via NGSolve by discretizing the unit cell in Fig. 2.5(b) with triangular elements of order 5 and maximum size $h_{max} = 0.05a$.

For the purposes of numerical verification, the reference global solution is computed via NGSolve over a parallelepiped $\Omega = \{\boldsymbol{x} \in S,\ |x^j| < 23,\ j\ \in \overline{1,2}\}$ (subject to homogeneous Dirichlet boundary conditions) that is discretized with triangular elements of order 3 and maximum size $h_{max} = 0.05a$. Since the finite element simulations require the source distribution in space $f(\boldsymbol{x})$, we similarly extend the domain of integration in (2.16) to $\mathbb{R}^2$ in order to facilitate analytical evaluation. Note that the use of Dirichlet (in lieu of radiation) conditions on $\partial\Omega$ is permitted by the exponential decay of $u(\boldsymbol{x})$ at driving frequencies inside the band gap.

As an illustration, Fig. 2.10 plots the real parts of the eigenfunction $\tilde{\phi}_2$ and the components of $\boldsymbol{\chi}^{(1)}$ and $\boldsymbol{\chi}^{(2)}$. With reference to (2.173)–(2.174), Fig. 2.11 shows the periodic function ϕ for $M = 8$ and the associated cell function $\zeta^{(0)}$ featured in the expression $\eta^{(0)}(\boldsymbol{k}, \boldsymbol{x}) = F(\boldsymbol{k})\zeta^{(0)}(\boldsymbol{x})$, see Remark 6. Fig. 2.12 plots both the computed source distribution, $f(\boldsymbol{x})$, in the physical space and the NGSolve simulations of $u(\boldsymbol{x})$ for $\epsilon \in \{0.25, 0.5\}$ over a hexagonal truncation of Ω centered at $\boldsymbol{x}_\circ$. From the display, we observe that the medium response (i) conforms with the symmetries of the source and the Kagome lattice, and (ii) decays fast with $\|\boldsymbol{x} - \boldsymbol{x}_\circ\|$ as expected for solutions inside a band gap. Fig. 2.13 (resp. Fig. 2.14) compares, for $\epsilon = 0.25$ (resp. $\epsilon = 0.5$), the finite element response with the asymptotic approximations $u^{[\mathrm{p}]}$ and $\langle u \rangle_\rho^{[\mathrm{p}]}$ $(p = 0, 1, 2)$ across example cross-sections of the lattice. From the panels, one may observe both a clear increase in the fidelity of asymptotic approximation with p, and the ability of the effective solution (supported in $\mathbb{R}^2$ instead of S) to describe the essential response of the Kagome lattice.

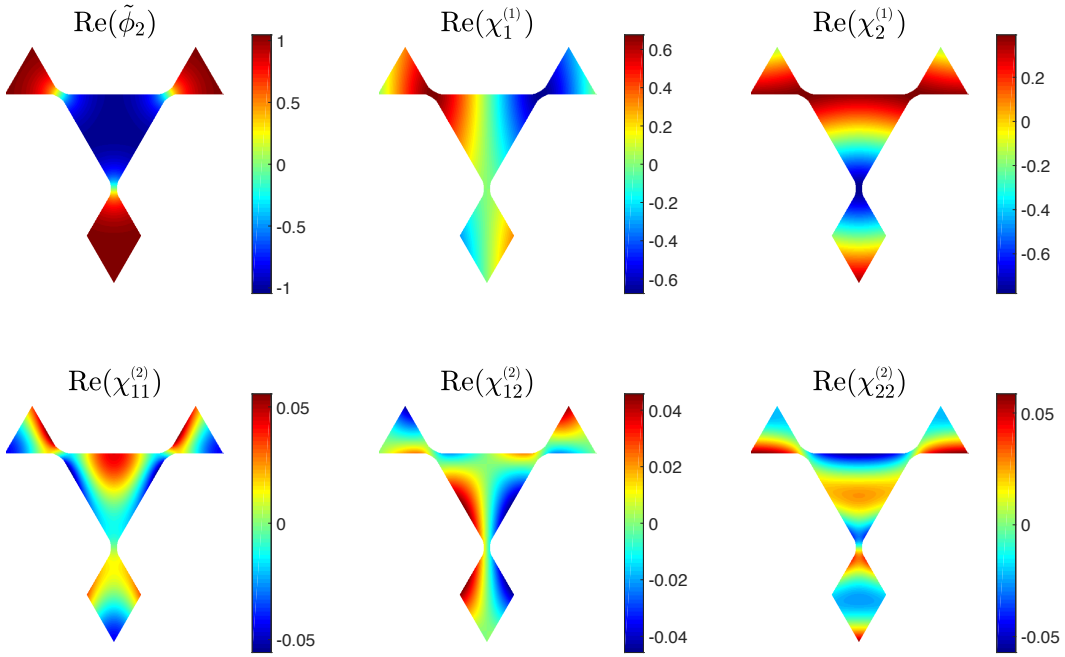

Figure 2.10: Eigenfunction $\tilde{\phi}_2(\boldsymbol{x})$ and components of the affiliated cell functions $\boldsymbol{\chi}^{(1)}(\boldsymbol{x})$ and $\boldsymbol{\chi}^{(2)}(\boldsymbol{x})$ of the Kagome lattice at $\boldsymbol{k}_s = \boldsymbol{0}$ (real parts only) obtained by NGsolve.

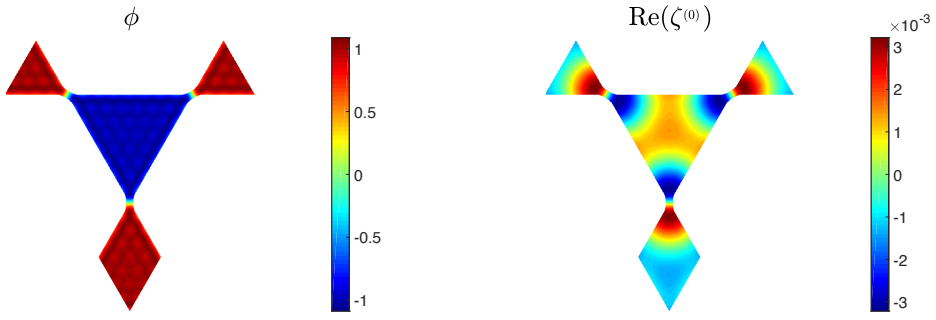

Figure 2.11: Periodic function $\phi(\boldsymbol{x})$ as defined in (2.174) for $M = 8$ and affiliated cell function $\zeta^{(0)}(\boldsymbol{x})$ (real part only) obtained by NGsolve.

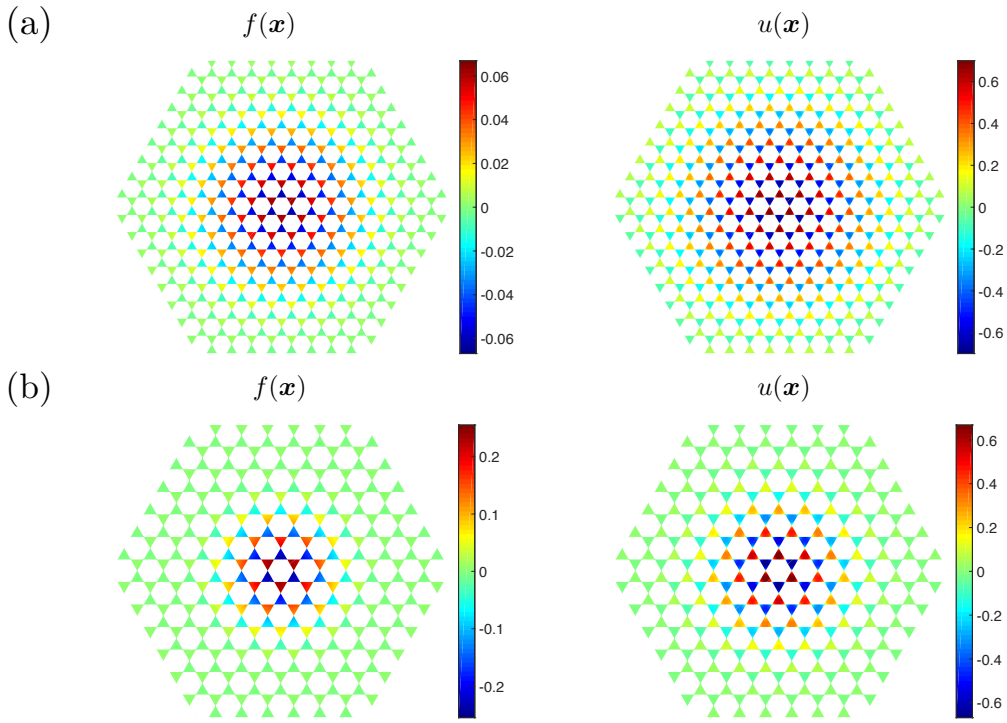

Figure 2.12: Source distributions $f(\boldsymbol{x})$ (left panels) and respective responses $u(\boldsymbol{x})$ of the Kagome lattice (right panels) for: (a) $\epsilon = 0.25$, and (b) $\epsilon = 0.5$. The plots are made over a hexagonal subdomain of Ω centered at $\boldsymbol{x}_\circ$.

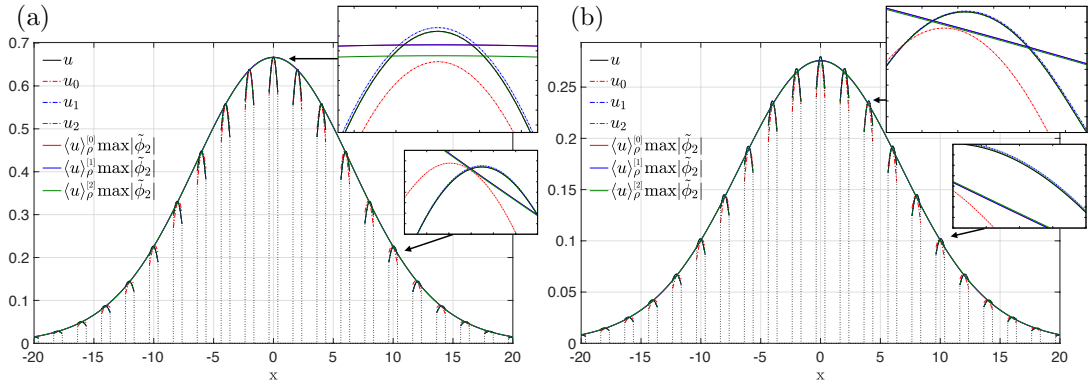

Figure 2.13: Response of the Kagome lattice for $\epsilon = 0.25$: numerical values versus leading-, first-, and second-order (full and effective) asymptotic approximations for (a) $\boldsymbol{x}\cdot\boldsymbol{i}_2 = 1.5$, and (b) $\boldsymbol{x}\cdot\boldsymbol{i}_2 = 8.43$. The leading- and first- order effective approximations overlap due to symmetry of the problem.

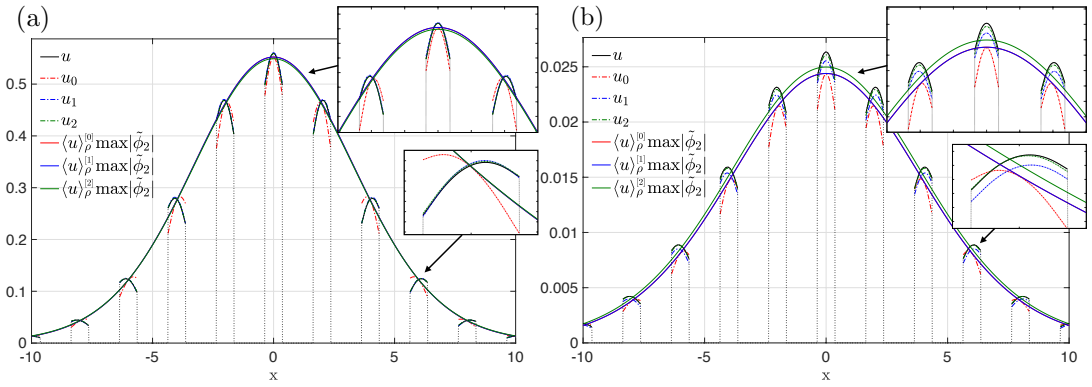

Figure 2.14: Response of the Kagome lattice for $\epsilon = 0.5$: numerical values versus leading-, first-, and second-order (full and effective) asymptotic approximations for (a) $\boldsymbol{x}\cdot\boldsymbol{i}_2 = 1.5$, and (b) $\boldsymbol{x}\cdot\boldsymbol{i}_2 = 8.43$. The leading- and first- order effective approximations overlap due to symmetry of the problem.

Chapter 3

Effective wave motion in periodic origami-inspired structures

In this chapter, we establish a dynamic homogenization framework catering for the linear elastic wave motion in periodic origami structures. The latter are modeled via "bar-and-hinge" paradigm where: (i) the folding of the structure and the bending of individual panels are modeled via elastic hinges, and (ii) the in-plane deformation of each panel is modeled with elastic bars. Using the so-formulated discrete model of an origami structure, we pursue finite wavenumber-finite frequency (FW-FF) homogenization of the wave motion in a spectral neighborhood of simple, repeated, and nearby eigenfrequencies at an arbitrary wavenumber within the first Brillouin zone. The lynchpin of the proposed approach is the "projection" of the nodal displacements over each unit cell onto a suitable Bloch eigenvector, evaluated at the "center" of the spectral region of interest. For completeness, we make an account for: (i) the source term acting at the nodes of a discrete structure, and (ii) periodic Dirichlet boundary conditions. We obtain the leading-order (system of) effective equation(s) synthesizing the wave motion in a selected spectral neighborhood, and we describe asymptotically the corresponding dispersion relationship. We illustrate the proposed framework by comparing numerically the Bloch dispersion relationship to its asymptotic approximation for (a) a 2D-periodic Miura-ori structure, and (b) a 1D-periodic Miura tube. The dispersion analysis is complemented by evaluating the effective wave motion in a 2D-periodic Miura-ori structure due to spatially-localized source term acting either inside a band gap or within a passband.

3.1 Preliminaries

3.1.1 Geometry

Consider a periodic origami structure $S_{\boldsymbol{\alpha}} \in \mathbb{R}^{\mathfrak{d}}$ ($\mathfrak{d} \geqslant 2$) composed of several sheets i.e. surfaces that are periodically folded in flat panels, where $\boldsymbol{\alpha} \in \mathbb{R}^m$ ($m \geqslant 1$) is the vector of rigid folding parameters that control its geometrical configuration i.e. folding state. For $\mathfrak{p} \in \overline{1,\mathfrak{d}}$, let $\mathbb{R}^{\mathfrak{p}} \subset \mathbb{R}^{\mathfrak{d}}$ denote the (sub-) space over which the origami structure is periodic, and let $\boldsymbol{e}_j$ ($j = \overline{1,\mathfrak{d}}$) be a basis of $\mathbb{R}^{\mathfrak{d}}$ such that $\boldsymbol{e}_j$ ($j = \overline{1,\mathfrak{p}}$) spans the periodicity space $\mathbb{R}^{\mathfrak{p}}$ and $\boldsymbol{e}_i \cdot \boldsymbol{e}_j = 0$ for $i = \overline{1,\mathfrak{p}}$ and $j = \overline{\mathfrak{p}+1,\mathfrak{d}}$. By denoting by x^j the contravariant components of the position vector $\boldsymbol{x} \in \mathbb{R}^{\mathfrak{d}}$ with reference to the basis $\boldsymbol{e}_j$, the unit cell Y of $S_{\boldsymbol{\alpha}}$ and the affiliated Bravais lattice $\boldsymbol{R}$ are defined as

$$Y \;=\; \{\boldsymbol{x} \in S_{\boldsymbol{\alpha}} \colon 0 \leq x^j < 1,\; j = \overline{1,\mathfrak{p}}\}, \tag{3.1}$$

$$\boldsymbol{R} \;=\; \Big\{ \sum_{j=1}^{\mathfrak{p}} r^j \boldsymbol{e}_j \colon\; r^j \in \mathbb{Z} \Big\}. \tag{3.2}$$

Note that the present definition of a periodic origami structure (POS) is quite general in that includes: (i) 3D origami structures featuring two-dimensional periodicity space for which $(\mathfrak{p},\mathfrak{d}) = (2,3)$; (ii) 3D origami tubes for which $(\mathfrak{p},\mathfrak{d}) = (1,3)$; (iii) periodically-stacked origami structures for which $(\mathfrak{p},\mathfrak{d}) = (3,3)$, and (iv) "perforated" origami configurations where individual panels are periodically eliminated to form a Kirigami structure. For clarity, the first three POS classes are illustrated in Fig. 3.1 that includes (a) single folded surface in $\mathbb{R}^3$ carrying Miura pattern, (b) three-dimensional "Miura-tube" featuring one-dimensional periodicity, and (c) stacked Miura-ori tessellation that is periodic in $\mathbb{R}^3$.

To facilitate the analysis, we also introduce the covariant lattice basis $\boldsymbol{e}^j \in \mathbb{R}^{\mathfrak{d}}$ ($j \in \overline{1,\mathfrak{d}}$) so that $\boldsymbol{e}^j \cdot \boldsymbol{e}_i = 2\pi\delta_{ij}$ ($i,j = \overline{1,\mathfrak{d}}$) where δ_{ij} is the Kronecker delta. This allows us to define the reciprocal Bravais lattice as

$$\boldsymbol{R}^* \;=\; \Big\{ \sum_{j=1}^{\mathfrak{p}} r_j^* \boldsymbol{e}^j \;:\; r_j^* \in \mathbb{Z} \Big\}. \tag{3.3}$$

In the context of the Bloch wave representation, we also introduce the reciprocal of the unit cell Y given by

$$Y^* \;=\; \Big\{ \boldsymbol{k} = \sum_{l=1}^{\mathfrak{p}} k_l\, \boldsymbol{e}^l \colon\; 0 < k_l < 1 \Big\},$$

where $\boldsymbol{k}$ carries the physical meaning of the wave vector. With such definitions, we focus our attention on the first Brillouin zone of the lattice, namely

$$\mathcal{B} \;=\; \Big\{\boldsymbol{k}\in\mathbb{R}^{\mathfrak{d}}\colon\; k_\ell = 0\;(\ell\in\overline{\mathfrak{p}+1,\mathfrak{d}})\;\wedge\;\boldsymbol{k}\cdot\boldsymbol{\kappa}\leqslant\tfrac{1}{2}\|\boldsymbol{\kappa}\|^2,\;\boldsymbol{\kappa}=\sum_{j=1}^{\mathfrak{p}} n_j\boldsymbol{e}^j,\;n_j\in\{-1,0,1\}\Big\}. \tag{3.4}$$

We emphasize that all geometrical parameters introduced above are implicitly $\boldsymbol{\alpha}$-dependent. For future reference, we let $\boldsymbol{i}_j$ $(j\in\overline{1,\mathfrak{d}})$ denote the Cartesian basis of $\mathbb{R}^{\mathfrak{d}}$.

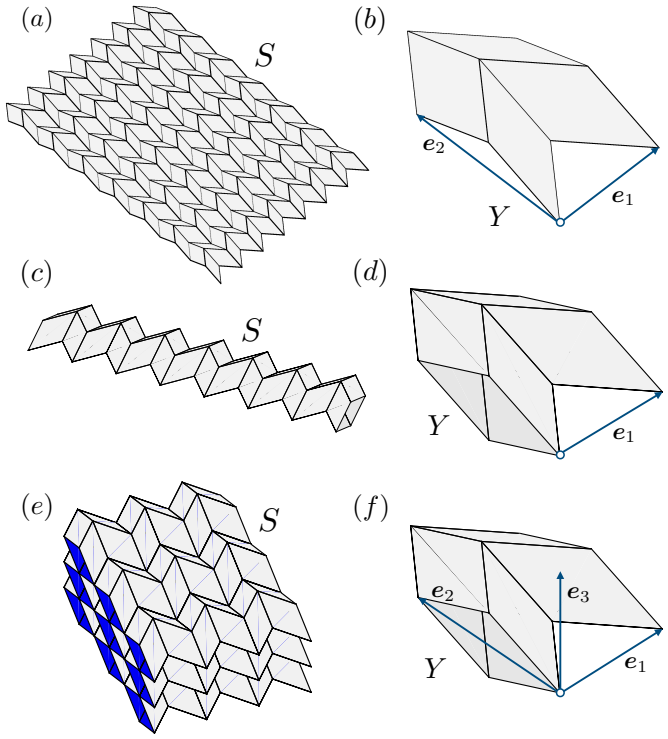

Figure 3.1: Examples of periodic origami structures: (a) Periodic Miura-ori structure with two dimensional periodicity, i.e. $(\mathfrak{d},\mathfrak{p}) = (3,2)$ and its (b) unit cell of periodicity and associated Bravais lattice basis $(\boldsymbol{e}_1,\boldsymbol{e}_2)$; (c) Miura-tube structure with one dimensional periodicity for which $(\mathfrak{d},\mathfrak{p}) = (3,1)$, and its (d) unit cell of periodicity and associated Bravais lattice basis $\boldsymbol{e}_1$; and (e) stacked Miura-ori structure for which $(\mathfrak{d},\mathfrak{p}) = (3,3)$, and its (e) unit cell of periodicity and associated Bravais lattice basis $(\boldsymbol{e}_1,\boldsymbol{e}_2,\boldsymbol{e}_3)$.

3.1.2 Dynamic model and periodic boundary conditions

The elastodynamic behavior of origami structures can be analyzed numerically via finite element analysis via e.g., a shell model for the origami panels. To reduce the high computational cost of origami simulations, a simplified bar-and-hinge model of the origami panels has been proposed first by Schenk and Guest [81] and expanded later by Filipov et al. [58] to capture the essential dynamic behavior of origami structures. In this framework, (i) the sheering and stretching of the origami panels are modeled via elastic bars that link the panels vertices, and (ii) the folding of the origami structure and individual panel bending are modeled via elastic hinges placed along the crease lines and diagonal bars of the origami panels, respectively. Here we distinguish between three particular bar-and-hinge models that were introduced respectively in [81, 58, 78]. With reference to Fig. 3.2, the N4B5 element represents each parallelepiped panel of the origami structure with 4 nodes, 5 bars, and folding hinges placed at the peripheral bars, where the diagonal bar is placed along the shorter diagonal of the parallelepiped. In the N4B6 element, an additional bar is added along the second diagonal to reinforce the in-plane isotropy of the element [58]. The N5B8 element contains 5 nodes and 8 bars, where the additional node is placed in the middle of the panel to allow for better approximation of its bending response. Here the bending hinges are placed along the internal bars, while the folding rotational hinges are placed along the peripheral bars. In the present work, we adopt the linear N5B8 model for parallelepiped panels to capture small deformations of POSs undergoing wave motion. Triangular panels, when present, are modeled with three nodes and three bars (N3B3 element), where the folding hinges are placed along the (peripheral) bars. In contrast to the quadrilateral panels, triangular panels provide subpar approximation of the bending response due to high in-plane stiffness of the surrounding panels that prevent the folding creases from buckling [58].

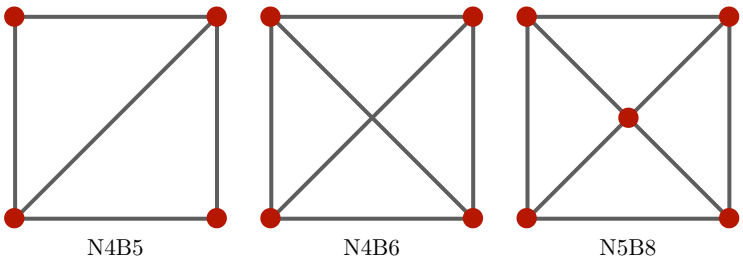

Figure 3.2: Schematics of the N4B5, N4B6 and N5B8 bar-and-hinge models [58].

Let $S'_{\boldsymbol{\alpha}}$ be a discrete model of the periodic origami structure $S_{\boldsymbol{\alpha}}$; let Y' denote its unit cell of periodicity, and let N_{n}, N_{b} and N_{h} be respectively the number of nodes,

bars and hinges within Y'. In what follows, we index the individual unit cells of $S'_{\boldsymbol{\alpha}}$ via lattice vectors $\boldsymbol{r} = \sum_{j=1}^{\mathfrak{p}} r^j \boldsymbol{e}_j \in \boldsymbol{R}$ and their respective internal nodes using $\mathfrak{p}$-tuples

$$\hat{\mathbf{p}}^{(\mathrm{n})} = \mathbf{i} + \hat{\mathbf{r}}^{(\mathrm{n})} \in \mathbb{Z}^{\mathfrak{p}}, \tag{3.5}$$

where

$$\begin{aligned} \mathbf{i} &= (i, 0, \ldots, 0) \in \mathbb{Z}^{\mathfrak{p}}, \quad i \in \overline{1, N_{\mathrm{n}}}, \\ \hat{\mathbf{r}}^{(\mathrm{n})} &= (N_{\mathrm{n}} r^1, r^2, \ldots, r^{\mathfrak{p}}). \end{aligned} \tag{3.6}$$

Hence, by denoting by $\boldsymbol{x}_{\hat{\mathbf{p}}}$ the position vector of the $\hat{\mathbf{p}}$th node, we have

$$\boldsymbol{x}_{\hat{\mathbf{p}}^{(\mathrm{n})} + \hat{\mathbf{r}}^{(\mathrm{n})}} = \boldsymbol{x}_{\hat{\mathbf{p}}^{(\mathrm{n})}} + \boldsymbol{r}. \tag{3.7}$$

Analogous indexing scheme is also introduced for the bars and hinges constituting $S'_{\boldsymbol{\alpha}}$ by replacing the superscript "(n)" in (3.5) respectively by "(b)" and "(h)" for bars and hinges, respectively.

Letting hereon $\hat{\mathbf{p}}, \hat{\mathbf{q}}, \hat{\mathbf{s}} \in \mathbb{Z}^{\mathfrak{p}}$, we compute the extension $e_{\hat{\mathbf{p}}^{(\mathrm{b})}}$ of the $\hat{\mathbf{p}}^{(\mathrm{b})}$th *bar* and angle change $\varphi_{\hat{\mathbf{p}}^{(\mathrm{h})}}$ of the $\hat{\mathbf{p}}^{(\mathrm{h})}$th *hinge* as

$$e_{\hat{\mathbf{p}}^{(\mathrm{b})}} = \sum_{\hat{\mathbf{q}}^{(\mathrm{n})}} \boldsymbol{c}^{e}_{\hat{\mathbf{p}}^{(\mathrm{b})} \hat{\mathbf{q}}^{(\mathrm{n})}} \cdot \boldsymbol{u}_{\hat{\mathbf{q}}^{(\mathrm{n})}}, \tag{3.8}$$

$$\varphi_{\hat{\mathbf{p}}^{(\mathrm{h})}} = \sum_{\hat{\mathbf{q}}^{(\mathrm{n})}} \boldsymbol{c}^{\varphi}_{\hat{\mathbf{p}}^{(\mathrm{h})} \hat{\mathbf{q}}^{(\mathrm{n})}} \cdot \boldsymbol{u}_{\hat{\mathbf{q}}^{(\mathrm{n})}}, \tag{3.9}$$

where $\boldsymbol{u}_{\hat{\mathbf{q}}^{(\mathrm{n})}} \in \mathbb{R}^{\mathfrak{d}}$ is the displacement of the $\hat{\mathbf{q}}^{(\mathrm{n})}$th node; "$\cdot$" is the usual dot product; and $\boldsymbol{c}^{e}_{\hat{\mathbf{p}}^{(\mathrm{b})} \hat{\mathbf{q}}^{(\mathrm{n})}} \in \mathbb{R}^{\mathfrak{d}}$ and $\boldsymbol{c}^{\varphi}_{\hat{\mathbf{p}}^{(\mathrm{h})} \hat{\mathbf{q}}^{(\mathrm{n})}} \in \mathbb{R}^{\mathfrak{d}}$ are the families of compatibility vectors that map $\boldsymbol{u}_{\hat{\mathbf{q}}^{(\mathrm{n})}}$ to the bar extensions $e_{\hat{\mathbf{p}}^{(\mathrm{b})}}$ and hinge angle changes $\varphi_{\hat{\mathbf{p}}^{(\mathrm{h})}}$ respectively, see Appendix B.1 for explicit expressions. Note that the sums (3.8)–(3.9) are finite thanks to the finiteness of the respective compatibility families, even if the elastic interaction between the nodes within a DPOS is nonlocal. Further, by denoting by $t_{\hat{\mathbf{p}}^{(\mathrm{b})}} \in \mathbb{R}$ and $m_{\hat{\mathbf{p}}^{(\mathrm{h})}} \in \mathbb{R}$ the tension of the $\hat{\mathbf{p}}^{(\mathrm{b})}$th bar and resisting moment of the $\hat{\mathbf{p}}^{(\mathrm{h})}$th hinge, we have

$$t_{\hat{\mathbf{p}}^{(\mathrm{b})}} = k^{e}_{\hat{\mathbf{p}}^{(\mathrm{b})}} \, e_{\hat{\mathbf{p}}^{(\mathrm{b})}}, \tag{3.10}$$

$$m_{\hat{\mathbf{p}}^{(\mathrm{h})}} = k^{\varphi}_{\hat{\mathbf{p}}^{(\mathrm{h})}} \, \varphi_{\hat{\mathbf{p}}^{(\mathrm{h})}}, \tag{3.11}$$

where $k^{e}_{\hat{\mathbf{p}}^{(\mathrm{b})}}$ and $k^{\varphi}_{\hat{\mathbf{p}}^{(\mathrm{h})}}$ are the axial and rotational stiffnesses of the $\hat{\mathbf{p}}^{(\mathrm{b})}$th bar and $\hat{\mathbf{p}}^{(\mathrm{h})}$th hinge respectively. Using the principle of virtual work, the internal force vector $\boldsymbol{g}_{\hat{\mathbf{p}}^{(\mathrm{n})}} \in \mathbb{R}^{\mathfrak{d}}$ acting on the $\hat{\mathbf{p}}^{(\mathrm{n})}$th node can then be computed as

$$\boldsymbol{g}_{\hat{\mathbf{p}}^{(\mathrm{n})}} \;=\; \sum_{\hat{\mathbf{s}}^{(\mathrm{b})}} t_{\hat{\mathbf{s}}^{(\mathrm{b})}}\, \boldsymbol{c}^{e}_{\hat{\mathbf{s}}^{(\mathrm{b})}\hat{\mathbf{p}}^{(\mathrm{n})}} \;+\; \sum_{\hat{\mathbf{s}}^{(\mathrm{h})}} m_{\hat{\mathbf{s}}^{(\mathrm{h})}}\, \boldsymbol{c}^{\varphi}_{\hat{\mathbf{s}}^{(\mathrm{h})}\hat{\mathbf{p}}^{(\mathrm{n})}}, \tag{3.12}$$

which yields

$$\begin{aligned}
\boldsymbol{g}_{\hat{\mathbf{p}}^{(\mathrm{n})}} \;&=\; \sum_{\hat{\mathbf{q}}^{(\mathrm{n})}} \Big(\sum_{\hat{\mathbf{s}}^{(\mathrm{b})}} k^{e}_{\hat{\mathbf{s}}^{(\mathrm{b})}}\; \boldsymbol{c}^{e}_{\hat{\mathbf{s}}^{(\mathrm{b})}\hat{\mathbf{p}}^{(\mathrm{n})}} \otimes \boldsymbol{c}^{e}_{\hat{\mathbf{s}}^{(\mathrm{b})}\hat{\mathbf{q}}^{(\mathrm{n})}} + \sum_{\hat{\mathbf{s}}^{(\mathrm{h})}} k^{\varphi}_{\hat{\mathbf{s}}^{(\mathrm{h})}}\; \boldsymbol{c}^{\varphi}_{\hat{\mathbf{s}}^{(\mathrm{h})}\hat{\mathbf{p}}^{(\mathrm{n})}} \otimes \boldsymbol{c}^{\varphi}_{\hat{\mathbf{s}}^{(\mathrm{h})}\hat{\mathbf{q}}^{(\mathrm{n})}} \Big) \cdot \boldsymbol{u}_{\hat{\mathbf{q}}^{(\mathrm{n})}} \\
&=\; \sum_{\hat{\mathbf{q}}^{(\mathrm{n})}} \big(\boldsymbol{K}^{e}_{\hat{\mathbf{p}}^{(\mathrm{n})}\hat{\mathbf{q}}^{(\mathrm{n})}} + \boldsymbol{K}^{\varphi}_{\hat{\mathbf{p}}^{(\mathrm{n})}\hat{\mathbf{q}}^{(\mathrm{n})}} \big) \cdot \boldsymbol{u}_{\hat{\mathbf{q}}^{(\mathrm{n})}} \\
&=\; \sum_{\hat{\mathbf{q}}^{(\mathrm{n})}} \boldsymbol{K}_{\hat{\mathbf{p}}^{(\mathrm{n})}\hat{\mathbf{q}}^{(\mathrm{n})}} \cdot \boldsymbol{u}_{\hat{\mathbf{q}}^{(\mathrm{n})}},
\end{aligned} \tag{3.13}$$

where "$\otimes$" indicate the (outer) tensor product; $\boldsymbol{K}^{e}_{\hat{\mathbf{p}}^{(\mathrm{n})}\hat{\mathbf{q}}^{(\mathrm{n})}} \in \mathbb{R}^{\mathfrak{d}^2}$ and $\boldsymbol{K}^{\varphi}_{\hat{\mathbf{p}}^{(\mathrm{n})}\hat{\mathbf{q}}^{(\mathrm{n})}} \in \mathbb{R}^{\mathfrak{d}^2}$ are the respective families of the bar and hinge stiffness families; $\boldsymbol{K}_{\hat{\mathbf{p}}^{(\mathrm{n})}\hat{\mathbf{q}}^{(\mathrm{n})}} \in \mathbb{R}^{\mathfrak{d}^2}$ is the family of (total) stiffness matrices characterizing DPOS $S'_{\boldsymbol{\alpha}}$, and $\mathbb{R}^{\mathfrak{d}^m} = \mathbb{R}^{\mathfrak{d}} \times \mathbb{R}^{\mathfrak{d}} \times \cdots \times \mathbb{R}^{\mathfrak{d}}$ m times. It is easy to demonstrate that

$$\boldsymbol{K}^{\mathrm{T}}_{\hat{\mathbf{p}}^{(\mathrm{n})}\hat{\mathbf{q}}^{(\mathrm{n})}} \;=\; \boldsymbol{K}_{\hat{\mathbf{q}}^{(\mathrm{n})}\hat{\mathbf{p}}^{(\mathrm{n})}}. \tag{3.14}$$

Remark 19 *Thanks to the periodicity of $S'_{\boldsymbol{\alpha}}$, we find that for any $\boldsymbol{r} \in \boldsymbol{R}$ matrices $\boldsymbol{K}_{\hat{\mathbf{q}}^{(n)}\hat{\mathbf{p}}^{(n)}}$ carry an additional property*

$$\boldsymbol{K}_{(\hat{\mathbf{p}}^{(n)}+\hat{\mathbf{r}}^{(n)})\hat{\mathbf{q}}^{(n)}} \;=\; \boldsymbol{K}_{\hat{\mathbf{p}}^{(n)}(\hat{\mathbf{q}}^{(n)}-\hat{\mathbf{r}}^{(n)})}, \tag{3.15}$$

where the index vector $\hat{\mathbf{r}}^{(n)}$ is given by (3.6)*. See Appendix B.2 for proof.*

Next, assuming constant thickness of the origami panels, the mass of a POS is distributed across DPOS nodes via lumped mass approximation, and we denote the so-defined nodal masses by $M_{\hat{\mathbf{p}}^{(\mathrm{n})}} \in \mathbb{R}$. As a result, the linear elastodynamic behavior of DPOS $S'_{\boldsymbol{\alpha}}$ is governed by

$$\sum_{\hat{\mathbf{q}}^{(\mathrm{n})}} \boldsymbol{K}_{\hat{\mathbf{p}}^{(\mathrm{n})}\hat{\mathbf{q}}^{(\mathrm{n})}} \cdot \boldsymbol{u}_{\hat{\mathbf{q}}^{(\mathrm{n})}} \;+\; M_{\hat{\mathbf{p}}^{(\mathrm{n})}}\, \ddot{\boldsymbol{u}}_{\hat{\mathbf{p}}^{(\mathrm{n})}} \;=\; \boldsymbol{f}_{\hat{\mathbf{p}}^{(\mathrm{n})}}, \tag{3.16}$$

where $\ddot{\boldsymbol{u}}_{\hat{\mathbf{p}}^{(\mathrm{n})}}$ is the acceleration of the $\hat{\mathbf{p}}^{(\mathrm{n})}$th node and $\boldsymbol{f}_{\hat{\mathbf{p}}^{(\mathrm{n})}}$ is the external force acting on it.

3.1.3 Discrete wave equation and discrete Bloch wave expansion

On assuming time-harmonic motion with implicit time dependence $e^{-i\omega t}$, governing equation (3.16) reduces to

$$\sum_{\hat{\mathbf{q}}^{(\mathrm{n})}} \boldsymbol{K}_{\hat{\mathbf{p}}^{(\mathrm{n})}\hat{\mathbf{q}}^{(\mathrm{n})}} \cdot \boldsymbol{u}_{\hat{\mathbf{q}}^{(\mathrm{n})}} \; - \; \omega^2 M_{\hat{\mathbf{p}}^{(\mathrm{n})}} \, \boldsymbol{u}_{\hat{\mathbf{p}}^{(\mathrm{n})}} \; = \; \boldsymbol{f}_{\hat{\mathbf{p}}^{(\mathrm{n})}}. \tag{3.17}$$

For mappings of type $\boldsymbol{h}_{\hat{\mathbf{p}}^{(\mathrm{n})}} : \mathbb{I} \mapsto \mathbb{C}^{\mathfrak{d}}$ for some $\mathbb{I} \subseteq \mathbb{Z}^{\mathfrak{p}}$, we define the space $L^2(\mathbb{I})$ of square-summable mappings as

$$L^2(\mathbb{I}) \; = \; \big\{ \boldsymbol{h}_{\hat{\mathbf{p}}^{(\mathrm{n})}} : \sum_{\hat{\mathbf{p}} \in \mathbb{I}} \boldsymbol{h}_{\hat{\mathbf{p}}^{(\mathrm{n})}} \cdot \overline{\boldsymbol{h}_{\hat{\mathbf{p}}^{(\mathrm{n})}}} < \infty \big\}, \tag{3.18}$$

By analogy to the Bloch wave Expansion (BWE) [75] for square-integrable functions, we define a *discrete Bloch wave expansion* (DBWE) for family $\boldsymbol{h}_{\hat{\mathbf{p}}^{(\mathrm{n})}} \in L^2(\mathbb{Z}^{\mathfrak{p}})$ as

$$\boldsymbol{h}_{\hat{\mathbf{p}}^{(\mathrm{n})}} \; = \; |\mathcal{B}|^{-1} \int_{\mathcal{B}} \tilde{\boldsymbol{h}}_{\hat{\mathbf{p}}^{(\mathrm{n})}}(\boldsymbol{k}) \; e^{i\boldsymbol{k}\cdot\boldsymbol{x}_{\hat{\mathbf{p}}^{(\mathrm{n})}}} \, \mathrm{d}\boldsymbol{k} \tag{3.19}$$

where, recalling (3.7), $\tilde{\boldsymbol{h}}_{\hat{\mathbf{p}}^{(\mathrm{n})}}$ is $\boldsymbol{R}$-periodic and given by

$$\tilde{\boldsymbol{h}}_{\hat{\mathbf{p}}^{(\mathrm{n})}}(\boldsymbol{k}) \; = \sum_{\boldsymbol{r} \in \boldsymbol{R}} \boldsymbol{h}_{\hat{\mathbf{p}}^{(\mathrm{n})} + \hat{\mathbf{r}}^{(\mathrm{n})}} \; e^{-i\boldsymbol{k}\cdot\boldsymbol{x}_{\hat{\mathbf{p}}^{(\mathrm{n})} + \hat{\mathbf{r}}^{(\mathrm{n})}}}. \tag{3.20}$$

In the sequel, we assume that the source term in (3.17) is (i) square summable, i.e. $\boldsymbol{f}_{\hat{\mathbf{p}}^{(\mathrm{n})}} \in L^2(\mathbb{Z}^{\mathfrak{p}})$, and (ii) has *compact wavenumber support* $\mathcal{C} \subset \mathcal{B}$ in the neighborhood of some $\boldsymbol{k}_s \in \mathcal{B}$ so that

$$\boldsymbol{f}_{\hat{\mathbf{p}}^{(\mathrm{n})}} \; = \; |\mathcal{C}|^{-1} \int_{\boldsymbol{k}_s + \mathcal{C}} \tilde{\boldsymbol{f}}_{\hat{\mathbf{p}}^{(\mathrm{n})}}(\boldsymbol{k}) \; e^{i\boldsymbol{k}\cdot\boldsymbol{x}_{\hat{\mathbf{p}}^{(\mathrm{n})}}} \, \mathrm{d}\boldsymbol{k}. \tag{3.21}$$

Thanks to the linearity of (3.17), this motivates consideration of a single Bloch-wave component of the source term in the governing equation, namely

$$\sum_{\hat{\mathbf{q}}^{(\mathrm{n})}} \boldsymbol{K}_{\hat{\mathbf{p}}^{(\mathrm{n})}\hat{\mathbf{q}}^{(\mathrm{n})}} \cdot \boldsymbol{u}_{\hat{\mathbf{q}}^{(\mathrm{n})}} \; - \; \omega^2 M_{\hat{\mathbf{p}}^{(\mathrm{n})}} \, \boldsymbol{u}_{\hat{\mathbf{p}}^{(\mathrm{n})}} \; = \; \tilde{\boldsymbol{f}}_{\hat{\mathbf{p}}^{(\mathrm{n})}} \; e^{i\boldsymbol{k}\cdot\boldsymbol{x}_{\hat{\mathbf{p}}^{(\mathrm{n})}}} \tag{3.22}$$

where $\tilde{\boldsymbol{f}}_{\hat{\mathbf{p}}^{(\mathrm{n})}}$ is periodic over the lattice nodes. Then, thanks to the $\boldsymbol{R}$-periodicity of scalars $M_{\hat{\mathbf{p}}^{(\mathrm{n})}}$ and matrices $\boldsymbol{K}_{\hat{\mathbf{p}}^{(\mathrm{n})}\hat{\mathbf{q}}^{(\mathrm{n})}}$, the nodal displacement $\boldsymbol{u}_{\hat{\mathbf{p}}^{(\mathrm{n})}}$ can be expressed as

a Bloch wave $\boldsymbol{u}_{\hat{\mathbf{p}}^{(\mathrm{n})}} = \tilde{\boldsymbol{u}}_{\hat{\mathbf{p}}^{(\mathrm{n})}}\, e^{i\boldsymbol{k}\cdot\boldsymbol{x}_{\hat{\mathbf{p}}^{(\mathrm{n})}}}$, where $\tilde{\boldsymbol{u}}_{\hat{\mathbf{p}}^{(\mathrm{n})}}$ is $\boldsymbol{R}$-periodic and solves

$$\sum_{\hat{\mathbf{q}}^{(\mathrm{n})}} \check{\boldsymbol{K}}_{\hat{\mathbf{p}}^{(\mathrm{n})}\hat{\mathbf{q}}^{(\mathrm{n})}} \cdot \tilde{\boldsymbol{u}}_{\hat{\mathbf{q}}^{(\mathrm{n})}} \,-\, \omega^2 M_{\hat{\mathbf{p}}^{(\mathrm{n})}}\, \tilde{\boldsymbol{u}}_{\hat{\mathbf{p}}^{(\mathrm{n})}} \;=\; \tilde{\boldsymbol{f}}_{\hat{\mathbf{p}}^{(\mathrm{n})}} \tag{3.23}$$

with

$$\check{\boldsymbol{K}}_{\hat{\mathbf{p}}^{(\mathrm{n})}\hat{\mathbf{q}}^{(\mathrm{n})}} \;=\; e^{i\boldsymbol{k}\cdot(\boldsymbol{x}_{\hat{\mathbf{q}}^{(\mathrm{n})}} - \boldsymbol{x}_{\hat{\mathbf{p}}^{(\mathrm{n})}})} \boldsymbol{K}_{\hat{\mathbf{p}}^{(\mathrm{n})}\hat{\mathbf{q}}^{(\mathrm{n})}} \;\in\; \mathbb{C}^{\mathfrak{d}\times\mathfrak{d}}. \tag{3.24}$$

We note from (3.14) and (3.24) that $\check{\boldsymbol{K}}^{*}_{\hat{\mathbf{p}}^{(\mathrm{n})}\hat{\mathbf{q}}^{(\mathrm{n})}} = \check{\boldsymbol{K}}_{\hat{\mathbf{q}}^{(\mathrm{n})}\hat{\mathbf{p}}^{(\mathrm{n})}}$ and

$$\sum_{\hat{\mathbf{q}}^{(\mathrm{n})}} \check{\boldsymbol{K}}_{\hat{\mathbf{p}}^{(\mathrm{n})}\hat{\mathbf{q}}^{(\mathrm{n})}} \cdot \tilde{\boldsymbol{u}}_{\hat{\mathbf{q}}^{(\mathrm{n})}} \;=\; \sum_{i=1}^{N_{\mathrm{n}}} \Big(\sum_{\boldsymbol{r}\in\boldsymbol{R}} \check{\boldsymbol{K}}_{\hat{\mathbf{p}}^{(\mathrm{n})}(\mathbf{i}+\hat{\mathbf{r}}^{(\mathrm{n})})} \Big) \cdot \tilde{\boldsymbol{u}}_{\mathbf{i}}, \tag{3.25}$$

where $\mathbf{i}$ and $\hat{\mathbf{r}}^{(\mathrm{n})}$ are defined in (3.6). As a result, the system of algebraic equations (3.23) governing the periodic part, $\tilde{\boldsymbol{u}}_{\hat{\mathbf{p}}^{(\mathrm{n})}}$, of the Bloch wave $\boldsymbol{u}_{\hat{\mathbf{p}}^{(\mathrm{n})}}$, can be conveniently rewritten for the unit cell containing the origin ($\boldsymbol{r}=\mathbf{0}$) which yields

$$\sum_{j=1}^{N_{\mathrm{n}}} \tilde{\boldsymbol{K}}_{\mathbf{ij}} \cdot \tilde{\boldsymbol{u}}_{\mathbf{j}} \,-\, \omega^2 M_{\mathbf{i}}\, \tilde{\boldsymbol{u}}_{\mathbf{i}} \;=\; \tilde{\boldsymbol{f}}_{\mathbf{i}}, \quad i \in \overline{1, N_{\mathrm{n}}}, \tag{3.26}$$

where $\mathbf{j} := (j, 0, \ldots, 0) \in \mathbb{Z}^{\mathfrak{p}}$ and

$$\tilde{\boldsymbol{K}}_{\mathbf{ij}} \;=\; \sum_{\boldsymbol{r}\in\boldsymbol{R}} \check{\boldsymbol{K}}_{\mathbf{i}(\mathbf{j}+\hat{\mathbf{r}}^{(\mathrm{n})})} \;=\; \tilde{\boldsymbol{K}}^{*}_{\mathbf{ji}}, \tag{3.27}$$

see Appendix B.3 for proof. We emphasize again that the sum in (3.27) is finite due to the fact that the compatibility vectors $\boldsymbol{c}^{e}_{\hat{\mathbf{p}}^{(\mathrm{b})}\hat{\mathbf{q}}^{(\mathrm{n})}}$ and $\boldsymbol{c}^{\phi}_{\hat{\mathbf{p}}^{(\mathrm{h})}\hat{\mathbf{q}}^{(\mathrm{n})}}$ used to construct $\check{\boldsymbol{K}}_{\mathbf{i}(\mathbf{j}+\hat{\mathbf{r}}^{(\mathrm{n})})}$ via (3.13) and (3.24) are non-trivial only over a disk of *finite radius* in terms of $\|\hat{\mathbf{p}}^{(\mathrm{b})} - \hat{\mathbf{q}}^{(\mathrm{n})}\|$ and $\|\hat{\mathbf{p}}^{(\mathrm{h})} - \hat{\mathbf{q}}^{(\mathrm{n})}\|$, respectively. For further reference, the $\mathfrak{d}N_{\mathrm{n}} \times \mathfrak{d}N_{\mathrm{n}}$ system of equations (3.26) for the components of $\tilde{\boldsymbol{u}}_{\mathbf{i}}$ can be compactly expressed in matrix form as

$$\tilde{\boldsymbol{K}}_{\boldsymbol{k}} \cdot \tilde{\boldsymbol{u}} \,-\, \omega^2 \tilde{\boldsymbol{M}} \cdot \tilde{\boldsymbol{u}} \;=\; \tilde{\boldsymbol{f}}_{\boldsymbol{k}}, \tag{3.28}$$

where $\tilde{\boldsymbol{u}}, \tilde{\boldsymbol{f}}_{\boldsymbol{k}} \in \mathbb{C}^{\mathfrak{d}N_{\mathrm{n}}}$; $\tilde{\boldsymbol{M}} \in \mathbb{R}^{\mathfrak{d}N_{\mathrm{n}}\times\mathfrak{d}N_{\mathrm{n}}}$ is diagonal, and $\tilde{\boldsymbol{K}}_{\boldsymbol{k}} \in \mathbb{C}^{\mathfrak{d}N_{\mathrm{n}}\times\mathfrak{d}N_{\mathrm{n}}}$ is Hermitian thanks to (3.27) and positive semi-definite. Here, we use subscript $\boldsymbol{k}$ for denoting the stiffness matrix and the source term to highlight their respective dependencies on the wave vector.

To account for situations where the continuum POS S is subjected to *periodic* homogeneous Dirichlet boundary conditions, we introduce an auxiliary rectangular matrix $\boldsymbol{G} \in \mathbb{R}^{\mathfrak{d}N_\mathrm{n} \times \mathfrak{m}}$ with $\mathfrak{m} \leqslant \mathfrak{d}N_\mathrm{n}$ that prevents the motion of constrained nodes via mapping

$$\tilde{u} = \boldsymbol{G} \cdot \hat{\boldsymbol{u}}, \quad \hat{\boldsymbol{u}} \in \mathbb{C}^{\mathfrak{m}}, \quad \boldsymbol{G}^{\mathrm{T}} \cdot \boldsymbol{G} = \boldsymbol{I}, \tag{3.29}$$

where $\boldsymbol{I}$ is the $\mathbb{R}^{\mathfrak{m}} \times \mathbb{R}^{\mathfrak{m}}$ identity matrix and $\hat{\boldsymbol{u}}$ collects the non-trivial degrees of freedom within the unit cell. On substituting (3.29) in (3.28) and multiplying the result by $\boldsymbol{G}^{\mathrm{T}}$, we find that $\hat{\boldsymbol{u}}$ satisfies

$$\hat{\boldsymbol{K}}_{\boldsymbol{k}} \cdot \hat{\boldsymbol{u}} \, - \, \omega^2 \hat{\boldsymbol{M}} \cdot \hat{\boldsymbol{u}} \, = \, \hat{\boldsymbol{f}}_{\boldsymbol{k}}, \tag{3.30}$$

where $\hat{\boldsymbol{f}} \in \mathbb{C}^{\mathfrak{m}}$, $\hat{\boldsymbol{M}} \in \mathbb{R}^{\mathfrak{m} \times \mathfrak{m}}$ is block-diagonal and symmetric, and $\hat{\boldsymbol{K}}_{\boldsymbol{k}} \in \mathbb{C}^{\mathfrak{m} \times \mathfrak{m}}$ is Hermitian positive semi-definite according to

$$\hat{\boldsymbol{K}}_{\boldsymbol{k}} = \boldsymbol{G}^{\mathrm{T}} \cdot \tilde{\boldsymbol{K}}_{\boldsymbol{k}} \cdot \boldsymbol{G} = \hat{\boldsymbol{K}}_{\boldsymbol{k}}^{*}, \qquad \hat{\boldsymbol{M}} = \boldsymbol{G}^{\mathrm{T}} \cdot \tilde{\boldsymbol{M}} \cdot \boldsymbol{G} = \hat{\boldsymbol{M}}^{\mathrm{T}}, \qquad \hat{\boldsymbol{f}}_{\boldsymbol{k}} = \boldsymbol{G}^{\mathrm{T}} \cdot \tilde{\boldsymbol{f}}_{\boldsymbol{k}}. \tag{3.31}$$

In the sequel, we designate by $\tilde{\boldsymbol{v}} \in \mathbb{C}^{\mathfrak{d}N_\mathrm{n}}$ the product $\boldsymbol{G} \cdot \hat{\boldsymbol{v}}$ for some $\hat{\boldsymbol{v}} \in \mathbb{C}^{\mathfrak{m}}$.

3.1.4 Eigenvalue problem and "Origamons"

Thanks to fact that $\hat{\boldsymbol{K}}_{\boldsymbol{k}}$ is Hermitian and positive semi-definite, the source term-free counterpart of (3.30) generates a finite sequence of eigenvalues $\tilde{\lambda}_n \in \mathbb{R}^{+}$ and affiliated eigenvectors $\hat{\boldsymbol{\phi}}_n \in \mathbb{C}^{\mathfrak{m}}$ ($n \in \overline{1, \mathfrak{m}}$) that satisfy

$$\hat{\boldsymbol{K}}_{\boldsymbol{k}} \cdot \hat{\boldsymbol{\phi}}_n \, - \, \tilde{\lambda}_n \hat{\boldsymbol{M}} \cdot \hat{\boldsymbol{\phi}}_n \, = \, \boldsymbol{0}. \tag{3.32}$$

Since the eigenvectors are orthogonal with respect to the mass matrix $\hat{\boldsymbol{M}}$, we conveniently normalize them so that

$$\hat{\boldsymbol{\phi}}_n^{*} \cdot \hat{\boldsymbol{M}} \cdot \hat{\boldsymbol{\phi}}_m \, = \, \delta_{nm}, \qquad m, n \in \overline{1, \mathfrak{m}}, \tag{3.33}$$

where the superscript "*" denotes conjugate transpose and δ_{nm} is the Kronecker delta. For given $\boldsymbol{k} \in \mathbb{R}^{\mathfrak{p}}$, the DPOS S' thus permits the propagation of "Origamons", which are free Bloch waves $\tilde{\boldsymbol{\phi}}_n(\boldsymbol{k}) e^{i(\boldsymbol{k} \cdot \boldsymbol{x}_{\hat{\mathfrak{p}}} - \omega_n t)}$, at eigenfrequency $\omega_n(\boldsymbol{k}) = (\tilde{\lambda}_n)^{\frac{1}{2}}$. The set of all wavenumber-eigenfrequency pairs $(\boldsymbol{k}, \omega_n) \in \mathbb{R}^{\mathfrak{p}} \times \mathbb{R}^{+}$ defines the *Bloch dispersion relationship* of the DPOS. The latter is periodic in the reciprocal space, and is described completely by the first Brillouin zone $\mathcal{B}$ of the lattice. Since the eigenvectors $\hat{\boldsymbol{\phi}}_n$ form a complete basis in $\mathbb{C}^{\mathfrak{m}}$, for any $\omega^2 \neq \tilde{\lambda}_n$ ($n = \overline{1, \mathfrak{m}}$) the solution $\hat{\boldsymbol{u}}$ of (3.31) can be

expanded as

$$\hat{\boldsymbol{u}} \;=\; \sum_{n=1}^{\mathfrak{m}} \alpha_n \hat{\boldsymbol{\phi}}_n. \tag{3.34}$$

On solving for α_n from (3.31), one obtains

$$\tilde{\boldsymbol{u}} = -\sum_{n=1}^{\mathfrak{m}} \frac{\overline{\tilde{\boldsymbol{\phi}}_n} \cdot \tilde{\boldsymbol{f}}_{\boldsymbol{k}}}{(\omega^2 - \tilde{\lambda}_n)}\; \tilde{\boldsymbol{\phi}}_n, \tag{3.35}$$

Thanks to the linearity of (3.17), the total motion at node $\hat{\mathbf{p}}^{(\mathrm{n})}$ is then computed via (3.19) as

$$\boldsymbol{u}_{\hat{\mathbf{p}}^{(\mathrm{n})}} = \frac{1}{|\mathcal{C}|} \int_{\boldsymbol{k}_s + \mathcal{C}} \Big(-\sum_{n=1}^{\mathfrak{m}} \frac{\overline{\tilde{\boldsymbol{\phi}}_n} \cdot \tilde{\boldsymbol{f}}_{\boldsymbol{k}}}{(\omega^2 - \tilde{\lambda}_n)}\; \tilde{\boldsymbol{\phi}}_n\big|_{\hat{\mathbf{p}}^{(\mathrm{n})}}\; e^{i\boldsymbol{k}\cdot\boldsymbol{x}_{\hat{\mathbf{p}}^{(\mathrm{n})}}} \Big)\, \mathrm{d}\boldsymbol{k}, \tag{3.36}$$

where $\tilde{\boldsymbol{\phi}}_n\big|_{\hat{\mathbf{p}}^{(\mathrm{n})}}$ is the value of $\tilde{\boldsymbol{\phi}}_n$ (interpreted as $\boldsymbol{R}$-periodic vector) at $\hat{\mathbf{p}}^{(\mathrm{n})}$. For future reference, we note that the weight of the nth Bloch eigenvector in (3.36) is inversely proportional to the spectral distance $|\omega^2 - \tilde{\lambda}_n|$.

3.1.5 Scaling

Let $\omega_n(\boldsymbol{k}) = \tilde{\lambda}_n^{\frac{1}{2}}(\boldsymbol{k})$. In what follows, we consider the spectral neighborhood of the wavenumber-frequency pair

$$\big(\boldsymbol{k}_s, \omega_n(\boldsymbol{k}_s)\big) \in \overline{\mathcal{B}} \times \mathbb{R}, \qquad n \in \overline{1, \mathfrak{m}},$$

and we assume all quantities to be *a priori* normalized by some reference "mass" m_0, "stiffness" κ_0 and lengthscale ℓ_0. On making use of the short-hand notation $\tilde{\lambda}_n = \tilde{\lambda}_n(\boldsymbol{k}_s)$ and $\omega_n = \omega_n(\boldsymbol{k}_s)$ hereon, we next introduce the perturbation parameter $\epsilon = o(1)$ defining the spectral neighborhood as

$$\begin{aligned} &\boldsymbol{k} = \boldsymbol{k}_s + \epsilon\hat{\boldsymbol{k}}, \qquad \omega^2 = \tilde{\lambda}_n + \epsilon\check{\sigma}\check{\omega}^2 + \epsilon^2\hat{\sigma}\hat{\omega}^2, \\ &\check{\sigma}, \hat{\sigma} \in \{-1, 0, 1\}, \quad \check{\sigma}\,\hat{\sigma} = 0, \quad |\check{\sigma} + \hat{\sigma}| = 1. \end{aligned} \tag{3.37}$$

Remark 20 *Through the design of $\check{\sigma}$ and $\hat{\sigma}$, frequency separation parameters $\check{\omega}$ and $\hat{\omega}$ are meant to be used in the "either or" sense, depending on the driving frequency (when $\tilde{\boldsymbol{f}}_{\boldsymbol{k}} \neq 0$) and the local geometry of germane dispersion surface (when $\tilde{\boldsymbol{f}}_{\boldsymbol{k}} = 0$).*

Specifically when $\tilde{\boldsymbol{f}}_{\boldsymbol{k}} \neq 0$ whereby ω is given, we have

$$\omega^2 - \tilde{\lambda}_n \;=\; \begin{cases} O(\epsilon) & \Rightarrow \quad |\check{\sigma}| = 1, \quad \hat{\sigma} \;= 0 \\ O(\epsilon^2) & \Rightarrow \quad \check{\sigma} \;= 0, \quad |\hat{\sigma}| = 1 \end{cases} \tag{3.38}$$

In the context of (3.37), the reduced stiffness matrix $\hat{\boldsymbol{K}}_{\boldsymbol{k}}$ can be conveniently expanded as

$$\hat{\boldsymbol{K}}_{\boldsymbol{k}} \;=\; \sum_{m=0}^{\infty} \epsilon^m (i\hat{\boldsymbol{k}})^m : \hat{\boldsymbol{K}}^{(\mathrm{m})}, \qquad \hat{\boldsymbol{K}}^{(\mathrm{m})} \;=\; \frac{(-i)^m}{m!} \Big[\frac{\partial^m}{\partial \boldsymbol{k}^m} \hat{\boldsymbol{K}}_{\boldsymbol{k}} \Big]_{\boldsymbol{k}=\boldsymbol{k}_s} \tag{3.39}$$

where $(i\hat{\boldsymbol{k}})^m := (i\hat{\boldsymbol{k}}) \otimes (i\hat{\boldsymbol{k}}) \otimes \cdots \otimes (i\hat{\boldsymbol{k}})$ m times; $\hat{\boldsymbol{K}}^{(0)} \in \mathbb{C}^{\mathtt{m}\times\mathtt{m}}$; $\hat{\boldsymbol{K}}^{(m)} \in \mathbb{C}^{\mathtt{p}^m\times\mathtt{m}\times\mathtt{m}}$ for $m>0$, and ":" stands for the usual product, the inner product, and the m-tuple matrix contraction when $m = 0$, $m = 1$ and $m > 1$, respectively.

Remark 21 *For clarity, we note that the dependence of $\hat{\boldsymbol{K}}_{\boldsymbol{k}}$ on the wave vector is confined to the factor $e^{i\boldsymbol{k}\cdot(\boldsymbol{x}_{\hat{\mathbf{q}}^{(n)}} - \boldsymbol{x}_{\hat{\mathbf{p}}^{(n)}})}$ appearing in* (3.24)*, which permits explicit evaluation of $\hat{\boldsymbol{K}}^{(m)}$, see Appendix B.4 for details. As shown there, $\hat{\boldsymbol{K}}^{(m)}$ is Hermitian (resp. skew-Hermitian) in the last two indices for even (resp. odd) m. In what follows, matrices $\hat{\boldsymbol{K}}^{(m)}$ are shown to provide a lynchpin for the homogenization of wave motion in DPOS.*

Given (3.39), we are now in position to postulate the ansatz

$$\hat{\boldsymbol{u}} \;=\; \epsilon^{-2} \sum_{m=0}^{\infty} \epsilon^m \hat{\boldsymbol{u}}_m, \tag{3.40}$$

catering the asymptotic expansion of (3.30), see also [72, 23, 75] in the context of continuous systems. For completeness, we note that the presence of the factor ϵ^{-2} in front of the series is motivated by (3.35) and the smallness of $|\omega^2 - \tilde{\lambda}_n(\boldsymbol{k})|$ according to (3.37). On inserting (3.37)–(3.40) into (3.23) and letting $\tilde{\boldsymbol{f}}_{\boldsymbol{k}} = O(1)$, we obtain a cascade of governing equations, namely

$$O(\epsilon^{-2}): \qquad -\tilde{\lambda}_n \hat{\boldsymbol{M}} \cdot \hat{\boldsymbol{u}}_0 + \hat{\boldsymbol{K}}^{(0)} \cdot \hat{\boldsymbol{u}}_0 \;=\; \boldsymbol{0}, \tag{3.41}$$

$$O(\epsilon^{-1}): \quad -\tilde{\lambda}_n \hat{\boldsymbol{M}} \cdot \hat{\boldsymbol{u}}_1 + \hat{\boldsymbol{K}}^{(0)} \cdot \hat{\boldsymbol{u}}_1 + (i\hat{\boldsymbol{k}}) \cdot \hat{\boldsymbol{K}}^{(1)} \cdot \hat{\boldsymbol{u}}_0 - \check{\sigma}\check{\omega}^2 \hat{\boldsymbol{M}} \cdot \hat{\boldsymbol{u}}_0 \;=\; \boldsymbol{0}, \tag{3.42}$$

$$O(1): \quad -\hat{\lambda}_n \hat{\boldsymbol{M}} \cdot \hat{\boldsymbol{u}}_2 + \hat{\boldsymbol{K}}^{(0)} \cdot \hat{\boldsymbol{u}}_2 + (i\hat{\boldsymbol{k}}) \cdot \hat{\boldsymbol{K}}^{(1)} \cdot \hat{\boldsymbol{u}}_1 + (i\hat{\boldsymbol{k}})^2 : \hat{\boldsymbol{K}}^{(2)} \cdot \hat{\boldsymbol{u}}_0$$
$$-\check{\sigma}\check{\omega}^2 \hat{\boldsymbol{M}} \cdot \hat{\boldsymbol{u}}_1 - \hat{\sigma}\hat{\omega}^2 \hat{\boldsymbol{M}} \cdot \hat{\boldsymbol{u}}_0 \;=\; \hat{\boldsymbol{f}}_{\boldsymbol{k}}. \tag{3.43}$$

3.1.6 Averaging operators and effective motion

Let $n_q \in \overline{1,\mathfrak{m}}$ ($q = \overline{1,Q}$, $Q < \mathfrak{m}$) collect the "nearby" dispersion branches, $\omega_{n_q}(\boldsymbol{k})$ traversing the vicinity of $(\boldsymbol{k}_s, \tilde{\lambda}_n^{1/2})$, where we aim to pursue ansatz (3.40). With such setup in mind, we introduce the *averaging* operators $\langle\cdot\rangle^{n_q}$ and $\langle\cdot\rangle_\rho^{n_q}$, for tensors $\hat{\boldsymbol{T}} \in \mathbb{C}^{\mathfrak{p}^m\times\mathfrak{m}}$ ($m \in \mathbb{N}$) and vectors $\hat{\boldsymbol{v}} \in \mathbb{C}^{\mathfrak{m}}$ respectively, as well as the vector space $\mathcal{H} \subset \mathbb{C}^{\mathfrak{m}}$ as

$$\begin{aligned}
\langle\hat{\boldsymbol{T}}\rangle^{n_q} &= \hat{\boldsymbol{T}}\cdot\overline{\hat{\boldsymbol{\phi}}_{n_q}} \in (\mathbb{C}^{\mathfrak{p}})^m, && (3.44)\\
\langle\hat{\boldsymbol{v}}\rangle_\rho^{n_q} &= \hat{\boldsymbol{\phi}}_{n_q}^*\cdot\hat{\boldsymbol{M}}\cdot\hat{\boldsymbol{v}} \in \mathbb{C}, && (3.45)\\
\mathcal{H} &= \{\hat{\boldsymbol{v}}\in\mathbb{C}^{\mathfrak{m}}\colon \langle\hat{\boldsymbol{v}}\rangle_\rho^{n_q} = 0,\ q\in\overline{1,Q}\}. && (3.46)
\end{aligned}$$

For $\hat{\boldsymbol{v}} = \hat{\boldsymbol{u}}_m$, we will use the short-hand notation

$$u_{mq}(\epsilon\hat{\boldsymbol{k}}) \;:=\; \langle\hat{\boldsymbol{u}}_m\rangle_\rho^{n_q}, \qquad q = \overline{1,Q}. \tag{3.47}$$

On the basis of (3.40) and (3.47), we can adapt the definition of *effective solution* [23] at wavenumber $\boldsymbol{k}_s + \epsilon\hat{\boldsymbol{k}}$ as

$$\langle\hat{\boldsymbol{u}}\rangle_\rho^{n_q}(\epsilon\hat{\boldsymbol{k}}) \;=\; \sum_{m=0}^{\infty}\epsilon^{m-2}u_{mq}, \qquad q = \overline{1,Q}, \tag{3.48}$$

which then provides the basis for computing the (set of) effective solution(s) near $\boldsymbol{k}_s$ in the physical space as

$$\langle\boldsymbol{u}_{\hat{\mathfrak{p}}}\rangle_\rho^{n_q} \;=\; |\mathcal{C}|^{-1}\int_{\mathcal{C}}\langle\hat{\boldsymbol{u}}\rangle_\rho^{n_q}(\epsilon\hat{\boldsymbol{k}})\, e^{i(\boldsymbol{k}_s+\epsilon\hat{\boldsymbol{k}})\cdot\boldsymbol{x}_{\hat{\mathfrak{p}}}}\,\mathrm{d}(\epsilon\hat{\boldsymbol{k}}), \quad \boldsymbol{x}_{\hat{\mathfrak{p}}}\in\mathbb{R}^{\mathfrak{p}}. \tag{3.49}$$

Remark 22 *In situations where $Q=1$ and $n_1=n$ which corresponds to the case of an isolated branch, $\langle\cdot\rangle^{n_q}$, $\langle\cdot\rangle_\rho^{n_q}$ and u_{mq} will be conveniently denoted as $\langle\cdot\rangle$, $\langle\cdot\rangle_\rho$ and u_m, respectively. In this case,* (3.48) *and* (3.49) *reduce to*

$$\langle\hat{\boldsymbol{u}}\rangle_\rho(\epsilon\hat{\boldsymbol{k}}) \;=\; \sum_{m=0}^{\infty}\epsilon^{m-2}u_m, \qquad \langle\boldsymbol{u}_{\hat{\mathfrak{p}}^{(n)}}\rangle_\rho \;=\; |\mathcal{C}|^{-1}\int_{\mathcal{C}}\langle\hat{\boldsymbol{u}}\rangle_\rho(\epsilon\hat{\boldsymbol{k}})\, e^{i(\boldsymbol{k}_s+\epsilon\hat{\boldsymbol{k}})\cdot\boldsymbol{x}_{\hat{\mathfrak{p}}^{(n)}}}\, d(\epsilon\hat{\boldsymbol{k}}). \tag{3.50}$$

Remark 23 *When $\hat{\boldsymbol{f}}_{\boldsymbol{k}}=\boldsymbol{0}$ identically, the applicability of any effective model for given perturbation vector $\hat{\boldsymbol{k}}$ also implies its validity for $\alpha\hat{\boldsymbol{k}}$, $\alpha\leqslant O(1)$ thanks to the arbitrariness of $\epsilon = o(1)$ in* (3.41)–(3.43). *When $\hat{\boldsymbol{f}}_{\boldsymbol{k}} \neq \boldsymbol{0}$, on the other hand, this implication holds as long as the pair $(\boldsymbol{k}_s+\alpha\epsilon\hat{\boldsymbol{k}},\omega)$ does not lie on the germane dispersion branch, i.e. as long as $\omega_{n_q}(\boldsymbol{k}_s+\alpha\epsilon\hat{\boldsymbol{k}}) \neq \omega$. To provide a focus for the analysis, we hereon (i) identify the wavenumber perturbations by their direction $\hat{\boldsymbol{k}}/\|\hat{\boldsymbol{k}}\|$, and (ii) for $f_{\boldsymbol{k}} \neq 0$ we restrict*

our consideration to $\hat{\boldsymbol{k}} \in \mathcal{K}_\epsilon$*, where*

$$\mathcal{K}_\epsilon = \{\hat{\boldsymbol{k}} \in \mathbb{R}^{\mathfrak{d}} : \epsilon\hat{\boldsymbol{k}} \in \mathcal{C},\ \omega_{n_q}^{(m)}(\boldsymbol{k}_s + \epsilon\hat{\boldsymbol{k}}) \neq \omega\}, \qquad q = \overline{1, Q}, \tag{3.51}$$

where $\omega_{n_q}^{(m)}(\boldsymbol{k})$ *is the* m*th order approximation of* $\omega_{n_q}(\boldsymbol{k})$ *affiliated with* u_{mq} *in* (3.47)*. We will relax this restriction later in Section 3.3.1.*

3.2 Effective motion

We study in this section wave motion in unbounded DPOSs by seeking the leading-order effective motion equations of (3.23) in the spectral vicinity of eigenfrequency clusters that include simple and/or repeated eigenfrequencies.

3.2.1 Simple eigenvalue

Considering the eigenvalue problem (3.32) at $\boldsymbol{k} = \boldsymbol{k}_s$, the solution of (3.41) in the vicinity of a simple eigenfrequency ω_n is expressed as

$$\hat{\boldsymbol{u}}_0 \ = \ u_0\hat{\boldsymbol{\phi}}_n, \quad u_0 \in \mathbb{C}, \tag{3.52}$$

where $u_0 = \langle\hat{\boldsymbol{u}}_0\rangle_\rho$. Then, by inserting (3.52) into (3.42) and projecting (3.42) onto $\hat{\boldsymbol{\phi}}_n$, we obtain the averaged $O(\epsilon^{-1})$ statement as

$$-\,(\boldsymbol{\theta}^{(0)}\cdot(i\hat{\boldsymbol{k}}) + \check{\sigma}\check{\omega}^2)u_0 \ = \ 0, \tag{3.53}$$

where

$$\boldsymbol{\theta}^{(0)} \ = \ -\langle\hat{\boldsymbol{K}}^{(1)}\cdot\,\hat{\boldsymbol{\phi}}_n\rangle \ \in \ i\mathbb{R}^{\mathfrak{p}} \tag{3.54}$$

thanks to the fact that $\hat{\boldsymbol{K}}^{(1)}$ is skew-Hermitian in the last two arguments, see Remark 21. On substituting (3.52) in (3.42), one finds by the linearity of the problem that

$$\hat{\boldsymbol{u}}_1(\boldsymbol{x}) \ = \ u_0\ (i\hat{\boldsymbol{k}})\cdot\boldsymbol{\chi}^{(1)} \ + \ u_1\hat{\boldsymbol{\phi}}_n, \quad u_1 \in \mathbb{C}, \tag{3.55}$$

where $u_1 = \langle\hat{\boldsymbol{u}}_1\rangle_\rho$, $\boldsymbol{\chi}^{(1)} \in \mathbb{C}^{\mathfrak{p}\times\mathfrak{m}}$, and $\boldsymbol{\chi}_j^{(1)} := (\boldsymbol{i}_j)\cdot\boldsymbol{\chi}^{(1)} \in \mathcal{H}$ $(j \in \overline{1,\mathfrak{p}})$ uniquely solve the respective linear systems

$$-\,\tilde{\lambda}_n\hat{\boldsymbol{M}}\cdot\boldsymbol{\chi}_j^{(1)} + \hat{\boldsymbol{K}}^{(0)}\cdot\boldsymbol{\chi}_j^{(1)} + (\boldsymbol{i}_j)\cdot\hat{\boldsymbol{K}}^{(1)}\cdot\hat{\boldsymbol{\phi}}_n + \boldsymbol{\theta}^{(0)}\cdot(\boldsymbol{i}_j)\,\hat{\boldsymbol{M}}\cdot\hat{\boldsymbol{\phi}}_n = \boldsymbol{0}. \tag{3.56}$$

We next consider the $O(1)$ field equation (3.43). On recalling (3.52) and (3.55), we

can project (3.43) on $\tilde{\boldsymbol{\phi}}_n$ to obtain the averaged $O(1)$ statement

$$-\big(\boldsymbol{\mu}^{(0)} : (i\hat{\boldsymbol{k}})^2 + \hat{\sigma}\hat{\omega}^2\big)u_0 - (\boldsymbol{\theta}^{(0)}\cdot(i\hat{\boldsymbol{k}}) + \check{\sigma}\check{\omega}^2)u_1 \;=\; \langle\hat{\boldsymbol{f}}_{\boldsymbol{k}}\rangle, \tag{3.57}$$

where $\boldsymbol{\mu}^{(0)} \in \mathbb{C}^{\mathfrak{p}\times\mathfrak{p}}$ is the effective "stiffness" matrix whose components $\mu^{(0)}_{q_1q_2}$ for $q_1, q_2 \in \overline{1,\mathfrak{p}}$ are given by

$$\begin{aligned}\mu^{(0)}_{q_1q_2} \;&=\; -\sum_{q_3=1}^{\mathfrak{m}}\sum_{q_4=1}^{\mathfrak{m}} \hat{K}^{(2)}_{q_1q_2q_3q_4}(\hat{\phi}_n)_{q_4}\overline{(\hat{\phi}_n)_{q_3}} \\ &\quad -\sum_{q_3=1}^{\mathfrak{m}}\sum_{q_4=1}^{\mathfrak{m}} \tfrac{1}{2}\big(\hat{K}^{(1)}_{q_1q_3q_4}(\chi^{(1)})_{q_2q_4} + \hat{K}^{(1)}_{q_2q_3q_4}(\chi^{(1)})_{q_1q_4}\big)\overline{(\hat{\phi}_n)_{q_3}}.\end{aligned} \tag{3.58}$$

Claim 12 *For any $\boldsymbol{k}_s \in \overline{\mathcal{B}}$, effective tensor $\boldsymbol{\mu}^{(0)}$ is real-valued and symmetric, i.e. $\boldsymbol{\mu}^{(0)} \in \mathbb{R}^{\mathfrak{p}\times\mathfrak{p}}$, see Appendix B.5 for proof.*

Claim 13 *For wavenumbers $\boldsymbol{k}_s = \frac{1}{2}\sum_{l=1}^{\mathfrak{p}} n_l\boldsymbol{e}^l$, $n_l \in \{-1,0,1\}$, which include the origin and apexes of the first Brillouin zone $\mathcal{B}$, the Bloch wave $\boldsymbol{\phi}_n|_{\mathfrak{i}} = \tilde{\boldsymbol{\phi}}_n|_{\mathfrak{i}}e^{i\boldsymbol{k}\cdot\boldsymbol{x}_{\mathfrak{i}}}$ is real-valued up to a scalar multiplier and the corresponding effective coefficient $\boldsymbol{\theta}^{(0)} = \boldsymbol{0}$. See Appendix B.5 for proof.*

In the sequel, we treat separately the situations when $\boldsymbol{\theta}^{(0)} \neq \boldsymbol{0}$ and $\boldsymbol{\theta}^{(0)} = \boldsymbol{0}$, which we address next.

Effective model for non-trivial $\boldsymbol{\theta}^{(0)}$

As can be seen from the foregoing analysis, the presence of the source term in the $O(1)$ statement (3.57) requires that its $O(\epsilon^{-1})$ predecessor (3.53) be satisfied *identically*. When $\hat{\boldsymbol{f}}_{\boldsymbol{k}} \neq 0$ and $\omega^2 - \omega_n^2 = O(\epsilon)$ whereby $|\check{\sigma}| = 1$ due to (3.38), we must have $u_0 = 0$ in (3.53) thanks to Remark 23 which guarantees that the multiplier $\boldsymbol{\theta}^{(0)}\cdot(i\hat{\boldsymbol{k}}) + \check{\sigma}\check{\omega}^2$ is non-trivial. As a result when $\boldsymbol{\theta}^{(0)} \neq \boldsymbol{0}$, from (3.57) we obtain the leading-order effective "Dirac" equation

$$-(\boldsymbol{\theta}^{(0)}\cdot(i\hat{\boldsymbol{k}}) + \check{\sigma}\check{\omega}^2)u_1 \;=\; \langle\hat{\boldsymbol{f}}_{\boldsymbol{k}}\rangle. \tag{3.59}$$

A similar treatment can be pursued for the situation when $\omega^2 - \omega_n^2 = O(\epsilon^2)$, in which case $|\hat{\sigma}| = 1$. This case is not addressed for reasons of brevity.

In the absence of the source term $\hat{\boldsymbol{f}}_{\boldsymbol{k}}$, on the other hand, the existence of a non-trivial wavefield solving (3.53) and (3.57) independently requires that $|\check{\sigma}| = 1$. In this case, (3.59) with $\langle\tilde{f}_{\boldsymbol{k}}\rangle = 0$ furnishes the leading-order asymptotic approximation of the

dispersion relationship and group velocity near $(\boldsymbol{k}_s, \omega_n > 0)$ as

$$\omega_n^2(\boldsymbol{k}) \;=\; \omega_n^2 - i\boldsymbol{\theta}^{(0)}\cdot(\epsilon\hat{\boldsymbol{k}}), \qquad \boldsymbol{c}_g = \frac{\mathrm{d}\omega_n(\boldsymbol{k})}{\mathrm{d}\boldsymbol{k}} \;=\; \frac{-1}{2\omega_n} i\boldsymbol{\theta}^{(0)} \tag{3.60}$$

respectively, where ω_n (without an argument) refers to $\omega_n(\boldsymbol{k}_s)$ as stated earlier. Geometrically, (3.60) describes the nth dispersion (hyper-) surface locally as a (hyper-) plane, where $\boldsymbol{c}_g$ signifies its tangent slope. Practically, (3.60) can be used to evaluate the energy velocity of DPOSs by only solving (3.32) for wavenumbers spanning the first Brillouin zone without the need for numerical differentiation.

Effective model for trivial $\boldsymbol{\theta}^{(0)}$

When $\hat{\boldsymbol{f}}_{\boldsymbol{k}} \neq 0$ and $\omega^2 - \omega_n^2 = O(\epsilon^2)$, we have that $|\hat{\sigma}| = 1$ thanks to (3.38). In this case the $O(\epsilon^{-1})$ statement (3.53) is satisfied identically, while its $O(1)$ companion (3.57) produces the effective "wave" equation

$$-\left(\boldsymbol{\mu}^{(0)} : (i\hat{\boldsymbol{k}})^2 + \hat{\sigma}\hat{\omega}^2\right) u_0 \;=\; \langle \hat{\boldsymbol{f}}_{\boldsymbol{k}} \rangle, \tag{3.61}$$

Equation (3.61) in particular describes the response of a DPOS near the *origin* and *apexes* of the first Brillouin zone ($\boldsymbol{k}_s = \frac{1}{2}\sum_l n_l \boldsymbol{e}^l$, $n_l \in \{-1, 0, 1\}$). The nature of such response depends on (i) the sign definiteness of $\boldsymbol{\mu}^{(0)}$, and (ii) the sign of $\omega^2 - \omega_n^2$. For example, when $\boldsymbol{\mu}^{(0)}$ is sign-definite oppositely to the sign of $\omega^2 - \omega_n^2$, the effective medium is "dissipative" in that ω resides inside a band gap [23] terminating at ω_n. On the other hand, when $\omega^2 - \omega_n^2$ and $\boldsymbol{\mu}^{(0)}$ have the same sign, i.e. when the driving frequency ω is in a band pass, the effective medium allows for propagating motion. To the leading order, the isotropy of the induced effective motion hinges on that of $\boldsymbol{\mu}^{(0)}$. Specifically when the eigenvalues of $\boldsymbol{\mu}^{(0)}$ are equal (resp. not equal), the effective motion is isotropic (resp. anisotropic) in $\mathbb{R}^{\mathfrak{p}}$. We will encounter such situations in Section 3.4. Another interesting class of situations arise when the eigenvalues of $\boldsymbol{\mu}^{(0)}$ have opposite signs. In such instances, we observe direction-selective behavior of the original POS, where energy is propagating only in selected directions depending on the (sign of) frequency separation $\omega - \omega_n$.

When $\hat{\boldsymbol{f}}_{\boldsymbol{k}} = 0$, on the other hand, from (3.53) and (3.57) we find that a non-trivial solution is possible only if $\breve{\sigma} = 0$, i.e. $|\hat{\sigma}| = 1$. In this case (3.53) is again satisfied identically, while (3.57) provides the leading-order approximation of dispersion relationship and group velocity near $(\boldsymbol{k}_s, \omega_n > 0)$ as

$$\omega_n^2(\boldsymbol{k}) \;=\; \omega_n^2 + \boldsymbol{\mu}^{(0)} : (\epsilon\hat{\boldsymbol{k}})^2, \qquad \boldsymbol{c}_g(\boldsymbol{k}) \;=\; \frac{1}{\omega_n}\, \boldsymbol{\mu}^{(0)} \cdot (\epsilon\hat{\boldsymbol{k}}). \tag{3.62}$$

We observe from (3.62) that the group velocity (given by the tangent slope of $\omega_n(\boldsymbol{k})$) is near-trivial, while the phase velocity (i.e. the secant slope) is guaranteed to be trivial.

3.2.2 Repeated eigenvalue

Let ω_n be an eigenfrequency of multiplicity $Q>1$, and let n_q ($q=\overline{1,Q}$) be the indexes of the affiliated eigenfunctions.

Remark 24 *In what follows, we assume that $p,q,s \in \overline{1,Q}$ unless stated otherwise. Further, we will use the short-hand notation $\sum_q$ for $\sum_{q=1}^{Q}$.*

With reference to the eigenvalue problem (3.32), the solution of (3.41) in the vicinity of a repeated eigenfrequency ω_n can be decomposed as

$$\hat{\boldsymbol{u}}_0 = \sum_q u_{0q}\ \hat{\boldsymbol{\phi}}_{n_q}, \quad u_{0q} \in \mathbb{C}, \tag{3.63}$$

consistent with the definition (3.47) of u_{0q}. Then, on substituting (3.63) into (3.42) and projecting the result onto $\hat{\boldsymbol{\phi}}_{n_p}$, we obtain the averaged $O(\epsilon^{-1})$ system

$$\sum_q \big(\boldsymbol{\theta}^{(0)}_{pq}\cdot\ (i\hat{\boldsymbol{k}}) + \check{\sigma}\check{\omega}^2\delta_{pq}\big)\, u_{0q}\ =\ 0, \qquad p=\overline{1,Q}, \tag{3.64}$$

where

$$\boldsymbol{\theta}^{(0)}_{pq}\ =\ -\langle \hat{\boldsymbol{K}}^{(1)}\hat{\boldsymbol{\phi}}_{n_q}\rangle^{n_p} \in \mathbb{C}^{\mathfrak{p}}. \tag{3.65}$$

For further reference, system of equations (3.64) can be expressed more compactly in matrix form as

$$(\boldsymbol{A}^{(0)}(\hat{\boldsymbol{k}})\ +\ \check{\sigma}\check{\omega}^2\boldsymbol{I})\boldsymbol{u}_0\ =\ \boldsymbol{0}, \qquad A^{(0)}_{pq}(\hat{\boldsymbol{k}})\ =\ \boldsymbol{\theta}^{(0)}_{pq}\cdot i\hat{\boldsymbol{k}} \qquad (p,q=\overline{1,Q}) \tag{3.66}$$

where $\boldsymbol{I}$ is the $Q\times Q$ identity matrix.

Remark 25 *Thanks to the fact that $\hat{\boldsymbol{K}}^{(1)}$ is skew-Hermitian (see Remark 21), effective vectors $\boldsymbol{\theta}^{(0)}_{qq}$ are imaginary-valued (i.e. $\boldsymbol{\theta}^{(0)}_{qq}\in i\mathbb{R}^{\mathfrak{p}}$) and the coefficient matrix $\boldsymbol{A}^{(0)}\in\mathbb{C}^{Q\times Q}$ is Hermitian.*

On the basis of (3.63)–(3.64), we can solve the $O(\epsilon^{-1})$ field equation (3.42) for $\hat{\boldsymbol{u}}_1$ as

$$\hat{\boldsymbol{u}}_1(\boldsymbol{x}) = \sum_q \big(u_{0q}\ (i\hat{\boldsymbol{k}})\cdot\boldsymbol{\chi}^{(1)}_q(\boldsymbol{x}) + u_{1q}\ \hat{\boldsymbol{\phi}}_{n_q}(\boldsymbol{x})\big), \quad u_{1q}\in\mathbb{C}, \tag{3.67}$$

where $u_{1q} = \langle \hat{\boldsymbol{u}}_1 \rangle_\rho^{n_q}$, $\boldsymbol{\chi}_q^{(1)} \in \mathbb{C}^{\mathfrak{p}\times\mathfrak{m}}$, and $\boldsymbol{\chi}_{qj}^{(1)} := (\boldsymbol{i}_j)\cdot\boldsymbol{\chi}_q^{(1)} \in \mathcal{H}$ $(j \in \overline{1,\mathfrak{p}})$ uniquely solve the respective linear systems

$$-\tilde{\lambda}_n \hat{\boldsymbol{M}}\cdot\boldsymbol{\chi}_{qj}^{(1)} + \hat{\boldsymbol{K}}^{(0)}\cdot\boldsymbol{\chi}_{qj}^{(1)} + (\boldsymbol{i}_j)\cdot\hat{\boldsymbol{K}}^{(1)}\cdot\hat{\boldsymbol{\phi}}_{nq} + \sum_s \boldsymbol{\theta}_{sq}^{(0)}\cdot(\boldsymbol{i}_j)\hat{\boldsymbol{M}}\cdot\hat{\boldsymbol{\phi}}_{n_s} \;=\; \mathbf{0}. \tag{3.68}$$

We next consider the $O(1)$ field equation (3.43). On substituting (3.63) and (3.67) into (3.43) and projecting the result onto $\hat{\boldsymbol{\phi}}_{n_p}$, we obtain the averaged $O(1)$ system

$$-\sum_q \Big(\big(\boldsymbol{\mu}_{pq}^{(0)} : (i\hat{\boldsymbol{k}})^2 + \hat{\sigma}\hat{\omega}^2\delta_{pq}\big)\, u_{0q} + \big(\boldsymbol{\theta}_{pq}^{(0)}\cdot(i\hat{\boldsymbol{k}}) + \check{\sigma}\check{\omega}^2\delta_{pq}\big)\, u_{1q}\Big) \;=\; \langle \hat{\boldsymbol{f}}_{\boldsymbol{k}} \rangle^{n_p}, \qquad p = \overline{1,Q}, \tag{3.69}$$

where $\boldsymbol{\mu}_{pq}^{(0)} \in \mathbb{C}^{\mathfrak{p}\times\mathfrak{p}}$ with components given by

$$\begin{aligned} (\mu_{pq}^{(0)})_{q_1q_2} \;=\; & -\sum_{q_3=1}^{\mathfrak{m}}\sum_{q_4=1}^{\mathfrak{m}} \hat{K}^{(2)}_{q_1q_2q_3q_4}(\hat{\phi}_{n_q})_{q_4}\overline{(\hat{\phi}_{n_p})_{q_3}} \\ & -\sum_{q_3=1}^{\mathfrak{m}}\sum_{q_4=1}^{\mathfrak{m}} \frac{1}{2}\big(\hat{K}^{(1)}_{q_1q_3q_4}(\chi_q^{(1)})_{q_2q_4} + \hat{K}^{(1)}_{q_2q_3q_4}(\chi_q^{(1)})_{q_1q_4}\big)\overline{(\hat{\phi}_{n_p})_{q_3}}. \end{aligned} \tag{3.70}$$

Equations (3.69) can be compactly rewritten in matrix form as

$$-(\boldsymbol{B}^{(0)}(\hat{\boldsymbol{k}}) + \hat{\sigma}\hat{\omega}^2\boldsymbol{I})\boldsymbol{u}_0 - (\boldsymbol{A}^{(0)}(\hat{\boldsymbol{k}}) + \check{\sigma}\check{\omega}^2\boldsymbol{I})\boldsymbol{u}_1 \;=\; \mathbf{f}_0, \tag{3.71}$$

where the components of $\boldsymbol{A}^{(0)}$ are specified in (3.66), while those of $\boldsymbol{B}^{(0)}$ and $\mathbf{f}_0$ are given respectively by

$$B_{pq}^{(0)}(\hat{\boldsymbol{k}}) = \boldsymbol{\mu}_{pq}^{(0)} : (i\hat{\boldsymbol{k}})^2, \qquad \mathrm{f}_{0p} = \langle \hat{\boldsymbol{f}}_{\boldsymbol{k}} \rangle^{n_p} \qquad (p,q = \overline{1,Q}) \tag{3.72}$$

Claim 14 *Matrix $\boldsymbol{B}^{(0)} \in \mathbb{C}^{Q\times Q}$ is Hermitian, see Appendix B.5 for proof.*

Eigenfunction basis

For a fixed direction $\hat{\boldsymbol{k}}/\|\hat{\boldsymbol{k}}\|$, let $\boldsymbol{P} \in \mathbb{C}^{Q\times Q}$ be the matrix of orthonormal eigenvectors stemming from the eigenvalue problem

$$\boldsymbol{A}^{(0)}\boldsymbol{v} \;=\; \tau\boldsymbol{v}. \tag{3.73}$$

In this setting, we conveniently introduce the "recombined" eigenfunctions $\hat{\boldsymbol{\psi}}_q$ as

$$\hat{\boldsymbol{\psi}}_q = \sum_s P_{sq}\, \hat{\boldsymbol{\phi}}_{n_s} \qquad (q \in \overline{1,Q}). \tag{3.74}$$

Then, by taking the eigenfunctions $\{\hat{\boldsymbol{\psi}}_q\}$ as the projection basis in (3.63) and (3.65) instead of $\{\hat{\boldsymbol{\phi}}_{n_q}\}$, we find that

$$\boldsymbol{A}^{(0)}(\hat{\boldsymbol{k}}) = \mathrm{diag}(0,\ldots,0,\tau_{N_0+1},\tau_{N_0+2},\ldots,\tau_Q) \tag{3.75}$$

where $\tau_q = \boldsymbol{\theta}^{(0)}_{qq} \cdot i\hat{\boldsymbol{k}}$ and $0 \leqslant N_0 \leqslant Q$ is the number of trivial diagonal entries of $\boldsymbol{A}^{(0)}$, see also [23, 75] in the context of continuous systems. In this setting, we also define the sub-matrices $\bar{\boldsymbol{B}}^{(0)}(\hat{\boldsymbol{k}}) \in \mathbb{C}^{N_0\times N_0}$ such that

$$\bar{B}^{(0)}_{pq} \;=\; B^{(0)}_{pq}, \qquad p,q \in \overline{1,N_0}.$$

When $N_0 > 0$, we denote by $\bar{\boldsymbol{P}} = [\boldsymbol{v}_1\ \boldsymbol{v}_2\ \ldots\ \boldsymbol{v}_{N_0}]$ the matrix of orthonormal eigenvectors of the eigenvalue problem

$$\bar{\boldsymbol{B}}^{(0)}\boldsymbol{v} \;=\; \tau\boldsymbol{v}, \tag{3.76}$$

and we introduce an auxiliary eigenfunction basis $\hat{\boldsymbol{\psi}}'_q$ as

$$\hat{\boldsymbol{\psi}}'_q \;=\; \begin{cases} \sum_{s=1}^{N_0} \bar{P}_{sq}\, \hat{\boldsymbol{\psi}}_s, & q \leqslant N_0 \\ \hat{\boldsymbol{\psi}}_q, & q > N_0 \end{cases} . \tag{3.77}$$

Remark 26 *Eigenfunctions $\hat{\boldsymbol{\psi}}'_q$ $(q = \overline{1,Q})$ are orthogonal. For simplicity of discussion, we hereon relabel $\hat{\boldsymbol{\psi}}'_q$ as $\hat{\boldsymbol{\phi}}_{n_q}$. In this setting, we have*

$$\bar{\boldsymbol{B}}^{(0)} \;=\; diag(\boldsymbol{\mu}^{(0)}_{11}{:}(i\hat{\boldsymbol{k}})^2,\ldots,\boldsymbol{\mu}^{(0)}_{N_0N_0}{:}(i\hat{\boldsymbol{k}})^2). \tag{3.78}$$

Additional scaling

Depending on the perturbation direction, certain non-zero diagonal entries of $\boldsymbol{A}^{(0)}(\hat{\boldsymbol{k}})$ in (3.75) can become vanishingly small, namely $\tau_q = o(1)$ for some q. In the context of Section 3.2.1, for instance, this situation would correspond to directions $\hat{\boldsymbol{k}}/\|\hat{\boldsymbol{k}}\|$ for

which $\boldsymbol{\theta}^{(0)}\cdot(i\hat{\boldsymbol{k}}) = o(1)$. To account for such situations, we decompose $\boldsymbol{A}^{(0)}$ as

$$\boldsymbol{A}^{(0)}(\hat{\boldsymbol{k}}) \;=\; \mathrm{diag}(0,\ldots,0,\underbrace{\tau_{N_0+1},\ldots,\tau_N}_{O(\epsilon)},\underbrace{\tau_{N+1},\ldots\tau_Q}_{O(1)}) \;=\; \dot{\boldsymbol{A}}^{(0)}(\hat{\boldsymbol{k}}) + \epsilon\ddot{\boldsymbol{A}}^{(0)}(\hat{\boldsymbol{k}}) \tag{3.79}$$

$$\dot{\boldsymbol{A}}^{(0)}(\hat{\boldsymbol{k}}) \;=\; \mathrm{diag}(0,\ldots,0,\underbrace{\tau_{N+1},\ldots\tau_Q}_{O(1)}) \;\in\; \mathbb{R}^{Q\times Q}, \tag{3.80}$$

$$\ddot{\boldsymbol{A}}^{(0)}(\hat{\boldsymbol{k}}) \;=\; \mathrm{diag}(0,\ldots,0,\underbrace{\epsilon^{-1}\tau_{N_0+1},\ldots,\epsilon^{-1}\tau_N}_{O(1)},0,\ldots,0), \;\in\; \mathbb{R}^{Q\times Q}, \tag{3.81}$$

and we *carry over* thus incurred $O(\epsilon)$ residual in (3.66) to (3.71). In this way, we arrive at the averaged $O(\epsilon^{-1})$ and $O(1)$ statements respectively as

$$(\dot{\boldsymbol{A}}^{(0)}(\hat{\boldsymbol{k}}) + \check{\sigma}\check{\omega}^2\boldsymbol{I})\boldsymbol{u}_0 \;=\; \mathbf{0}, \tag{3.82}$$

$$-(\boldsymbol{B}^{(0)}(\hat{\boldsymbol{k}}) + \ddot{\boldsymbol{A}}^{(0)}(\hat{\boldsymbol{k}}) + \hat{\sigma}\hat{\omega}^2\boldsymbol{I})\boldsymbol{u}_0 - (\dot{\boldsymbol{A}}^{(0)}(\hat{\boldsymbol{k}}) + \check{\sigma}\check{\omega}^2\boldsymbol{I})\boldsymbol{u}_1 \;=\; \mathbf{f}_0. \tag{3.83}$$

On the basis of (3.82)–(3.83), we next pursue a family of first-order effective field equations (in prescribed direction $\hat{\boldsymbol{k}}/\|\hat{\boldsymbol{k}}\|$) as controlled by: (i) proximity of the driving frequency ω^2 to $\tilde{\lambda}_n$ (see Remark 20), and (ii) the nature of $\boldsymbol{A}^{(0)}(\hat{\boldsymbol{k}})$ according to (3.79)–(3.81).

Effective solution for full-rank $\boldsymbol{A}^{(0)}$ when $\ddot{\boldsymbol{A}}^{(0)}=\mathbf{0}$

We first consider the case where $\mathrm{rank}(\boldsymbol{A}^{(0)}(\hat{\boldsymbol{k}})) = Q$ and $\ddot{\boldsymbol{A}}^{(0)} = \mathbf{0}$. With reference to (3.75), this specifically implies that $\tau_q = \boldsymbol{\theta}^{(0)}_{qq}\cdot i\hat{\boldsymbol{k}} = O(1)$, $q = \overline{1,Q}$. Letting further $\hat{\boldsymbol{f}}_{\boldsymbol{k}} \neq \mathbf{0}$ and $\omega^2 - \omega_n^2 = O(\epsilon)$ so that $|\check{\sigma}| = 1$ by Remark 20, we find from the $O(\epsilon^{-1})$ statement (3.82) that $\boldsymbol{u}_0 = \mathbf{0}$ thanks to Remark 23. From (3.83), we then obtain the leading-order model

$$-(\boldsymbol{A}^{(0)}(\hat{\boldsymbol{k}}) + \check{\sigma}\check{\omega}^2\boldsymbol{I})\boldsymbol{u}_1 \;=\; \mathbf{f}_0. \tag{3.84}$$

In the absence of the source term $\hat{\boldsymbol{f}}_{\boldsymbol{k}}$, the existence of a non-trivial solution to (3.82)–(3.83) also requires that $|\check{\sigma}| = 1$. As a result, (3.82) constitutes an eigenvalue problem (EP) whose eigenvalues

$$\omega^2_{n_q}(\boldsymbol{k}) \;=\; \omega_n^2 - i\boldsymbol{\theta}^{(0)}_{qq}\cdot(\epsilon\hat{\boldsymbol{k}}), \tag{3.85}$$

describe the leading-order, *linear* dispersion relationship in direction $\hat{\boldsymbol{k}}$.

Effective solution for near-trivial $\boldsymbol{A}^{(0)}$

When $\boldsymbol{A}^{(0)}(\hat{\boldsymbol{k}}) = \epsilon\ddot{\boldsymbol{A}}^{(0)}$ i.e. $\dot{\boldsymbol{A}}^{(0)} = \boldsymbol{0}$, we first consider the situation where $\hat{\boldsymbol{f}}_{\boldsymbol{k}} \neq \boldsymbol{0}$ and $\omega^2 - \omega_n^2 = O(\epsilon^2)$ so that $|\hat{\sigma}| = 1$. In this case (3.82) is satisfied identically, and we find from (3.83) that the leading-order solution $\boldsymbol{u}_0$ solves

$$-(\boldsymbol{B}^{(0)}(\hat{\boldsymbol{k}}) + \ddot{\boldsymbol{A}}^{(0)}(\hat{\boldsymbol{k}}) + \hat{\sigma}\hat{\omega}^2\boldsymbol{I})\boldsymbol{u}_0 \;=\; \mathrm{f}_0. \tag{3.86}$$

In the degenerate case when $\boldsymbol{A}^{(0)} = \epsilon\ddot{\boldsymbol{A}}^{(0)} = \boldsymbol{0}$, (3.86) becomes

$$-(\boldsymbol{B}^{(0)}(\hat{\boldsymbol{k}}) + \hat{\sigma}\hat{\omega}^2\boldsymbol{I})\boldsymbol{u}_0 \;=\; \mathrm{f}_0. \tag{3.87}$$

In this case we conveniently let $P_{sq} = \delta_{sq}$ in (3.74), and we have $N_0 = Q$ whereby $\boldsymbol{B}^{(0)} = \bar{\boldsymbol{B}}^{(0)}$ becomes diagonal due to (3.78).

When $\hat{\boldsymbol{f}}_{\boldsymbol{k}} = \boldsymbol{0}$, the existence of a non-trivial solution requires that $\breve{\sigma} = 0$ i.e. $|\hat{\sigma}| = 1$. In this case, the leading-order approximation of the dispersion relationships $\omega_{n_q}(\boldsymbol{k})$, $q = \overline{1, Q}$ is obtained by solving the eigenvalue problem $(\boldsymbol{B}^{(0)} + \ddot{\boldsymbol{A}}^{(0)})\boldsymbol{v} = \tau\boldsymbol{v}$. When $\ddot{\boldsymbol{A}}^{(0)}$ vanishes, the solution is given explicitly by

$$\omega_{n_q}^2(\boldsymbol{k}) \;=\; \omega_n^2 + \boldsymbol{\mu}_{qq}^{(0)} : (\epsilon\hat{\boldsymbol{k}})^2, \tag{3.88}$$

thanks to the fact that $\boldsymbol{B}^{(0)}$ is diagonal in this case.

Effective solution for partial rank $\boldsymbol{A}^{(0)}$

We next assume that $\boldsymbol{A}^{(0)}$ has a partial rank, i.e. $0 < N_0 < Q$. Letting $\hat{\boldsymbol{f}}_{\boldsymbol{k}} \neq \boldsymbol{0}$ and $\omega^2 - \omega_n^2 = O(\epsilon^2)$, we have $|\hat{\sigma}| = 1$. Thanks to the fact that $\boldsymbol{A}^{(0)}$ is diagonal due to (3.75), the last $Q - N$ components of $\boldsymbol{u}_0$ must vanish by enforcing (3.82) to the leading order. By virtue of this result and (3.83), we find that

$$-\sum_{q=1}^{N}(B_{pq}^{(0)}(\hat{\boldsymbol{k}}) + \ddot{A}_{pq}^{(0)}(\hat{\boldsymbol{k}}) + \hat{\sigma}\hat{\omega}^2\delta_{pq})u_{0q} \;=\; \mathrm{f}_{0p}, \quad p \in \overline{1, N}, \tag{3.89}$$

$$u_{0p} \;=\; 0, \quad p \in \overline{N+1, Q}. \tag{3.90}$$

When $\hat{\boldsymbol{f}}_{\boldsymbol{k}} = 0$, we obtain a non-trivial solution to (3.82)–(3.83) in terms of $\boldsymbol{u}_0$ by taking $|\hat{\sigma}| = 1$. In this case, (3.89) with $\mathrm{f}_{0p} = 0$ constitute an EP yielding the leading-order approximation the first N dispersion branches $\omega_{n_q}(\boldsymbol{k})$, $q = \overline{1, N}$.

Letting $\hat{\boldsymbol{f}}_{\boldsymbol{k}} \neq \boldsymbol{0}$ and $\omega^2 - \omega_n^2 = O(\epsilon)$, on the other hand, we have $|\breve{\sigma}| = 1$ whereby

$\boldsymbol{u}_0 = \mathbf{0}$ thanks to (3.82). From (3.83), we accordingly find that $\boldsymbol{u}_1$ solves

$$-(\dot{\boldsymbol{A}}^{(0)}(\hat{\boldsymbol{k}}) + \check{\sigma}\check{\omega}^2\boldsymbol{I})\boldsymbol{u}_1 \;=\; \mathbf{f}_0, \tag{3.91}$$

to the leading order (specifically, we discard the $O(\epsilon)$ residual in (3.83) by superseding $\boldsymbol{A}^{(0)}$ with $\dot{\boldsymbol{A}}^{(0)}$). Assuming $\hat{\boldsymbol{f}}_{\boldsymbol{k}} = \mathbf{0}$, we are now left with exposing the leading-order behavior the last $Q-N$ dispersion branches $\omega_{n_q}(\boldsymbol{k})$, $q=\overline{N+1,Q}$. In this case we must set $|\check{\sigma}| = 1$ because all dispersion branches permitting the $\hat{\sigma}$-description are already given by (3.89) with $\mathrm{f}_{0p} = 0$. This yields the sought approximation via (3.91) with $\mathbf{f}_0 = \mathbf{0}$ as

$$\omega^2_{n_q}(\boldsymbol{k}) \;=\; \omega^2_n - i\boldsymbol{\theta}^{(0)}_{qq}\cdot(\epsilon\hat{\boldsymbol{k}}), \qquad q=\overline{N+1,Q}. \tag{3.92}$$

3.2.3 Cluster of nearby eigenvalues

We complete the spectral analysis of DPOS by letting the driving frequency be near a cluster of nearby eigenfrequencies $\{\omega_{n_q}\}$, $q=\overline{1,Q}$. This situation was originally considered in [23] in an effort to handle the "short asymptotic range" exhibited by single- and repeated-eigenfrequency models within $(\boldsymbol{k},\omega)$ regions characterized by closely spaced dispersion curves, and extended in [75] to: (i) allow expansion about an arbitrary point $(\boldsymbol{k}_s,\omega)$, $\boldsymbol{k}_s \in \overline{\mathcal{B}}$, and (ii) expose the first-order correction of the leading-order model. In this section, we generalize the approach to elastic DPOS by expressing the leading-order motion.

We let $\bar{Q}$ be the number of distinct eigenvalues within set $\{\omega_{n_q}\}$, and we denote by $(\boldsymbol{k}_s,\omega_{n_0})$ for some $n_0 \in \{n_q\}$ the origin of asymptotic expansion in (3.37). In this setting, we conveniently redeploy the scaling parameter $\epsilon = o(1)$ to quantify the "smallness" of distances between the neighboring eigenvalues by letting

$$\lambda_{n_q} \;=\; \lambda_{n_0} - \epsilon\gamma_q, \qquad q=\overline{1,Q}. \tag{3.93}$$

With (3.93) in place, we consider the local eigenfunction basis $\{\hat{\boldsymbol{\phi}}_{n_q}(\boldsymbol{k})\}$ that satisfies

$$-(\tilde{\lambda}_{n0} - \epsilon\gamma_q)\hat{\boldsymbol{M}}\cdot\hat{\boldsymbol{\phi}}_{n_q} + \hat{\boldsymbol{K}}_{\boldsymbol{k}}\cdot\hat{\boldsymbol{\phi}}_{n_q} = \mathbf{0}, \qquad q=\overline{1,Q}. \tag{3.94}$$

As can be seen from (3.94), the current problem can be described as an "almost repeated" eigenvalue case, which allows us to take advantage of the earlier developments.

With the insight into $\hat{\boldsymbol{u}}$ which solves (3.31) gained in Section 3.2.1 and Section 3.2.2,

we skip intermediate steps and proceed by specifying the ansatz (3.40) up to $m = 1$ as

$$\hat{\boldsymbol{u}}(\boldsymbol{x}) \stackrel{\epsilon}{=} \sum_q \Big(\epsilon^{-2} u_{0q}\ \hat{\boldsymbol{\phi}}_{n_q} + \epsilon^{-1} u_{1q}\ \hat{\boldsymbol{\phi}}_{n_q} + \epsilon^{-1} u_{0q}\ \boldsymbol{\chi}_q^{(1)} \cdot (i\hat{\boldsymbol{k}})\Big), \quad u_{0q}, u_{1q} \in \mathbb{C}, \tag{3.95}$$

where $\boldsymbol{\chi}_q^{(1)} \in \mathbb{C}^{\mathfrak{p}} \times \mathbb{C}^{\mathfrak{m}}$ and $\boldsymbol{\chi}_{qj}^{(1)} := (\boldsymbol{i}_j) : \boldsymbol{\chi}_q^{(1)} \in \mathcal{H}$ $(j \in \overline{1,\mathfrak{p}})$ uniquely solve the respective linear systems

$$-\tilde{\lambda}_n \hat{\boldsymbol{M}} \cdot \boldsymbol{\chi}_{qj}^{(1)} + \hat{\boldsymbol{K}}^{(0)} \cdot \boldsymbol{\chi}_{qj}^{(1)} + (\boldsymbol{i}_j) \cdot \hat{\boldsymbol{K}}^{(1)} \cdot \hat{\boldsymbol{\phi}}_{nq} + \sum_s \boldsymbol{\theta}_{sq}^{(0)} \cdot (\boldsymbol{i}_j) \hat{\boldsymbol{M}} \cdot \hat{\boldsymbol{\phi}}_{n_s} \ = \ \boldsymbol{0}. \tag{3.96}$$

In the context of (3.95), our goal is then to find the coupled effective equations satisfied by u_{0q} and u_{2q}. To this end, we (i) insert (3.95) in (3.31); (ii) project the result onto $\hat{\boldsymbol{\phi}}_{n_q}$, and (iii) expand the result in powers of ϵ as

$$O(\epsilon^{-1}): \qquad (\boldsymbol{A}^{\gamma}(\hat{\boldsymbol{k}}) + \check{\sigma}\check{\omega}^2 \boldsymbol{I})\boldsymbol{u}_0 \ = \ \boldsymbol{0}, \tag{3.97}$$

$$O(1): \qquad -(\boldsymbol{B}^{(0)}(\hat{\boldsymbol{k}}) + \hat{\sigma}\hat{\omega}^2 \boldsymbol{I})\boldsymbol{u}_0 - (\boldsymbol{A}^{\gamma}(\hat{\boldsymbol{k}}) + \check{\sigma}\check{\omega}^2 \boldsymbol{I})\boldsymbol{u}_1 \ = \ \mathbf{f}_0, \tag{3.98}$$

where the matrix

$$\boldsymbol{A}^{\gamma}(\hat{\boldsymbol{k}}) \ = \ \boldsymbol{A}^{(0)}(\hat{\boldsymbol{k}}) + \boldsymbol{\Gamma}, \qquad \boldsymbol{\Gamma}_{pq} = \delta_{pq}\gamma_q \tag{3.99}$$

accounts for the eigenvalue separations in (3.94), while $\boldsymbol{A}^{(0)}$, $\boldsymbol{B}^{(0)}$ and $\mathbf{f}_0$ are given by (3.66) and (3.71) as before.

Remark 27 *We observe a clear similarity between* (3.97), (3.98) *and their repeated-eigenvalue predecessors* (3.66) *and* (3.71) *respectively. In fact, the differences are in this case confined to the appearance of the diagonal matrix* $\boldsymbol{\Gamma} = \boldsymbol{A}^{\gamma} - \boldsymbol{A}^{(0)}$ *that accounts for separations between the neighboring eigenvalues according to* (3.93). *Further, we note that since* $\boldsymbol{A}^{(0)}$ *is Hermitian, so is* $\boldsymbol{A}^{\gamma}$.

Eigenfunction basis of $\boldsymbol{A}^{\gamma}$

Let $\boldsymbol{P} = [\boldsymbol{v}_1\ \boldsymbol{v}_2\ \ldots\ \boldsymbol{v}_Q]$ the matrix of orthonormal eigenvectors stemming from the eigenvalue problem

$$\boldsymbol{A}^{\gamma}(\hat{\boldsymbol{k}})\boldsymbol{v} \ = \ \tau \boldsymbol{v}.$$

In order to diagonalize $\boldsymbol{A}^{\gamma}$, we factorize $\boldsymbol{u}_0, \boldsymbol{u}_1, \boldsymbol{u}_2, \mathbf{f}_0$ and $\mathbf{f}_1$ in terms of $\boldsymbol{P}$ as

$$\boldsymbol{u}_0 = \boldsymbol{P}\boldsymbol{u}_0', \quad \boldsymbol{u}_1 = \boldsymbol{P}\boldsymbol{u}_1', \quad \boldsymbol{u}_2 = \boldsymbol{P}\boldsymbol{u}_2', \quad \mathbf{f}_0 = \boldsymbol{P}\mathbf{f}_0', \quad \mathbf{f}_1 = \boldsymbol{P}\mathbf{f}_1' \tag{3.100}$$

and we premultiply (3.97)–(3.98) by $\overline{\boldsymbol{P}}^{\mathrm{T}}$. For brevity of notation, we drop the prime symbol from the "rotated" vectors $\boldsymbol{u}_0', \boldsymbol{u}_1'$ and $\mathbf{f}_0'$, and we keep the original notation of the transformed matrices in (3.97)–(3.98). In this setting, we obtain

$$\boldsymbol{A}^{\gamma}(\hat{\boldsymbol{k}}) \;=\; \mathrm{diag}(\tau_1, \tau_2, \ldots, \tau_Q), \tag{3.101}$$

noting for future reference that $\tau_q = 0$ ($q = \overline{1, N_0}$) when $\mathrm{rank}(\boldsymbol{A}^{\gamma}) = Q - N_0$.

Thanks to the presence of the "penalty" term $\boldsymbol{\Gamma}$ in (3.99), $\boldsymbol{A}^{\gamma}$ is of at least partial rank when $\boldsymbol{A}^{(0)} = \mathbf{0}$. As a result, in the sequel we present the effective models for full- and partial-rank $\boldsymbol{A}^{\gamma}$ only.

Effective solution for full-rank $\boldsymbol{A}^{\gamma}$

When $\mathrm{rank}(\boldsymbol{A}^{\gamma}) = Q$, $\hat{\boldsymbol{f}}_{\boldsymbol{k}} \neq 0$, and $\omega^2 - \omega_n^2 = O(\epsilon)$ i.e. $|\hat{\sigma}| = 1$, we must have $\boldsymbol{u}_0 = \mathbf{0}$ due to (3.97). As a result, (3.98) yields the leading-order effective equation

$$-(\boldsymbol{A}^{\gamma} + \check{\sigma}\check{\omega}^2 \boldsymbol{I})\boldsymbol{u}_1 \;=\; \mathbf{f}_0. \tag{3.102}$$

When $\tilde{f}_{\boldsymbol{k}} = 0$, eigenvalues of the EP stemming from (3.97) (or equivalently (3.102)) define the leading-order asymptotic approximation of the dispersion relationships in direction $\hat{\boldsymbol{k}}/\|\hat{\boldsymbol{k}}\|$ as

$$\omega_{n_q}^2 \;=\; \omega_{n_0}^2 - \epsilon\tau_q, \tag{3.103}$$

where τ_q is the qth eigenvalue of $\boldsymbol{A}^{\gamma}(\hat{\boldsymbol{k}})$.

Remark 28 *When $\boldsymbol{A}^{\gamma}$ is of full rank,* (3.102) *and* (3.103) *provide a general framework to handle the clusters of nearby dispersion branches, regardless of the fact whether they intersect or "almost touch" for example at $\boldsymbol{k} = \boldsymbol{k}_s$.*

Effective solution for partial-rank $\boldsymbol{A}^{\gamma}$

When $\mathrm{rank}(\boldsymbol{A}^{\gamma}) = Q - N_0$ for some $N_0 > 0$ and $\hat{\boldsymbol{f}}_{\boldsymbol{k}} \neq 0$, we first consider the situation where $\omega^2 - \lambda_{n_0} = O(\epsilon)$ i.e. $|\check{\sigma}| = 1$. In this case the leading-order effective equation is again given by (3.102), while the last $Q - N_0$ dispersion branches are approximated by (3.103) for $q \in \overline{N_0+1, Q}$.

On the other hand, when $\omega^2 - \omega_{n_0}^2 = O(\epsilon^2)$ i.e. $|\hat{\sigma}| = 1$, the leading-order effective

model $\boldsymbol{u}_0$ is given by

$$-\sum_{q=1}^{N_0}(B_{pq}^{(0)}(\hat{\boldsymbol{k}})+\hat{\sigma}\hat{\omega}^2\delta_{pq})\,u_{0q} \;=\; \mathrm{f}_{0p}, \quad p\in\overline{1,N_0}, \tag{3.104}$$

$$u_{0p} \;=\; 0, \quad p\in\overline{N_0+1,Q}. \tag{3.105}$$

When $\hat{\boldsymbol{f}}_{\boldsymbol{k}}=0$, the leading-order approximation of the first N_0 dispersion branches is obtained by solving the EP affiliated with (3.104).

3.3 Asymptotic approximation of DPOS motion in special spectral neighborhoods

3.3.1 Simple eigenvalue

With reference to the class (3.21) of source distributions, one immediate application of the foregoing analysis is the case where: (i) $\boldsymbol{k}_s=\frac{1}{2}(\sum_{l=1}^{\mathfrak{p}}n_l\boldsymbol{e}^l)$, $n_l\in\{-1,0,1\}$; (ii) the driving frequency is within a band gap near simple eigenfrequency $\omega_n(\boldsymbol{k}_s)$, and (iii) the source function $\tilde{\boldsymbol{f}}_{\boldsymbol{k}}$ is given by

$$\tilde{\boldsymbol{f}}_{\boldsymbol{k}}|_{\hat{\mathbf{p}}^{(\mathrm{n})}} \;=\; F(\boldsymbol{k})\boldsymbol{\phi}|_{\hat{\mathbf{p}}^{(\mathrm{n})}}, \quad \mathrm{supp}(F)=\mathcal{C}\subset\mathcal{B}, \tag{3.106}$$

where $\boldsymbol{\phi}$ is periodic in S' and $\mathbf{i}$ is given by (3.6). On recalling DBWE (3.36) and ansatz (3.40), we conveniently introduce the Mth-order asymptotic solution in the physical space as

$$\boldsymbol{u}_{\hat{\mathbf{p}}^{(\mathrm{n})}}^{[\mathrm{M}]} \;:=\; \sum_{m=0}^{M}\epsilon^{m-2}\,|\mathcal{C}|^{-1}\int_{\mathcal{C}}\tilde{\boldsymbol{u}}_m|_{\hat{\mathbf{p}}^{(\mathrm{n})}}\,e^{i(\boldsymbol{k}_s+\epsilon\hat{\boldsymbol{k}})\cdot\boldsymbol{x}_{\hat{\mathbf{p}}^{(\mathrm{n})}}}\,\mathrm{d}(\epsilon\hat{\boldsymbol{k}}), \tag{3.107}$$

From (3.52), (3.55), (3.57) and Remark 13, we specifically find that

$$\tilde{\boldsymbol{u}}_0(\boldsymbol{x}) \;=\; -\epsilon^2\,\frac{\langle\hat{\boldsymbol{f}}_{\boldsymbol{k}}\rangle}{(\omega^2-\omega_n^2)+\boldsymbol{\mu}^{(0)}:(i\epsilon\hat{\boldsymbol{k}})^2}\,\tilde{\boldsymbol{\phi}}_n, \tag{3.108}$$

where $\hat{\boldsymbol{f}}_{\boldsymbol{k}}=\boldsymbol{G}^{\mathrm{T}}\tilde{\boldsymbol{f}}_{\boldsymbol{k}}$. In terms of the *effective solution*, by (3.50) we can similarly introduce the Mth-order mean motion in the physical space as

$$\langle\boldsymbol{u}\rangle_{\rho}^{[\mathrm{M}]}(\boldsymbol{x}) \;:=\; \sum_{m=0}^{[\mathrm{M}]}\epsilon^{m-2}\,|\mathcal{C}|^{-1}\int_{\mathcal{C}}u_m(\epsilon\hat{\boldsymbol{k}})\,e^{i(\boldsymbol{k}_s+\epsilon\hat{\boldsymbol{k}})\cdot\boldsymbol{x}}\,\mathrm{d}(\epsilon\hat{\boldsymbol{k}}), \quad \boldsymbol{x}\in\mathbb{R}^{\mathfrak{d}}, \tag{3.109}$$

via superposition of the averaged Bloch-wave solutions, $u_m(\epsilon\hat{\boldsymbol{k}}) = \langle \hat{\boldsymbol{u}}_m \rangle_\rho$. From (3.108), we specifically find that

$$u_0(\epsilon\hat{\boldsymbol{k}}) \;=\; -\epsilon^2 \,\frac{\langle \hat{f}_{\boldsymbol{k}} \rangle}{(\omega^2 - \omega_n^2) + \boldsymbol{\mu}^{(0)} : (i\epsilon\hat{\boldsymbol{k}})^2}. \tag{3.110}$$

which the yields the leading-order solution in (3.109).

Remark 29 *Due to its "effective" nature, scalar wave motion* (3.109) *is defined* everywhere *in* $\mathbb{R}^{\mathfrak{d}}$ *even though is independent of the components of* $\boldsymbol{x}$ *in* $\mathbb{R}^{\mathfrak{d}} \backslash \mathbb{R}^{\mathfrak{p}}$. *This is in contrast to the vector wave motion* (3.107) *that is restricted to the nodal points,* $\boldsymbol{x}_{\hat{\mathbf{p}}^{(n)}} \in S'_{\boldsymbol{\alpha}} \subset \mathbb{R}^{\mathfrak{d}}$.

Effective wave motion: band gap vs. passband excitation

When the driving frequency is within a band gap, matrix $\text{sign}(\omega - \omega_n)\boldsymbol{\mu}^{(0)}$ is negative-definite and the leading-order integrand in (3.109) is *regular*. By contrast, in situations where the driving frequency is within a passband, $\text{sign}(\omega - \omega_n)\boldsymbol{\mu}^{(0)}$ is positive-definite and the leading-order integrand in (3.109) becomes *singular*. To deal with the latter case, let

$$\mathcal{L} \;=\; \left\{ \boldsymbol{k} \in \mathcal{B} \colon \boldsymbol{k} = \boldsymbol{k}_s + \epsilon\hat{\boldsymbol{k}}_0(\boldsymbol{e}),\; \epsilon\hat{\boldsymbol{k}}_0 = \frac{\omega^2 - \omega_n^2}{\boldsymbol{\mu}^{(0)} : (\boldsymbol{e})^2}\,\boldsymbol{e},\; \boldsymbol{e} \in \mathbb{R}^{\mathfrak{p}},\; \|\boldsymbol{e}\| = 1 \right\}$$

specify the pair of points (when $\mathfrak{p} = 1$), closed contour (when $\mathfrak{p} = 2$), or closed surface (when $\mathfrak{p} = 3$) over which the denominator in (3.110) vanishes. In the neighborhood of any $\boldsymbol{k}_s + \epsilon\hat{\boldsymbol{k}}_0 \in \mathcal{L}$ the local variation of the leading-order integrand in the direction of the unit normal on $\mathcal{L}$, $\boldsymbol{n} = \boldsymbol{n}(\hat{\boldsymbol{k}}_0)$, as specified by the perturbation $\hat{\boldsymbol{k}} = \hat{\boldsymbol{k}}_0 + \delta\boldsymbol{n}$ with $\delta = o(1)$ is given by

$$\begin{aligned} -\frac{\langle \tilde{f}_{\boldsymbol{k}} \rangle e^{i(\boldsymbol{k}_s + \epsilon\hat{\boldsymbol{k}})\cdot\boldsymbol{x}}}{(\omega^2 - \omega_n^2) + \boldsymbol{\mu}^{(0)} : (i\epsilon\hat{\boldsymbol{k}})^2} \;&\propto\; -\frac{F(\epsilon(\hat{\boldsymbol{k}}_0 + \delta\boldsymbol{n}))e^{i\epsilon(\hat{\boldsymbol{k}}_0 + \delta\boldsymbol{n})\cdot\boldsymbol{x}}}{2\delta\,\boldsymbol{\mu}^{(0)} : (\epsilon\boldsymbol{n} \otimes \epsilon\hat{\boldsymbol{k}}_0) + \delta^2\,\boldsymbol{\mu}^{(0)} : (\epsilon\boldsymbol{n})^2} \\ &\simeq\; \frac{F(\epsilon\,\hat{\boldsymbol{k}}_0)e^{i\epsilon\hat{\boldsymbol{k}}_0\cdot\boldsymbol{x}}}{2\boldsymbol{\mu}^{(0)} : (\epsilon\boldsymbol{n} \otimes \epsilon\hat{\boldsymbol{k}}_0)}\,\frac{e^{i\epsilon\delta\,\boldsymbol{n}\cdot\boldsymbol{x}}}{\delta} + O(\delta^0). \end{aligned} \tag{3.111}$$

Despite the singularity of (3.111) across $\delta = 0$, its cumulative contribution to (3.109) over a narrow patch centered at $\boldsymbol{k}_s + \epsilon\hat{\boldsymbol{k}}_0$ (see the right panel in Fig. 3.3) is finite i.e. *regular* due to the fact that $e^{i\epsilon\delta\,\boldsymbol{n}\cdot\boldsymbol{x}}/\delta \simeq 1/\delta + i\,\epsilon\,\boldsymbol{n}\boldsymbol{x}$ for $\delta = o(1)$. Hence, the integral in (3.109) can be effectively approximated by excluding an $o(\epsilon)$-wide strip surrounding $\mathcal{L}$ (the shaded area in Fig. 3.3) from $\mathcal{C}$. Alternatively, (3.109) can be approximated by the

introduction of an imaginary penalty term to the denominator of (3.110). In Section 3.4, we shall make use of the above results toward approximating the effective wave motion near a simple eigenvalue.

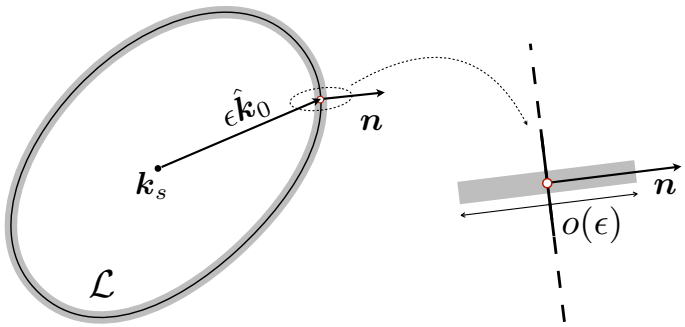

Figure 3.3: Singularity contour (assuming $\mathfrak{p} = 2$) of the leading-order integrand in (3.109) when ω is within a passband.

3.3.2 Pair of nearby eigenvalues for $\mathfrak{p} = 2$

Consider a POS $S \subset \mathbb{R}^3$ with two-dimensional periodicity ($\mathfrak{p}=2$) whose spectral neighborhood (3.37) features two nearby eigenfrequencies $\omega_{n_1} = \omega_{n_1}(\boldsymbol{k}_s)$ and $\omega_{n_2} = \omega_{n_2}(\boldsymbol{k}_s)$, i.e. $Q=2$. In this case, matrix $\boldsymbol{A}^\gamma$ in (3.99) reads

$$\boldsymbol{A}^\gamma = \begin{pmatrix} \boldsymbol{\theta}_{11}^{(0)} \cdot i\hat{\boldsymbol{k}} & \boldsymbol{\theta}_{12}^{(0)} \cdot i\hat{\boldsymbol{k}} \\ -\overline{\boldsymbol{\theta}_{12}^{(0)}} \cdot i\hat{\boldsymbol{k}} & \boldsymbol{\theta}_{22}^{(0)} \cdot i\hat{\boldsymbol{k}} + \gamma \end{pmatrix}, \qquad \gamma = \epsilon^{-1}(\omega_{n1}^2 - \omega_{n2}^2). \tag{3.112}$$

By way of (3.97), the two dispersion relationships are accordingly given by

$$\begin{aligned} \omega_{n_{1/2}}^2(\boldsymbol{k}) \;\; &= \;\; \omega_{n_1}^2 - \frac{\epsilon}{2}\big(\gamma + \boldsymbol{\theta}_{11}^{(0)} \cdot i\hat{\boldsymbol{k}} + \boldsymbol{\theta}_{22}^{(0)} \cdot i\hat{\boldsymbol{k}}\big) \\ &\quad \mp \frac{\epsilon}{2}\sqrt{\big(\gamma - \boldsymbol{\theta}_{11}^{(0)} \cdot i\hat{\boldsymbol{k}} + \boldsymbol{\theta}_{22}^{(0)} \cdot i\hat{\boldsymbol{k}}\big)^2 + 4(\boldsymbol{\theta}_{12}^{(0)} \otimes \overline{\boldsymbol{\theta}_{12}^{(0)}}) : (\hat{\boldsymbol{k}})^2}, \end{aligned} \tag{3.113}$$

where the matrix $\boldsymbol{\theta}_{12}^{(0)} \otimes \overline{\boldsymbol{\theta}_{12}^{(0)}} \in \mathbb{R}^{2\times 2}$ is in general positive semi-definite, and specifically positive definite when

$$\boldsymbol{\theta}_{12}^{(0)} \cdot \boldsymbol{i}_1 \neq 0, \quad \boldsymbol{\theta}_{12}^{(0)} \cdot \boldsymbol{i}_2 \neq 0, \quad \text{and} \quad \arg(\boldsymbol{\theta}_{12}^{(0)} \cdot \boldsymbol{i}_1) - \arg(\boldsymbol{\theta}_{12}^{(0)} \cdot \boldsymbol{i}_2) \neq n\pi, \quad n \in \mathbb{Z}. \tag{3.114}$$

Equations (3.113) describe "almost touching" (resp. crossing) branches when $\gamma \neq 0$ (resp. $\gamma = 0$) featuring the middle plane

$$\mathcal{P}: \quad \omega^2_{\mathcal{P}}(\boldsymbol{k}) \;=\; \omega^2_{n_1} - \frac{\epsilon}{2}\big(\gamma + (\boldsymbol{\theta}^{(0)}_{11}\cdot i\hat{\boldsymbol{k}}) + \boldsymbol{\theta}^{(0)}_{22}\cdot i\hat{\boldsymbol{k}}\big). \tag{3.115}$$

When $\mathcal{P}$ is horizontal, we further have

$$\boldsymbol{\theta}^{(0)}_{11} + \boldsymbol{\theta}^{(0)}_{22} \;=\; \boldsymbol{0}, \tag{3.116}$$

which holds true for any ρ-orthogonal eigenfunction basis by the conservation of the trace of $\boldsymbol{A}^\gamma$. In this case, dispersion relationship (3.113) simplifies to

$$\omega^2_{n_{1/2}}(\boldsymbol{k}) \;=\; \omega^2_{n_1} - \frac{\epsilon}{2}\big(\gamma \pm \sqrt{\big(\gamma - 2\boldsymbol{\theta}^{(0)}_{11}\cdot i\hat{\boldsymbol{k}}\big)^2 + 4\{\boldsymbol{\theta}^{(0)}_{12}\otimes\overline{\boldsymbol{\theta}^{(0)}_{12}}\}:(\hat{\boldsymbol{k}})^2}\big). \tag{3.117}$$

When $\gamma \neq 0$ in (3.117), assuming $\mathrm{d}\omega_{n_{1/2}}/\mathrm{d}\boldsymbol{k}|_{\boldsymbol{k}=\boldsymbol{k}_s} \;=\; \boldsymbol{0}$ implies that $\boldsymbol{\theta}^{(0)}_{11} = \boldsymbol{0}$ and thus $\boldsymbol{\theta}^{(0)}_{22} = \boldsymbol{0}$ by (3.116). This reduces (3.117) to

$$\omega^2_{n_{1/2}}(\boldsymbol{k}) = \omega^2_{n_1} - \frac{\epsilon}{2}\big(\gamma \pm \sqrt{\gamma^2 + 4\{\boldsymbol{\theta}^{(0)}_{12}\otimes\overline{\boldsymbol{\theta}^{(0)}_{12}}\}:(\hat{\boldsymbol{k}})^2}\big). \tag{3.118}$$

Further, if $\boldsymbol{\theta}^{(0)}_{12}\otimes\overline{\boldsymbol{\theta}^{(0)}_{12}}$ is positive definite due to (3.114), the dispersion relationships in (3.118) are characterized by elliptic iso-contours and thus exhibit cone-like geometry. As a special case, $\boldsymbol{\theta}^{(0)}_{12}\otimes\overline{\boldsymbol{\theta}^{(0)}_{12}}$ becomes isotropic when $\boldsymbol{\theta}^{(0)}_{12} \parallel \boldsymbol{i}_1 \pm i\boldsymbol{i}_2$, which reduces (3.118) to

$$\omega^2_{n_{1/2}}(\boldsymbol{k}) \;=\; \omega^2_{n_1} - \frac{\epsilon}{2}\big(\gamma \pm \sqrt{\gamma^2 + 4\|\boldsymbol{\theta}^{(0)}_{12}\|^2\|\hat{\boldsymbol{k}}\|^2}\big). \tag{3.119}$$

When $\boldsymbol{\theta}^{(0)}_{12}\otimes\overline{\boldsymbol{\theta}^{(0)}_{12}}$ is isotropic and the structure is excited by $\tilde{\boldsymbol{f}}_{\boldsymbol{k}}$ at frequency ω such that $\omega^2 - \omega^2_{n_1} = O(\omega^2_{n_2} - \omega^2_{n_1})$, the leading-order effective model (3.102) becomes axisymmetric and reads

$$\begin{aligned}
\big(\tfrac{1}{2}\|\boldsymbol{\theta}^{(0)}_{12}\|^2\|\hat{\boldsymbol{k}}\|^2 - (\gamma + \check{\sigma}\check{\omega}^2)\check{\sigma}\check{\omega}^2\big)u_{11} \;&=\; (\gamma + \check{\sigma}\check{\omega}^2)\langle\hat{\boldsymbol{f}}_{\boldsymbol{k}}\rangle^{n_1} - (\boldsymbol{\theta}^{(0)}_{12}\cdot i\hat{\boldsymbol{k}})\langle\hat{\boldsymbol{f}}_{\boldsymbol{k}}\rangle^{n_2},\\
\big(\tfrac{1}{2}\|\boldsymbol{\theta}^{(0)}_{12}\|^2\|\hat{\boldsymbol{k}}\|^2 - (\gamma + \check{\sigma}\check{\omega}^2)\check{\sigma}\check{\omega}^2\big)u_{12} \;&=\; (\overline{\boldsymbol{\theta}^{(0)}_{12}}\cdot i\hat{\boldsymbol{k}})\langle\hat{\boldsymbol{f}}_{\boldsymbol{k}}\rangle^{n_1} + (\check{\sigma}\check{\omega}^2)\langle\hat{\boldsymbol{f}}_{\boldsymbol{k}}\rangle^{n_2},
\end{aligned} \tag{3.120}$$

where $\hat{\boldsymbol{f}}_{\boldsymbol{k}} = \boldsymbol{G}^{\mathrm{T}}\tilde{\boldsymbol{f}}_{\boldsymbol{k}}$. With such result in place, the leading-order total motion of a DPOS near an axisymmetric avoided crossing (assuming a force term $\boldsymbol{f}$ that admits DBWE (3.21)) is given by

$$\boldsymbol{u}^{[0]}_{\hat{\mathbf{p}}^{(\mathrm{n})}} \;=\; \epsilon^{-2}|\mathcal{C}|^{-1}\int_{\mathcal{C}}\Big(u_{11}(\epsilon\hat{\boldsymbol{k}})\,\tilde{\boldsymbol{\phi}}_{n_1}|_{\hat{\mathbf{p}}^{(\mathrm{n})}} \;+\; u_{12}(\epsilon\hat{\boldsymbol{k}})\,\tilde{\boldsymbol{\phi}}_{n_2}|_{\hat{\mathbf{p}}^{(\mathrm{n})}}\Big)\,e^{i(\boldsymbol{k}_s+\epsilon\hat{\boldsymbol{k}})\cdot\boldsymbol{x}_{\hat{\mathbf{p}}^{(\mathrm{n})}}}\,\mathrm{d}(\epsilon\hat{\boldsymbol{k}}). \tag{3.121}$$

3.4 Numerical results

In the sequel, we illustrate the performance of the proposed homogenization framework as a tool for synthesizing the wave motion in periodic origami structures. To this end, we consider homogenized models of both the dispersion relationship and forced motion near the edge of a band gap. A 2D-periodic Miura-ori structure and a 1D-periodic Miura tube are used as test platforms for numerical simulations.

The adopted N5B8 bar-and-hinge model (see Fig. 3.2) is implemented in MATLAB to construct the mass matrix $\hat{\boldsymbol{M}}$, the stiffness matrix $\hat{\boldsymbol{K}}_{\boldsymbol{k}}$, and its Taylor series components $\hat{\boldsymbol{K}}^{(\mathrm{m})}$ ($m \in \overline{0,2}$). These matrices are then used to evaluate the dispersion relationship of the periodic structure by: (i) solving the eigenvalue problem (3.32) for given $\boldsymbol{k} \in \mathcal{B}$, and (ii) computing the unit cell vectors $\boldsymbol{\chi}_p^{(1)}$ via (3.56) and (3.68) as they enter the expressions of the effective coefficients $\boldsymbol{\theta}_{pq}^{(0)}$ and $\boldsymbol{\mu}_{pq}^{(0)}$ ($p, q \in \overline{1,Q}$).

3.4.1 Dispersion relationship

Our immediate focus are the leading- and first-order asymptotic approximations of the dispersion relationship for 1D and 2D-periodic origami-inspired structures. Making use of the effective equations derived in the neighborhoods of simple, repeated, and nearby eigenfrequencies (see Sections 3.2.1–3.2.3), we evaluate the asymptotic approximation of the dispersion relationships for a 2D-periodic Miura-ori structure and a 1D-periodic Miura tube.

2D-periodic Miura-ori structure

As the first example we consider 2D-periodic unbounded Miura-ori structure S shown in Fig. 3.4(a), for which $(\mathfrak{d}, \mathfrak{p}) = (3, 2)$. For completeness, Fig. 3.4(b) shows the unit cell of periodicity Y and its geometrical parameters $a = 1,\ b = 1,\ \beta = \pi/4 \in (0, \pi/2)$ and folding angle $\alpha = \pi/2 - \beta/2 \in (\pi/2 - \beta, \pi/2 + \beta)$; Fig. 3.4(c) provides the schematics of the unit cell Y', and Fig. 3.4(d) plots the affiliated first Brillouin zone $\mathcal{B} \subset \mathbb{R}^2$. We assume that (i) the structure panels have a uniform surface mass density ($\rho_0 = 1$) so that the mass of each triangular partition of a given panel is distributed uniformly among its vertices; (ii) the bars are endowed with constant Young modulus E_0 and cross-sectional area A_0 such that $E_0 A_0 = 10^3$; (iii) the folding hinges have uniform linear stiffness $k_{fs} = 1$, and (iv) the bending hinges have uniform linear stiffness $k_{bs} = 10$. With so-defined material properties, we set the normalization parameters as ($\ell_0 = a$, $\kappa_0 = E_0 A_0/a$, $m_0 = \rho_0 a^2$), and we let $\omega_0 = \sqrt{\kappa_0/m_0}$ and $k_0 = \pi/\ell_0$.

We note from Fig. 3.4(c) that the unit cell Y' of DPOS S' has $\mathfrak{m} = \mathfrak{d} \times 8 = 24$ degrees of freedom. With reference to Fig. 3.4, the Miura-ori Bravais lattice basis and

reciprocal lattice basis are given respectively by

$$\boldsymbol{e}_1 = 2b\,\frac{\sqrt{\sin(\alpha)^2-\cos(\beta)^2}}{\sin(\alpha)}\,\boldsymbol{i}_1, \quad \boldsymbol{e}_2 = 2a\sin(\alpha)\;\boldsymbol{i}_2,$$
$$\boldsymbol{e}^1 = \frac{\pi\sin(\alpha)}{b\sqrt{\sin(\alpha)^2-\cos(\beta)^2}}\,\boldsymbol{i}_1, \quad \boldsymbol{e}^2 = \frac{\pi}{a\sin(\alpha)}\;\boldsymbol{i}_2. \tag{3.122}$$

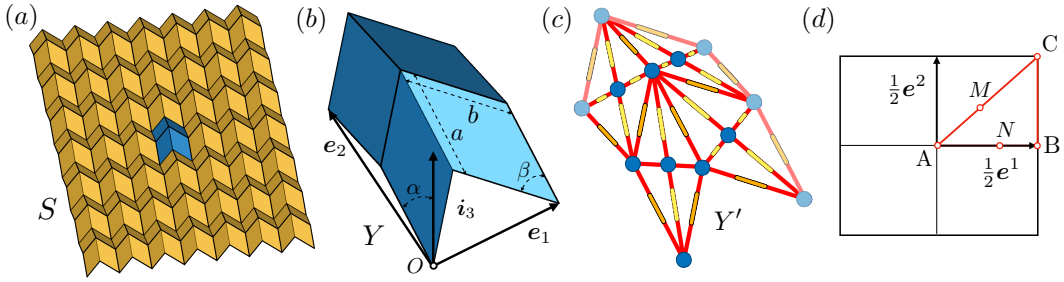

Figure 3.4: (a) Truncated two-dimensional periodic Miura-ori sheet for which $(\mathfrak{d},\mathfrak{p}) = (3,2)$; (b) unit cell of periodicity Y; (c) bar-and-hinge discretization where the bars are indicated by continuous lines, the folding (resp. bending) hinges by rounded rectangles with continuous (resp. dashed) contours, and the nodes by balls (nodes, bars and hinges that do not belong to Y' are shaded); and (d) first Brillouin zone $\mathcal{B}$ of the lattice featuring apex points A, B and C.

In the absence of the source term ($\hat{\boldsymbol{f}}_{\boldsymbol{k}} = \boldsymbol{0}$), the foregoing homogenization framework enables local approximation of the dispersion relationship in the vicinity of an *arbitrary pair* $(\boldsymbol{k}_s, \omega_n(\boldsymbol{k}_s))$, $\boldsymbol{k}_s \in \overline{\mathcal{B}}$, which is a way to access the effective properties of the medium. With reference to Fig. 3.4(d), we illustrate this by taking $\boldsymbol{k}_s$ as the origin of the Brillouin zone (point A), apex points B and C, and internal points M and N given respectively by

$$\overrightarrow{\mathrm{AB}} = \tfrac{1}{2}\boldsymbol{e}^1, \quad \overrightarrow{\mathrm{AC}} = \tfrac{1}{2}\boldsymbol{e}^1 + \tfrac{1}{2}\boldsymbol{e}^2, \quad \overrightarrow{\mathrm{AM}} = 0.4\,\overrightarrow{\mathrm{AC}}, \quad \overrightarrow{\mathrm{AN}} = 0.7201\,\overrightarrow{\mathrm{AB}}.$$

Fig. 3.5 compares the first 12 dispersion branches with their respective approximations in the neighborhood of points A, B, C, M and N, while Fig. 3.6 focuses on branches 13–24. We specify the extent of repeated- or cluster-eigenvalue asymptotic approximation (as applicable) by the set

$$\mathcal{N}_\ell^\star = \{n_1, n_2, \ldots n_Q\}, \qquad \star \in \{A, B, C, M, N\}$$

where, for given index $\star$, ℓ locates the cluster in the order of increasing frequency as summarized in Table 3.1.

We note from Figs. 3.5–3.6 that the leading-order asymptotic approximation of the dispersion relationship near simple eigenfrequencies (dashed lines) at the origin of the first Brillouin zone A, captures very well their curvature. Using the results from Section 3.2.1, the first-order asymptotic approximation of the dispersion relationship is also obtained for simple eigenfrequencies at the "interior" points M and N. Here, the local approximation captures with good veracity both the slope and curvature of the dispersion relationship.

With reference to Figs. 3.5–3.6 and Table 3.1, the dispersion relationship near clusters $\mathcal{N}_3^A$, $\mathcal{N}_4^A$, $\mathcal{N}_1^M$, $\mathcal{N}_1^N$ and $\mathcal{N}_2^N$ of size $Q = 2$ is approximated by solving the effective eigenvalue problem (3.97). We note from the figures that the leading-order asymptotic approximation of the dispersion relationship reconstructs accurately the interaction between the branches composing the cluster. For clusters $\mathcal{N}_1^B$, $\mathcal{N}_2^B$, $\mathcal{N}_4^B$, $\mathcal{N}_5^B$, $\mathcal{N}_6^B$, $\mathcal{N}_7^B$, $\mathcal{N}_8^B$, $\mathcal{N}_9^B$, $\mathcal{N}_{10}^B$ and $\mathcal{N}_{11}^B$ (also of size $Q = 2$), the local approximation is established using the results from Section 3.2.3 as the featured effective matrix $\boldsymbol{A}^\gamma$ is of *full rank* in direction BA and *partial rank* in direction BC.

In the low-wavenumber, low-frequency neighborhood, approximation of the acoustic branches near the origin ($\omega_1 = 0, \boldsymbol{k}_s = \boldsymbol{0}$) is obtained using model (3.85) where the effective matrix $\boldsymbol{A}^{(0)}$ of size $Q = 3$ is trivial in all directions. Finally, in the neighborhood of clusters $\mathcal{N}_1^C$ and $\mathcal{N}_2^C$ of size $Q = 4$ and clusters $\mathcal{N}_3^C$, $\mathcal{N}_4^C$, $\mathcal{N}_5^C$ and $\mathcal{N}_6^C$ of size $Q = 5$, the matrix $\boldsymbol{A}^\gamma$ is full-rank and model (3.97) is used to approximate the featured dispersion relationships with high fidelity.

Table 3.1: Example eigenfrequency clusters near points A, B, C, M and N (see Fig 3.4(d)) featured by the 2D-periodic Miura-ori structure.

Cluster	A	B	C	M	N
$\mathcal{N}_1$	1, 2, 3	1, 2	1, 2, 3, 4	4, 5	2, 3
$\mathcal{N}_2$	7, 8	3, 4	5, 6, 7, 8	–	5, 6
$\mathcal{N}_3$	14, 15	5, 6, 7, 8	9, 10, 11, 12	–	–
$\mathcal{N}_4$	16, 17	9, 10	13, 14,15, 16	–	–
$\mathcal{N}_5$	–	11, 12	17, 18, 19, 20	–	–
$\mathcal{N}_6$	–	13, 14	21, 22, 23, 24	–	–
$\mathcal{N}_7$	–	15, 16	–	–	–
$\mathcal{N}_8$	–	17, 18	–	–	–
$\mathcal{N}_9$	–	19, 20	–	–	–
$\mathcal{N}_{10}$	–	21, 22	–	–	–
$\mathcal{N}_{11}$	–	23, 24	–	–	–

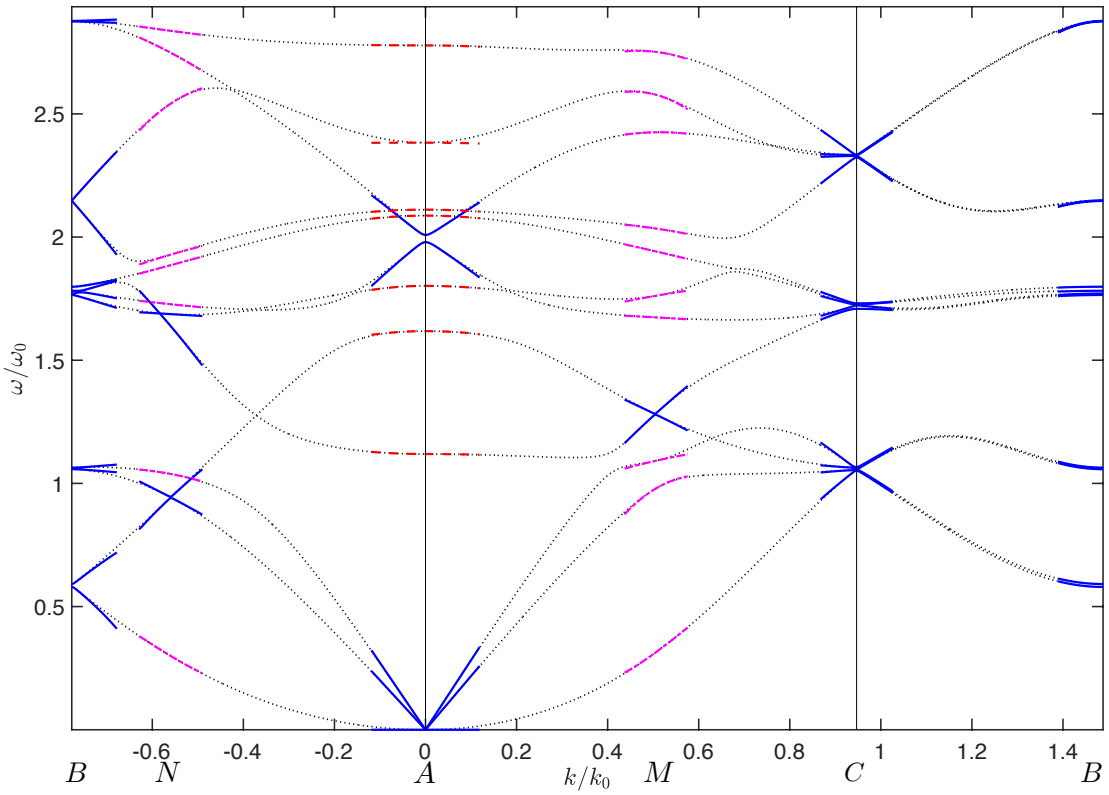

Figure 3.5: Approximation of the first twelve dispersion branches for the Miura-ori periodic structure near points A, B, C, M and N in Fig 3.4(d). In the display, dotted lines track the reference numerical results; solid lines signify the leading-order approximation of the clusters of nearby branches ($Q > 1$); dashed lines indicate the leading-order approximation of isolated dispersion branches ($Q = 1$), and dash-dotted lines plot the first-order approximation of isolated dispersion branches at points M and N. The normalization parameters are $k_0 = \pi/\ell_0$ and $\omega_0 = \sqrt{\kappa_0/m_0}$.

1D-periodic Miura tube

As the second example, we construct 1D-periodic unbounded Miura tube with $(\mathfrak{d}, \mathfrak{p}) = (3, 1)$ by (i) stacking the Miura-ori unit cell (see Fig. 3.4(b)) and its mirror image with respect to the plane $(O, \boldsymbol{e}_1, \boldsymbol{e}_2)$ and (ii) extending it periodically in direction $\boldsymbol{e}_1$. As an illustration, Fig. 3.7(a) depicts a truncation of the periodic structure; Fig. 3.7(b) shows the top view of its unit cell of periodicity Y, and Fig. 3.7(c) presents the top view of its bar-and-hinge model Y'. The dimensions of the Miura tube panels repeat those in Section 3.4.1 in that $a = 1, b = 1, \beta = \pi/4 \in (0, \pi/2)$, and $\alpha = \pi/2 - \beta/2 \in$

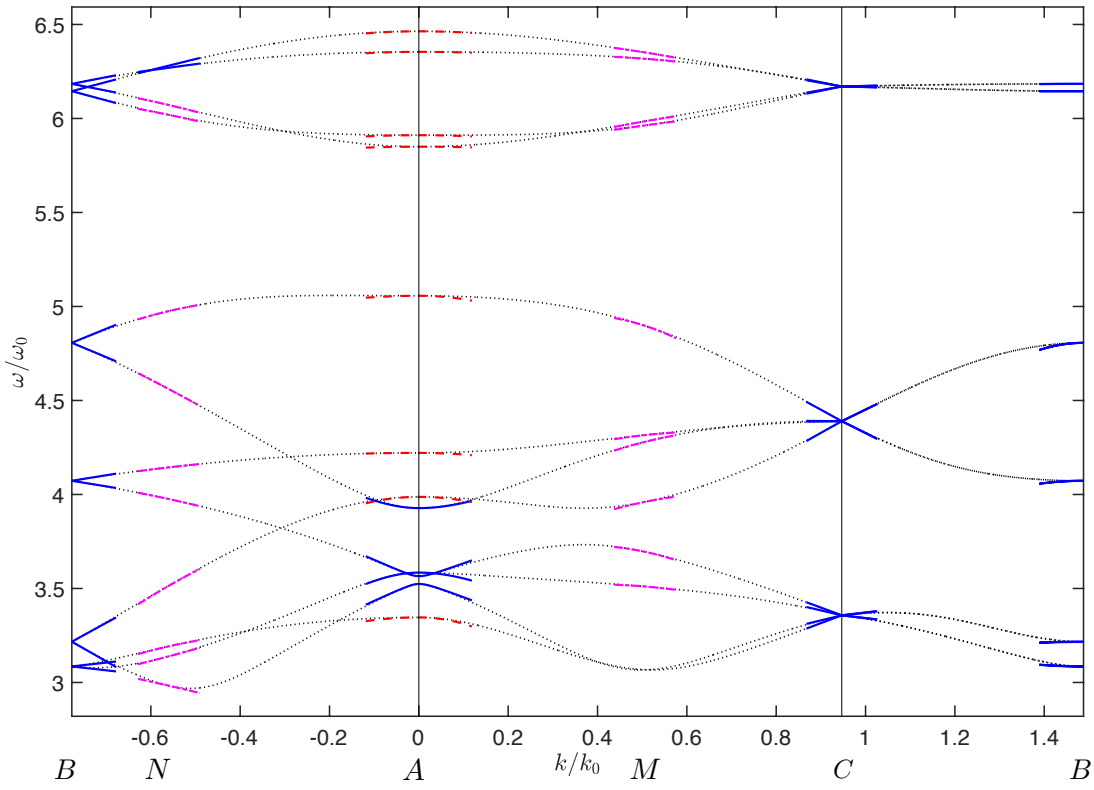

Figure 3.6: Approximation of the dispersion branches 13-24 for the Miura-ori periodic structure near points A, B, C, M and N in Fig 3.4(d). Here, dotted lines track the reference numerical results; solid lines signify the leading-order approximation of the clusters of nearby branches ($Q>1$); dashed lines indicate the leading-order approximation of isolated dispersion branches ($Q=1$), and dash-dotted lines plot the first-order approximation of isolated dispersion branches at points M and N.

$(\pi/2-\beta, \pi/2+\beta)$. Again, we assume that (i) the structure panels have a uniform surface mass density $\rho_0 = 1$; (ii) the bars are uniformly characterized by $E_0A_0 = 10^2$; (iii) the folding hinges have stiffness $k_{fs} = 1$, and (iv) the bending hinges have stiffness $k_{bs} = 10$. We maintain the same normalization parameters ($\ell_0 = a$, $\kappa_0 = E_0A_0/a$, $m_0 = \rho_0 a^2$) and auxiliary coefficients $\omega_0 = \sqrt{\kappa_0/m_0}$ and $k_0 = \pi/\ell_0$.

In this case, the unit cell Y' of DPOS S' has $\mathfrak{m} = \mathfrak{d} \times 16 = 48$ degrees of freedom. With reference to Fig. 3.5, the Miura tube Bravais lattice basis and reciprocal lattice basis are given respectively by

$$\boldsymbol{e}_1 = 2b\,\frac{\sqrt{\sin(\alpha)^2-\cos(\beta)^2}}{\sin(\alpha)}\,\boldsymbol{i}_1, \qquad \boldsymbol{e}^1 = \frac{\pi\sin(\alpha)}{b\sqrt{\sin(\alpha)^2-\cos(\beta)^2}}\,\boldsymbol{i}_1. \tag{3.123}$$

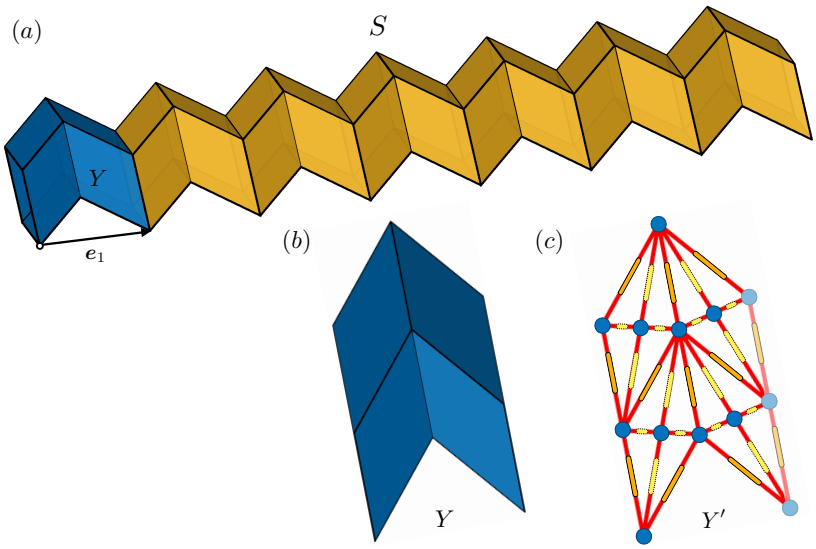

Figure 3.7: (a) Truncated one-dimensional periodic Miura tube for which $(\mathfrak{d},\mathfrak{p}) = (3,1)$, (b) top view of its unit cell of periodicity Y and (c) top view of the associated discretization via the bar-and-hinge model Y' where (i) bars are presented via continuous lines, folding (resp. bending) hinges via rounded rectangles with continuous (resp. dashed) contours and nodes via balls and (ii) nodes, bars and hinges that do not belong to Y' are shaded

Fig. 3.8 examines the performance of the asymptotic models in terms of the first twelve branches of the dispersion relationship. The comparison is made in a neighborhood of the origin A, apex point B, and internal points $\mathrm{M}_1 - \mathrm{M}_8$ of the first Brillouin zone given by

$$\begin{gathered}\overrightarrow{\mathrm{AB}} = \tfrac{1}{2}\boldsymbol{e}^1, \quad \overrightarrow{\mathrm{AM}_1} = 0.425\,\overrightarrow{\mathrm{AB}}, \quad \overrightarrow{\mathrm{AM}_2} = 0.605\,\overrightarrow{\mathrm{AB}}, \quad \overrightarrow{\mathrm{AM}_3} = 0.545\,\overrightarrow{\mathrm{AB}},\\ \overrightarrow{\mathrm{AM}_4} = 0.455\,\overrightarrow{\mathrm{AB}}, \quad \overrightarrow{\mathrm{AM}_5} = 0.275\,\overrightarrow{\mathrm{AB}}, \quad \overrightarrow{\mathrm{AM}_6} = 0.840\,\overrightarrow{\mathrm{AB}},\\ \overrightarrow{\mathrm{AM}_7} = 0.610\,\overrightarrow{\mathrm{AB}}, \quad \overrightarrow{\mathrm{AM}_8} = 0.875\,\overrightarrow{\mathrm{AB}}.\end{gathered} \tag{3.124}$$

The example eigenfrequency clusters for which we pursue asymptotic approximation are summarized in Table 3.2.

From Fig. 3.8, we first observe that the leading-order (resp. first-order) asymptotic

Table 3.2: Example eigenfrequency clusters near points A, B, and M_1-M_8 (see (3.124)) featured by the 1D-periodic Miura tube.

Cluster	A	B	M_3	M_4	M_5	M_6	M_7	M_8
$\mathcal{N}_1$	1, 2, 3, 4	3, 4	3, 4	5, 6	9, 8, 10	9, 10, 11	7, 8	4, 5
$\mathcal{N}_2$	–	5, 6	–	–	–	–	10, 11, 12	–
$\mathcal{N}_3$	–	7, 8	–	–	–	–	–	–
$\mathcal{N}_4$	–	9, 10	–	–	–	–	–	–
$\mathcal{N}_5$	–	11, 12	–	–	–	–	–	–

approximation of the dispersion relationship near simple eigenfrequencies at the apex points A and B (resp. internal points M and N) captures very well the local dispersion behavior. The model for these examples is provided in Section 3.2.1. On the other hand, the dispersion relationship near clusters $\mathcal{N}_1^B$, $\mathcal{N}_2^B$, $\mathcal{N}_3^B$, $\mathcal{N}_4^B$, $\mathcal{N}_5^B$, $\mathcal{N}_1^{M_3}$, $\mathcal{N}_1^{M_4}$, $\mathcal{N}_1^{M_5}$, $\mathcal{N}_1^{M_7}$ and $\mathcal{N}_1^{M_8}$ (of size $Q = 2$) is approximated by solving the effective eigenvalue problem (3.97). Again, we observe from the figure that the leading-order asymptotic approximation of the dispersion relationship reconstructs very well the interaction between the branches composing the cluster. In the neighborhood of clusters $\mathcal{N}_1^{M_6}$ and $\mathcal{N}_2^{M_7}$ of size $Q = 3$, matrix $\boldsymbol{A}^\gamma$ is of full-rank and model (3.97) is used to approximate the local dispersion behavior. Near the origin ($\omega_1 = 0, \boldsymbol{k}_s = \boldsymbol{0}$) of the Brillouin zone, the dispersion map is approximated using model (3.85) where the effective matrix $\boldsymbol{A}^{(0)}$ of size $Q = 4$ is found to be trivial in all directions.

3.4.2 Forced motion

In this section, we examine the leading-order effective motion of the 2D-periodic Miura-ori structure described in Section 3.4.1 due to a body force $\boldsymbol{f}$ near the edge of a band gap where $\boldsymbol{\mu}^{(0)}$ is sign-definite. To this end, we consider the excitation frequency $\omega^2 = \omega_{20}^2 + \sigma\epsilon^2\omega_0^2$, where $\sigma \in \{-1, 1\}$ determines the position of ω relative to the eigenfrequency ω_{20}. With reference to (3.21), we consider three "uni-component"realizations of the force term $\boldsymbol{f}^{(j)}_{\hat{\mathbf{p}}^{(\mathrm{n})}}$ according to

$$\boldsymbol{f}^{(j)}_{\hat{\mathbf{p}}^{(\mathrm{n})}} \;=\; F_{\hat{\mathbf{p}}^{(\mathrm{n})}}\, \boldsymbol{i}_j \quad (j \in \{1,2,3\}), \qquad F_{\hat{\mathbf{p}}^{(\mathrm{n})}} = \int_C e^{-\varepsilon_0^{-2}\|\boldsymbol{k}\|^2} e^{i\boldsymbol{k}\cdot\boldsymbol{x}_{\hat{\mathbf{p}}^{(\mathrm{n})}}}\, \mathrm{d}\boldsymbol{k}, \tag{3.125}$$

where $\mathcal{C} \subset \mathcal{B}$ is a disc centered on the origin of the first Brillouin zone with radius $\|\boldsymbol{e}^2\|/2$, and $\boldsymbol{e}^2$ is the second reciprocal lattice basis vector. The leading-order approximation of the effective motion $\langle \boldsymbol{u} \rangle_\rho^{[0]}(\boldsymbol{x})$ for $\boldsymbol{x} \in \mathbb{R}^2$ is evaluated by integrating (3.109) numerically

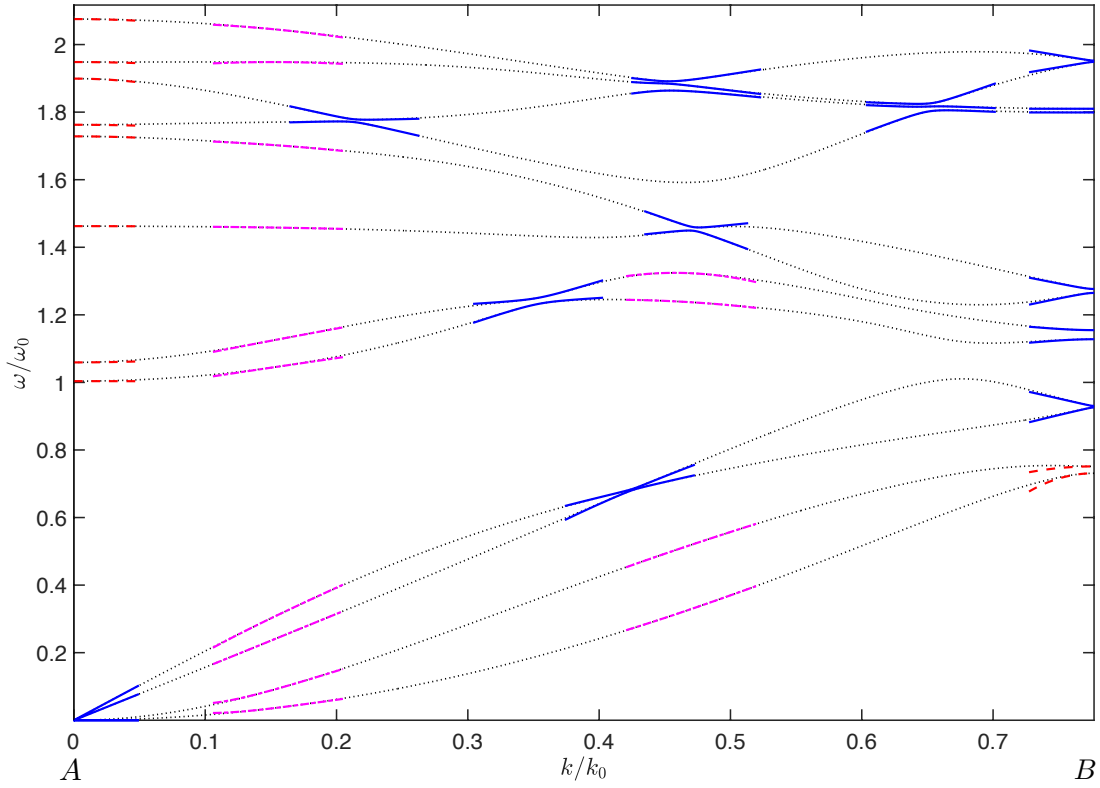

Figure 3.8: Approximation of the first twelve dispersion branches for the Miura tube near points A, B and $M_1 - M_8$ as defined in (3.124). In the display, dotted lines track the reference numerical results; solid lines signify the leading-order approximation of the clusters of nearby branches ($Q > 1$), and dash-dotted lines plot the first-order approximation of isolated dispersion branches ($Q = 1$). The normalization parameters are defined as $k_0 = \pi/\ell_0$ and $\omega_0 = \sqrt{\kappa_0/m_0}$.

over $\mathcal{C}$. Allowing for a slight abuse of notation, we also introduce an auxiliary constant vector $\boldsymbol{f}^{(j)} \in \mathbb{R}^{\mathfrak{d}N_n}$, defined over the unit cell of DPOS, so that its value at each node equals $\boldsymbol{i}_j$.

Driving frequency inside a band gap

First, we consider the situation where the driving frequency is within the band gap ($\omega > \omega_{20}$), for which $\sigma = 1$. For the purpose of numerical simulations, we take $\varepsilon_0 = 0.5$

and $\epsilon \in \{0.0994, 0.1265, 0.1581\}$, see Fig 3.9. In Fig. 3.10, we plot continuous interpolation of the amplitude of the driving force due to (3.125) and the corresponding leading-order *effective motion*, $\langle \boldsymbol{u} \rangle_{\rho}^{[0]}$, over 70×70 unit cells of the Miura-ori periodic structure for: (a) $\epsilon = 0.0994$, (b) $\epsilon = 0.1265$ and (c) $\epsilon = 0.1581$. Thanks to (3.109)–(3.110), we observe that the ratio $\langle \boldsymbol{u} \rangle_{\rho}^{[0]} / \langle \boldsymbol{i}_j \rangle$ is independent of the choice of the direction j of the source term in (3.125). As a result, the mean motion results in Fig. 3.10 are conveniently normalized by $\langle \boldsymbol{f}^{(j)} \rangle$, noting that $\langle \boldsymbol{f}^{(1)} \rangle = 6.6703\,10^{-5}$, $\langle \boldsymbol{f}^{(2)} \rangle = 5.7615\,10^{-4}$, and $\langle \boldsymbol{f}^{(3)} \rangle = 6.9777\,10^{-1}$. From the display, we observe rapid decay of the solution away from the source (as expected for driving frequencies inside the band gap) and anisotropic character of the effective motion near ω_{20}. Further, the rate of decay is seen to increase monotonically with increasing ϵ, i.e. increasing "incursion" into the band gap.

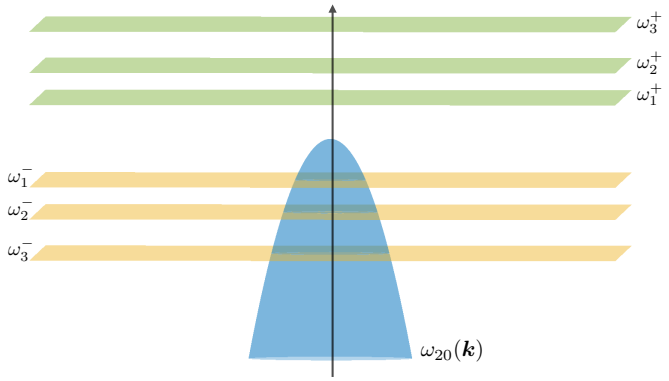

Figure 3.9: Relative position of the excitation frequencies $\omega_1^+ = \sqrt{\omega_{20}^2 + 0.0994^2}$, $\omega_2^+ = \sqrt{\omega_{20}^2 + 0.1265^2}$, $\omega_3^+ = \sqrt{\omega_{20}^2 + 0.1581^2}$, $\omega_1^- = \sqrt{\omega_{20}^2 - 0.0994^2}$, $\omega_2^- = \sqrt{\omega_{20}^2 - 0.1265^2}$ and $\omega_3^- = \sqrt{\omega_{20}^2 - 0.1581^2}$ where $\omega_{20} = \omega_{20}(\boldsymbol{0})$. The frequency interval covered by the shaded "parabolic" region indicates a passband.

Driving frequency inside a passband

Next, we excite the periodic Miura-ori structure in the passband by setting $\sigma = -1$, $\varepsilon_0 = 0.5$ and $\epsilon \in \{0.0994, 0.1265, 0.1581\}$, see Fig 3.9. In this case, the integrand in (3.109) is singular yet integrable as demonstrated in Section 3.3.1. As a result, we aid the numerical integration (implemented in Matlab) by adding an imaginary penalty i.e. regularization term $i\tau$ to the denominator in (3.110); in particular, we let $\tau = 0.3, 0.5, 0.7$ for $\epsilon = 0.0994$, $\epsilon = 0.1265$ and $\epsilon = 0.1581$, respectively. In Fig. 3.11, we plot the normalized *effective motion* $\langle \boldsymbol{f}^{(j)} \rangle^{-1} \langle \boldsymbol{u} \rangle_{\rho}^{[0]}$ (real part) over 70×70 unit cells of the Miura -ori periodic structure for (a) $\epsilon = 0.0994$, (b) $\epsilon = 0.1265$ and (c) $\epsilon = 0.1581$.

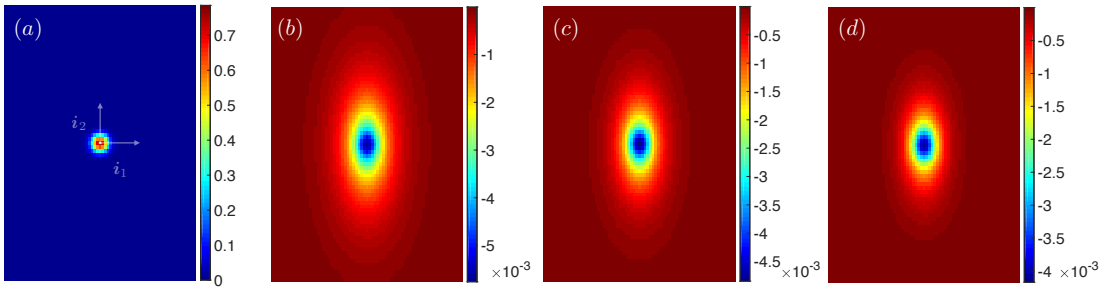

Figure 3.10: Excitation inside a band gap: (a) amplitude of the driving force $\boldsymbol{f}^{(j)}_{\hat{\mathbf{p}}^{(\mathrm{n})}}$ ($j \in \{1,2,3\}$) and leading-order approximations of the induced effective motion $\langle \boldsymbol{f}^{(j)} \rangle^{-1} \langle \boldsymbol{u} \rangle^{[0]}_{\rho}(\boldsymbol{x})$ (real part) over 70×70 unit cells for $\sigma = 1$ and (a) $\epsilon = 0.0994$, (b) $\epsilon = 0.1265$, and (c) $\epsilon = 0.1581$.

In this case, we clearly observe the manifestation of (anisotropic) wave propagation, characterized by diminishing wavelength with increasing ϵ, i.e. increasing "incursion" into the passband.

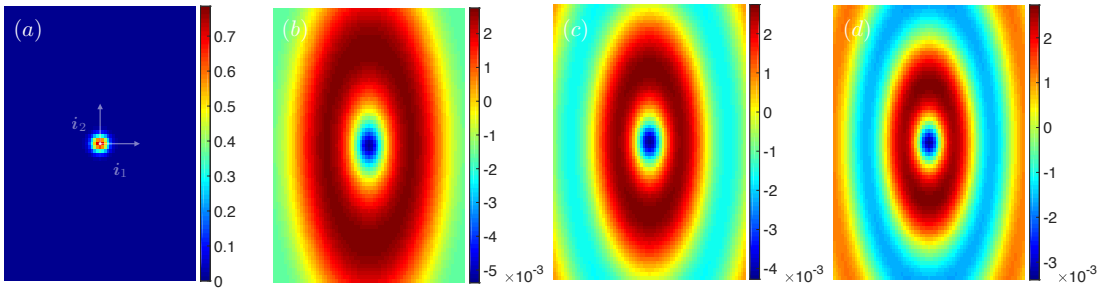

Figure 3.11: Excitation inside a passband: (a) amplitude of the driving force $\boldsymbol{f}^{(j)}_{\hat{\mathbf{p}}^{(\mathrm{n})}}$ ($j \in \{1,2,3\}$) and leading-order approximations of the induced effective motion $\langle \boldsymbol{f}^{(j)} \rangle^{-1} \langle \boldsymbol{u} \rangle^{[0]}_{\rho}(\boldsymbol{x})$ (real part) over 70×70 unit cells for $\sigma = -1$ and (a) $\epsilon = 0.0994$, (b) $\epsilon = 0.1265$ and (c) $\epsilon = 0.1581$.

Chapter 4

Summary and outlook

In the first part of this dissertation, we established a rational framework for finite-wavenumber, finite-frequency (FW-FF) homogenization of the scalar wave equation in (generally non-orthogonal) periodic media with Dirichlet and Neumann "perforations", i.e. exclusions. The proposed asymptotic ansatz applies to spectral neighborhoods of (i) an arbitrary wavenumber within the first Brillouin zone, and (ii) either simple, repeated, or nearby eigenfrequencies. With the aid of the Bloch-wave expansion that provides us with handle on the wavenumber, we also account for, and homogenize, the source term featured in the field equation. A systematic asymptotic analysis of tightly-spaced eigenfrequency clusters (covering the most general asymptotic configuration) reveals an effective system of field equations featuring a "matrix" operator weaving Dirac- and wave-like behaviors, and a vector source term built from the projections of the (scalar) source term onto participating phonons, i.e. Bloch eigenfunctions. As numerical examples, we provide asymptotic description of the dispersion relationship for a Kagome lattice with Neumann exclusions, and a square lattice of Dirichlet obstacles. We also examine the performance of the effective model with a source term, up to the second order of asymptotic correction, by considering the response of the Kagome lattice to a dipole-like source acting near the edge of an internal band gap.

In the second part of this work, by leveraging the bar-and-hinge paradigm we developed a homogenization framework that physically informs and numerically simplifies the dynamic analysis of linear periodic origami structure. To this end, we specifically adopt the N5B8 linear elastic element that endows each parallelepipedal panel of the origami structure with five inertial nodes, eight extending bars that link the nodes, linear folding hinges along the peripheral bars, and linear bending hinges along the internal bars. For generality, the discrete origami model is designed to admit periodic homogenous Dirichlet boundary conditions and a "body force" acting on the nodes of

a discrete structure. In this setting, we formulate the leading-order (system of) effective equation(s) governing the wave motion in origami structures near simple, repeated, and nearby eigenfrequencies at an arbitrary wavenumber within the first Brillouin zone. On setting the source term to zero, from this system we obtain a low-order algebraic eigenvalue problem that yields the leading-order asymptotic approximation of the Bloch dispersion relationship of the periodic origami structure over a given spectral neighborhood. Using a 2D-periodic Miura-ori structure and a 1D-periodic Miura tube as the basis for numerical simulations, the proposed homogenization framework is shown to provide an accurate local description of the dispersion relationship in all spectral situations. The numerical illustrations of the dispersion relationship are complemented by simulations of the effective wave motion in 2D-periodic Miura-ori structure at frequencies (i) near the edge of a band gap and (ii) within a pass band. From the simulations, we observe that the dynamic anisotropy of the periodic origami structure is well captured in both excitation regimes. We also note that the featured homogenization framework is independent from the adopted bar-and-hinge model, and it inherently applies to any origami model where the panels are linked with linear extending and folding membranes [60, 87]. The proposed analysis can be extended toward describing the effective wave motion in viscoelastic (damped) DPOSs, as well as that in nonlinear (periodic) origami structures.

References

[1] Y. Achaoui, T. Antonakakis, S. Brl, R.V. Craster, S. Enoch and S. Guenneau (2017). Clamped seismic metamaterials: ultra-low frequency stop bands. *New Journal of Physics*, 19(6), 063022.

[2] G. Allaire, Homogenization and two-scale convergence, *SIAM J. Math. Anal.*, 23, 1482–1518.

[3] G. Allaire, M. Briane, M. Vanninathan (2016). A comparison between two-scale asymptotic expansions and Bloch wave expansions for the homogenization of periodic structures, *SeMA J.* 73, 237–259.

[4] G. Allaire, C. Conca (1998). Bloch wave homogenization and spectral asymptotic analysis, *J. Math. Pures Appl.*, 77, 153–208.

[5] I.V. Andrianov, V.I. Bolshakov, V.V. Danishevs' kyy and D. Weichert (2008). Higher order asymptotic homogenization and wave propagation in periodic composite materials. *Proc. Roy. Soc. A* 464(2093),1181-1201.

[6] T. Antonakakis, R.V. Craster and S. Guenneau (2013). Asymptotics for metamaterials and photonic crystals.*Proc. Roy. Soc. A* 469(2152), 20120533.

[7] T. Antonakakis , R.V. Craster and S. Guenneau (2013). High-frequency homogenization of zero-frequency stop band photonic and phononic crystals. *New Journal of Physics*, 15,103014.

[8] T. Antonakakis, R.V. Craster and S. Guenneau (2014). Homogenization for elastic photonic crystals and dynamic anisotropy. *Journal of the Mechanics and Physics of Solids*, 71, 84-96.

[9] M.W. Ashraf and M. Faryad (2015). Dirac-like cone dispersion in two-dimensional core-shell dielectric photonic crystals. *J. Nanophotonics*, 9(1), 093057.

[10] J.L. Auriault and C. Boutin (2012). Long wavelength inner-resonance cut-off frequencies in elastic composite materials. *Int. J. Solids Struct*, 49(23-24), 3269–3281.

[11] E. Bavarelli, M. Ruzzene (2013). Internally resonating lattices for bandgap generation and low-frequency vibration control, *J. Sound Vibr.* 332, 6562–6579.

[12] A. Bensoussan, J.-L. Lions, G. Papanicolaou (1978). *Asymptotic Analysis for Periodic Structures*, North-Holland.

[13] M.S. Birman (2004). On homogenization procedure for periodic operators near the edge of an internal gap, *St. Petersbg. Math. J.*, 15(4), 507-513.

[14] M.S. Birman, T.A. Suslina (2006). Homogenization of a multidimensional periodic elliptic operator in a neighborhood of the edge of an internal gap, *J. Math. Sci.* 136(2), 3682–3690.

[15] F. Capolino, ed. (2009). *Applications of Metamaterials*, CRC Press.

[16] L. Ceresoli, R. Abdeddaim, T. Antonakakis, B. Maling, M. Chmiaa, P. Sabouroux, G. Tayeb, S. Enoch, R.V. Craster and S. Guenneau (2015). Dynamic effective anisotropy: Asymptotics, simulations, and microwave experiments with dielectric fibers. *Physical Review B*, 92(17), 174307.

[17] W. Chen, J. Fish (2001). A dispersive model for wave propagation in periodic heterogeneous media based on homogenization with multiple spatial and temporal scales, *ASME J. Appl. Mech.* 68(2), 153–161.

[18] R.V. Craster, J. Kaplunov, A.V. Pichugin (2010). High-frequency homogenization for periodic media, *Proc. Roy. Soc. A* 466(2120), 234-2362.

[19] R.V. Craster, J. Kaplunov, E. Nolde, S. Guenneau (2011). High-frequency homogenization for checkerboard structures: defect modes, ultrarefraction, and all-angle negative refraction, *J. Opt. Soc. Am. A* 28(6), 1032–1040.

[20] K.B. Dossou, L.C. Botten, R.C. McPhedran, C.G. Poulton, A.A. Asatryan, C. Martijn de Sterke (2008). Shallow defect states in two-dimensional photonic crystals, *Phys. Rev. A* 77(6), 133–18.

[21] Z. Liu, X. Zhang, Y. Mao,Y.Y. Zhu, Z. Yang, C.T. Chan and P. Sheng (2000). Locally resonant sonic materials. *science, 289*(5485), 1734-1736.

[22] S. Gonella, M. Ruzzene (2010). Multicell homogenization of one-dimensional periodic structures, *J. Vibr. Acoustics*, 132(1).

[23] B.B. Guzina, S. Meng, O. Oudghiri-Idrissi (2019). A rational framework for dynamic homogenization at finite wavelengths and frequencies. *Proc. Roy. Soc. A* 475(2223), 20180547.

[24] R. Hill (1964). Elastic properties of reinforced solids: some theoretical principles. *J. Mech. Phys. Solids*, 11(5), 357-372.

[25] G. Hu and M. Sini (2013). Elastic scattering by finitely many point-like obstacles. *Journal of Mathematical Physics*, 54(4), 042901.

[26] X. Huang, Y. Lai, Z.H. Hang, H. Zheng and C.T. Chan (2011). Dirac cones induced by accidental degeneracy in photonic crystals and zero-refractive-index materials. *Nature materials*, 10(8), 582-586.

[27] J. Hyun, W. Choi, S. Wang, C.S. Park and M. Kim (2018). Systematic realization of double-zero-index phononic crystals with hard inclusions. *Scientific reports*, 8(1), 1-9.

[28] J. Ma, K. Sun and S. Gonella, 2019. Valley Hall In-Plane Edge States as Building Blocks for Elastodynamic Logic Circuits. *Physical Review Applied*, 12(4), 044015.

[29] J. Ma, D. Zhou, K. Sun, X. Mao and S. Gonella (2018). Edge modes and asymmetric wave transport in topological lattices: Experimental characterization at finite frequencies. *Physical review letters*, 121(9), 094301.

[30] M. Makwana , T. Antonakakis , B. Maling , S. Guenneau and R.V. Craster (2016). Wave mechanics in media pinned at Bravais lattice points. *SIAM Journal on Applied Mathematics*, 76(1), 1–26.

[31] P.A. Martin and A.J. Hull (2020). Dynamic response of an infinite thin plate loaded with concentrated masses. *Wave Motion*, 98, 102643.

[32] A. Movchan and M. Nieves (2021). On meso-scale approximations for vibrations of membranes with lower-dimensional clusters of inertial inclusions. *St. Petersburg Mathematical Journal*, 32(3), 551-564.

[33] S. Meng, B. Guzina (2017). On the dynamic homogenization of periodic media: Willis' approach versus two-scale paradigm, *Proc. R. Soc. A* 474(2213), 20170638.

[34] S. Meng, O. Oudghiri-Idrissi and B.B. Guzina (2021). A convergent low-wavenumber, high-frequency homogenization of the wave equation in periodic media with a source term. *Applicable Analysis*, 1-34.

[35] G.W. Milton, J.R. Willis (2007). On modifications of Newton's second law and linear continuum elastodynamics, *Proc. R. Soc. A* 463(2079), 855–880.

[36] H. Nassar, Q.-C. He, N. Auffray (2016). A generalized theory of elastodynamic homogenization for periodic media, *Int. J. Solids Struct.* , 84, 139–146.

[37] F. Odeh and J.B. Keller (1964). Partial differential equations with periodic coefficients and Bloch waves in crystals. *Journal of Mathematical Physics*, 5(11), 1499-504.

[38] W.J. Parnell and P.A. Martin (2011). Multiple scattering of flexural waves by random configurations of inclusions in thin plates. *Wave Motion*, 48(2), 161-175.

[39] F. Santosa, W.W. Symes (1991). A dispersive effective medium for wave propagation in periodic composites. *SIAM J. Appl. Math*, 51(4), 98–1005.

[40] J. Schöberl (2014). C++11 Implementation of Finite Elements in NGSolve, *ASC Report 30/2014*, Institute for Analysis and Scientific Computing, Vienna University of Technology.

[41] O. Schnitzer and R.V. Craster (2017). Bloch waves in an arbitrary two-dimensional lattice of subwavelength Dirichlet scatterers. *SIAM Journal on Applied Mathematics*, 77(6), 2119-2135.

[42] D. Sjöberg, C. Engström, G. Kristensson, D.J. Wall, N. Wellander, (2005). A Floquet–Bloch Decomposition of Maxwell's Equations Applied to Homogenization. *Multiscale Model. Simul.*, 4(1), 149–171.

[43] A. Wautier, B. Guzina (2015). On the second-order homogenization of wave motion in periodic media and the sound of a chessboard, *J. Mech. Phys. Solids* 78, 382–414.

[44] C.H. Wilcox (1978). *Theory of Bloch waves*, *J. Analyse Math.*, 33(1), 146–167.

[45] J.R. Willis (1983). The overall elastic response of composite materials. *J. Appl. Mech. ASME* 50, 1202–1209.

[46] J.R. Willis (2011). Effective constitutive relationships for waves in composites and metamaterials, *Proc. R. Soc. A* 467(2131), 1865–1879.

[47] J.R. Willis (2016). Negative refraction in a laminate, *J. Mech. Phys. Solids*, 97, 10–18.

[48] A.G. Ramm (2007). Many-body wave scattering by small bodies and applications. *Journal of mathematical physics*, 48(10), 103511.

[49] A.G. Ramm (2011). Wave scattering by small bodies and creating materials with a desired refraction coefficient. *Afrika Matematika*, 22(1), 33-55.

[50] M. Arya (2016). Packaging and deployment of large planar spacecraft structures (Doctoral dissertation, California Institute of Technology).

[51] G. Bordiga, L. Cabras, A. Piccolroaz and D. Bigoni (2021). Dynamics of prestressed elastic lattices: Homogenization, instabilities, and strain localization. *Journal of the Mechanics and Physics of Solids*, 146, 104198.

[52] V. Brunck, F. Lechenault, A. Reid and M. Adda-Bedia (2016). Elastic theory of origami-based metamaterials. *Physical Review E*, 93(3), 033005.

[53] R.V. Craster, J. Kaplunov and J. Postnova (2010). High-frequency asymptotics, homogenisation and localisation for lattices. *The Quarterly Journal of Mechanics and Applied Mathematics*, 63(4), 497-519.

[54] Y. Du, C. Song, J. Xiong and L. Wu (2019). Fabrication and mechanical behaviors of carbon fiber reinforced composite foldcore based on curved-crease origami. *Composites Science and Technology*, 174, 94-105.

[55] A.A. Evans, J.L. Silverberg and C.D. Santangelo (2015). Lattice mechanics of origami tessellations. *Physical Review E* , 92(1), 013205.

[56] E.T. Filipov, T. Tachi and G.H. Paulino (2015). Toward optimization of stiffness and flexibility of rigid, flat-foldable origami structures. In *The 6th International Meeting on Origami in Science, Mathematics and Education*, 121.

[57] E.T. Filipov, T. Tachi and G.H. Paulino (2015). Origami tubes assembled into stiff, yet reconfigurable structures and metamaterials. *Proceedings of the National Academy of Sciences*, 112(40), pp.12321-12326.

[58] E.T. Filipov, K. Liu, T. Tachi, M. Schenk and G.H. Paulino (2017). Bar and hinge models for scalable analysis of origami. *International Journal of Solids and Structures*, 124, 26-45.

[59] S.W. Grey, F. Scarpa and M. Schenk (2019). Strain reversal in actuated origami structures. *Physical Review Letters*, 123(2), 025501.

[60] E.A.P. Hernandez , D.J. Hartl , E. Akleman and D.C. Lagoudas (2016). Modeling and analysis of origami structures with smooth folds. *Computer-Aided Design*, 78, 93-106.

[61] D.T., Ho, S.Y. Kim and U. Schwingenschlgl (2020). Graphene origami structures with superflexibility and highly tunable auxeticity. *Physical Review B*, 102(17), 174106.

[62] K. Kuribayashi, K. Tsuchiya, Z. You, D. Tomus, M. Umemoto, T. Ito and M. Sasaki (2006). Self-deployable origami stent grafts as a biomedical application of Ni-rich TiNi shape memory alloy foil. *Materials Science and Engineering: A*, 419(1-2), 131-137.

[63] S. Li, H. Fang, S. Sadeghi, P. Bhovad and K.W. Wang (2019). Architected origami materials: How folding creates sophisticated mechanical properties. *Advanced materials*, 31(5), 1805282.

[64] J. Liu, H. Ou, R. Zeng, J. Zhou, K. Long, G. Wen and Y.M. Xie (2019). Fabrication, dynamic properties and multi-objective optimization of a metal origami tube with Miura sheets. *Thin-Walled Structures*, 144, 106352.

[65] K. Liu and G.H. Paulino (2017). Nonlinear mechanics of non-rigid origami: an efficient computational approach. *Proc. Roy. Soc. A* 473(2206), 20170348.

[66] A. Lebe and K. Sab (2010). Transverse shear stiffness of a chevron folded core used in sandwich construction. *International Journal of Solids and Structures*, 47(18-19), 2620-2629.

[67] A. Lebe and K. Sab (2011). A Bending-Gradient model for thick plates. Part I: Theory. *International Journal of Solids and Structures*, 48(20), 2878-2888.

[68] A. Lebe and K. Sab (2012). Homogenization of thick periodic plates: Application of the Bending-Gradient plate theory to a folded core sandwich panel. *International Journal of Solids and Structures*, 49(19-20), 2778-2792.

[69] F. Lechenault, B. Thiria and M. Adda-Bedia (2014). Mechanical response of a creased sheet. *Physical Review Letters*, 112(24), 244301.

[70] S. Li, D.M. Vogt, D. Rus and R.J. Wood (2017). Fluid-driven origami-inspired artificial muscles. *Proceedings of the National academy of Sciences*, 114(50), 13132-13137.

[71] M. Makwana and R.V. Craster (2014). Homogenization for hexagonal lattices and honeycomb structures. *The Quarterly Journal of Mechanics and Applied Mathematics*, 67(4), 599-630.

[72] S. Meng, B. Guzina (2017). On the dynamic homogenization of periodic media: Willis' approach versus two-scale paradigm, *Proc. R. Soc. A* 474(2213), 20170638.

[73] M. Norman and K. Arjomandi (2017) (2017). Origami applications in structural engineering: a look at temporary shelters. *Proceedings of the 2-nd world congress on civil, structural, and environmental engineering (CSEE'17)*,130, 2371-52.

[74] E. Nolde, R.V. Craster and J. Kaplunov (2011). High frequency homogenization for structural mechanics. *Journal of the Mechanics and Physics of Solids*, 59(3), 651-671.

[75] O. Oudghiri-Idrissi, B.B. Guzina and S. Meng (2021). On the spectral asymptotics of waves in periodic media with Dirichlet or Neumann exclusions. *The Quarterly Journal of Mechanics and Applied Mathematics*, 74(2), 173-221.

[76] N.S.N. Ota, L. Wilson, A.G. Neto, S. Pellegrino and P. Pimenta (2016). Nonlinear dynamic analysis of creased shells. *Finite Elements in Analysis and Design*, 121, 64-74.

[77] C. Pradier, J. Cavoret, D. Dureisseix, C. Jean-Mistral and F. Ville (2016). An experimental study and model determination of the mechanical stiffness of paper folds. *Journal of Mechanical Design*, 138(4), 041401.

[78] P.P. Pratapa, P. Suryanarayana and G.H. Paulino (2018). Bloch wave framework for structures with nonlocal interactions: Application to the design of origami acoustic metamaterials. *Journal of the Mechanics and Physics of Solids*, 118, 115-132.

[79] P.P. Pratapa, K. Liu and G.H. Paulino (2019). Geometric mechanics of origami patterns exhibiting Poisson's ratio switch by breaking mountain and valley assignment. *Physical Review Letters*, 122(15),155501.

[80] J. Song, Y. Chen and G. Lu (2012). Axial crushing of thin-walled structures with origami patterns. *Thin-Walled Structures*, 54, 65-71.

[81] M. Schenk and S.D. Guest (2011). Origami folding: A structural engineering approach. *Origami, 5*, 291-304.

[82] M. Schenk, A.D. Viquerat , K.A. Seffen and S.D. Guest (2014). Review of inflatable booms for deployable space structures: packing and rigidization. *Journal of Spacecraft and Rockets*, 51(3), 762-778.

[83] M.Thota and K.W. Wang (2017). Reconfigurable origami sonic barriers with tunable bandgaps for traffic noise mitigation. *Journal of Applied Physics*, 122(15), 154901.

[84] H. Wu, H. Fang, L. Chen and J. Xu (2020). Transient Dynamics of a Miura-Origami Tube during Free Deployment. *Physical Review Applied*, 14(3), 034068.

[85] Z.Y. Wei, Z.V. Guo, L. Dudte, H.Y. Liang and L. Mahadevan (2013). Geometric mechanics of periodic pleated origami. *Physical Review Letters*, 110(21), 215501.

[86] H. Yasuda (2018). Wave dynamics in origami-based mechanical metamaterials (Doctoral dissertation, University of Washington).

[87] Y. Zhu and E.T. Filipov (2020). A bar and hinge model for simulating bistability in origami structures with compliant creases. *Journal of Mechanisms and Robotics* 12(2).

[88] Q. Zhang, H. Fang and J. Xu (2020). Programmable stopbands and supratransmission effects in a stacked miura-origami metastructure. *Physical Review E*, 101(4), 042206.

[89] M. Zhang, J. Yang and R. Zhu (2021). Origami-Based Bistable Metastructures for Low-Frequency Vibration Control. *Journal of Applied Mechanics*, 88(5), 051009.

Appendix A

Supporting results for Chapter 2

A.1 Bloch wave expansion (BWE)

Assume $f \in L^2(S)$. Leting $\boldsymbol{x} \in S$, we define the function $\tilde{f}_{\boldsymbol{k}} \in L^2_p(Y)$ as

$$\tilde{f}_{\boldsymbol{k}}(\boldsymbol{x}) = \sum_{\boldsymbol{r}\in\boldsymbol{R}} f(\boldsymbol{x}+\boldsymbol{r}) e^{-i\boldsymbol{k}\cdot(\boldsymbol{x}+\boldsymbol{r})}.$$

For $\boldsymbol{k}_s \in \mathbb{R}^d$, we have

$$\begin{aligned}
\int_{\boldsymbol{k}_s+\mathcal{B}} \frac{1}{|\mathcal{B}|} \tilde{f}_{\boldsymbol{k}}(\boldsymbol{x}) e^{i\boldsymbol{k}\cdot\boldsymbol{x}} d\boldsymbol{k} &= \int_{\boldsymbol{k}_s+\mathcal{B}} \frac{1}{|\mathcal{B}|} \sum_{\boldsymbol{r}\in\boldsymbol{R}} f(\boldsymbol{x}+\boldsymbol{r}) e^{-i\boldsymbol{k}\cdot\boldsymbol{r}} d\boldsymbol{k} \\
&= \sum_{\boldsymbol{r}\in\boldsymbol{R}} f(\boldsymbol{x}+\boldsymbol{r}) \frac{e^{-i\boldsymbol{k}_s\cdot\boldsymbol{r}}}{|\mathcal{B}|} \int_{\mathcal{B}} e^{-i\boldsymbol{k}\cdot\boldsymbol{r}} d\boldsymbol{k} \\
&= f(\boldsymbol{x}), \qquad \text{(A.1)}
\end{aligned}$$

since the last integral vanishes for all $\boldsymbol{r} \neq \boldsymbol{0}$ due to (2.7).

A.2 Relationship between the plane wave expansion (PWE) and BWE

Let $\psi(\boldsymbol{k})$ be a Y_0^*-periodic function defined on the reciprocal space $\mathbb{R}^d$ as

$$\psi(\boldsymbol{k}) = \sum_{\boldsymbol{r}\in\boldsymbol{R}} e^{i\boldsymbol{r}\cdot\boldsymbol{k}}.$$

For $\boldsymbol{r}^* \in \boldsymbol{R}^*$, it is clear that $\psi(\boldsymbol{k}+\boldsymbol{r}^*) = \psi(\boldsymbol{k})$ since $\boldsymbol{r}\cdot\boldsymbol{r}^* \in 2\pi\mathbb{Z}$ by (2.1) and (3.3). Next, let $\phi(\boldsymbol{k})$ be Y_0^*-periodic and square-integrable over Y_0^* and let $\Phi(\boldsymbol{r})$, with $\boldsymbol{r}\in\boldsymbol{R}$, denote its Fourier series coefficient. For $\boldsymbol{k}_\circ \in \mathbb{R}^d$, we then have

$$\begin{aligned}
\int_{Y_0^*} \psi(\boldsymbol{k}-\boldsymbol{k}_\circ)\phi(\boldsymbol{k})d\boldsymbol{k} &= \int_{Y_0^*} \Big(\sum_{\boldsymbol{r}\in\boldsymbol{R}} e^{i\boldsymbol{r}\cdot(\boldsymbol{k}-\boldsymbol{k}_\circ)}\Big)\phi(\boldsymbol{k})d\boldsymbol{k} \\
&= \sum_{\boldsymbol{r}\in\boldsymbol{R}} e^{-i\boldsymbol{r}\cdot\boldsymbol{k}_\circ} \int_{Y_0^*} e^{i\boldsymbol{r}\cdot\boldsymbol{k}}\phi(\boldsymbol{k})d\boldsymbol{k} \qquad \text{(A.2)} \\
&= \sum_{\boldsymbol{r}\in\boldsymbol{R}} e^{-i\boldsymbol{r}\cdot\boldsymbol{k}_\circ}\,|Y_0^*|\,\Phi(-\boldsymbol{r}) \;=\; |Y_0^*|\sum_{\boldsymbol{r}\in\boldsymbol{R}} e^{i\boldsymbol{r}\cdot\boldsymbol{k}_\circ}\,\Phi(\boldsymbol{r}) \\
&= |Y_0^*|\,\phi(\boldsymbol{k}_\circ) \;=\; |\mathcal{B}|\,\phi(\boldsymbol{k}_\circ+\boldsymbol{c}^*), \quad \boldsymbol{c}^*\in\boldsymbol{R}^*. \qquad \text{(A.3)}
\end{aligned}$$

Next, recall the PWE of $f\in L_2(S)$ given by (2.17). For given $\boldsymbol{k}_\circ \in \boldsymbol{k}_s+\mathcal{B}$, we first define a unique translation vector $\boldsymbol{c}^*(\boldsymbol{k}_\circ)\in\boldsymbol{R}^*$ such that

$$\boldsymbol{k}_\circ \in \boldsymbol{k}_s+\mathcal{B} \quad\to\quad \boldsymbol{k}_\circ+\boldsymbol{c}^*(\boldsymbol{k}_\circ)\in Y_0^*.$$

With reference to definition (2.15) of the Bloch transform and (2.17), one accordingly has

$$\begin{aligned}
\tilde{f}_{\boldsymbol{k}_\circ}(\boldsymbol{x}) &= \sum_{\boldsymbol{r}\in\boldsymbol{R}} f(\boldsymbol{x}+\boldsymbol{r})\; e^{-i\boldsymbol{k}_\circ\cdot(\boldsymbol{x}+\boldsymbol{r})} \;=\; \sum_{\boldsymbol{r}\in\boldsymbol{R}} \int_{\mathbb{R}^d} \mathfrak{F}(\boldsymbol{k}) e^{i(\boldsymbol{k}-\boldsymbol{k}_\circ)\cdot(\boldsymbol{x}+\boldsymbol{r})}\,\mathrm{d}\boldsymbol{k} \\
&= \int_{\mathbb{R}^d} \mathfrak{F}(\boldsymbol{k}) e^{i(\boldsymbol{k}-\boldsymbol{k}_\circ)\cdot\boldsymbol{x}} \Big(\sum_{\boldsymbol{r}\in\boldsymbol{R}} e^{i(\boldsymbol{k}-\boldsymbol{k}_\circ)\cdot\boldsymbol{r}}\Big)\,\mathrm{d}\boldsymbol{k} \;=\; \int_{\mathbb{R}^d} \mathfrak{F}(\boldsymbol{k}) e^{i(\boldsymbol{k}-\boldsymbol{k}_\circ)\cdot\boldsymbol{x}}\;\psi(\boldsymbol{k}-\boldsymbol{k}_\circ)\,\mathrm{d}\boldsymbol{k} \\
&= \sum_{\boldsymbol{r}^*\in\boldsymbol{R}^*} \int_{\boldsymbol{r}^*+Y_0^*} \mathfrak{F}(\boldsymbol{k}) e^{i(\boldsymbol{k}-\boldsymbol{k}_\circ)\cdot\boldsymbol{x}}\;\psi(\boldsymbol{k}-\boldsymbol{k}_\circ)\,\mathrm{d}\boldsymbol{k}. \\
&= \sum_{\boldsymbol{r}^*\in\boldsymbol{R}^*} \int_{Y_0^*} \mathfrak{F}(\boldsymbol{r}^*+\boldsymbol{k}) e^{i(\boldsymbol{r}^*+\boldsymbol{k}-\boldsymbol{k}_\circ)\cdot\boldsymbol{x}}\;\psi(\boldsymbol{k}-\boldsymbol{k}_\circ)\,\mathrm{d}\boldsymbol{k} \qquad \text{(A.4)} \\
&= |\mathcal{B}| \sum_{\boldsymbol{r}^*\in\boldsymbol{R}^*} \mathfrak{F}(\boldsymbol{r}^*+\boldsymbol{k}_\circ+\boldsymbol{c}^*(\boldsymbol{k}_\circ)) e^{i(\boldsymbol{r}^*+\boldsymbol{c}^*(\boldsymbol{k}_\circ))\cdot\boldsymbol{x}} \;=\; |\mathcal{B}| \sum_{\boldsymbol{r}^*\in\boldsymbol{R}^*} \mathfrak{F}(\boldsymbol{r}^*+\boldsymbol{k}_\circ) e^{i\boldsymbol{r}^*\cdot\boldsymbol{x}} \qquad \text{(A.5)}
\end{aligned}$$

Note that (A.5) is obtained from (A.4) by (i) setting, for any given $\boldsymbol{r}^*$, $\phi(\boldsymbol{k}) := \mathfrak{F}(\boldsymbol{r}^*+\boldsymbol{k})e^{i(\boldsymbol{r}^*+\boldsymbol{k}-\boldsymbol{k}_\circ)\cdot\boldsymbol{x}}$ over Y_0^*; (ii) extending the support of such defined $\phi(\boldsymbol{k})$ to $\mathbb{R}^d$ by the application of Y_0^*-periodicity, and (iii) applying (A.3) with $\boldsymbol{c}^* = \boldsymbol{c}^*(\boldsymbol{k}_\circ)$ to *each term* in the sum. This establishes claim (2.18). Assuming further that $\mathfrak{F}(\boldsymbol{k})$ is compactly supported inside $\boldsymbol{k}_s+\mathcal{B}$, we obtain (2.19) thanks to the fact that $\mathfrak{F}(\boldsymbol{r}^*+\boldsymbol{k}) = 0$ for all $\boldsymbol{r}^*\neq\boldsymbol{0}$.

A.3 Cell functions

Simple eigenvalue, cell functions $\boldsymbol{\chi}^{(2)}$ and $\eta^{(0)}$: The cell functions $\boldsymbol{\chi}^{(2)} \in \left(\bar{H}^1_{p0}(Y)\right)^{d\times d}$ and $\eta^{(0)} \in \bar{H}^1_{p0}(Y)$ uniquely solve the respective unit cell problems

$$\tilde{\lambda}_n \rho \boldsymbol{\chi}^{(2)} + \nabla_{\boldsymbol{k}_s}\cdot\big(G(\nabla_{\boldsymbol{k}_s}\boldsymbol{\chi}^{(2)} + \{\boldsymbol{I}\otimes\boldsymbol{\chi}^{(1)}\}')\big) + G(\nabla_{\boldsymbol{k}_s}\boldsymbol{\chi}^{(1)} + \tilde{\phi}_n \boldsymbol{I}) \;=\; \frac{\rho}{\rho^{(0)}}\{\boldsymbol{\theta}^{(0)}\otimes\boldsymbol{\chi}^{(1)}\} + \frac{\rho}{\rho^{(0)}}\tilde{\phi}_n\boldsymbol{\mu}^{(0)}, \tag{A.6}$$

$$-\tilde{\lambda}_n\rho\eta^{(0)} - \nabla_{\boldsymbol{k}_s}\cdot\big(G\nabla_{\boldsymbol{k}_s}\eta^{(0)}\big) \;=\; \tilde{f}_{\boldsymbol{k}} - \frac{\rho}{\rho^{(0)}}\langle\tilde{f}_{\boldsymbol{k}}\rangle\tilde{\phi}_n, \tag{A.7}$$

with $G(\nabla_{\boldsymbol{k}_s}\boldsymbol{\chi}^{(2)} + \{\boldsymbol{I}\otimes\boldsymbol{\chi}^{(1)}\}')$ and $G\nabla_{\boldsymbol{k}_s}\eta^{(0)}$ each satisfying the flux boundary conditions (2.38).

Simple eigenvalue, cell functions $\boldsymbol{\chi}^{(3)}$ and $\eta^{(1)}$: The cell functions $\boldsymbol{\chi}^{(3)} \in \left(\bar{H}^1_{p0}(Y)\right)^{d\times d\times d}$, $\boldsymbol{\eta}^{(1)} \in \left(\bar{H}^1_{p0}(Y)\right)^{d}$ and $\eta^{(2)} \in \bar{H}^1_{p0}(Y)$ uniquely solve the respective unit cell problems

$$\begin{aligned}\tilde{\lambda}_n\rho\boldsymbol{\chi}^{(3)} + \nabla_{\boldsymbol{k}_s}\cdot\big(G(\nabla_{\boldsymbol{k}_s}\boldsymbol{\chi}^{(3)} + \{\boldsymbol{I}\otimes\boldsymbol{\chi}^{(2)}\}')\big) + G\{\nabla_{\boldsymbol{k}_s}\boldsymbol{\chi}^{(2)} + \boldsymbol{I}\otimes\boldsymbol{\chi}^{(1)}\} \\ = \tfrac{\rho}{\rho^{(0)}}\big\{\boldsymbol{\theta}^{(0)}\otimes\boldsymbol{\chi}^{(2)}\big\} + \tfrac{\rho}{\rho^{(0)}}\big\{\boldsymbol{\mu}^{(0)}\otimes\boldsymbol{\chi}^{(1)}\big\} + \tfrac{\rho}{\rho^{(0)}}\tilde{\phi}_n\boldsymbol{\theta}^{(1)},\end{aligned} \tag{A.8}$$

$$\tilde{\lambda}_n\rho\boldsymbol{\eta}^{(1)} + \nabla_{\boldsymbol{k}_s}\cdot\big(G(\nabla_{\boldsymbol{k}_s}\boldsymbol{\eta}^{(1)} + \eta^{(0)}\boldsymbol{I})\big) + G\nabla_{\boldsymbol{k}_s}\eta^{(0)} + \tfrac{\rho}{\rho^{(0)}}\tilde{\phi}_n(\tilde{f}_{\boldsymbol{k}}, \boldsymbol{\chi}^{(1)}) \;=\; \tfrac{\rho}{\rho^{(0)}}\langle\tilde{f}_{\boldsymbol{k}}\rangle\boldsymbol{\chi}^{(1)}, \tag{A.9}$$

$$-\tilde{\lambda}_n\rho\eta^{(2)} - \nabla_{\boldsymbol{k}_s}\cdot(G\nabla_{\boldsymbol{k}_s}\eta^{(2)}) \;=\; \rho\eta^{(0)}, \tag{A.10}$$

with $G(\nabla_{\boldsymbol{k}_s}\boldsymbol{\chi}^{(3)} + \tilde{\phi}_n\ \{\boldsymbol{I}\otimes\boldsymbol{\chi}^{(2)}\}')$, $G(\nabla_{\boldsymbol{k}_s}\boldsymbol{\eta}^{(1)} + \eta^{(0)}\boldsymbol{I})$ and $G\nabla_{\boldsymbol{k}_s}\eta^{(2)}$ each satisfying the flux boundary conditions (2.38). For future reference, we note that $\eta^{(0)}$, $\boldsymbol{\eta}^{(1)}$ and $\eta^{(2)}$ are all $\tilde{f}_{\boldsymbol{k}}$-dependent.

Remark 30 *With reference to Remark 6, we find assuming $\tilde{f}_{\boldsymbol{k}}(\boldsymbol{x}) = F(\epsilon\hat{\boldsymbol{k}})\phi(\boldsymbol{x})$ that the respective solutions of* (A.9) *and* (A.10) *can be computed as $\boldsymbol{\eta}^{(1)}(\boldsymbol{x}) = F(\epsilon\hat{\boldsymbol{k}})\boldsymbol{\zeta}^{(1)}(\boldsymbol{x})$ and $\eta^{(2)}(\boldsymbol{x}) = F(\epsilon\hat{\boldsymbol{k}})\zeta^{(2)}(\boldsymbol{x})$, where $\boldsymbol{\zeta}^{(1)} \in \left(\bar{H}^1_{p0}(Y)\right)^{d}$ and $\zeta^{(2)} \in \bar{H}^1_{p0}(Y)$ uniquely solve*

$$\tilde{\lambda}_n\rho\boldsymbol{\zeta}^{(1)} + \nabla_{\boldsymbol{k}_s}\cdot\big(G(\nabla_{\boldsymbol{k}_s}\boldsymbol{\zeta}^{(1)} + \zeta^{(0)}\boldsymbol{I})\big) + G\nabla_{\boldsymbol{k}_s}\zeta^{(0)} + \tfrac{\rho}{\rho^{(0)}}\tilde{\phi}_n(\phi, \boldsymbol{\chi}^{(1)}) \;=\; \tfrac{\rho}{\rho^{(0)}}\langle\phi\rangle\boldsymbol{\chi}^{(1)}, \tag{A.11}$$

$$-\tilde{\lambda}_n\rho\zeta^{(2)} - \nabla_{\boldsymbol{k}_s}\cdot(G\nabla_{\boldsymbol{k}_s}\zeta^{(2)}) \;=\; \rho\zeta^{(0)}, \tag{A.12}$$

with $G(\nabla_{\boldsymbol{k}_s}\boldsymbol{\zeta}^{(1)} + \zeta^{(0)}\boldsymbol{I})$ and $G\nabla_{\boldsymbol{k}_s}\zeta^{(2)}$ each being subject to the flux boundary conditions (2.38).

Repeated eigenvalue, cell functions $\boldsymbol{\chi}_q^{(2)}$ and $\eta^{(0)}$: The cell functions $\boldsymbol{\chi}_q^{(2)} \in \big(\bar{H}^1_{p0}(Y)\big)^{d\times d}$ and $\eta^{(0)} \in \bar{H}^1_{p0}(Y)$ solve uniquely the respective equations

$$\begin{aligned}\tilde{\lambda}_n \rho \boldsymbol{\chi}_q^{(2)} + \nabla_{\boldsymbol{k}_s}\cdot\big(G(\nabla_{\boldsymbol{k}_s}\boldsymbol{\chi}_q^{(2)} + \tilde{\phi}_{n_q}\{\boldsymbol{I}\otimes\boldsymbol{\chi}_q^{(1)}\}')\big) + \{G(\nabla_{\boldsymbol{k}_s}\boldsymbol{\chi}_q^{(1)} + \tilde{\phi}_{n_q}\boldsymbol{I})\} \\ = \textstyle\sum_s \Big(\frac{\rho}{\rho_s^{(0)}}\{\boldsymbol{\theta}_{sq}^{(0)}\otimes\boldsymbol{\chi}_s^{(1)}\} + \frac{\rho}{\rho_s^{(0)}}\tilde{\phi}_{n_s}\boldsymbol{\mu}_{sq}^{(0)}\Big),\end{aligned} \tag{A.13}$$

$$-\tilde{\lambda}_n\rho\eta^{(0)} - \nabla_{\boldsymbol{k}_s}\cdot\big(G\nabla_{\boldsymbol{k}_s}\eta^{(0)}\big) \;=\; \tilde{f}_{\boldsymbol{k}} - \sum_s \frac{\rho}{\rho_s^{(0)}}\langle\tilde{f}_{\boldsymbol{k}}\rangle^{n_s}\tilde{\phi}_{n_s}. \tag{A.14}$$

with $G(\nabla_{\boldsymbol{k}_s}\boldsymbol{\chi}_q^{(2)}+\{\boldsymbol{I}\otimes\boldsymbol{\chi}_q^{(1)}\}')$ and $G\nabla_{\boldsymbol{k}_s}\eta^{(0)}$ satisfying the flux boundary conditions (2.38). See also Remark 31.

Remark 31 *When $\tilde{f}_{\boldsymbol{k}}(\boldsymbol{x}) = F(\epsilon\hat{\boldsymbol{k}})\phi(\boldsymbol{x})$, the solution of* (A.14) *is given by $\eta^{(0)}(\boldsymbol{x}) = F(\epsilon\hat{\boldsymbol{k}})\zeta^{(0)}(\boldsymbol{x})$, where $\zeta^{(0)}\in\bar{H}^1_{p0}(Y)$ uniquely solves*

$$-\tilde{\lambda}_n\rho\zeta^{(0)} - \nabla_{\boldsymbol{k}_s}\cdot\big(G\nabla_{\boldsymbol{k}_s}\zeta^{(0)}\big) \;=\; \phi - \sum_s \frac{\rho}{\rho_s^{(0)}}\langle\phi\rangle^{n_s}\tilde{\phi}_{n_s}, \tag{A.15}$$

subject to the flux boundary conditions (2.38) *in terms of $G\nabla_{\boldsymbol{k}_s}\zeta^{(0)}$.*

A.4 Effective coefficients

Proof of Claim 2. We integrate $\{\overline{((2.53)\otimes\overline{\boldsymbol{\chi}^{(1)}},1)}\}$ using the divergence theorem and the flux boundary conditions (2.38) written in terms of $G(\nabla_{\boldsymbol{k}_s}\boldsymbol{\chi}^{(1)}+\tilde{\phi}_n\boldsymbol{I})$ to obtain

$$\boldsymbol{\mu}^{(0)} = \langle G\tilde{\phi}_n\boldsymbol{I}\rangle + \lambda_n\{(\rho\boldsymbol{\chi}^{(1)}\otimes\overline{\boldsymbol{\chi}^{(1)}},1)\} - \{(G(\overline{\nabla_{\boldsymbol{k}_s}\boldsymbol{\chi}^{(1)}})\cdot(\nabla_{\boldsymbol{k}_s}\boldsymbol{\chi}^{(1)}),1)\} \;\in\mathbb{R}^{d\times d}. \tag{A.16}$$

Remark 32 *The "dot" operator in* (A.16) *and thereafter assumes inner tensor contraction with respect to the first index.*

Proof of Claim 5. We evaluate integrals $\{((\text{A.6})\otimes\overline{\boldsymbol{\chi}^{(1)}},1)\}$ and $\{\overline{((2.53)\otimes\overline{\boldsymbol{\chi}^{(2)}},1)}\}$ by applying the divergence theorem and exploiting the boundary conditions (2.38) satisfied by $G(\nabla_{\boldsymbol{k}_s}\boldsymbol{\chi}^{(1)}+\tilde{\phi}_n\boldsymbol{I})$ and $G(\nabla_{\boldsymbol{k}_s}\boldsymbol{\chi}^{(2)}+\{\boldsymbol{I}\otimes\boldsymbol{\chi}^{(1)}\}')$. In this way, we find that

$$\begin{aligned}\boldsymbol{\theta}^{(1)} \;=\; &\{(G\boldsymbol{\chi}^{(1)}\otimes\overline{\nabla_{\boldsymbol{k}_s}\boldsymbol{\chi}^{(1)}},1)\} - \{(G\overline{\boldsymbol{\chi}^{(1)}}\otimes\nabla_{\boldsymbol{k}_s}\boldsymbol{\chi}^{(1)},1)\} + \{(G\boldsymbol{I}\otimes\boldsymbol{\chi}^{(1)},\tilde{\phi}_n)\} \\ &-\overline{\{(G\boldsymbol{I}\otimes\boldsymbol{\chi}^{(1)},\tilde{\phi}_n)\}} + \{\boldsymbol{\theta}^{(0)}\otimes\frac{1}{\rho^{(0)}}\{(\rho\boldsymbol{\chi}^{(1)}\otimes\overline{\boldsymbol{\chi}^{(1)}},1)\}\} \;\in i\mathbb{R}^{d\times d\times d}.\end{aligned} \tag{A.17}$$

Proof of Claim 6. We evaluate integrals $\{((\text{A.8})\otimes\overline{\boldsymbol{\chi}^{(1)}},1)\}$, $\{\overline{((2.53)\otimes\overline{\boldsymbol{\chi}^{(3)}},1)}\}$ and $\{((\text{A.6})\otimes\overline{\boldsymbol{\chi}^{(2)}},1)\}$ by applying the divergence theorem and exploiting the boundary conditions (2.38) satisfied by $G(\nabla_{\boldsymbol{k}_s}\boldsymbol{\chi}^{(1)}+\tilde{\phi}_n\boldsymbol{I})$, $G(\nabla_{\boldsymbol{k}_s}\boldsymbol{\chi}^{(2)}+\{\boldsymbol{I}\otimes\boldsymbol{\chi}^{(1)}\}')$ and $G(\nabla_{\boldsymbol{k}_s}\boldsymbol{\chi}^{(3)}+\{\boldsymbol{I}\otimes\boldsymbol{\chi}^{(2)}\}')$. We then obtain

$$\begin{aligned}\boldsymbol{\mu}^{(2)} \;=\; &-\lambda_n\{(\rho\boldsymbol{\chi}^{(2)}\otimes\overline{\boldsymbol{\chi}^{(2)}},1)\}+\{(G(\overline{\nabla_{\boldsymbol{k}_s}\boldsymbol{\chi}^{(2)}})\cdot(\nabla_{\boldsymbol{k}_s}\boldsymbol{\chi}^{(2)}),1)\}-\{(G\boldsymbol{I}\otimes\boldsymbol{\chi}^{(1)}\otimes\overline{\boldsymbol{\chi}^{(1)}},1)\}\\ &+\{\boldsymbol{\mu}^{(0)}\otimes\frac{1}{\rho^{(0)}}\{(\rho\boldsymbol{\chi}^{(1)}\otimes\overline{\boldsymbol{\chi}^{(1)}},1)\}\}\;\in\mathbb{R}^{d\times d\times d\times d}.\end{aligned}\tag{A.18}$$

Proof of Claim 9. We integrate $\{((2.85)\otimes\overline{\boldsymbol{\chi}_p^{(1)}},1)\}$ by applying the divergence theorem and making use of the boundary conditions (2.38) satisfied by $G(\nabla_{\boldsymbol{k}_s}\boldsymbol{\chi}_q^{(1)}+\tilde{\phi}_{n_p}\boldsymbol{I})$ to obtain

$$\boldsymbol{\mu}_{qp}^{(0)} \;=\; \langle G\tilde{\phi}_{n_p}\boldsymbol{I}\rangle^{n_q}+\lambda_n\{(\rho\overline{\boldsymbol{\chi}_q^{(1)}}\otimes\boldsymbol{\chi}_p^{(1)},1)\}-\{(G(\nabla_{\boldsymbol{k}_s}\boldsymbol{\chi}_p^{(1)})\cdot(\overline{\nabla_{\boldsymbol{k}_s}\boldsymbol{\chi}_q^{(1)}}),1)\}.$$

As a result, for $p\in\overline{1,Q}$ we have

$$\begin{aligned}\boldsymbol{\mu}_{qp}^{(0)}:(i\hat{\boldsymbol{k}})^2 \;&=\; \Big(\langle G\tilde{\phi}_{n_p}\boldsymbol{I}\rangle^{n_q}+\lambda_n\{(\rho\overline{\boldsymbol{\chi}_q^{(1)}}\otimes\boldsymbol{\chi}_p^{(1)},1)\}\Big):(i\hat{\boldsymbol{k}})^2\\ &\quad-\Big(\{(G(\nabla_{\boldsymbol{k}_s}\boldsymbol{\chi}_p^{(1)})\cdot(\overline{\nabla_{\boldsymbol{k}_s}\boldsymbol{\chi}_q^{(1)}}),1)\}\Big):(i\hat{\boldsymbol{k}})^2\\ &=\; \overline{\boldsymbol{\mu}_{pq}^{(0)}:(i\hat{\boldsymbol{k}})^2},\end{aligned}$$

which demonstrates that the matrix $\boldsymbol{B}^{(0)}$ is Hermitian.

Proof of Claim 10. By construction, family $\tilde{\psi}_q$, $q\in\overline{N_0,N}$ is ρ-orthogonal. Thus for $p,q\in\overline{N_0,N}$ we have

$$(\rho\tilde{\psi}_p',\tilde{\psi}_q') \;=\; (\rho\tilde{\psi}_p,\tilde{\psi}_q) \;=\; \delta_{pq}(\rho\tilde{\psi}_p,\tilde{\psi}_p).$$

For $p,q\in\overline{1,N_0}$, we have

$$\begin{aligned}(\rho\tilde{\psi}_p',\tilde{\psi}_q') \;&=\; \sum_{s=1}^{N_0}\sum_{r=1}^{N_0}\bar{P}_{sp}\overline{\bar{P}_{rq}}(\rho\tilde{\psi}_s,\tilde{\psi}_r) \;=\; \sum_{s=1}^{N_0}\bar{P}_{sp}\overline{\bar{P}_{sq}}(\rho\tilde{\psi}_s,\tilde{\psi}_s) \;=\; \sum_{s=1}^{N_0}\bar{P}_{sp}\overline{\bar{P}_{sq}}\rho_s^{(0)}\\ &=\; \sum_{s=1}^{N_0}\overline{\bar{P}_{sq}}D_{ss}\bar{P}_{sp} \;=\; \delta_{pq}\Big(\sum_{s=1}^{N_0}\overline{\bar{P}_{sp}}D_{ss}\bar{P}_{sp}\Big).\end{aligned}$$

Further, for $p \in \overline{1, N_0}$ and $q \in \overline{N_0, N}$, we have

$$(\rho\tilde{\psi}'_p, \tilde{\psi}'_q) \;=\; \sum_{s=1}^{N_0} \bar{P}_{sp}(\rho\tilde{\psi}_s, \tilde{\psi}_q) \;=\; 0,$$

whereby family $\tilde{\psi}'_p$ is ρ-orthogonal as well.

A.4.1 Cell functions identities

Proof of Claim 4. Identity (2.62) is obtained by evaluating integrals $\overline{((2.53)\overline{\eta^{(0)}}, 1)}$ and $((\mathrm{A}.7)\overline{\boldsymbol{\chi}^{(1)}}, 1)$ via the divergence theorem and use of the boundary conditions (2.38) satisfied by $G\nabla_{\boldsymbol{k}_s}\eta^{(0)}$ and $G(\nabla_{\boldsymbol{k}_s}\boldsymbol{\chi}^{(1)} + \tilde{\phi}_n\boldsymbol{I})$.

Proof of Claim 7(1). Identity (2.69) is obtained by evaluating integrals $\overline{((2.53)\overline{\eta^{(2)}}, 1)}$ and $((\mathrm{A}.10)\overline{\boldsymbol{\chi}^{(1)}}, 1)$ via the divergence theorem and use of the boundary conditions (2.38) satisfied by $G\nabla_{\boldsymbol{k}_s}\eta^{(2)}$ and $G(\nabla_{\boldsymbol{k}_s}\boldsymbol{\chi}^{(1)} + \tilde{\phi}_n\boldsymbol{I})$.

Proof of Claim 7(2). Identity (2.70) is obtained by evaluating integrals $\overline{((2.53)\overline{\boldsymbol{\eta}^{(1)}}, 1)}$, $((\mathrm{A}.9)\overline{\boldsymbol{\chi}^{(1)}}, 1)$ and $\overline{((\mathrm{A}.6)\overline{\eta^{(0)}}, 1)}$ via the divergence theorem and use of the boundary conditions (2.38) satisfied by $G\nabla_{\boldsymbol{k}_s}\eta^{(0)}$, $G(\nabla_{\boldsymbol{k}_s}\boldsymbol{\eta}^{(1)} + \eta^{(0)}\boldsymbol{I})$ and $G(\nabla_{\boldsymbol{k}_s}\boldsymbol{\chi}^{(1)} + \tilde{\phi}_n\boldsymbol{I})$.

A.4.2 Cell functions and effective coefficients at special wavenumbers

Proof of Claim 3. At a wavenumber-eigenfrequency pair $(\boldsymbol{k}_s, \omega_n)$, $n \in \mathbb{Z}^+$, where $\boldsymbol{k}_s = \frac{1}{2}(\sum_j n_j \boldsymbol{e}^j)$, $n_j \in \{-1, 0, 1\}$, and ω_n is simple, the Bloch function $\phi_n(\boldsymbol{x}) = \tilde{\phi}_n(\boldsymbol{x})e^{i\boldsymbol{k}_s\cdot\boldsymbol{x}}$ with $\tilde{\phi}_n \in H^1_{p0}(Y)$ uniquely solves the field equation

$$-\tilde{\lambda}_n\rho(\boldsymbol{x})\phi_n - \nabla\cdot\big(G(\boldsymbol{x})\nabla\phi_n\big) \;=\; 0 \quad \text{in} \;\; Y, \tag{A.19}$$

subject to the boundary conditions

$$\begin{aligned}
\phi_n|_{\partial Y'_{j0}} &= e^{-i\boldsymbol{k}_s\cdot\boldsymbol{e}_j}\phi_n|_{\partial Y'_{j1}}, \\
\boldsymbol{\nu}\cdot G\nabla\phi_n|_{\partial Y'_{j0}} &= -e^{-i\boldsymbol{k}_s\cdot\boldsymbol{e}_j}\boldsymbol{\nu}\cdot G\nabla\phi_n|_{\partial Y'_{j1}}, \\
\boldsymbol{\nu}\cdot G\nabla\phi_n|_{\partial Y^{(\mathrm{N})}} &= 0, \\
\phi_n|_{\partial Y^{(\mathrm{D})}} &= 0,
\end{aligned} \tag{A.20}$$

where $e^{-i\boldsymbol{k}_s\cdot\boldsymbol{e}_j} = (-1)^{n_j}$, i.e. $e^{-i\boldsymbol{k}_s\cdot\boldsymbol{e}_j} \in \{-1, 1\}$. Hence, by the uniqueness of the solution, we find that the real and imaginary parts of $\phi_n(\boldsymbol{x})$ are proportional, which factorizes $\phi_n(\boldsymbol{x})$ into a (real-valued function) $\times\, e^{i\varphi_0}$, and we let $\varphi_0 = 0$ without affecting

the normalization (2.26). We then obtain

$$\begin{aligned}\boldsymbol{\theta}^{(0)} &= \langle G\nabla_{\boldsymbol{k}_s}\tilde{\phi}_n\rangle - \overline{\langle G\nabla_{\boldsymbol{k}_s}\tilde{\phi}_n\rangle} \\ &= 2i\ \mathrm{Im}(\langle G\nabla_{\boldsymbol{k}_s}\tilde{\phi}_n\rangle) = 2i\ \mathrm{Im}((G\nabla\phi_n,\phi_n)) = \mathbf{0}.\end{aligned}$$

Similarly, we define $\boldsymbol{X}^{(1)}(\boldsymbol{x}) = \boldsymbol{\chi}^{(1)}(\boldsymbol{x})e^{i\boldsymbol{k}_s\cdot\boldsymbol{x}}$ with $\boldsymbol{\chi}^{(1)} \in (\bar{H}^1_{p0}(Y))^d$ that uniquely solves the field equation

$$\tilde{\lambda}_n\rho\boldsymbol{X}^{(1)} + \nabla_{\boldsymbol{k}_s}\cdot\big(G(\nabla\boldsymbol{X}^{(1)} + \phi_n\boldsymbol{I})\big) + G\nabla\phi_n = \mathbf{0}, \tag{A.21}$$

subject to the boundary conditions

$$\begin{aligned}\boldsymbol{X}^{(1)}|_{\partial Y'_{j0}} &= e^{-i\boldsymbol{k}_s\cdot\boldsymbol{e}_j}\boldsymbol{X}^{(1)}|_{\partial Y'_{j1}}, \\ \boldsymbol{\nu}\cdot G(\nabla\boldsymbol{X}^{(1)} + \phi_n\boldsymbol{I})|_{\partial Y'_{j0}} &= -e^{-i\boldsymbol{k}_s\cdot\boldsymbol{e}_j}\boldsymbol{\nu}\cdot G(\nabla\boldsymbol{X}^{(1)} + \phi_n\boldsymbol{I})|_{\partial Y'_{j1}}, \\ \boldsymbol{\nu}\cdot G(\nabla\boldsymbol{X}^{(1)} + \phi_n\boldsymbol{I})|_{\partial Y^{(\mathrm{N})}} &= \mathbf{0}, \\ \boldsymbol{X}^{(1)}|_{\partial Y^{(\mathrm{D})}} &= \mathbf{0},\end{aligned}$$

from which we conclude that $\boldsymbol{X}^{(1)}(\boldsymbol{x})$ is real-valued up to a constant factor $e^{i\varphi_0}$.

Proof of Claim 8. On recalling Claim 3 and (A.17), we have

$$\begin{aligned}\boldsymbol{\theta}^{(1)} = {} & \{(G\boldsymbol{X}^{(1)}\otimes\overline{\nabla\boldsymbol{X}^{(1)}},1)\} - \{(G\overline{\boldsymbol{X}^{(1)}}\otimes\nabla\boldsymbol{X}^{(1)},1)\} \\ & + \{(G\boldsymbol{I}\otimes\boldsymbol{X}^{(1)},\phi_n)\} - \{\overline{(G\boldsymbol{I}\otimes\boldsymbol{X}^{(1)},\phi_n)}\} \\ & + \{\boldsymbol{\theta}^{(0)}\otimes\frac{1}{\rho^{(0)}}\{(\rho\boldsymbol{X}^{(1)}\otimes\overline{\boldsymbol{X}^{(1)}},1)\}\} = \mathbf{0}.\end{aligned} \tag{A.22}$$

We next define the Bloch functions $\boldsymbol{X}^{(2)}(\boldsymbol{x}) = \boldsymbol{\chi}^{(2)}(\boldsymbol{x})e^{i\boldsymbol{k}_s\cdot\boldsymbol{x}}$ and $\boldsymbol{X}^{(3)}(\boldsymbol{x}) = \boldsymbol{\chi}^{(3)}(\boldsymbol{x})e^{i\boldsymbol{k}_s\cdot\boldsymbol{x}}$, with $\boldsymbol{\chi}^{(2)} \in \big(\bar{H}^1_{p0}(Y)\big)^{d\times d}$ and $\boldsymbol{\chi}^{(3)} \in \big(\bar{H}^1_{p0}(Y)\big)^{d\times d\times d}$, that uniquely solve the respective boundary value problems

$$\tilde{\lambda}_n\rho\boldsymbol{X}^{(2)} + \nabla_{\boldsymbol{k}_s}\cdot\big(G(\nabla\boldsymbol{X}^{(2)} + \{\boldsymbol{I}\otimes\boldsymbol{X}^{(1)}\}')\big) + G(\nabla\boldsymbol{X}^{(1)} + \phi_n\boldsymbol{I}) = \tfrac{\rho}{\rho^{(0)}}\phi_n\boldsymbol{\mu}^{(0)}, \tag{A.23}$$

$$\begin{aligned}\boldsymbol{X}^{(2)}|_{\partial Y'_{j0}} &= e^{-i\boldsymbol{k}_s\cdot\boldsymbol{e}_j}\boldsymbol{X}^{(2)}|_{\partial Y'_{j1}}, \\ \boldsymbol{\nu}\cdot G(\nabla\boldsymbol{X}^{(2)} + \{\boldsymbol{I}\otimes\boldsymbol{X}^{(1)}\}')|_{\partial Y'_{j0}} &= -e^{-i\boldsymbol{k}_s\cdot\boldsymbol{e}_j}\boldsymbol{\nu}\cdot G(\nabla\boldsymbol{X}^{(2)} + \{\boldsymbol{I}\otimes\boldsymbol{X}^{(1)}\}')|_{\partial Y'_{j1}}, \\ \boldsymbol{\nu}\cdot G(\nabla\boldsymbol{X}^{(2)} + \{\boldsymbol{I}\otimes\boldsymbol{X}^{(1)}\}')|_{\partial Y^{(\mathrm{N})}} &= \mathbf{0}, \\ \boldsymbol{X}^{(2)}|_{\partial Y^{(\mathrm{D})}} &= \mathbf{0},\end{aligned}$$

where $\boldsymbol{\theta}^{(0)} = \mathbf{0}$ due to Claim 3, and

$$\begin{aligned} &\tilde{\lambda}_n \rho \boldsymbol{X}^{(3)} + \nabla\cdot\big(G(\nabla \boldsymbol{X}^{(3)} + \{\boldsymbol{I}\otimes \boldsymbol{X}^{(2)}\}')\big) \\ &+G\{\nabla \boldsymbol{X}^{(2)} + \boldsymbol{I}\otimes \boldsymbol{X}^{(1)}\} = \tfrac{\rho}{\rho^{(0)}}\big\{\boldsymbol{\mu}^{(0)}\otimes \boldsymbol{X}^{(1)}\big\}, \end{aligned} \tag{A.24}$$

$$\begin{aligned} \boldsymbol{X}^{(3)}|_{\partial Y'_{j0}} &= e^{-i\boldsymbol{k}_s\cdot\boldsymbol{e}_j}\boldsymbol{X}^{(3)}|_{\partial Y'_{j1}}, \\ \boldsymbol{\nu}\cdot G(\nabla \boldsymbol{X}^{(3)} + \{\boldsymbol{I}\otimes \boldsymbol{X}^{(2)}\}')|_{\partial Y'_{j0}} &= -e^{-i\boldsymbol{k}_s\cdot\boldsymbol{e}_j}\boldsymbol{\nu}\cdot G(\nabla \boldsymbol{X}^{(3)} + \{\boldsymbol{I}\otimes \boldsymbol{X}^{(2)}\}')|_{\partial Y'_{j1}} \\ \boldsymbol{\nu}\cdot G(\nabla \boldsymbol{X}^{(3)} + \{\boldsymbol{I}\otimes \boldsymbol{X}^{(2)}\}')|_{\partial Y^{(\mathrm{N})}} &= \mathbf{0}, \\ \boldsymbol{X}^{(3)}|_{\partial Y^{(\mathrm{D})}} &= \mathbf{0}, \end{aligned}$$

where $\boldsymbol{\theta}^{(0)} = \mathbf{0}$ due to Claim 3 and $\boldsymbol{\theta}^{(1)} = \mathbf{0}$ by (A.22). Recalling the properties of $\phi_n(\boldsymbol{x})$ and $\boldsymbol{X}^{(1)}(\boldsymbol{x})$, we then conclude that $\boldsymbol{X}^{(2)}(\boldsymbol{x})$ and $\boldsymbol{X}^{(3)}(\boldsymbol{x})$ are each real-valued up to a constant factor $e^{i\varphi_0}$.

Proof of Claim 10. At wavenumber-eigenfrequency pair $(\boldsymbol{k}_s, \omega_n)$ where $\boldsymbol{k}_s = \frac{1}{2}(\sum_j n_j \boldsymbol{e}^j)$ $n_j \in \{-1, 0, 1\}$, and ω_n is of multiplicity $Q > 1$, Bloch functions $\phi_{n_p}(\boldsymbol{x}) = \tilde{\phi}_{n_p}(\boldsymbol{x})e^{i\boldsymbol{k}_s\cdot\boldsymbol{x}}$ $(p = \overline{1, Q})$ independently solve the boundary value problem (A.19)–(A.20). In a way that is similar to the simple eigenfrequency case, one finds that $\overline{\phi_{n_p}}$ are also solutions of (A.19)–(A.20), and so are $\mathrm{Re}(\phi_{n_p})$ and $\mathrm{Im}(\phi_{n_p})$. Thus, by proceeding with the Gram-Schmidt ρ-orthogonalization of the $2Q$ *real-valued* solutions, we can obtain Q real-valued solutions that are ρ-orthogonal and normalized in the sense of (2.26). On relabeling the new (real-valued) basis using original notation, we find

$$\begin{aligned} \boldsymbol{\theta}^{(0)}_{pq} &= \langle G\nabla_{\boldsymbol{k}_s}\tilde{\phi}_{n_q}\rangle^{n_p} - \overline{\langle G\nabla_{\boldsymbol{k}_s}\tilde{\phi}_{n_p}\rangle^{n_q}} \\ &= (G\nabla\phi_{n_q}, \phi_{n_p}) - \overline{(G\nabla\phi_{n_p}, \phi_{n_q})} \\ &= (G\nabla\phi_{n_q}, \phi_{n_p}) - (G\nabla\phi_{n_p}, \phi_{n_q}) \ \in \mathbb{R}^d, \end{aligned} \tag{A.25}$$

which vanishes identically for $p = q$. We also note that in such case $\boldsymbol{\theta}^{(0)}_{qp} = -\boldsymbol{\theta}^{(0)}_{pq}$, which makes $i\boldsymbol{A}^{(0)}$ skew-symmetric and $\boldsymbol{A}^{(0)}$ itself Hermitian.

To complete the proof of the claim, we note that $\boldsymbol{A}^{(0)}$ admits real eigenvalues thanks to its Hermitian nature. Let τ be a non-zero eigenvalue, and let $\boldsymbol{v}$ denote the affiliated eigenvector so that $\boldsymbol{A}^{(0)}\boldsymbol{v} = \tau\boldsymbol{v}$. By conjugating this relationship, we find that $\overline{\boldsymbol{A}^{(0)}}\overline{\boldsymbol{v}} = \tau\overline{\boldsymbol{v}}$, which yields $\boldsymbol{A}^{(0)}\overline{\boldsymbol{v}} = -\tau\overline{\boldsymbol{v}}$ thanks to the fact that $\overline{\boldsymbol{A}^{(0)}} = -\boldsymbol{A}^{(0)}$. Hence, $-\tau$ is also an eigenvalue of $\boldsymbol{A}^{(0)}$, and $\overline{\boldsymbol{v}}$ is the affiliated eigenvector.

Appendix B

Supporting results for Chapter 3

B.1 Bar and hinge model: compatibility vectors and stiffness coefficients

For bar $\hat{\mathbf{p}}^{(\mathrm{b})}$ (resp. hinge $\hat{\mathbf{p}}^{(\mathrm{h})}$) and node $\hat{\mathbf{q}}^{(\mathrm{n})}$, the compatibility vector $\boldsymbol{c}^{e}_{\hat{\mathbf{p}}^{(\mathrm{b})}\hat{\mathbf{q}}^{(\mathrm{n})}} \in \mathbb{R}^{\mathfrak{d}}$ (resp. $\boldsymbol{c}^{\varphi}_{\hat{\mathbf{p}}^{(\mathrm{h})}\hat{\mathbf{q}}^{(\mathrm{n})}} \in \mathbb{R}^{\mathfrak{d}}$) is non-trivial only if node $\hat{\mathbf{q}}^{(\mathrm{n})}$ belongs to bar $\hat{\mathbf{p}}^{(\mathrm{b})}$ (resp. hinge $\hat{\mathbf{p}}^{(\mathrm{h})}$). In what follows, we summarize the linear compatibility vectors of the bar and hinge elements that are used to define the compatibility vector families $\boldsymbol{c}^{e}_{\hat{\mathbf{p}}^{(\mathrm{b})}\hat{\mathbf{q}}^{(\mathrm{n})}}$ and $\boldsymbol{c}^{\varphi}_{\hat{\mathbf{p}}^{(\mathrm{h})}\hat{\mathbf{q}}^{(\mathrm{n})}}$ [65].

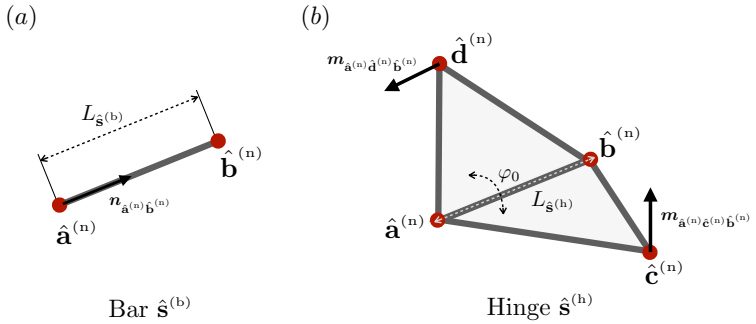

Figure B.1: Components of (a) bar element $\hat{\mathbf{s}}^{(\mathrm{b})}$, and (b) hinge element $\hat{\mathbf{s}}^{(\mathrm{h})}$ where φ_0 is the initial angle between the panels connected by the hinge.

Let $\hat{\mathbf{a}}^{(\mathrm{n})}$ and $\hat{\mathbf{b}}^{(\mathrm{n})}$ be the nodes that belong to bar $\hat{\mathbf{s}}^{(\mathrm{b})}$. With reference to Fig. B.1(a), the length and orientation of the bar are given respectively by

$$L_{\hat{\mathbf{s}}^{(\mathrm{b})}} = \|\boldsymbol{x}_{\hat{\mathbf{b}}^{(\mathrm{n})}} - \boldsymbol{x}_{\hat{\mathbf{a}}^{(\mathrm{n})}}\|, \quad \text{and} \quad \boldsymbol{n}_{\hat{\mathbf{a}}^{(\mathrm{n})}\hat{\mathbf{b}}^{(\mathrm{n})}} = \frac{1}{L^{(\mathrm{e})}}(\boldsymbol{x}_{\hat{\mathbf{b}}^{(\mathrm{n})}} - \boldsymbol{x}_{\hat{\mathbf{a}}^{(\mathrm{n})}}). \tag{B.1}$$

Its deformation reads

$$e_{\hat{\mathbf{s}}^{(\mathrm{b})}} = \boldsymbol{C}^{e}_{\hat{\mathbf{s}}^{(\mathrm{b})}} \cdot \boldsymbol{u}^{e}_{\hat{\mathbf{s}}^{(\mathrm{b})}}, \tag{B.2}$$

where $\boldsymbol{C}^{e}_{\hat{\mathbf{s}}^{(\mathrm{b})}}, \boldsymbol{u}^{e}_{\hat{\mathbf{s}}^{(\mathrm{b})}} \in \mathbb{R}^{2\mathfrak{d}}$ are given by

$$\boldsymbol{u}^{e}_{\hat{\mathbf{s}}^{(\mathrm{b})}} = [\boldsymbol{u}_{\hat{\mathbf{a}}^{(\mathrm{n})}}, \boldsymbol{u}_{\hat{\mathbf{b}}^{(\mathrm{n})}}], \qquad \boldsymbol{C}^{e}_{\hat{\mathbf{s}}^{(\mathrm{b})}} = \frac{1}{L^e}[-\boldsymbol{n}_{\hat{\mathbf{a}}^{(\mathrm{n})}\hat{\mathbf{b}}^{(\mathrm{n})}}, \boldsymbol{n}_{\hat{\mathbf{a}}^{(\mathrm{n})}\hat{\mathbf{b}}^{(\mathrm{n})}}], \tag{B.3}$$

and $\boldsymbol{u}_{\hat{\mathbf{a}}^{(\mathrm{n})}}$ (resp. $\boldsymbol{u}_{\hat{\mathbf{b}}^{(\mathrm{n})}}$) is the displacement of node $\hat{\mathbf{a}}^{(\mathrm{n})}$ (resp. $\hat{\mathbf{b}}^{(\mathrm{n})}$). The stiffness $k^{e}_{\hat{\mathbf{s}}^{(\mathrm{b})}}$ of a bar element $\hat{\mathbf{s}}^{(\mathrm{b})}$ derives from its cross-sectional area $A^{e}_{\hat{\mathbf{s}}^{(\mathrm{b})}}$ and Young modulus $E_{\hat{\mathbf{s}}^{(\mathrm{b})}}$ according to $k^{e}_{\hat{\mathbf{s}}^{(\mathrm{b})}} = E_{\hat{\mathbf{s}}^{(\mathrm{b})}} A_{\hat{\mathbf{s}}^{(\mathrm{b})}} L_{\hat{\mathbf{s}}^{(\mathrm{b})}}$.

Let $\hat{\mathbf{a}}^{(\mathrm{n})}, \hat{\mathbf{b}}^{(\mathrm{n})}, \hat{\mathbf{c}}^{(\mathrm{n})}$ and $\hat{\mathbf{d}}^{(\mathrm{n})}$ be the nodes that belong to a hinge element $\hat{\mathbf{s}}^{(\mathrm{h})}$. With reference to Fig. B.1(b), we define the vectors $\boldsymbol{m}_{\hat{\mathbf{p}}^{(\mathrm{n})}\hat{\mathbf{q}}^{(\mathrm{n})}}$ for $\hat{\mathbf{p}}^{(\mathrm{n})}, \hat{\mathbf{q}}^{(\mathrm{n})} \in \{\hat{\mathbf{a}}^{(\mathrm{n})}, \hat{\mathbf{b}}^{(\mathrm{n})}, \hat{\mathbf{c}}^{(\mathrm{n})}, \hat{\mathbf{d}}^{(\mathrm{n})}\}$ as

$$\boldsymbol{m}_{\hat{\mathbf{p}}^{(\mathrm{n})}\hat{\mathbf{q}}^{(\mathrm{n})}} = \boldsymbol{x}_{\hat{\mathbf{p}}^{(\mathrm{n})}} - \boldsymbol{x}_{\hat{\mathbf{q}}^{(\mathrm{n})}}, \tag{B.4}$$

and the "cross" vectors $\boldsymbol{m}_{\hat{\mathbf{a}}^{(\mathrm{n})}\hat{\mathbf{c}}^{(\mathrm{n})}\hat{\mathbf{b}}^{(\mathrm{n})}}$ and $\boldsymbol{m}_{\hat{\mathbf{a}}^{(\mathrm{n})}\hat{\mathbf{d}}^{(\mathrm{n})}\hat{\mathbf{b}}^{(\mathrm{n})}}$ as

$$\boldsymbol{m}_{\hat{\mathbf{a}}^{(\mathrm{n})}\hat{\mathbf{c}}^{(\mathrm{n})}\hat{\mathbf{b}}^{(\mathrm{n})}} = \boldsymbol{m}_{\hat{\mathbf{a}}^{(\mathrm{n})}\hat{\mathbf{c}}^{(\mathrm{n})}} \times \boldsymbol{m}_{\hat{\mathbf{a}}^{(\mathrm{n})}\hat{\mathbf{b}}^{(\mathrm{n})}}, \quad \boldsymbol{m}_{\hat{\mathbf{a}}^{(\mathrm{n})}\hat{\mathbf{d}}^{(\mathrm{n})}\hat{\mathbf{b}}^{(\mathrm{n})}} = \boldsymbol{m}_{\hat{\mathbf{a}}^{(\mathrm{n})}\hat{\mathbf{d}}^{(\mathrm{n})}} \times \boldsymbol{m}_{\hat{\mathbf{a}}^{(\mathrm{n})}\hat{\mathbf{b}}^{(\mathrm{n})}}, \tag{B.5}$$

where $\times$ denotes the cross (vector) product. The rotation $\varphi_{\hat{\mathbf{s}}^{(\mathrm{h})}}$ of the hinge element $\hat{\mathbf{s}}^{(\mathrm{h})}$ is given by

$$\varphi_{\hat{\mathbf{s}}^{(\mathrm{h})}} = \boldsymbol{C}^{\varphi}_{\hat{\mathbf{s}}^{(\mathrm{h})}} \cdot \boldsymbol{u}^{\varphi}_{\hat{\mathbf{s}}^{(\mathrm{h})}}, \tag{B.6}$$

where $\boldsymbol{C}^{\varphi}_{\hat{\mathbf{s}}^{(\mathrm{b})}}, \boldsymbol{u}^{\varphi}_{\hat{\mathbf{s}}^{(\mathrm{b})}} \in \mathbb{R}^{4\mathfrak{d}}$ are given by

$$\boldsymbol{u}^{\varphi}_{\hat{\mathbf{s}}^{(\mathrm{h})}} = [\boldsymbol{u}_{\hat{\mathbf{a}}^{(\mathrm{n})}}, \boldsymbol{u}_{\hat{\mathbf{b}}^{(\mathrm{n})}}, \boldsymbol{u}_{\hat{\mathbf{c}}^{(\mathrm{n})}}, \boldsymbol{u}_{\hat{\mathbf{d}}^{(\mathrm{n})}}], \qquad \boldsymbol{C}^{\varphi}_{\hat{\mathbf{s}}^{(\mathrm{h})}} = [\boldsymbol{C}^{\varphi}_{\hat{\mathbf{a}}^{(\mathrm{n})}}, \boldsymbol{C}^{\varphi}_{\hat{\mathbf{b}}^{(\mathrm{n})}}, \boldsymbol{C}^{\varphi}_{\hat{\mathbf{c}}^{(\mathrm{n})}}, \boldsymbol{C}^{\varphi}_{\hat{\mathbf{d}}^{(\mathrm{n})}}], \tag{B.7}$$

$$\begin{aligned}
\boldsymbol{C}^{\varphi}_{\hat{\mathbf{d}}^{(\mathrm{n})}} &= \frac{\|\boldsymbol{m}_{\hat{\mathbf{a}}^{(\mathrm{n})}\hat{\mathbf{b}}^{(\mathrm{n})}}\|}{\|\boldsymbol{m}_{\hat{\mathbf{a}}^{(\mathrm{n})}\hat{\mathbf{d}}^{(\mathrm{n})}\hat{\mathbf{b}}^{(\mathrm{n})}}\|^2} \boldsymbol{m}_{\hat{\mathbf{a}}^{(\mathrm{n})}\hat{\mathbf{d}}^{(\mathrm{n})}\hat{\mathbf{b}}^{(\mathrm{n})}}, \\
\boldsymbol{C}^{\varphi}_{\hat{\mathbf{c}}^{(\mathrm{n})}} &= -\frac{\|\boldsymbol{m}_{\hat{\mathbf{a}}^{(\mathrm{n})}\hat{\mathbf{b}}^{(\mathrm{n})}}\|}{\|\boldsymbol{m}_{\hat{\mathbf{a}}^{(\mathrm{n})}\hat{\mathbf{c}}^{(\mathrm{n})}\hat{\mathbf{b}}^{(\mathrm{n})}}\|^2} \boldsymbol{m}_{\hat{\mathbf{a}}^{(\mathrm{n})}\hat{\mathbf{c}}^{(\mathrm{n})}\hat{\mathbf{b}}^{(\mathrm{n})}}, \\
\boldsymbol{C}^{\varphi}_{\hat{\mathbf{a}}^{(\mathrm{n})}} &= \Big(\frac{\boldsymbol{m}_{\hat{\mathbf{d}}^{(\mathrm{n})}\hat{\mathbf{a}}^{(\mathrm{n})}} \cdot \boldsymbol{m}_{\hat{\mathbf{b}}^{(\mathrm{n})}\hat{\mathbf{a}}^{(\mathrm{n})}}}{\|\boldsymbol{m}_{\hat{\mathbf{b}}^{(\mathrm{n})}\hat{\mathbf{a}}^{(\mathrm{n})}}\|^2} - 1\Big)\boldsymbol{C}^{\varphi}_{\hat{\mathbf{d}}^{(\mathrm{n})}} - \Big(\frac{\boldsymbol{m}_{\hat{\mathbf{b}}^{(\mathrm{n})}\hat{\mathbf{c}}^{(\mathrm{n})}} \cdot \boldsymbol{m}_{\hat{\mathbf{b}}^{(\mathrm{n})}\hat{\mathbf{a}}^{(\mathrm{n})}}}{\|\boldsymbol{m}_{\hat{\mathbf{b}}^{(\mathrm{n})}\hat{\mathbf{a}}^{(\mathrm{n})}}\|^2}\Big)\boldsymbol{C}^{\varphi}_{\hat{\mathbf{c}}^{(\mathrm{n})}}, \\
\boldsymbol{C}^{\varphi}_{\hat{\mathbf{b}}^{(\mathrm{n})}} &= \Big(\frac{\boldsymbol{m}_{\hat{\mathbf{b}}^{(\mathrm{n})}\hat{\mathbf{c}}^{(\mathrm{n})}} \cdot \boldsymbol{m}_{\hat{\mathbf{b}}^{(\mathrm{n})}\hat{\mathbf{a}}^{(\mathrm{n})}}}{\|\boldsymbol{m}_{\hat{\mathbf{b}}^{(\mathrm{n})}\hat{\mathbf{a}}^{(\mathrm{n})}}\|^2} - 1\Big)\boldsymbol{C}^{\varphi}_{\hat{\mathbf{c}}^{(\mathrm{n})}} - \Big(\frac{\boldsymbol{m}_{\hat{\mathbf{d}}^{(\mathrm{n})}\hat{\mathbf{a}}^{(\mathrm{n})}} \cdot \boldsymbol{m}_{\hat{\mathbf{b}}^{(\mathrm{n})}\hat{\mathbf{a}}^{(\mathrm{n})}}}{\|\boldsymbol{m}_{\hat{\mathbf{b}}^{(\mathrm{n})}\hat{\mathbf{a}}^{(\mathrm{n})}}\|^2}\Big)\boldsymbol{C}^{\varphi}_{\hat{\mathbf{d}}^{(\mathrm{n})}}.
\end{aligned}$$

and $\boldsymbol{u}_{\hat{\mathbf{a}}^{(\mathrm{n})}}, \boldsymbol{u}_{\hat{\mathbf{b}}^{(\mathrm{n})}}, \boldsymbol{u}_{\hat{\mathbf{c}}^{(\mathrm{n})}}$ and $\boldsymbol{u}_{\hat{\mathbf{d}}^{(\mathrm{n})}}$ denote the respective displacements of nodes $\hat{\mathbf{a}}^{(\mathrm{n})}, \hat{\mathbf{b}}^{(\mathrm{n})}, \hat{\mathbf{c}}^{(\mathrm{n})}$ and $\hat{\mathbf{d}}^{(\mathrm{n})}$. The stiffness $k^{\varphi}_{\hat{\mathbf{s}}^{(\mathrm{h})}}$ of a folding (resp. bending) hinge element $\hat{\mathbf{s}}^{(\mathrm{h})}$ characterized by its length $L_{\hat{\mathbf{s}}^{(\mathrm{h})}} = \|\boldsymbol{m}_{\hat{\mathbf{a}}^{(\mathrm{n})}\hat{\mathbf{b}}^{(\mathrm{n})}}\|$ and specific linear stiffness k_{fs} (resp. k_{bs}) is given by $k^{\varphi}_{\hat{\mathbf{s}}^{(\mathrm{h})}} = k_{fs} L_{\hat{\mathbf{s}}^{(\mathrm{h})}}$ (resp. $k^{\varphi}_{\hat{\mathbf{s}}^{(\mathrm{h})}} = k_{bs} L_{\hat{\mathbf{s}}^{(\mathrm{h})}}$).

B.2 Periodicity of the stiffness matrix

By recalling the definition of $\hat{\mathbf{r}}^{(\mathrm{n})}$, $\hat{\mathbf{r}}^{(\mathrm{b})}$ and $\hat{\mathbf{r}}^{(\mathrm{h})}$ given by (A.3) for a lattice vector $\boldsymbol{r} \in \boldsymbol{R}$, we have for $\hat{\mathbf{p}}^{(\mathrm{b})}, \hat{\mathbf{p}}^{(\mathrm{h})}, \hat{\mathbf{q}}^{(\mathrm{n})} \in \mathbb{Z}^{\mathfrak{p}}$

$$
\begin{gathered}
k^{e}_{\hat{\mathbf{s}}^{(\mathrm{b})}+\hat{\mathbf{r}}^{(\mathrm{b})}} = k^{e}_{\hat{\mathbf{s}}^{(\mathrm{b})}}, \quad k^{\varphi}_{\hat{\mathbf{s}}^{(\mathrm{h})}+\hat{\mathbf{r}}^{(\mathrm{h})}} = k^{\varphi}_{\hat{\mathbf{s}}^{(\mathrm{h})}}, \\
\boldsymbol{c}^{e}_{(\hat{\mathbf{p}}^{(\mathrm{b})}+\hat{\mathbf{r}}^{(\mathrm{b})})(\hat{\mathbf{q}}^{(\mathrm{n})}+\hat{\mathbf{r}}^{(\mathrm{n})})} = \boldsymbol{c}^{e}_{\hat{\mathbf{p}}^{(\mathrm{b})}\hat{\mathbf{q}}^{(\mathrm{n})}}, \quad \text{and} \quad \boldsymbol{c}^{\varphi}_{(\hat{\mathbf{p}}^{(\mathrm{h})}+\hat{\mathbf{r}}^{(\mathrm{h})})(\hat{\mathbf{q}}^{(\mathrm{n})}+\hat{\mathbf{r}}^{(\mathrm{n})})} = \boldsymbol{c}^{\varphi}_{\hat{\mathbf{p}}^{(\mathrm{b})}\hat{\mathbf{q}}^{(\mathrm{n})}},
\end{gathered}
$$

thanks to the periodicity of $S'_{\boldsymbol{\alpha}}$. Recalling (3.13), for $\hat{\mathbf{p}}^{(\mathrm{n})}, \hat{\mathbf{q}}^{(\mathrm{n})} \in \mathbb{Z}^{\mathfrak{p}}$ and $\boldsymbol{r} \in \boldsymbol{R}$ we thus obtain

$$
\begin{aligned}
\boldsymbol{K}^{e}_{(\hat{\mathbf{p}}^{(\mathrm{n})}+\hat{\mathbf{r}}^{(\mathrm{n})})\hat{\mathbf{q}}^{(\mathrm{n})}} &= \sum_{\hat{\mathbf{s}}^{(\mathrm{b})}} k^{e}_{\hat{\mathbf{s}}^{(\mathrm{b})}} \; \boldsymbol{c}^{e}_{\hat{\mathbf{s}}^{(\mathrm{b})}(\hat{\mathbf{p}}^{(\mathrm{n})}+\hat{\mathbf{r}}^{(\mathrm{n})})} \otimes \boldsymbol{c}^{e}_{\hat{\mathbf{s}}^{(\mathrm{b})}\hat{\mathbf{q}}^{(\mathrm{n})}} \\
&= \sum_{\hat{\mathbf{s}}^{(\mathrm{b})}} k^{e}_{\hat{\mathbf{s}}^{(\mathrm{b})}-\hat{\mathbf{r}}^{(\mathrm{b})}} \; \boldsymbol{c}^{e}_{(\hat{\mathbf{s}}^{(\mathrm{b})}-\hat{\mathbf{r}}^{(\mathrm{b})})\hat{\mathbf{p}}^{(\mathrm{n})}} \otimes \boldsymbol{c}^{e}_{(\hat{\mathbf{s}}^{(\mathrm{b})}-\hat{\mathbf{r}}^{(\mathrm{b})})(\hat{\mathbf{q}}^{(\mathrm{n})}-\hat{\mathbf{r}}^{(\mathrm{n})})} \\
&= \sum_{\hat{\mathbf{s}}^{(\mathrm{b})}} k^{e}_{\hat{\mathbf{s}}^{(\mathrm{b})}} \; \boldsymbol{c}^{e}_{\hat{\mathbf{s}}^{(\mathrm{b})}\hat{\mathbf{p}}^{(\mathrm{n})}} \otimes \boldsymbol{c}^{e}_{\hat{\mathbf{s}}^{(\mathrm{b})}(\hat{\mathbf{q}}^{(\mathrm{n})}-\hat{\mathbf{r}}^{(\mathrm{n})})} \;=\; \boldsymbol{K}^{e}_{\hat{\mathbf{p}}^{(\mathrm{n})}(\hat{\mathbf{q}}^{(\mathrm{n})}-\hat{\mathbf{r}}^{(\mathrm{n})})}.
\end{aligned}
$$

By proving similarly that $\boldsymbol{K}^{\varphi}_{(\hat{\mathbf{p}}^{(\mathrm{n})}+\hat{\mathbf{r}}^{(\mathrm{n})})\hat{\mathbf{q}}^{(\mathrm{n})}} = \boldsymbol{K}^{\varphi}_{\hat{\mathbf{p}}^{(\mathrm{n})}(\hat{\mathbf{q}}^{(\mathrm{n})}-\hat{\mathbf{r}}^{(\mathrm{n})})}$, we find

$$
\begin{aligned}
\boldsymbol{K}_{(\hat{\mathbf{p}}^{(\mathrm{n})}+\hat{\mathbf{r}}^{(\mathrm{n})})\hat{\mathbf{q}}^{(\mathrm{n})}} &= \boldsymbol{K}^{e}_{(\hat{\mathbf{p}}^{(\mathrm{n})}+\hat{\mathbf{r}}^{(\mathrm{n})})\hat{\mathbf{q}}^{(\mathrm{n})}} + \boldsymbol{K}^{\varphi}_{(\hat{\mathbf{p}}^{(\mathrm{n})}+\hat{\mathbf{r}}^{(\mathrm{n})})\hat{\mathbf{q}}^{(\mathrm{n})}} \\
&= \boldsymbol{K}^{e}_{\hat{\mathbf{p}}^{(\mathrm{n})}(\hat{\mathbf{q}}^{(\mathrm{n})}-\hat{\mathbf{r}}^{(\mathrm{n})})} + \boldsymbol{K}^{\varphi}_{\hat{\mathbf{p}}^{(\mathrm{n})}(\hat{\mathbf{q}}^{(\mathrm{n})}-\hat{\mathbf{r}}^{(\mathrm{n})})} \;=\; \boldsymbol{K}_{\hat{\mathbf{p}}^{(\mathrm{n})}(\hat{\mathbf{q}}^{(\mathrm{n})}-\hat{\mathbf{r}}^{(\mathrm{n})})}. \qquad \text{(B.8)}
\end{aligned}
$$

B.3 Symmetry of the stiffness matrix

With reference to Remark 19, (3.14), (3.24) and (3.25), we have for $i, j \in \overline{1, N_{\mathrm{n}}}$

$$
\begin{aligned}
\tilde{\boldsymbol{K}}_{\mathbf{ij}} &= \sum_{\boldsymbol{r}\in\boldsymbol{R}} \check{\boldsymbol{K}}_{\mathbf{i}(\mathbf{j}+\hat{\mathbf{r}}^{(\mathrm{n})})} \\
&= \sum_{\boldsymbol{r}\in\boldsymbol{R}} e^{i\boldsymbol{k}\cdot(\boldsymbol{x}_{\mathbf{j}+\hat{\mathbf{r}}^{(\mathrm{n})}}-\boldsymbol{x}_{\mathbf{i}})}\boldsymbol{K}_{\mathbf{i}(\mathbf{j}+\hat{\mathbf{r}}^{(\mathrm{n})})} \\
&= \sum_{\boldsymbol{r}\in\boldsymbol{R}} e^{i\boldsymbol{k}\cdot\boldsymbol{r}}e^{i\boldsymbol{k}\cdot(\boldsymbol{x}_{\mathbf{j}}-\boldsymbol{x}_{\mathbf{i}})}\boldsymbol{K}_{(\mathbf{i}-\hat{\mathbf{r}}^{(\mathrm{n})})\mathbf{j}} \\
&= \sum_{\boldsymbol{r}\in\boldsymbol{R}} e^{-i\boldsymbol{k}\cdot\boldsymbol{r}}e^{i\boldsymbol{k}\cdot(\boldsymbol{x}_{\mathbf{j}}-\boldsymbol{x}_{\mathbf{i}})}\boldsymbol{K}_{(\mathbf{i}+\hat{\mathbf{r}}^{(\mathrm{n})})\mathbf{j}} \\
&= \sum_{\boldsymbol{r}\in\boldsymbol{R}} e^{-i\boldsymbol{k}\cdot\boldsymbol{r}}e^{-i\boldsymbol{k}\cdot(\boldsymbol{x}_{\mathbf{i}}-\boldsymbol{x}_{\mathbf{j}})}\boldsymbol{K}^{\mathrm{T}}_{\mathbf{j}(\mathbf{i}+\hat{\mathbf{r}}^{(\mathrm{n})})} \\
&= \sum_{\boldsymbol{r}\in\boldsymbol{R}} e^{-i\boldsymbol{k}\cdot(\boldsymbol{x}_{\mathbf{i}+\hat{\mathbf{r}}^{(\mathrm{n})}}-\boldsymbol{x}_{\mathbf{j}})}\boldsymbol{K}^{\mathrm{T}}_{\mathbf{j}(\mathbf{i}+\hat{\mathbf{r}}^{(\mathrm{n})})} \;=\; \tilde{\boldsymbol{K}}^{*}_{\mathbf{ji}}.
\end{aligned}
\tag{B.9}
$$

B.4 Expansion of the stiffness matrix

For $\boldsymbol{k}=\boldsymbol{k}_s+\epsilon\hat{\boldsymbol{k}}\in\mathcal{B}$ and $i,j\in\overline{1,N_{\mathrm{n}}}$, we have

$$
\begin{aligned}
\tilde{\boldsymbol{K}}_{\mathbf{ij}} &= \sum_{\boldsymbol{r}\in\boldsymbol{R}} e^{i\boldsymbol{k}\cdot(\boldsymbol{x}_{\mathbf{j}+\hat{\mathbf{r}}^{(\mathrm{n})}}-\boldsymbol{x}_{\mathbf{i}})}\boldsymbol{K}_{\mathbf{i}(\mathbf{j}+\hat{\mathbf{r}}^{(\mathrm{n})})} \\
&= \sum_{\boldsymbol{r}\in\boldsymbol{R}} e^{i(\epsilon\hat{\boldsymbol{k}})\cdot(\boldsymbol{x}_{\mathbf{j}+\hat{\mathbf{r}}^{(\mathrm{n})}}-\boldsymbol{x}_{\mathbf{i}})}\big(e^{i\boldsymbol{k}_s\cdot(\boldsymbol{x}_{\mathbf{j}+\hat{\mathbf{r}}^{(\mathrm{n})}}-\boldsymbol{x}_{\mathbf{i}})}\boldsymbol{K}_{\mathbf{i}(\mathbf{j}+\hat{\mathbf{r}}^{(\mathrm{n})})}\big) \\
&= \sum_{m} \epsilon^m (i\hat{\boldsymbol{k}})^m : \tilde{\boldsymbol{K}}^{(\mathrm{m})}_{\mathbf{ij}},
\end{aligned}
\tag{B.10}
$$

where

$$
\begin{aligned}
\tilde{\boldsymbol{K}}^{(\mathrm{m})}_{\mathbf{ij}} &= \frac{(-i)^m}{m!}\Big[\frac{\partial^m}{\partial\boldsymbol{k}^m}\tilde{\boldsymbol{K}}_{\mathbf{ij}}\Big]_{\boldsymbol{k}=\boldsymbol{k}_s} \\
&= \frac{1}{m!}\sum_{\boldsymbol{r}\in\boldsymbol{R}}(\boldsymbol{x}_{\mathbf{j}+\hat{\mathbf{r}}^{(\mathrm{n})}}-\boldsymbol{x}_{\mathbf{i}})^m\otimes\big(e^{i\boldsymbol{k}_s\cdot(\boldsymbol{x}_{\mathbf{j}+\hat{\mathbf{r}}^{(\mathrm{n})}}-\boldsymbol{x}_{\mathbf{i}})}\boldsymbol{K}_{\mathbf{i}(\mathbf{j}+\hat{\mathbf{r}}^{(\mathrm{n})})}\big)
\end{aligned}
\tag{B.11}
$$

and

$$
(\boldsymbol{x}_{\mathbf{j}+\hat{\mathbf{r}}^{(\mathrm{n})}}-\boldsymbol{x}_{\mathbf{i}})^m = (\boldsymbol{x}_{\mathbf{j}+\hat{\mathbf{r}}^{(\mathrm{n})}}-\boldsymbol{x}_{\mathbf{i}})\otimes(\boldsymbol{x}_{\mathbf{j}+\hat{\mathbf{r}}^{(\mathrm{n})}}-\boldsymbol{x}_{\mathbf{i}})\otimes\ldots\otimes(\boldsymbol{x}_{\mathbf{j}+\hat{\mathbf{r}}^{(\mathrm{n})}}-\boldsymbol{x}_{\mathbf{i}})
\tag{B.12}
$$

m times, which defines the expansion of $\tilde{\boldsymbol{K}}_{\boldsymbol{k}}$ and thus that of $\hat{\boldsymbol{K}}_{\boldsymbol{k}}$. On denoting by $(\tilde{\boldsymbol{K}}^{(\mathrm{m})}_{\mathbf{ij}})^{\star}$ the conjugate transpose *with regard the last two indices* of $\tilde{\boldsymbol{K}}^{(\mathrm{m})}_{\mathbf{ij}}$, one further

finds that

$$
\begin{aligned}
(\tilde{\boldsymbol{K}}^{(\mathrm{m})}_{\mathbf{ij}})^{*} &= \frac{1}{m!}\sum_{\boldsymbol{r}\in\boldsymbol{R}}(\boldsymbol{x}_{\mathbf{j}+\hat{\mathbf{r}}^{(\mathrm{n})}}-\boldsymbol{x}_{\mathbf{i}})^{m}\otimes\big(e^{-i\boldsymbol{k}_s\cdot(\boldsymbol{x}_{\mathbf{j}+\hat{\mathbf{r}}^{(\mathrm{n})}}-\boldsymbol{x}_{\mathbf{i}})}\boldsymbol{K}^{\mathrm{T}}_{\mathbf{i}(\mathbf{j}+\hat{\mathbf{r}}^{(\mathrm{n})})}\big)\\
&= \frac{1}{m!}\sum_{\boldsymbol{r}\in\boldsymbol{R}}(\boldsymbol{x}_{\mathbf{j}+\hat{\mathbf{r}}^{(\mathrm{n})}}-\boldsymbol{x}_{\mathbf{i}})^{m}\otimes\big(e^{-i\boldsymbol{k}_s\cdot(\boldsymbol{x}_{\mathbf{j}+\hat{\mathbf{r}}^{(\mathrm{n})}}-\boldsymbol{x}_{\mathbf{i}})}\boldsymbol{K}_{(\mathbf{j}+\hat{\mathbf{r}}^{(\mathrm{n})})\mathbf{i}}\big)\\
&= \frac{1}{m!}\sum_{\boldsymbol{r}\in\boldsymbol{R}}(\boldsymbol{x}_{\mathbf{j}-\hat{\mathbf{r}}^{(\mathrm{n})}}-\boldsymbol{x}_{\mathbf{i}})^{m}\otimes\big(e^{-i\boldsymbol{k}_s\cdot(\boldsymbol{x}_{\mathbf{j}-\hat{\mathbf{r}}^{(\mathrm{n})}}-\boldsymbol{x}_{\mathbf{i}})}\boldsymbol{K}_{(\mathbf{j}-\hat{\mathbf{r}}^{(\mathrm{n})})\mathbf{i}}\big)\\
&= \frac{(-1)^{m}}{m!}\sum_{\boldsymbol{r}\in\boldsymbol{R}}(\boldsymbol{x}_{\mathbf{i}+\hat{\mathbf{r}}^{(\mathrm{n})}}-\boldsymbol{x}_{\mathbf{j}})^{m}\otimes\big(e^{i\boldsymbol{k}_s\cdot(\boldsymbol{x}_{\mathbf{i}+\hat{\mathbf{r}}^{(\mathrm{n})}}-\boldsymbol{x}_{\mathbf{j}})}\boldsymbol{K}_{\mathbf{j}(\mathbf{i}+\hat{\mathbf{r}}^{(\mathrm{n})})}\big)\\
&= (-1)^{m}\tilde{\boldsymbol{K}}^{(\mathrm{m})}_{\mathbf{ji}} \qquad \text{(B.13)}
\end{aligned}
$$

thanks to (3.14)–(3.15). As a result, matrix $\tilde{\boldsymbol{K}}^{(\mathrm{m})}$ and thus $\hat{\boldsymbol{K}}^{(\mathrm{m})}$ is Hermitian (resp. skew-Hermitian) in the last two indices when m is even (resp. odd).

B.5 Properties of effective coefficients

Proof of Claim 12. Thanks to the Hermitian nature of $\tilde{\boldsymbol{K}}^{(2)}$ and thus $\hat{\boldsymbol{K}}^{(2)}$ in the last two indices due to (B.13) and their symmetry in the first two indices due to (B.11)–(B.12), the first term in (3.58) is real-valued and symmetric with regard to q_1 and q_2. On projecting (3.56) for $j = q_1$ onto $\boldsymbol{\chi}^{(1)}_{q_2}$, we further find that

$$
\sum_{q_3=1}^{\mathfrak{m}}\sum_{q_4=1}^{\mathfrak{m}}\hat{K}^{(1)}_{q_1q_3q_4}(\chi^{(1)})_{q_2q_4}\overline{(\hat{\phi}_n)_{q_3}} = \sum_{q_3=1}^{\mathfrak{m}}\sum_{q_4=1}^{\mathfrak{m}}\big(\hat{K}^{(0)}_{q_3q_4}-\tilde{\lambda}_n\hat{M}_{q_3q_4}\big)\overline{(\chi^{(1)})_{q_1q_3}}(\chi^{(1)})_{q_2q_4}. \qquad \text{(B.14)}
$$

Hence, thanks to the Hermitian nature of $\hat{\boldsymbol{K}}^{(0)}$ and symmetry of $\hat{\boldsymbol{M}}$, the second term in (3.58) is real-valued and symmetric with regard q_1 and q_2, which proves the claim.

Proof of Claim 13. Let $\hat{\boldsymbol{\phi}}_n$, $n \in \overline{1,\mathfrak{m}}$ be an eigenvector satisfying (3.32), and let $\tilde{\boldsymbol{\phi}}_n = \boldsymbol{G}\cdot\hat{\boldsymbol{\phi}}_n$. With reference to (3.26), we have

$$
\sum_{j=1}^{N_{\mathrm{n}}}\tilde{\boldsymbol{K}}_{\mathbf{ij}}\cdot\tilde{\boldsymbol{\phi}}_n|_{\mathbf{j}} - \omega^2 M_{\mathbf{i}}\,\tilde{\boldsymbol{\phi}}_n|_{\mathbf{i}} = \mathbf{0}, \quad i\in\overline{1,N_{\mathrm{n}}}, \qquad \text{(B.15)}
$$

where $\tilde{\boldsymbol{\phi}}_n|_{\mathbf{j}}$ denotes the restriction of $\tilde{\boldsymbol{\phi}}_n$ to node $\mathbf{j}$ inside the unit cell containing the

origin. As a result, the Bloch vector $\boldsymbol{\phi}_n|_{\mathbf{i}} = \tilde{\boldsymbol{\phi}}_n|_{\mathbf{i}}\, e^{i\boldsymbol{k}\cdot\boldsymbol{x}_{\mathbf{i}}}$ satisfies

$$\sum_{j=1}^{N_{\mathrm{n}}} (e^{i\boldsymbol{k}\cdot(\boldsymbol{x}_{\mathbf{i}}-\boldsymbol{x}_{\mathbf{j}})}\tilde{\boldsymbol{K}}_{\mathbf{ij}})\cdot\boldsymbol{\phi}_n|_{\mathbf{j}} \,-\, \omega^2 M_{\mathbf{i}}\,\boldsymbol{\phi}_n|_{\mathbf{i}} \,=\, \mathbf{0}, \quad i\in\overline{1,N_{\mathrm{n}}}. \tag{B.16}$$

For wavenumbers $\boldsymbol{k}_s = \frac{1}{2}\sum_{l=1}^{\mathfrak{p}} n_l\boldsymbol{e}^l$, $n_l\in\{-1,0,1\}$, which include the origin and apexes of the first Brillouin zone $\mathcal{B}$, recalling (3.7), (3.24) and (3.27) we obtain

$$\begin{aligned}
e^{i\boldsymbol{k}_s\cdot(\boldsymbol{x}_{\mathbf{i}}-\boldsymbol{x}_{\mathbf{j}})}\tilde{\boldsymbol{K}}_{\mathbf{ij}} &= \sum_{\boldsymbol{r}\in\boldsymbol{R}} e^{i\boldsymbol{k}_s\cdot(\boldsymbol{x}_{\mathbf{i}}-\boldsymbol{x}_{\mathbf{j}})}\check{\boldsymbol{K}}_{\mathbf{i}(\mathbf{j}+\hat{\mathbf{r}}^{(\mathrm{n})})} \;=\; \sum_{\boldsymbol{r}\in\boldsymbol{R}} e^{i\boldsymbol{k}_s\cdot\boldsymbol{r}}\boldsymbol{K}_{\mathbf{i}(\mathbf{j}+\hat{\mathbf{r}}^{(\mathrm{n})})},\\
&= \sum_{\boldsymbol{r}\in\boldsymbol{R}} e^{i(\sum_{l=1}^{\mathfrak{p}} r^l n_l)\pi}\boldsymbol{K}_{\mathbf{i}(\mathbf{j}+\hat{\mathbf{r}}^{(\mathrm{n})})},\\
&= \sum_{\boldsymbol{r}\in\boldsymbol{R}} (-1)^{(\sum_{l=1}^{\mathfrak{p}} r^l n_l)}\boldsymbol{K}_{\mathbf{i}(\mathbf{j}+\hat{\mathbf{r}}^{(\mathrm{n})})},\\
&= \sum_{\boldsymbol{r}\in\boldsymbol{R}} (-1)^{(\sum_{l=1}^{\mathfrak{p}} r^l n_l)}\boldsymbol{K}_{(\mathbf{i}-\hat{\mathbf{r}}^{(\mathrm{n})})\mathbf{j}},\\
&= \sum_{\boldsymbol{r}\in\boldsymbol{R}} (-1)^{(\sum_{l=1}^{\mathfrak{p}} r^l n_l)}\boldsymbol{K}_{(\mathbf{i}+\hat{\mathbf{r}}^{(\mathrm{n})})\mathbf{j}},\\
&= \sum_{\boldsymbol{r}\in\boldsymbol{R}} (-1)^{(\sum_{l=1}^{\mathfrak{p}} r^l n_l)}\boldsymbol{K}^{\mathrm{T}}_{\mathbf{j}(\mathbf{i}+\hat{\mathbf{r}}^{(\mathrm{n})})},\\
&= e^{i\boldsymbol{k}_s\cdot(\boldsymbol{x}_{\mathbf{j}}-\boldsymbol{x}_{\mathbf{i}})}\tilde{\boldsymbol{K}}^{\mathrm{T}}_{\mathbf{ji}}, \qquad i,j\in\overline{1,N_{\mathrm{n}}}.
\end{aligned} \tag{B.17}$$

As a result, matrix $e^{i\boldsymbol{k}_s\cdot(\boldsymbol{x}_{\mathbf{i}}-\boldsymbol{x}_{\mathbf{j}})}\tilde{\boldsymbol{K}}_{\mathbf{ij}}$ is real-valued and has the symmetry property (B.17). Therefore, the stiffness matrix corresponding to the EP (B.16) is real and symmetric, which demonstrates that the Bloch eigenvector $\boldsymbol{\phi}_n$, $n\in\overline{1,\mathfrak{m}}$ can be taken as real-valued.

On the other hand recalling (B.11), for $\boldsymbol{k} = \boldsymbol{k}_s + \epsilon\hat{\boldsymbol{k}}$ and $\boldsymbol{k}_s = \frac{1}{2}\sum_{l=1}^{\mathfrak{p}} n_l\boldsymbol{e}^l$ ($n_l\in\{-1,0,1\}$) we have

$$
\begin{aligned}
e^{i\boldsymbol{k}_s\cdot(\boldsymbol{x}_{\mathbf{i}}-\boldsymbol{x}_{\mathbf{j}})}\tilde{\boldsymbol{K}}^{(\mathrm{m})}_{\mathbf{ij}} &= \frac{1}{m!}\sum_{\boldsymbol{r}\in\boldsymbol{R}}(\boldsymbol{x}_{\mathbf{j}+\hat{\mathbf{r}}^{(\mathrm{n})}}-\boldsymbol{x}_{\mathbf{i}})^m\otimes\left(e^{i\boldsymbol{k}_s\cdot\boldsymbol{r}}\boldsymbol{K}_{\mathbf{i}(\mathbf{j}+\hat{\mathbf{r}}^{(\mathrm{n})})}\right)\\
&= \frac{1}{m!}\sum_{\boldsymbol{r}\in\boldsymbol{R}}(\boldsymbol{x}_{\mathbf{j}+\hat{\mathbf{r}}^{(\mathrm{n})}}-\boldsymbol{x}_{\mathbf{i}})^m\otimes\left((-1)^{(\sum_{l=1}^{\mathfrak{p}}r^l n_l)}\boldsymbol{K}_{\mathbf{i}(\mathbf{j}+\hat{\mathbf{r}}^{(\mathrm{n})})}\right)\\
&= \frac{1}{m!}\sum_{\boldsymbol{r}\in\boldsymbol{R}}(\boldsymbol{x}_{\mathbf{j}-\hat{\mathbf{r}}^{(\mathrm{n})}}-\boldsymbol{x}_{\mathbf{i}})^m\otimes\left((-1)^{(\sum_{l=1}^{\mathfrak{p}}r^l n_l)}\boldsymbol{K}_{\mathbf{i}(\mathbf{j}-\hat{\mathbf{r}}^{(\mathrm{n})})}\right)\\
&= \frac{(-1)^m}{m!}\sum_{\boldsymbol{r}\in\boldsymbol{R}}(\boldsymbol{x}_{\mathbf{i}+\hat{\mathbf{r}}^{(\mathrm{n})}}-\boldsymbol{x}_{\mathbf{j}})^m\otimes\left((-1)^{(\sum_{l=1}^{\mathfrak{p}}r^l n_l)}\boldsymbol{K}_{(\mathbf{i}+\hat{\mathbf{r}}^{(\mathrm{n})})\mathbf{j}}\right)\\
&= \frac{(-1)^m}{m!}\sum_{\boldsymbol{r}\in\boldsymbol{R}}(\boldsymbol{x}_{\mathbf{i}+\hat{\mathbf{r}}^{(\mathrm{n})}}-\boldsymbol{x}_{\mathbf{j}})^m\otimes\left((-1)^{(\sum_{l=1}^{\mathfrak{p}}r^l n_l)}\boldsymbol{K}^{\mathrm{T}}_{\mathbf{j}(\mathbf{i}+\hat{\mathbf{r}}^{(\mathrm{n})})}\right)\\
&= (-1)^m e^{i\boldsymbol{k}_s\cdot(\boldsymbol{x}_{\mathbf{j}}-\boldsymbol{x}_{\mathbf{i}})}(\tilde{\boldsymbol{K}}^{(\mathrm{m})}_{\mathbf{ji}})^{\mathrm{T}}, \qquad i,j\in\overline{1,N_{\mathrm{n}}}. \qquad \text{(B.18)}
\end{aligned}
$$

where the transpose is applied *to the last two indices*. In other words, matrix $e^{i\boldsymbol{k}_s\cdot(\boldsymbol{x}_{\mathbf{i}}-\boldsymbol{x}_{\mathbf{j}})}\tilde{\boldsymbol{K}}^{(\mathrm{m})}_{\mathbf{ij}}$ is real-valued and satisfies symmetry (resp. anti-symmetry) with regard its last two indices when m is even (resp. odd).

With such result in place, for an eigenvector $\hat{\boldsymbol{\phi}}_n$, $n\in\overline{1,\mathfrak{m}}$, satisfying (3.32) at $\boldsymbol{k}_s=\frac{1}{2}\sum_{l=1}^{\mathfrak{p}}n_l\boldsymbol{e}^l$ ($n_l\in\{-1,0,1\}$), we recall (3.29) and (3.31) to obtain

$$
\begin{aligned}
\boldsymbol{\theta}^{(0)} &= -\langle\hat{\boldsymbol{K}}^{(1)}\cdot\hat{\boldsymbol{\phi}}_n\rangle \;=\; -(\hat{\boldsymbol{K}}^{(1)}\cdot\hat{\boldsymbol{\phi}}_n)\cdot\overline{\hat{\boldsymbol{\phi}}_n} \;=\; -(\tilde{\boldsymbol{K}}^{(1)}\cdot\tilde{\boldsymbol{\phi}}_n)\cdot\overline{\tilde{\boldsymbol{\phi}}_n}\\
&= -\sum_{i=1}^{N_{\mathrm{n}}}\sum_{j=1}^{N_{\mathrm{n}}}\left(e^{i\boldsymbol{k}_s\cdot(\boldsymbol{x}_{\mathbf{i}}-\boldsymbol{x}_{\mathbf{j}})}\tilde{\boldsymbol{K}}^{(1)}_{\mathbf{ij}}\cdot\boldsymbol{\phi}_n|_{\mathbf{j}}\right)\cdot\overline{\boldsymbol{\phi}_n|_{\mathbf{i}}}\\
&= -\sum_{i=1}^{N_{\mathrm{n}}}\sum_{j=1}^{N_{\mathrm{n}}}\left(e^{i\boldsymbol{k}_s\cdot(\boldsymbol{x}_{\mathbf{i}}-\boldsymbol{x}_{\mathbf{j}})}\tilde{\boldsymbol{K}}^{(1)}_{\mathbf{ij}}\cdot\boldsymbol{\phi}_n|_{\mathbf{j}}\right)\cdot\boldsymbol{\phi}_n|_{\mathbf{i}}\\
&= -\sum_{i=1}^{N_{\mathrm{n}}}\sum_{j=1}^{N_{\mathrm{n}}}\left(e^{i\boldsymbol{k}_s\cdot(\boldsymbol{x}_{\mathbf{i}}-\boldsymbol{x}_{\mathbf{j}})}(\tilde{\boldsymbol{K}}^{(1)}_{\mathbf{ij}})^{\mathrm{T}}\cdot\boldsymbol{\phi}_n|_{\mathbf{i}}\right)\cdot\boldsymbol{\phi}_n|_{\mathbf{j}}\\
&= \sum_{i=1}^{N_{\mathrm{n}}}\sum_{j=1}^{N_{\mathrm{n}}}\left(e^{i\boldsymbol{k}_s\cdot(\boldsymbol{x}_{\mathbf{j}}-\boldsymbol{x}_{\mathbf{i}})}\tilde{\boldsymbol{K}}^{(1)}_{\mathbf{ji}}\cdot\boldsymbol{\phi}_n|_{\mathbf{i}}\right)\cdot\boldsymbol{\phi}_n|_{\mathbf{j}} \;=\; -\boldsymbol{\theta}^{(0)} \;=\; \mathbf{0}, \qquad \text{(B.19)}
\end{aligned}
$$

which establishes the claim.

Proof of Claim 14. Thanks to the Hermitian nature of $\hat{\boldsymbol{K}}^{(2)}$ in the last two indices

and its symmetry in the first two indices, the first term in (3.70) satisfies

$$\sum_{q_3=1}^{\mathfrak{m}}\sum_{q_4=1}^{\mathfrak{m}}\overline{\hat{K}^{(2)}_{q_1q_2q_3q_4}(\hat{\phi}_{n_q})_{q_4}\overline{(\hat{\phi}_{n_p})_{q_3}}} \;=\; \sum_{q_3=1}^{\mathfrak{m}}\sum_{q_4=1}^{\mathfrak{m}}\hat{K}^{(2)}_{q_1q_2q_3q_4}(\hat{\phi}_{n_p})_{q_4}\overline{(\hat{\phi}_{n_q})_{q_3}}. \tag{B.20}$$

By projecting equation (3.68) for $j = q_1$ on $\boldsymbol{\chi}^{(1)}_{pq_2}$, with $q_1, q_2 \in \overline{1,\mathfrak{p}}$, we find that

$$\sum_{q_3=1}^{\mathfrak{m}}\sum_{q_4=1}^{\mathfrak{m}}\hat{K}^{(1)}_{q_1q_3q_4}(\chi^{(1)}_p)_{q_2q_4}\overline{(\hat{\phi}_{n_q})_{q_3}} \;=\; \sum_{q_3=1}^{\mathfrak{m}}\sum_{q_4=1}^{\mathfrak{m}}\big(\hat{K}^{(0)}_{q_3q_4}-\tilde{\lambda}_n\hat{M}_{q_3q_4}\big)\overline{(\chi^{(1)}_q)_{q_1q_3}}(\chi^{(1)}_p)_{q_2q_4}. \tag{B.21}$$

Hence, thanks to the Hermitian nature of $\hat{\boldsymbol{K}}^{(0)}$ and symmetry of $\hat{\boldsymbol{M}}$, we find that

$$\overline{(\mu^{(0)}_{pq})_{q_1q_2}} = (\mu^{(0)}_{qp})_{q_1q_2} \tag{B.22}$$

which establishes the claim.